Structural and Electrical Studies of $Ba(FeNb)_{0.5}O_3$ based High Dielectric Constant Materials Synthesized by Conventional and Microwave Processing Techniques

THESIS SUBMITTED IN PARTIAL FULFILLMENT OF THE REQUIREMENTS FOR THE DEGREE OF

DOCTOR OF PHILOSOPHY

By

Subrat Kumar Kar

Under the supervision of

Prof. P. Kumar (PH) & Prof. S. K. Pratihar (CR)

Department of Physics & Astronomy

National Institute of Technology, Rourkela

769008, Odisha, India

August – 2014

I firmly believe that the accomplishments, genius, higher education and learning and wealth that God has given me are His. I have right to spend for my own purposes only what is needed for the maintenance of the family and if otherwise absolutely essential...

If Divine is there, then there must be a way of experiencing His existence, of realizing His presence, however hard the path, I have taken a firm resolution to follow it…

Whereas others regard the country as an inert object and know it as the plains, the fields, the forests, the mountains and rivers, I look upon my country as the mother, I worship her and adore her as the mother….

An Illuminated Teacher and Yoga Master

Sri Aurobindo

DEDICATED

TO

MY BELOVED PARENTS & ALMIGHTY

DECLARATION

I hereby declare that the thesis entitled "**Structural and Electrical Studies of $Ba(FeNb)_{0.5}O_3$ based High Dielectric Constant Materials Synthesized by Conventional and Microwave Processing Techniques**" which is being submitted to the National Institute of Technology for the award of degree of **Doctor of Philosophy** is original and authentic work conducted by me in the Department of Physics & Astronomy, National Institute of Technology, Rourkela under the supervision of **Prof. P. Kumar**, Department of Physics & Astronomy and under the co-supervision of **Prof. S. K. Pratihar**, Department of Ceramic Engineering, National Institute of Technology, Rourkela. I confirm the norms and guidelines given in the ethical code of conduct of the institute. Whenever I have used materials (data, theoretical analysis, and text) from other sources, I have given due credit to them by citing them in the text of the thesis and giving their details in the references.

Subrat Kumar Kar

Department of Physics & Astronomy,

National Institute of Technology,

Rourkela

CERTIFICATE

This is to certify that the thesis entitled **“Structural and Electrical Studies of Ba(FeNb)$_{0.5}$O$_3$ based High Dielectric Constant Materials Synthesized by Conventional and Microwave Processing Techniques”** being submitted by Subrat Kumar Kar to the Department of Physics & Astronomy, National Institute of Technology, Rourkela, for the award of the Doctor of Philosophy, is a record of bonafide research carried out by him. He has worked under our guidance and supervision, and has fulfilled the requirements for the submission of this thesis, which to our knowledge has reached the requisite standard.

The results contained herein have not been submitted in part or full to any other university or institution for award of any degree or diploma.

Prof. P. Kumar
Associate Professor
Department of Physics & Astronomy,
National Institute of Technology,
Rourkela-769008, India

Prof. S. K. Pratihar
Associate Professor
Department of Ceramic Engineering,
National Institute of Technology,
Rourkela-769008, India

ACKNOWLEDGEMENTS

It is with immense gratitude that I acknowledge the support and help of my thesis supervisors Prof. P. Kumar & Prof. S. K. Pratihar for their constant encouragements during the tenure of this work. They were always available for helping me and provided me all kinds of facilities for carrying out my research work. I am grateful to them for being a constant source of motivation and guiding me throughout my research work.

It gives me great pleasure in acknowledging to my DSC committee members, Prof. D. K. Bisoyi, Prof. U. K. Mohanty, Prof. R. Mazumder and Prof. D. K. Pradhan for their valuable suggestions and encouragement during the course of this work.

I share the credit of my work with Prof S K Sarangi, Director, NIT Rourkela for allowing me to utilize all the relevant facilities available in the Institute in general and Department of Physics & Astronomy in particular**.**

I would like to thank Prof. J. P. Kar who supported and explained me some important parts of my research work whenever I was in doubt.

I express my gratitude for all the faculty members of the Department of Physics & Astronomy for their great support and motivation. It also gives me pleasure to thank Dr. Sonia Madam (Chemistry) for her continuous inspiration.

I am extremely thankful to all the supporting and technical staff of the Department of Physics & Astronomy, Department of Materials and Metallurgical Engineering and Department of Ceramic Engineering for their helps without which I could not have completed my work.

I thank my institute for the award of a research fellowship that helped me financially and encouraged me to pursue my research investigations successfully.

I am thankful to Sarat K. Rout, (Ceramic), Dr. B. Parija, Pradyumna K. Parida (ScientistC-IGCAR), B. Samantaray (IITG), Dr. Vinod (Pondicherry University) for their timely co-operation and encouragement to finish my work.

I am also thankful to S. Naresh Kumar and Chandrasekhar Mallam for their support and co-operation in my thesis work. I am extremely thankful to Miss Sridevi Swain for her support and co-operation during the last phase of this thesis work

Last but not the least; I am indebted to my parents, my family members and my uncle Sarat Parhi, for their unconditional love, affection and constant encouragement to complete this work.

ABSTRACT

There is an increasing interest in the field of dielectric ceramics. The oxide based dielectrics constitute a large portion of the materials which find large-scale technological applications in sensors, actuators, memory devices, high density capacitors etc. Generally, high dielectric constant (ε_r) is obtained in ferroelectric class of materials. But, for dielectric applications, the ferroelectric classes of materials have following disadvantages: (i) the max. ε_r is obtained near Curie temperature (Tc) (ii) the T_c is generally far away from RT. These disadvantages forbid the use of the ferroelectric classes of materials in different practical device applications near RT. To some extent, these disadvantages of the ferroelectric classes of materials are minimized by the relaxor ferroelectric materials. But, most of the relaxor ferroelectric materials are enriched with PbO, which is toxic and presently due to the environmental concern, the use of these types of materials is discouraged. Therefore, it is urgent and desirable to find out alternative lead oxide free high ε_r materials. Considering lead toxicity, there is an urgent need to develop effective lead-free/ low lead content high dielectric constant (HDC) materials, which are environmental friendly in nature. In the present study $Ba(Fe_{0.5}Nb_{0.5})O_3$/BFN system is chosen as the material of research. Main problems related to the processing of perovskite based oxide ceramics through conventional solid state reaction (CSSR) route are high processing temperature and difficulty in getting better densified product. High dielectric loss in the BFN based ceramics can be utilized for its synthesis by microwave processing technique.

The following series of BFN based ceramics are synthesized by CSSR route:

- **(i)** **$Ba_{(1-x)}La_{2x/3}(FeNb)_{0.5}O_3$ (x=0,0.02,0.04,0.06,0.08) [La^{3+} substituted series]**
- **(ii)** **$Ba_{(1-x)}Pb_x(FeNb)_{0.5}O_3$ (x=0,0.02,0.04,0.06,0.08) [Pb^{2+} substituted series]**
- **(iii)** **Ba $(FeNb)_{0.5}O_3$ – x wt% of $MnCO_3$ (x=0, 0.5,1.0,1.5,2.0) [Mn added series]**
- **(iv)** **Ba $(FeNb)_{0.5}O_3$ – x wt% of Cr_2O_3 (x=0, 0.5,1.0,1.5,2.0) [Cr added series]**

Based on the highest dielectric properties along with the parent BFN system, the following best compositions of each series were synthesized by microwave (MW) processing technique:

- **(i)** **$Ba(FeNb)_{0.5}O_3$**
- **(ii)** **$Ba(1-x)La_{2x/3}(FeNb)_{0.5}O_3$ (x=0.08)**
- **(iii)** **$Ba(1-x)Pb_x(FeNb)_{0.5}O_3$ (x=0.08)**
- **(iv)** **$Ba(FeNb)_{0.5}O_3$ – x wt% of $MnCO_3$ (x=0.5)**
- **(v)** **$Ba(FeNb)_{0.5}O_3$ – x wt% of Cr_2O_3 (x=0.5)**

Effect of conventional and microwave sintering on the structural, morphological and dielectric properties of the BFN ceramic samples were studied and compared. Experimental density of the CS and MWS BFN samples was nearly same. Dense microstructures with large grains were obtained in MWS BFN ceramics. High dielectric constant, observed in MW sintered BFN ceramics, was attributed to the large grain size and the Maxwell-Wagner type interfacial polarization. A non-Debye type relaxation at room temperature was observed in both the CS and MW sintered BFN ceramics.

La and Pb modified BFN ceramics were synthesized by conventional solid state reaction route. The XRD study confirmed the single phase with cubic structure without any trace of secondary phase. The average grain size decreased with the incorporation of La and Pb in the BFN ceramics and suggested the grain growth inhibitors nature of the dopants. The experimental densities of the La and Pb modified BFN ceramics increased compared to the parent BFN ceramics and the highest experimental densities were obtained for both the 8% La and Pb modified BFN ceramics. Room temperature highest dielectric constant (at 1kHz frequency) ~ 35844 for La and ~ 25999 for Pb modified BFN ceramics were obtained for x = 0.08 . Polarization with applied voltage showed no saturation in the loops with high leakage in both the BLFN and PBFN ceramics. The narrow optical band gap observed in both the BLFN and PBFN ceramics suggested their semiconducting nature and usefulness for photo-catalytic applications in solar cells.

Among the Cr and Mn added BFN ceramics, processed conventionally, the ceramics with the 0.5wt% addition of both the Cr and Mn exhibited highest experimental density of ~6.08g/cc and 6.02g/cc with corresponding ε_r values ~ 38832 and ~ 4245, respectively. Finally, among the conventionally processed, La, Pb, Cr, and Mn modified BFN ceramics, (i) $Ba_{(1-x)}La_{2x/3}(FeNb)_{0.5}O_3$ (x=0.08), (ii) $Ba_{(1-x)}Pb_x(FeNb)_{0.5}O_3$ (x=0.08), (iii) $Ba(FeNb)_{0.5}O_3$–x wt% of $MnCO_3$ (x=0.5) and the (iv)$Ba(FeNb)_{0.5}O_3$–x wt% of Cr_2O_3 (x=0.5) samples exhibited optimum dielectric properties.

Selected compositions of the La, Pb, Cr and Mn modified BFN ceramics were sintered in a MW furnace. The XRD patterns confirmed the formation of single phase with cubic structure in all the MWS ceramics. The grain size of the MWS ceramics increased with the increase in sintering time. Except Cr added BFN ceramics, all samples exhibited nearly same grain size as that of CS samples. The density of all the MWS samples, sintered for 45 min (except Mn added BFN ceramics), exhibited higher density than the corresponding CS ceramic samples. The dielectric properties study confirmed very high value of dielectric constant (ε_r) (~10^4) for all the samples (except Mn added BFN ceramics) at room temperature. The RT dielectric loss of all the MWS ceramics was lower compared to the corresponding CS ceramic samples. This indicated that the MW sintering can serve as an effective technique for reducing the dielectric loss with better dielectric properties in less processing time.

AC conductivity and the impedance spectroscopic technique were used to study the electrical phenomena of both the CS and MWS BFN based ceramics. Based on brick layer model, an equivalent circuit model was proposed for the observed electrical response of the CS and MWS BFN based ceramic samples. For all the samples, the grain and the grain boundary resistance decreased with the increase in temperature. Oxygen vacancies and related point defects, generated during sintering, were considered for explaining the various conduction and

relaxation mechanism, present in the CS and MWS BFN based ceramic. Resistance of the grain and grain boundary of the CS BLFN and PBFN ceramics was higher than that of the same samples sintered in microwave furnace.

Keywords: XRD; SEM; Dielectric properties; High dielectric constant; Dielectric relaxation; Conductivity; Impedance spectroscopy

The present work is reported in the following chapters

Chapter I present a short introduction about the dielectric materials, their types, and the origin of high dielectric constant, literature reviews on barium iron niobate (BFN) based ceramics along with the motivation and objectives of the present work.

Chapter II outlines the investigated parameters, i.e. principles of various experimental techniques used to characterize the materials under study.

Chapter III describes about the method of synthesis and experimental details of the current material.

Chapter IV describes about the structural, microstructural, dielectric and impedance studies of the BFN ceramics synthesized by conventional and MW processing route.

Chapter V describes about structural, morphological, optical and dielectric property studies of La^{3+} and Pb^{2+} modified BFN ceramics synthesized by conventional processing route.

Chapter VI describes about structural, morphological, optical and dielectric property studies of Cr_2O_3 and $MnCO_3$ modified BFN ceramics synthesized by conventional processing route.

Chapter VII presents the effect of microwave processing route on the microstructural and dielectric properties of the $Ba_{(1-x)}La_{2x/3}(FeNb)_{0.5}O_3$ (x=0.08), $Ba_{(1-x)}Pb_x(FeNb)_{0.5}O_3$ (x=0.08), Ba $(FeNb)_{0.5}O_3$ – x wt% of $MnCO_3$ (x=0.5), Ba $(FeNb)_{0.5}O_3$ – x wt% of Cr_2O_3 (x=0.5) ceramics.

Chapter VIII presents the conductivity and impedance spectroscopic study of selected La, Pb, Cr and Mn modified CS & MWS BFN ceramics.

Chapter IX presents the major conclusions of the present work with future work recommendations.

CONTENTS

CHAPTER 1 Introduction and Literature Survey

CHAPTER 2 Investigated Parameters

CHAPTER 3 Materials and Methods

CHAPTER 4 Structural, Dielectric, Conductivity and Impedance Studies of Ba(FeNb)$_{0.5}$O$_3$ Ceramics Synthesized by CS and MWS Techniques

CHAPTER 5 Structural, Morphological, Optical and Electrical Studies of La^{3+} and Pb^{2+} Modified BFN Ceramics

CHAPTER 6 Structural, Morphological and Electrical Studies of Cr and Mn Added BFN Ceramics

CHAPTER 7 Structural, Morphological and Electrical Studies of the MW Processed BFN Based Ceramics

CHAPTER 8 Conductivity and Impedance Spectroscopic Study of the CS & MWS Modified BFN Ceramics

CHAPTER 9 Conclusions and Future Work

LIST OF FIGURES

Page No.

CHAPTER 1

CHAPTER 2

CHAPTER 3

CHAPTER 4

CHAPTER 5

CHAPTER 6

CHAPTER 7

CHAPTER 8

List of Tables

Page No.

List of Symbols and Abbreviations

ε_r	Dielectric constant
$\tan\delta$	Dielectric loss
ε_0	Permittivity of free space
ε'	Real part of permittivity
ε''	Imaginary part of permittivity
ε_s	Static permittivity
ε_∞	High optical permittivity
T_c	Curie temperature
$P_{e,}$ $P_{i,}$ $P_{d,}$ $P_{s,}$ P_{dw}	Electronic, ionic, dipolar, space charge, domain wall polarizations respectively
a, b, c	Lattice parameters
V	Volume of the unit cell
σ	Conductivity
τ	Relaxation time
ω	Angular frequency
E_a	Activation energy
E_g	Band gap energy
Z'	Real part of impedance
Z"	Imaginary part of impedance
R_g	Grain resistance
R_{gb}	Grain boundary resistance
ac	Alternating current
dc	Direct current
HDC	High dielectric constant
PNR	Polar nano region
DPT	Displacive phase transition
M-W	Maxwell-Wagner
MLC	Multi-layer capacitor
BFN	$Ba(FeNb)_{0.5}O_3$

BT	$BaTiO_3$
PMN-PT	$Pb(Mg_{1/3}Nb_{2/3})O_3$-$PbTiO_3$
CCTO	$CaCu_3Ti_4O_{12}$
BLC	Barrier Layer Capacitors
IBLC	Internal barrier layer capacitor
PVA	Poly vinyl alcohol
DSC	Differential scanning calorimetry
TGA	Thermo gravimetric analysis
XRD	X-ray diffraction
SEM	Scanning electron microscope
CPE	Constant phase element
CIS	Complex impedance spectroscopy
JPL	Jonscher's power law
JRM	Jump relaxation model
CSSR	conventional solid-state reaction
CS	Conventionally sintered
MWS	Microwave sintered

CHAPTER 1

Introduction and Literature Survey

1.1 Introduction

Ceramic materials having versatile properties such as semiconducting, dielectric, piezoelectric, pyroelectric, electro-optic, magnetic and superconducting natures are widely used both in research and technology. Ceramic materials are inorganic, non-metallic solids and prepared by heating and subsequent cooling. By looking at the present and future growth of the worldwide ceramics market, the field of electronic-ceramics (electro-ceramics) has been recognised as one of the most exciting field in material science. The electrical properties of ceramic materials can be varied over several orders of magnitude and can be utilized in numerous device applications. Large portion of the ceramic materials, used for technological applications, is constituted by oxides based dielectrics. There is always search of new electro-ceramic materials with superior properties to meet the fast growing technological demand.

First in 1950's, barium titanate ($BaTiO_3$) based ceramics were used in capacitor and piezoelectric transducer device applications. Subsequently, many other ferroelectric ceramics including lead titanate ($PbTiO_3$), lead zirconate titanate (PZT), lead lanthanum zirconate titanate (PLZT), and relaxor ferroelectrics like lead magnesium niobate (PMN) have been developed and utilized in variety of other applications. With the development of newer ceramic processing and thin film technology, many new applications of electro-ceramics have also been emerged. The biggest use of the ferroelectric ceramics have been in the areas such as dielectric ceramics for capacitor applications, ferroelectric thin films for non- volatile memories, piezoelectric materials for medical ultrasound imaging and actuators, and electro-optic materials for data storage and displays [1].

Various electronic device applications have triggered the research work on the development of high dielectric constant (ε_r) with low dielectric loss (tanδ) in the materials. Materials with high ε_r are extensively used in technological applications like resonators, filters, wireless communication systems, such as cellular phones, global positioning systems, memory devices based on capacitive components such as static and dynamic random access memories etc. [2].

1.2 Classification of Materials Based on Crystal Symmetry

Crystal classification of materials and their different physical properties are related. This can be explained by Neumann's principle which says that every physical property, exhibited by a crystal, must possess at least the symmetry of the crystal [3]. All the materials show some common properties such as the electrostriction, dielectric permittivity and the elastic compliance, but piezoelectric and pyroelectric properties are possessed by materials having certain required symmetries. All possible combinations of the symmetry operations (rotation, inversion, reflection) plus allowed translations results 230 crystallographic space groups and 32 point groups or crystal symmetry classes. Fig.1.1 shows the classification of materials on the basis of crystal symmetry. Among 32 crystal symmetry classes, 11 classes have a centre of symmetry and non-polar in nature whereas the rest 21 classes are of non centrosymmetric in nature and polar in nature. Here, out of 21 non centrosymmetric classes except symmetry class having 432 group, the materials belonging to the 20 point group classes possess one or more crystallographic unique directional axes and exhibit the piezoelectric effect [4].

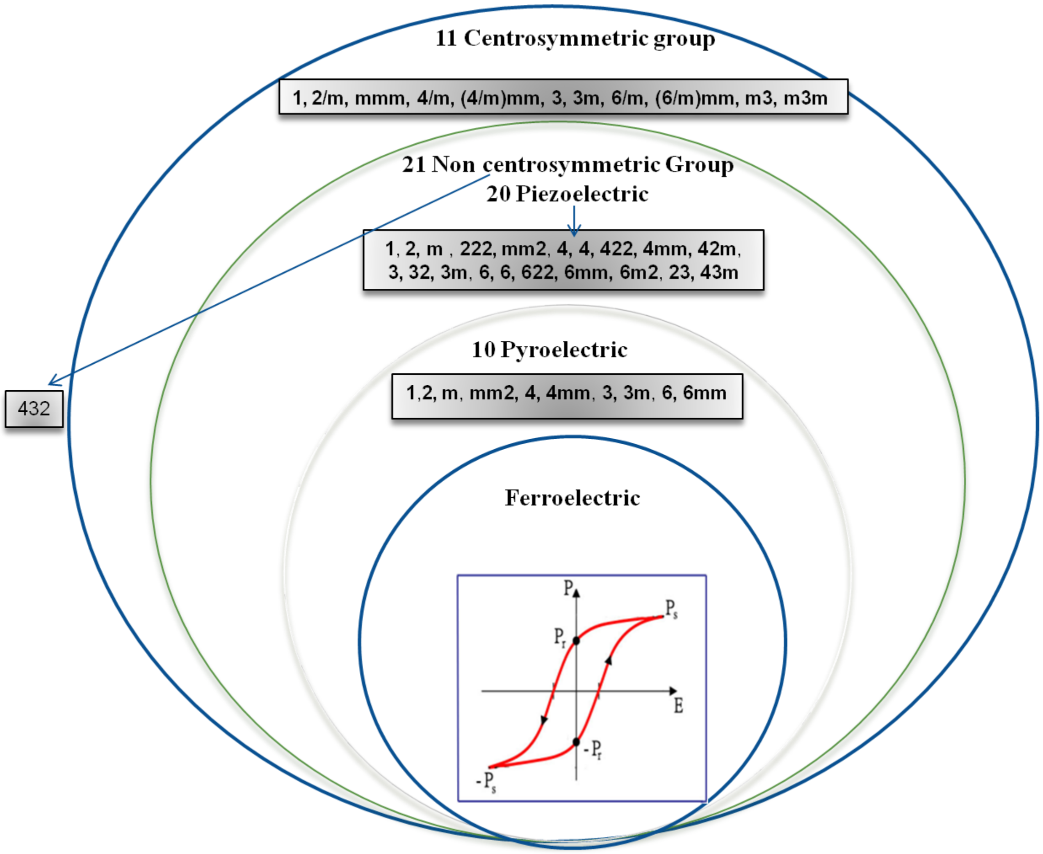

Fig. 1.1: Crystal classification based on symmetry principle [5].

Now, again out of these 20 non centro-symmetric point group classes, the crystals possessing a unique polar axis can have spontaneous polarization and these materials are known as pyroelectric in nature. As shown in Fig. 1.1, a restricted group of pyroelectric class of materials have the special property of switching of spontaneous polarization by the application of external electric field and are known as ferroelectric materials. Thus, all the ferroelectric class of materials inherently show pyroelectric and piezoelectric effects but the vice versa is not true.

Ferroelectric classes of materials are mostly made up of mixed oxides, containing corner sharing oxygen octahedra. Based on the position of the oxygen octahedra, these structures can be classified into four types such as: perovskite, tungsten bronze, bismuth oxide layer, and pyrochlore [1]. Among these four structures, the materials belonging to perovskite class possess high dielectric constant (ε_r). In the present study our studied system belongs to perovskite class. Therefore, in the next section the detail structural arrangement of atoms in the perovskite structure is described.

1.3 Perovskite (ABO_3) Ceramics

General formula ABO_3 is the prototype of perovskite structure. Here, the A-site cations (e.g. Ba^{2+}, Sr^{2+}, Ca^{2+}, Pb^{2+}) are normally larger than the B-site cations (e.g. Ti^{4+}, Zr^{4+}, Sn^{4+}) and O represents the oxygen. Fig. 1.2 (a) shows the three dimensional network of corner sharing O^{2-} ions octahedral. Here, A-site cations are surrounded by twelve anions in cube-octahedral coordination and the B site cations are surrounded by six anions in octahedral coordination. Fig.1.2 (b) shows the ideal perovskite with cubic unit cell [6, 7]. Most of the materials belonging to perovskite structure are ionic compounds, and the ions comprising it can be regarded to a first approximation as spheres with ionic radii R (Å). In real perovskite structure, because of the differences in the sizes of the O, A and B ions, the tolerance factor 't' which is given by,

$$t = \frac{R_A + R_B}{\sqrt{2}(R_B + R_o)} \tag{1.1}$$

Where, R_A, R_B and R_O are the ionic radii of A, B and O ions respectively [8]. For ideal cubic structure t=1.0, however, perovskite structures with $0.95 < t < 1.0$ are cubic in nature. The perovskite structures with $t > 1.0$ tend to be ferroelectric and with $t < 0.95$, leading to non-ferroelectric nature results in distorted perovskite structure. In addition to 't', the polarizability of the ions also plays a significant role in determining the nature of the material [9].

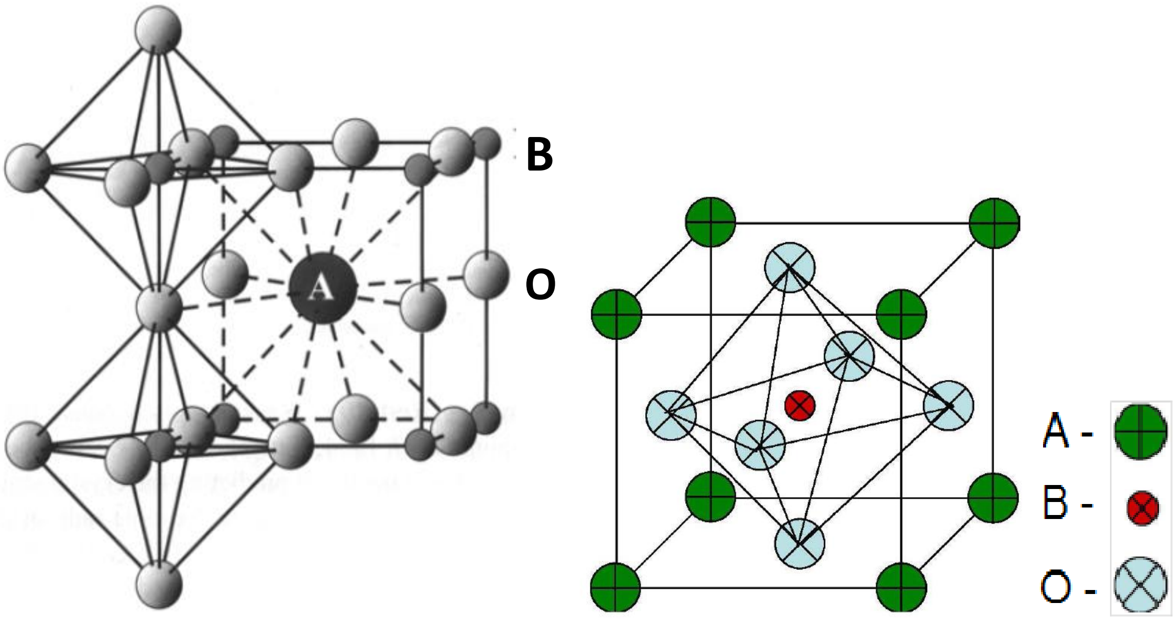

Fig. 1.2: (a) Three dimensional network of the corner sharing octahedra of O^{2-} ions, (b) A cubic ABO_3 perovskite-type unit cell [6, 7].

In few materials, the B site becomes complex by comprising more than one cation in the ABO_3 structure and denoted as $A(B_1B_2)O_3$ and known as complex perovskite structure. Generally, in this complex perovskite structure, A= Ba^{2+},Ca^{2+},Sr^{2+},Pb^{2+} etc., B_1 is a lower valence cation (like Mg^{2+}, Zn^{2+}, Ni^{2+}, Fe^{3+}) and B_2 is a higher valence cation (like Nb^{5+}, Ta^{5+}, W^{5+}) site. Compositional heterogeneities due to the B-site cations in these complex perovskite structures make the transition diffuse in nature.

1.4 Dielectric Materials

A great progress in the research field in the dielectric materials came in the 1950's with the widespread use of barium titanate ($BaTiO_3$) based ceramics in capacitor applications for its high dielectric constant. All dielectrics are insulators, and can be polarized by an applied electric field, although the capacity to support charge varies greatly between different dielectrics. A dielectric material supports charge without conducting it to a significant degree. The electrons of dielectric materials are bound to their parent molecules. Dielectrics are described by the parameters like dielectric constant or relative permittivity (ε_r) and dielectric loss (tanδ). The total capacitance 'C' of a parallel plate capacitor is given by,

$$C = \frac{\varepsilon_O \varepsilon_r A}{d} \qquad (1.2)$$

Where, 'ε_o' is the permittivity of the free space, 'ε_r' is the dielectric constant ('$\varepsilon_o\varepsilon_r$' is the permittivity of dielectric material), 'd' is the distance between the parallel plates, and 'A' is the area of the plates. The capacitance of a parallel plate capacitor increases with the increase of dielectric constant. The high dielectric constant desirable in enhancing the volumetric efficiency of the capacitor and preparing multi-layer ceramic capacitors (MLC), which can be exploited in miniaturizing the electric and electronic devices [10].

Dielectric loss quantifies a dielectric material's inherent dissipation of electromagnetic energy. The loss of energy goes into heating a dielectric material [11]. The capacitor in an alternating current (a.c.) field causes the alternation of polarity of the plates leads to displacement of charges first in one direction and then in the other. While doing so, the charges have to overcome the opposition due to inertia which leads to a production of heat hence dissipating some of the energy associated with the applied electric field. Hence, dielectric loss is a characteristic property of the material that must be considered when applying capacitors to electric circuits. Dielectric loss depends on the applied frequency and the working temperature. The dielectric loss of a material can be estimated by parameter the loss tangent (tanδ). The loss tangent of the material is calculated by finding the ratio between the equivalent series resistance (ESR) of the capacitor and the capacitive reactance (X_C) of the capacitor i.e.

$$\tan\delta = \frac{ESR}{X_C} \qquad (1.3)$$

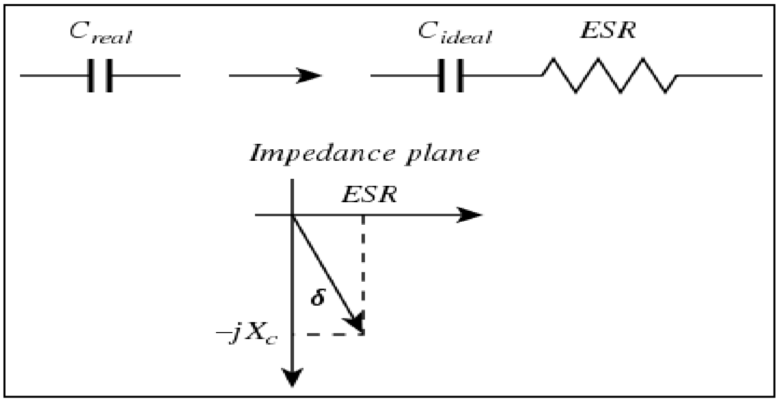

Fig. 1.3: Loss tangent illustrations in a complex plane [5].

Fig. 1.3 shows the loss tangent in a complex plane. The permittivity of materials is considered as a complex quantity i.e. $\varepsilon^* = \varepsilon' - j\,\varepsilon''$. Component ε′ represents the lossless permittivity and ε" represents the energy loss due to bound charges and dipole relaxation phenomena. In this case the loss tangent is given as follows:

$$\tan\delta = \frac{\varepsilon''}{\varepsilon'} \qquad (1.4)$$

When materials possess dielectric loss accompanied by long range dc conductivity, the total dielectric loss is given by,

$$\tan\delta = \frac{\varepsilon'}{\varepsilon''} + \frac{\sigma}{\omega\varepsilon'} \qquad (1.5)$$

Where ‘ω’ is the angular frequency of applied electric field and ‘σ’ is loss due to the free charge conduction.

1.4.1 Classification of Dielectrics

Based on the dielectric constant and dielectric loss, the ceramic dielectrics and insulators are identified and classified into different categories[12]. These different classes of dielectrics are as follows:

Class I: This class of dielectrics usually have low and medium permittivity with dissipation factors less than 0.003.

Class II/III: These classes of dielectrics consist of high permittivity ferroelectric ceramics. They have ε_r values between 2000 and 20,000 and their properties vary more with temperature, field strength and frequency than the Class I dielectrics. Their dissipation factors are generally below 0.03 but may exceed this level in some temperature ranges and in many cases become much higher when high a.c. fields are applied.

Class IV: This class of dielectrics contain a conductive phase that effectively reduces the thickness of dielectric in capacitors by at least an order of magnitude. Very simple structures such as small discs and tubes with two parallel electrodes can give capacitances of over 1 mF. Disadvantages of this class of dielectric are low working voltages i.e. mostly between 2 and 25 V and high losses.

1.4.2 Ferroelectricity in dielectrics

As discussed earlier, ferroelectrics are class of dielectric which exhibit spontaneous polarization at zero applied field and the polarization can be switched by the application of electric field. Ferroelectric materials are characterized by hysteresis loop which display polarization (P) as function of applied field (E) as shown in Fig. 1.4.

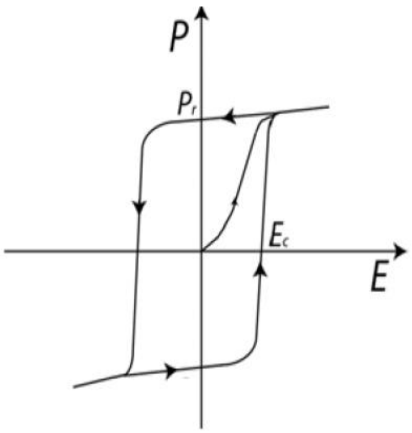

Fig. 1.4: Typical P-E hysteresis loop of a ferroelectric material [1].

The nature of the hysteresis loop depends on the origin of polarization in the material. These are (i) dielectric contribution, (ii) leakage current contribution and/or (iii) polarization (domain) switching contribution. Fig. 1.5 [13] shows the P-E hysteresis loops as a result of different types of contribution.

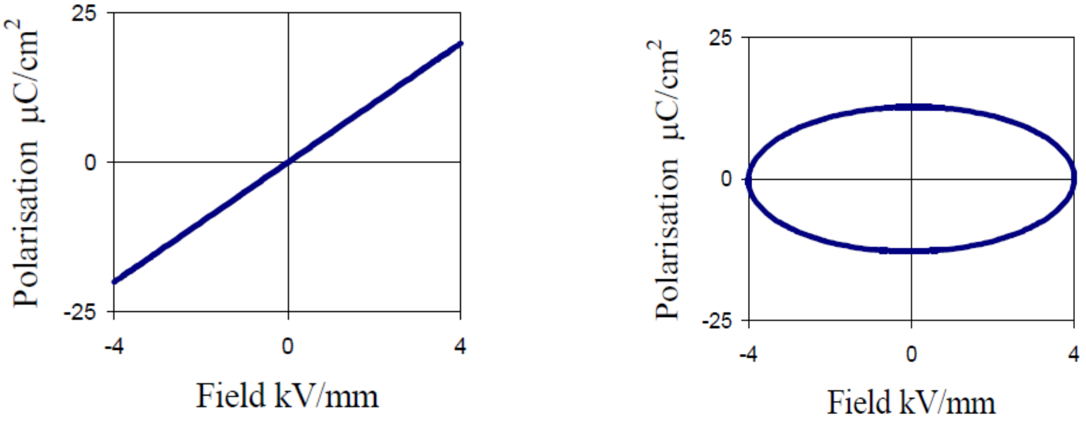

(a): Ideal linear capacitor response

(b): Ideal resistor response

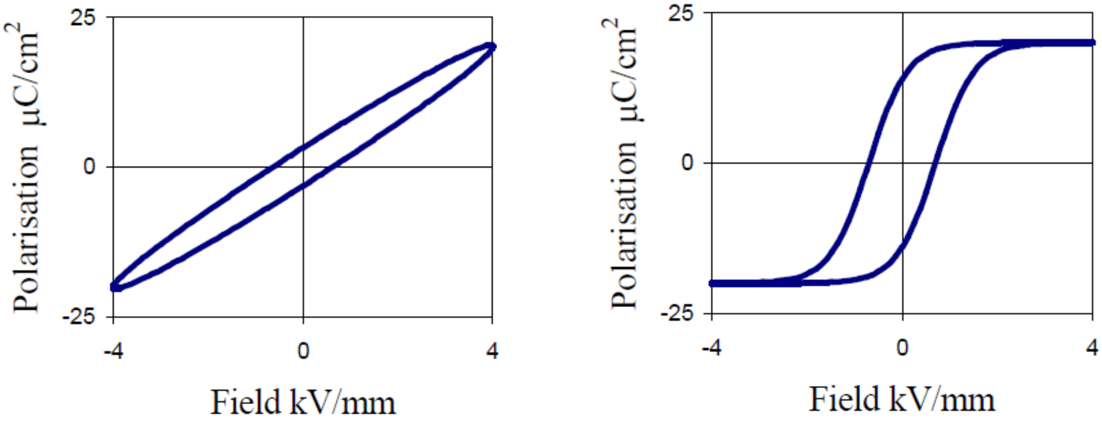

(c): Lossy capacitor response **(d):** Non-linear ferroelectric response

Fig. 1.5: Ferroelectric hysteresis loops [13].

The dielectric contribution produces a linear relationship between the polarization and electric field which is similar to that of ideal linear capacitor (Fig. 1.5 (a)). This is because for an ideal capacitor the current leads the voltage by 90 degrees, and therefore the charge (the integral of the current with time) is in phase with the voltage. For an ideal resistor the current and voltage are in phase and so the P-E loop is a circle with the centre at the origin (Fig. 1.5 (b)) which is attributed to the leakage current in the sample. If these two components are combined in parallel we get the P-E loop in Fig. 1.5(c) which is in effect a lossy capacitor, where the area within the loop is proportional to the loss tangent of the device, and the slope proportional to the capacitance. For ferroelectric materials switching polarization contribution produces a non linear P-E hysteresis loop as shown Fig. 1.5(d).

1.4.3 Applications of Dielectrics

The temperature dependence of the spontaneous polarization and permittivity of a normal ferroelectric is schematically shown in Fig.1.6 [4]. From the figure, it can be seen that the spontaneous polarization (P_s) decreases with the increase of temperature and vanishes at the Curie temperature (T_c), while permittivity tends to diverge near T_c. The reciprocal of permittivity is observed to be linear with respect to the temperature over a wide range in the paraelectric phase and obeys Curie-Weiss law.

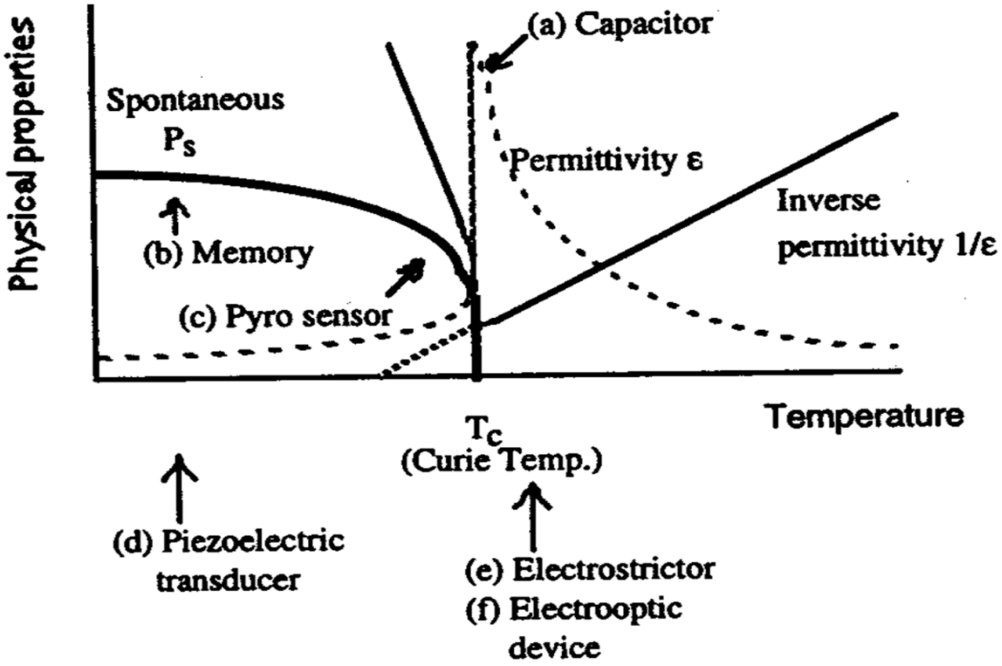

Fig. 1.6: Different application regions of dielectric materials [4].

Fig. 1.6 (a) to (f) indicates the various applications possible with a dielectric material as a whole considering its piezoelectric, pyroelectric and ferroelectric properties. For capacitor applications a material with high permittivity is required and usually dielectric material show high permittivity near transition temperature. Hence, if the operating temperature is near the transition temperature high capacitance is obtained. For room temperature capacitive applications the transition temperature should be near room temperature. But, the operational temperature range near T_c is small in the ferroelectric materials.

1.4.4 Dielectric Polarization Mechanisms

There are a number of different polarization mechanisms, distinguished the way it vary with the applied electric field, present in a dielectric material. Each mechanism has its characteristic frequency, which is the reciprocal of the characteristic time or the so called relaxation time of the process. In general, dielectric mechanisms can be divided into relaxation and resonance processes. The dependence of relative ε_r and tanδ with frequency are explained in this section and Fig. 1.7 (a) [14] shows the physical origins of different polarization processes.

(i) Electronic (Atomic) Polarization (P_e): Electronic polarization results from separation of effective centres of positive and negative charges in atoms or molecules of dielectric materials due to externally applied electric field. Hence the dipoles are induced within the material. The relaxation time of electronic polarization is in the range of 10^{-14} - 10^{-15} s. This polarization is independent of temperature.

(ii) Ionic Polarization (P_i): Ionic solids possess a net dipole moment even in the absence of external electric field. The separation between the ions increases with the applied external electric field and hence the polarization increases. Relaxation time of this type of polarizations is about 10^{-13} s and this polarization is also temperature independent.

(iii) Dipolar (Orientational) Polarization (P_d): This polarization involves the alignment of permanent dipoles, present in the lattice in the absence of an applied external electric field. Application of the electric field results in their orientation. The relaxation time or orientation time of dipolar polarization is much longer than the electronic and ionic polarization, i.e. 10^{-8} - 10^{-10} s and generated at frequencies lower than microwave frequency. This polarization is temperature dependent.

(iv) Space Charge (Interfacial) Polarization (P_s): In some materials the migration of charge carriers at the interfaces or grain boundaries results in space charge polarization. Polycrystalline or polyphasic materials exhibit an interfacial or space charge polarization, arising from the differences in the conductivities between the various phases present. Space charge polarization is also termed as the **Maxwell – Wagner (M-W) Polarization** and involves the deformation of the space charges, localized at grain boundaries, dislocations, at defect centres etc. This polarization usually disappears at frequencies higher than those of acoustic waves.

(v) Domain Wall Polarization: This polarization contributes to the overall dielectric response and plays a definite role in ferroelectric materials. The motion of a domain wall, which separates regions of differently oriented polarization, takes place by the fact that favoured oriented domains with respect to the applied field tends to grow.

The total polarization of dielectric material results from all the contributions discussed above. The contributions from the lattice are called intrinsic contributions, in contrast to extrinsic contributions[15].

$$P = \underbrace{(P_e + P_i)}_{INTRINSIC} + \underbrace{(P_d + P_s + P_{dw})}_{EXTRINSIC} \qquad (1.6)$$

Each contribution originates from a short-range movement of charges that responds to an electric field on different time scales and, hence, through a Fourier transform, in different frequency as shown in Fig. 1.7 (b).

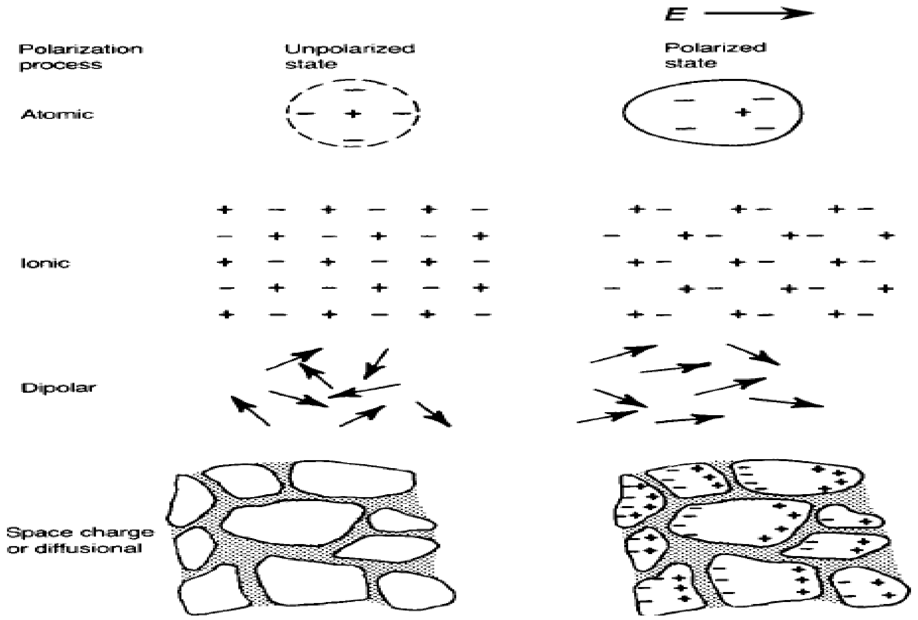

(a)

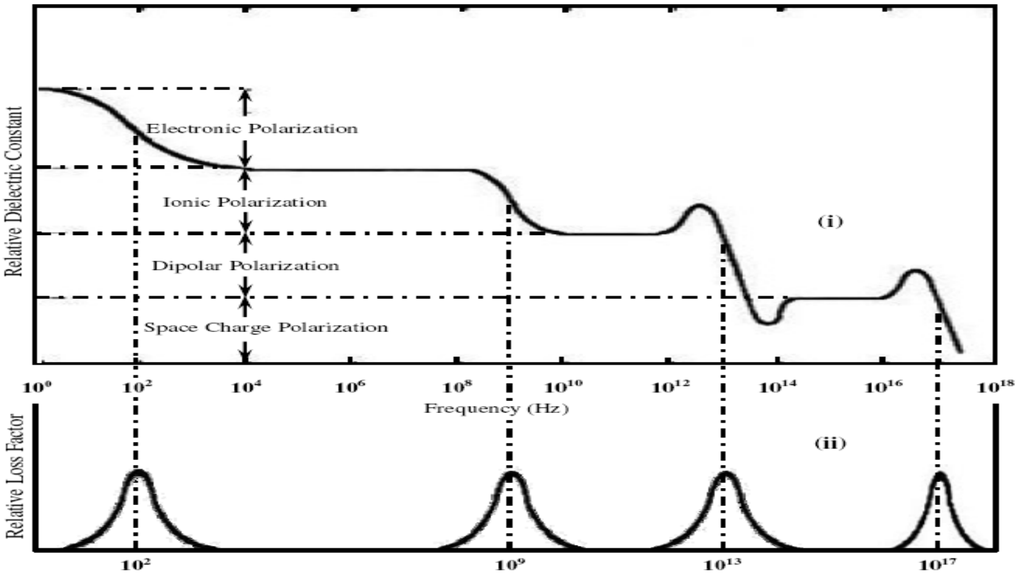

(b)

Fig. 1.7: (a) Different types of polarization processes [14] and (b) Frequency dependence of the different contributions to the relative dielectric constant and dielectric loss[16].

1.5 Debye Type and Non –Debye Type Relaxation

1.5.1 Debye Type Relaxation

Theoretical expressions of real (ε') and imaginary (ε") parts of the complex permittivity can be related with material properties, and in terms of these Debye formed the basis for understanding of dielectrics. Since, ε' and ε" are dependent on both frequency and temperature, the frequency is expressed explicitly in the Debye equations whilst temperature is introduced indirectly through other variables. In materials, commonly encountered in microwave applications, ionic and dipolar polarization dominates over electronic and space charge polarizations. These ionic and dipolar polarizations can be described by Debye's relaxation in terms of complex permittivity as follows [17]:

$$\varepsilon^* = \varepsilon_\infty + \frac{\varepsilon_S - \varepsilon_\infty}{1 + j\omega\tau} \qquad (1.7)$$

Whereas the real and imaginary parts of the permittivity can be written as

$$\varepsilon' = \varepsilon_\infty + \frac{(\varepsilon_s - \varepsilon_\infty)}{(1 + \omega^2\tau^2)} \qquad (1.8)$$

$$\varepsilon'' = \frac{(\varepsilon_s - \varepsilon_\infty)\omega\tau}{(1 + \omega^2\tau^2)} \qquad (1.9)$$

Where, τ = the relaxation time, ε_s = the static permittivity and ε_∞= the high frequency/optical permittivity.

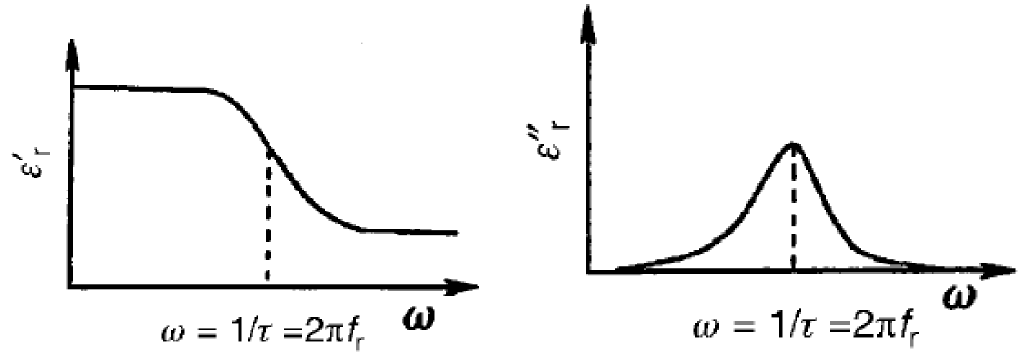

Fig. 1.8: Dielectric characteristics of a material under Debye model [18].

Fig. 1.8 shows the dielectric material characteristics in terms of real (ε_r') and imaginary (ε_r'') parts of complex permittivity as a function of frequency under Debye's model. Debye's model is valid up to microwave region. If the frequency exceeds the limit of Debye's model, other models which involve atomic and electron polarizations are taken into account. It is observed that ε'' exhibits a maximum for $\omega\tau=1$(or $\omega = 1/\tau$). For ω appreciably less than $1/\tau$, ε' becomes equal to the ε_s. In this frequency range, therefore, the losses vanish and the dipoles contribute their maximum to the polarization. On the other hand, for ω larger than $1/\tau$, the dipoles are no longer able to follow the field variations and the ε' approaches to the ε_∞. The maximum of the absorption curve and the midpoint of the dispersion curve occur at a frequency given by $\omega_{max}=1/\tau$, and the full width at half maximum of the absorption curve is approximately 1.14 decades in frequency. The Debye equations are based on the assumption that dipoles participating in the relaxation processes are non-interacting and the transient polarization can be represented by a simple exponential decay with a single relaxation time. Hence any model that represents a simple exponential polarization on applying ac electric field leads to dielectric dispersion (ε' vs. freq.) and dielectric absorption (ε'' vs. freq.) curves. The relationship between ε' and ε'' can be formulated by eliminating the parameter $\omega\tau$ and given in the following equation,

$$\left(\varepsilon' - \frac{\varepsilon_s + \varepsilon_\infty}{2}\right)^2 + \varepsilon''^2 = \left(\frac{\varepsilon_s - \varepsilon_\infty}{2}\right)^2 \qquad (1.10)$$

This is a form of a semicircular plot which is popularly known as Cole-Cole or Nyquist plot (Fig. 1.9).

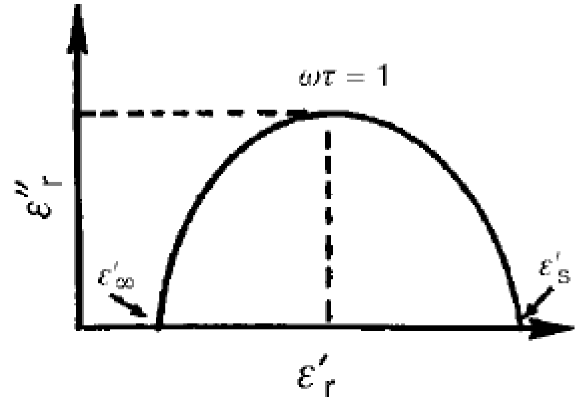

Fig. 1.9: Cole-Cole or Nyquist Plot showing the relationship between ε' and ε'' (Debye model).

1.5.2 Non-Debye Type Relaxation

Debye equations based on a single relaxation time do not suffice to describe the relaxation phenomena for most of the dielectric materials, e.g., polymers and polymer composites, ionic crystals with interacting defects, etc. In these materials, a distribution of relaxation times is necessary to interpret the experimental data. In order to consider the effect of distribution of relaxation times, Cole and Cole [17] have proposed the Argand diagram, in which ε' is plotted as a function of ε'', which can be constructed by using the following relation

$$\varepsilon^* = \varepsilon_\infty + \frac{\varepsilon_S - \varepsilon_\infty}{1 + (j\omega\tau)^{1-\alpha}} \qquad (1.11)$$

For $\alpha = 1$, Cole-Cole equation becomes equal to Debye equation. The dispersion curve with $\alpha > 0$ is broader than that of a single relaxation time but still symmetrical about $\omega\tau = 1$. The Cole–Cole plot exhibits a depressed semicircle because of $\alpha > 0$. Debye's ε' vs. ε'' semicircle is based on $\alpha = 0$, which represents the materials having only one single relaxation time. In general, there exists a distribution of relaxation times in all solid materials because there is always some non-uniformity in local domains, which would alter the individual dipoles or charges in addition to existing dipoles in the material. If the relaxation times are due to several different mechanisms, then the ε' vs. ε'' arc will be asymmetrical.

1.6 Defect Mechanism (Kröger and Vink Notation) in a Dielectric Material

The basic processes for diffusion in ionic solids require the presence of point defects in the crystal structure [10, 19]. Therefore, the conductivity is very closely related to the existence of these ionic defects, such as (1) cation vacancies, (2) cation interstitials, (3) anion vacancies, and (4) anion interstitials. In solids, the defects are mostly generated by (1) thermodynamic equilibrium (Schottky, Frenkel), (2) chemical substitution, (3) oxidation or reduction, and (4) energetic radiation. Among all of the above causes of defects in solids, the thermodynamic defects are intrinsic (inherent) defects, since they are present in the material at temperature above absolute zero and increase the configurational entropy and decrease the overall free energy. All the impurities existing in a material are called extrinsic defects since they can be created intentionally by suitable doping in order to alter the material properties. When the system is doped, then in order to maintain the charge balance, either, electrons (e') or holes (•) vacancies are generated instead of lattice vacancies.

1.6.1 Influence of Dopants on the Defect Structure

The impact of aliovalent dopant on the materials properties depends on the valence state difference of the host and the dopant ions; aliovalent doping can either be acceptor or donor-type. In perovskite structures, due to the ionic radius size, transition metal or rare-earth dopant ions can enter the structure at either A- or B-sites. In the case of acceptor dopant ions, in which the dopant ions have a lower charge than the replaced ions, excess charge is compensated by the formation of oxygen vacancies which may increase the conductivity of the material. If the oxygen vacancies are trapped in the defect complexes, then the ionic conductivity decreases. Otherwise, the high mobility of the generated vacancies at the oxygen sublattice cause enhanced ionic conductivity. On the other hand, for a donor dopant ion, the replacing ion has a higher valence state than the replaced one. In this case, the charge compensation is provided through the formation of cation vacancies either at the A-site or B-site sub-lattice or of holes [20].

1.7 Literature Review

This review covers the origins of high dielectric constant in different type of materials and their applications followed by brief discussion on the motivation and objective about the chosen ceramic materials. Under this literature review, we included three main topics as follows:

(i) Overview about the origins of HDC in ferroelectric ceramics i.e. the intrinsic contributions.

(ii) Origins of HDC through induced properties such as extrinsic contribution.

(iii) Origin of HDC, inherent in the materials.

1.7.1 HDC Materials (Intrinsic Origin)

As explained above, the electronic and ionic polarisation comes under intrinsic polarisations. There are two categories of materials which can show very high dielectric constant ~10^3 at room temperature. These are (i) normal, and (ii) relaxor ferroelectric class of materials. Ferroelectric materials exhibit a spontaneous polarization in the absence of an external electric field and the polarisation can be switched by the application of external electric field. Relaxor ferroelectrics are the type of materials in which the dielectric dispersion and high ε_r is governed by local inhomogeneities known as polar nanoregions (PNR). Relaxor ferroelectrics are special class of materials, which exhibits an enormous electromechanical response and can be easily polarized under an external applied electric field. These materials are more sensitive to temperature, field strength and frequency than lower-permittivity dielectrics. HDC in both these types of ferroelectrics is explained in the following sections.

1.7.1.1 Normal Ferroelectric Materials

Ferroelectrics are the special class of materials which possess high ε_r. Displacive phase transition (DPT) takes place in these types of materials [21-23]. Under DPT, below the phase transition temperature, the centres of the positive and negative charged ions do not coincides, which results in asymmetrical structure and inherent dipoles in the material. As the temperature decreases from above the T_c, the symmetry of the lattice changes from higher to lower symmetry. Displacement of ions from its equilibrium positions by an external force permanently settles the polarity in these types of materials and contributes to high ε_r.

$BaTiO_3$ is the typical ferroelectric material, which shows displacive phase transition where the ionic displacement is related to the relative position of Ti^{4+} ion with the O^{2-} ion.

Breaking of inversion symmetry is the main reason for the presence of ferroelectric nature in $BaTiO_3$ system [23]. In this case, the hybridization between the titanium 3d-states and the oxygen 2p-states plays crucial role for ferroelectricity. Lead titanate ($PbTiO_3$), $Pb(Zr,Ti)O_3$, $(Ba, Sr)TiO_3$ etc. are some other ferroelectric materials having perovskite structure and which exhibit high ε_r ($>10^3$) [1].

Ferroelectric materials undergo one or more number of structural phase transitions during cooling from higher temperature. In this case, materials transform from higher symmetry non polar paraelectric state to lower symmetry ferroelectric state. The transition temperature is called as Curie temperature (T_c). The ε_r of a linear dielectric has little variation with temperature, whereas for most ferroelectric materials ε_r has huge value (up to 10^4 to 10^5) near their T_c. This phenomenon is usually called as "dielectric anomaly". A sudden drop of dielectric constant is observed in both side of the T_c. The large change in dielectric constant with temperature in these materials is undesirable for many practical capacitor applications.

In most of the ferroelectric crystals the temperature dependence of the dielectric constant (ε_r), above the Curie point ($T>T_c$) can be explained by Curie-Weiss law[24]

$$\varepsilon = \varepsilon_0 + \frac{C}{T - T_0} \qquad (1.12)$$

Where, ε is the permittivity of the material, ε_0 is the permittivity of the vacuum, C is the Curie constant and T_0 is the Curie-Weiss temperature. In the case of polar dielectric ceramics, the value of ε, P_s and other properties are very sensitive to dopant, defects in the crystal, porosity, grain size, sintering time and sintering temperature etc. In general the Curie-Weiss temperature T_0, is different from the Curie temperature T_C. For first order transitions, $T_0<T_C$ while for second order phase transitions, $T_0=T_C$. Some ferroelectric materials also show diffuse

phase transition behaviour which is an additional subset of the ferroelectric phase transition that arises due to the compositional fluctuation in the material.

1.7.1.2 Relaxor Ferroelectric Materials

The high value of ε_r of ferroelectric materials is highly desirable for capacitor applications. It is also essential to maintain this high ε_r over a wide temperature range. Requirement of the above property led to systematic doping studies of ferroelectric materials, e.g. in BT ferroelectric ceramics where the temperature stability and the broadening of the maximum of the high ε_r can increase. Continuous studies to the above factors led to the development of structurally frustrated and compositionally disordered ferroelectrics in the materials best known as relaxor ferroelectrics.

There are various experimental proofs which confirm that the relaxor ferroelectric materials involve regions of short-range ferroelectric order, known as polar nano-regions (PNRs) [25]. PNRs were discovered through a change in the index of refraction n(T), which is related to the local polarization. The index of refraction deviated from its high temperature linear temperature dependence at temperature T_d (Burns temperature). Deviation from the linear dependence was interpreted as the formation of short-ranged local polarization, starting at ~ 600 K for PMN. The PNRs are estimated to have a typical size ~5 nm below T_d [26]. Unlike normal ferroelectrics, when the temperature is lowered further, the PNR grows slightly but fails to form long range order. Neutron and X-ray scattering experiments have shown that the PNRs freeze below approximately 210 K, and they are randomly distributed within a cubic matrix of disordered polarizations.

1.8 HDC Materials (Extrinsic Origin)

High ε_r observed in ferroelectrics and relaxor ferroelectric materials is accounted in terms of intrinsic polarizations of the material. However, there are certain non-ferroelectric materials in which the observed frequency and temperature dependent high ε_r cannot be explained on the basis of intrinsic polarizations. Extrinsic phenomenon such as space charge polarization contributes predominantly to the high ε_r of these non-ferroelectric materials. Barrier layer capacitors, discussed in the next section, belong to this category.

1.8.1 Barrier Layer Capacitors/BLC (Class IV)

The origin of HDC in the materials has been proposed by some theories. Strategies to produce ceramic materials with HDC involve surface barrier layers or grain-boundary barrier layers which are referred as barrier-layer (BL) capacitors. In this case, the conductive grain cores are formed by donor doping or reduction firing of the ceramics [12] and the surface or grain boundaries are then oxidized to produce thin resistive layers. The ease of reduction is strongly affected by the other ions present: acceptor ions tend to inhibit reduction and donor ions tend to enhance it. Barrier-layer capacitors are based on the limited re-oxidation of a reduced composition. BLC's in their simplest form consist of conductive core region with highly insulating thin layers on the surface (or below the electrode) as shown in Fig. 1.10. This results a surface layer of high resistivity and a central portion of conductive material so that the effective dielectric thickness is twice the thickness "h_o" of a single re-oxidized layer and there is an apparent gain in permittivity over that of a fully oxidized unit by a factor of "$h/2h_o$", where h is the overall dielectric thickness.

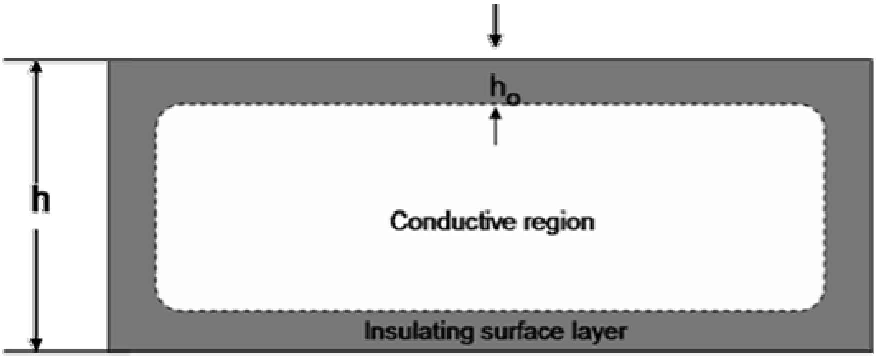

Fig. 1.10: Schematic diagram of a partially reoxidized dielectric material [12].

1.8.2 Surface (Electrode) Barrier Layer Capacitor

The materials used in fabrication of this type of capacitors layer are $BaTiO_3$ or $SrTiO_3$. Firstly, $BaTiO_3$ or $SrTiO_3$ discs of thickness (approximately 0.5 mm) are fired under reducing conditions, which makes the sample semiconducting or conducting. Silver electrode paint is applied to the surfaces of the disc and fired at about 800°C. The silver paint contains a PbO–Bi_2O_3–B_2O_3 glass frit to which is added a small amount (~ 1 atomic %) of acceptor ions, e.g. Cu. This leads to the formation of a thin (about 10 mm) reoxidized or insulating layers which separates the electrodes from the semiconducting titanate [12]. On the application of the voltages to such system, majority of the voltage is dropped across the two dielectric layers resulting in a very high capacitance. Capacitance values of ~10 mFm^{-2}/unit electrode area are readily achieved via this type of capacitors. Fig. 1.11 shows the electrode barrier layer capacitor [27].

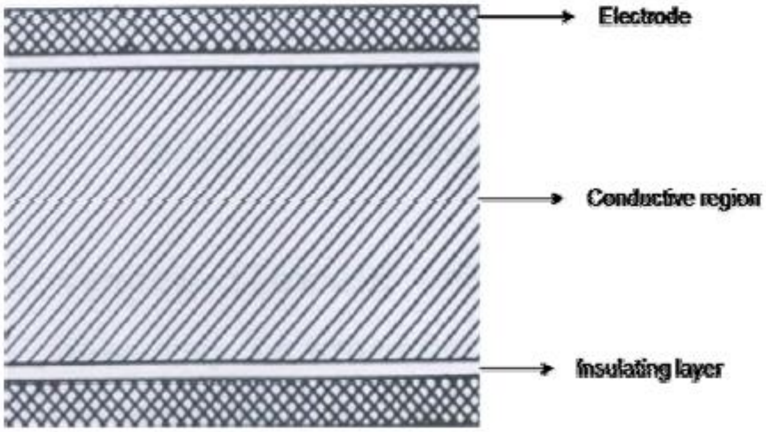

Fig. 1.11: Schematic diagram of electrode barrier layer capacitor [28].

1.8.3 Internal Barrier Layer Capacitor

Typical example of internal barrier layer capacitor (IBLC) is the grain boundary barrier layer capacitor (GBLC). In these types of materials, the grains are conducting and the grain boundaries are insulating. Fig. 1.12 shows the schematic diagram of the grain boundary barrier layer.

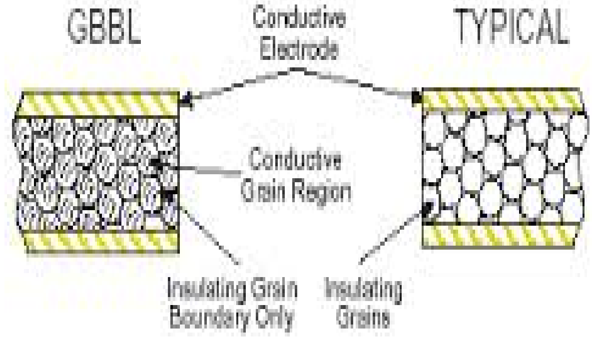

Fig. 1.12: Schematic diagram of grain boundary barrier layer [29].

By altering the stoichiometry at the grain boundary or by separating different phases, the barrier layer can be formed [30, 31]. Capacitor keeps electrical energy in the dielectric layer, i.e., barrier layer. Since the thickness of barrier layer is very thin, high capacitance density can be achieved in a small volume [32].

In this case, the discs are first fired in air to remove the organic matter and then sintered in air to obtain the required level of grain growth. A reducing atmosphere of carbon monoxide or hydrogen is then introduced. After cooling, Boric oxide frit containing acceptor ions such as Cu, Mn or Bi ion is painted on the surface which is then reheated in air at ~ 1300–1400°C. The acceptor ions diffuse along grain boundaries and modify the surface properties of the crystallites.

Such systems involve in the formation of Schottky barrier at the semiconducting surfaces of the grains which is very similar to those of back-to-back Schottky barriers. A small amount of (about 1%) of Silica and Alumina is added to improve the intergranular layers, which allow ionic movement and access to oxygen at high temperatures. Therefore, the artificial formation of IBLC involves complicated multistage processing and treatments to achieve the desired capacitance.

1.8.4 Schottky Barriers

Schottky barriers are created in many commercial electro-ceramics by deliberate introduction of compositional heterogeneity between the grain and grain boundary regions so that the grain boundaries act as an extrinsic source of impedance. Formation of Schottky barrier in the semiconducting surfaces of the grains results in the properties similar to those of back-to-back Schottky barriers. In many cases, double (back-to-back) Schottky potential barriers are created at the interfaces between the n - type grains due to the charge trapping at acceptor states, which results in the bending of the conduction band across the grain boundary[33]. This bending of conduction band produces an effective potential barrier of height, Φ_b, and depletion width (w) for conduction electrons between the grain and grain boundary regions. The barrier can typically be characterized as grain boundary impedance since it is both resistive (comparison to the bulk) and of high capacitive due to the thin width of the depletion region with respect to the grain size. Fig. 1.13 shows the back-to-back double Schottky potential barriers at the grain boundary. Under zero bias condition i.e. when V = 0, the barrier is symmetric and *w* is equal in both the directions. Under a dc bias, $V > 0$ and the barrier becomes asymmetric such that *w* in the reverse direction, (w_r), increases whereas the depletion width in the forward direction, w_f, decreases.

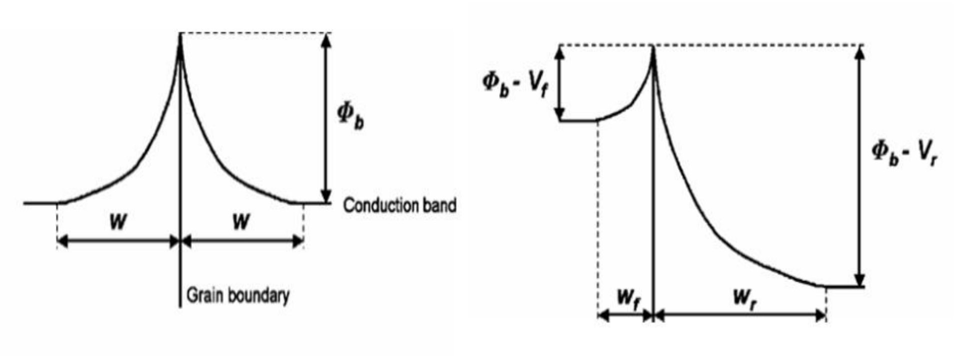

(a) (b)

Fig. 1.13: Illustration of back-to-back double Schottky potential barriers at the grain boundary (a) V = 0 and (b) V > 0 [33].

1.9 Theoretical Models for High Dielectric Constant (HDC) Materials

1.9.1 Maxwell-Wagner (M-W) Model

Maxwell-Wagner model deals with series of barrier phenomena or even with a complete series-parallel array of barrier-volume effects. These types of barriers often arises in a material consisting of grains separated by more insulating inter grain barriers [34]. This model is applied to a heterogeneous medium. Space charge polarization arises from differences in the conductivities due to inhomogeneity present in the material. In barrier layer capacitors, the fundamental process which has been exploited is the space charge polarization and M-W model is the theoretical models for the barrier layer capacitors. The motion of charge carriers get hindered at the interfaces due to the difference in conductivities of grain and grain boundaries. This causes a build-up of charges at the interface and leads to a large polarization and high ε_r and this phenomenon is known as M-W effect[35, 36]. This model can be simply described by considering the so called M-W capacitor, as shown in Fig. 1.14 (a). Here, the M-W capacitor is composed of two parallel layers of medium 1 and medium 2 which are characterized by electric permittivities ε_1 and ε_2, conductivities σ_1 and σ_2 and thicknesses d_1 and d_2, respectively. The actual system resembles with the equivalent circuit, consisting of two parallel RC circuits in series, as shown in Fig. 1.14 (b) [37, 38]. The time constant for current flow in each circuit, can be represented as $\tau_1= R_1C_1$ and $\tau_2= R_2C_2$. The time constant $\tau_1$and τ_2 could be related by constants a, and b such that $\tau_2 = aR_1bC_1=ab*\tau_1$. The resulting ε_r for the combined circuit varies with the frequency as shown in the Fig. 1.15 [27]. Depending on the value of $ab=((R_2/R_1)x(C_2/C_1))$, the low frequency ε_r resulting from the interfacial polarization can be several orders of magnitude larger than the value observed for high frequency.

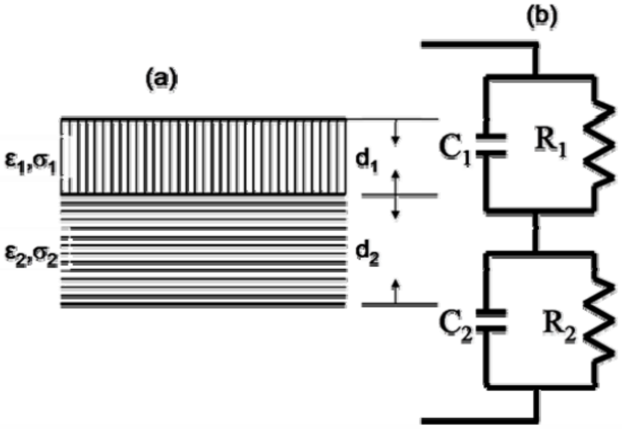

Fig. 1.14: (a) The Maxwell-Wagner capacitor and (b) Equivalent circuit of the two layer Maxwell-Wagner capacitor [27].

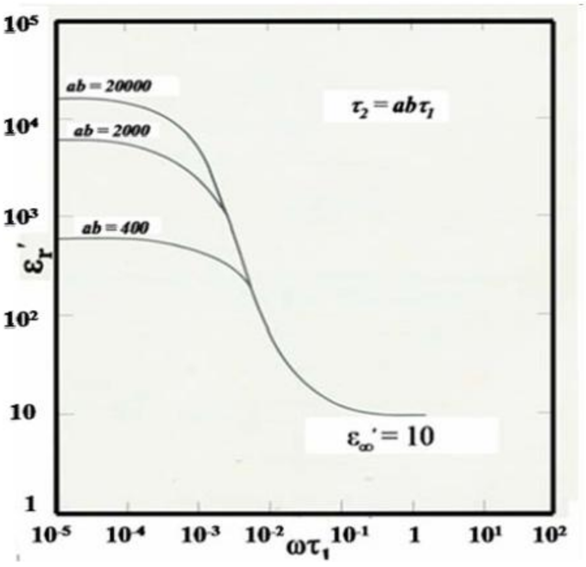

Fig. 1.15: Change in interfacial polarization with relative value of the boundary layer characteristics [28].

Electrostatic requirements of the equal charge density ($D_1 = D_2$) across each medium on the application of an electric field results the following expression for the resultant complex dielectric constant [34].

$$\varepsilon^*(\omega) = \varepsilon_\infty + \frac{\varepsilon_s - \varepsilon_\infty}{1 + j\omega\tau} - j\frac{\sigma}{\omega} \qquad (1.13)$$

Where,

$$\varepsilon_\infty = \frac{1}{C_o}\left[\frac{1}{\frac{1}{C_1} + \frac{1}{C_2}}\right] \qquad (1.14)$$

$$\varepsilon_s' = \frac{R_1^2 C_1 + R_2^2 C_2}{C_0 (R_1 + R_2)^2} \quad (1.15)$$

$$\sigma' = \frac{1}{C_0 (R_1 + R_2)} \quad (1.16)$$

$$\tau = \frac{R_1 R_2 (C_1 + C_2)}{R_1 + R_2} \quad (1.17)$$

Here, ε_s, ε_∞ are the static and high frequency dielectric constants respectively, σ' is Ohmic conductivity, C_o is empty cell capacitance, τ is the time constant.

1.9.2 Wernicke Model

The structure of internal-barrier-layer units can be represented by the simplified Wernicke model [12], shown in Fig. 1.16. This model involves semiconducting grains of size t_g, which are surrounded by uniform barrier layers of thickness t_b. The overall capacitance can be calculated as follows. The capacitance C_i of an individual element, assuming $t_g > t_b$, is given by

$$C_i = \frac{\varepsilon_r \varepsilon_o t_g^2}{t_b} \quad (1.18)$$

Where ε_r is the dielectric constant of the grain boundary material and ε_o is the permittivity of the free space. Capacitance of the series connected column is given by

$$C_i / (no.\, of\ \ elements\ in\ column) = \frac{\varepsilon_r \varepsilon_o t_g^2 / t_b}{t / t_g} \quad (1.19)$$

Since there are $1/t_g^2$ columns per unit area, the capacitance C per unit area is

$$C = \frac{\varepsilon_r \varepsilon_o t_g}{t t_b} \tag{1.20}$$

It follows that the effective relative permittivity ((ε_r)$_{eff}$) of the composite dielectric is given as

$$\varepsilon_{reff} = \frac{\varepsilon_r t_g}{t_b} \tag{1.21}$$

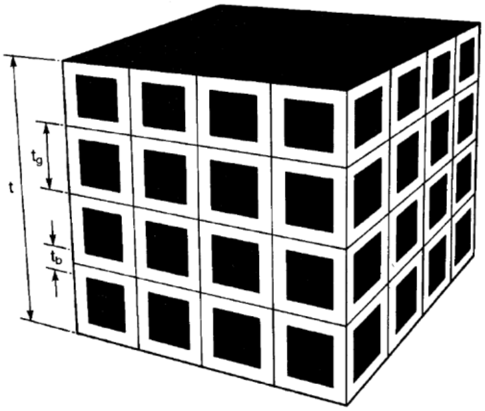

Fig. 1.16: Schematic diagram of a section through an internal barrier layer capacitor [12].

Assuming t_g = 50 mm, t_b = 0.2 mm and ε_r = 200, we obtain $(\varepsilon_r)_{eff}$ = 50 000. ε_r values as high as ~50 000 can be achieved with tanδ values of typically ~0.03. Units based on $SrTiO_3$ are more stable with respect to field and temperature than those based on $BaTiO_3$.

1.10 Previous Reports on HDC Materials

1.10.1 HDC Materials (Inherent Properties)

Large number of oxide based materials e.g. $CaCu_3Ti_4O_{12}$ (CCTO)[39], $Ln_{2/3}Cu_3Ti_4O_{12}$ with Ln = La, Ce, Pr, Nd, Sm, Eu, Gd, Tb, Dy, Ho, Er etc., $AFe_{1/2}B_{1/2}O3$ A=Ba, Sr, Ca; B=Nb, Ta, Sb etc.[38] and Li and Ti doped NiO [40] attracts the attention because of exhibiting HDC. The important features of these ceramics are: (i) dielectric constant (ε_r) >10^4 at RT, (ii) almost non-ferroelectric, (iii) stability of ε_r up to certain temperature range near RT and, (iv) weak frequency dependence below relaxation frequency. Table1.1 shows various HDC materials and their dielectric properties at 1 kHz.

Among the HDC materials, CCTO is the extensively studied system. The internal barrier layer capacitor (IBLC) origin was proposed by Sinclair *et al* for the high ε_r in the CCTO ceramics [41]. The electrically heterogeneity, consisting of semiconducting grains and insulating grain boundaries, was analyzed by using impedance spectroscopy in the CCTO ceramics. Grain and grain boundary structures play an important role in many material properties and are important elements of the microstructures of the polycrystalline materials. The observed microstructure and dielectric properties of the CCTO confirmed the formation of IBLC type ceramic at RT. Ferroelectric ceramic required multi step processing condition to fabricate IBLC, whereas IBLC in CCTO ceramic require the single step processing under normal atmosphere [42].

Li, Ti co-doped NiO ceramics are one of the leading high dielectric constant materials [40]. The low frequency dielectric constant is $\sim 10^5$ which weakly depend on the temperature over a broad range near the room temperature. Characteristically the material is a non-perovskite, lead-free, and non-ferroelectric material. The giant dielectric constant response in the doped NiO ceramics was attributed to the grain boundary-layer mechanism.

The giant dielectric response is also observed in some complex perovskites with general formula $AFe_{1/2}B_{1/2}O_3$ with A=Ba, Sr, Ca; B=Nb, Ta, Sb etc. These complex perovskite materials exhibit relaxor like dielectric response but these materials are non-ferroelectric in nature. As reported by *Raevaski et al.*, in these ceramics the high values of ε_r are the result of Maxwell-Wagner type interfacial polarization[38]

Grain boundaries often enable useful behavior, such as low-field magneto resistance, grain boundary Josephson junctions, positive temperature coefficient of resistivity, varistor effect, and the high-permittivity dielectric behavior. Normally, grain boundaries are regarded as two- dimensional defects and generally exist in lot of materials, e.g., metallic, and ceramic materials.

$Ba(FeNb)_{0.5}O_3$/BFN based ceramics are less studied in comparison to the CCTO ceramics. BFN structure is of $A(B_1B_2)O_3$ type, which is similar to that of the most of the lead based relaxor ferroelectric materials. BFN system has complex perovskite type structure in which the B-site is compositionally disordered. Compositionally it is very much similar to the most extensively studied $Pb(Fe_{0.5}Nb_{0.5})O_3$ relaxor ferroelectric system where Pb^{2+} cation is replaced by Ba^{2+} cation. The HDC at room temperature and interesting temperature dependent dielectric constant [43] behavior are the main reasons for considering this system as the material for present research investigation.

Table1.1 HDC materials and their room temperature dielectric properties at 1 kHz frequency

Compound	ε_r	tanδ	Reference
$CaCu_3Ti_4O_{12}$ (CCTO)	~ 3.50×10^4	~ 0.014	[44]
$Li_{0.3}Ti_{0.02}Ni_{0.68}O$	~ 1.7×10^4	~ 2.95	[45]
$Li_{0.05}Al_{0.04}Ni_{0.91}O$	~ 8468	~ 2	[46]
$Ba(Fe_{0.5}Nb_{0.5})O_3$	~ 10000	~ 0.4	[47]
$Sr_{0.09}Pr_{0.01}TiO_3$	~ 3000	~ 0.1	[48]

1.11 Barium Iron Niobate [$Ba(Fe_{0.5}Nb_{0.5})O_3$/BFN] System

Growing scientific interest among complex oxide materials is due to the existence of high ε_r. During the last two decades, perovskite-related oxides have attracted great attention in solid state physics, as they possess a variety of extraordinary magnetic and electronic properties. In this context, the barium iron niobate [$Ba(FeNb)_{0.5}O_3$/ BFN] ceramics with complex perovskite type structure have attracted attention because of its high ε_r and weak temperature dependent dielectric constant near RT.

A detailed research has already been conducted on the various aspects of BFN ceramics. High dielectric response is the most attracting feature of this system. Some researchers reported BFN as monoclinic system [49-51], whereas, some other researchers debated and reported that BFN system has cubic structure, supported by its non-ferroelectric [38, 52] behavior and further confirmed by the complete structural analysis.

Regarding the origin of HDC in the BFN ceramics, it remained an interesting topic for debate till date whether intrinsic or extrinsic. The temperature dependent dielectric constant in BFN ceramic interestingly looks like that of relaxors [49] [*Saha et al*]. However, later *Raveski et al* reported non-ferroelectricity in the BFN ceramic[38]. They reported extrinsic origin like Maxwell-Wagner type dielectric relaxation for the BFN ceramics. As a result of sintering of the BFN ceramic at high temperatures, semi-conductive grains and the insulating grain boundaries are formed. This makes the BFN compound as n-type semi-conducting in nature. The current versus electric field (J=f (E)) behavior of BFN ceramics shows varistor-like effect, which further suggest about the semiconducting nature of the BFN ceramics. *Wang et al* reported that the extrinsic polarization effect due to oxygen defects and other point defects contributes to the dielectric relaxation and relaxors ferroelectric like behavior in the BFN ceramics[43]. They showed the giant dielectric behavior ($\varepsilon_r \sim$ 2, 02,270 at 5 Hz, $\varepsilon_r \sim$ 91,930 at 1 kHz, and $\varepsilon_r \sim$

37,030 at 100 kHz) with very strong frequency dispersion in the 406–650 K temperature range. Two dielectric relaxations in the 150–400 K and 406–650 K temperature ranges are observed in the BFN ceramics. The relaxation activation energy calculated at low and high temperature regions are ~0.17 eV and ~0.83 eV, respectively.

Defect induced ferroelectricity in the BFN ceramic was reported by *Zhang et al* [52]. They prepared thin film of BFN by pulsed laser deposition technique and observed that with the increase in the oxygen deposition pressure, remnant polarization (P_r) decreased and further depressed by annealing in high pressure oxygen. The BFN thin film deposited in 1 Pa oxygen shows well-saturated loop with the largest remnant polarization $2P_r = 1.62$ μC/cm^2 and coercive field $2E_c = 26.4$ kV/cm. Oxygen deficiency plays a crucial role in the ferroelectricity observed in BFN thin film grown by PLD.

There are various reports on the existence of ferroelectricity in this ceramic, which suggest the presence of intrinsic or lattice polarizations in the BFN ceramics. *Ke et al.* reported that the BFN ceramics exhibit ferroelectricity and the observed colossal dielectric behavior is due to Maxwell-Wagner type interfacial polarization [53]. BFN system, prepared by both mixed oxide and columbite method, shows a very high dielectric constant of the order ~10^3-10^5. Dielectric loss at room temperature lies within 0.1 to 1. *Chung et al.* reported the dielectric and ferroelectric properties of the BFN ceramics [47]. The high value of dielectric constant ~ 20,000and dielectric loss ~ 0.2 at 100 Hz, whereas the remnant polarization ~ 0.2 μC/cm^2 and the coercive field ~ 5 V/μm are reported in this system. *Eitssayeam et al* studied the structural and dielectric properties of the BFN ceramics, synthesized by solid state reaction route [54]. Increase in conductivity of the BFN ceramics with temperature may be a main reason for its HDC. It is well known that Fe^{2+} and Fe^{3+} present on the same crystallographic sites can give rise to an electron-hopping conduction mechanism, which comes into effect at lower frequencies. Again in BFN system, Fe^{+3}(B_1) and Nb^{+5}(B_2) ions randomly occupy the octahedral B sites surrounded by O^{-2} anions. Due to the presence of larger Fe^{+3}(B_1) cations a ‘‘rattling space” is available for the relatively smaller Nb^{+5}(B_2) cations. When an oscillating ac signal is applied to such disordered systems, the smaller B_2 cations (with a large rattling space) can readily move without distorting the oxygen framework. In an ordered perovskite, a comparatively smaller rattling space is available for the B site cations. Therefore a larger dielectric constant is expected in disordered complex perovskite such as BFN system compared with the ordered perovskite (e.g., $PbTiO_3$) [50]. The values of ε_r at different temperatures of some important dielectric materials are given in Table 1.2.

Table 1.2 Value of ε_r at different temperatures of some important dielectric materials.

Material	**T_c (°C)**	**ε_r at T_m / T_c (1kHz)**	**ε_r (RT) (1kHz)**	**tanδ (RT)**	**References**
$BaTiO_3$	115	~9,000	1700	0.005	**[1, 55]**
Ba $(Zr_{0.20}Ti_{0.80})O_3$	50	7,000	~5000	0.04	**[56]**
PMN	-15	18,000	~11,000	0.02	**[1]**
PMN-PT(7%)	30	25,000	25,000	0.05	**[57]**
$Pb(Fe_{0.5}Nb_{0.5})O_3$	105	10,480	2860	0.022	**[58]**
$Ba(Fe_{0.5}Nb_{0.5})O_3$	-	91000	22,000	2.72	**[43, 59]**

1.11.1 Special Features of the BFN System

i) The observed high ε_r in the BFN system is an inherent property of the material.

ii) The value of ε_r obtained at single step processing condition in BFN ceramics is comparable to IBLC.

iii) Dielectric constant of the material remains independent of temperature over a wide range near RT. This behavior is very useful for capacitor application.

iv) The change of ε_r with temperature increases with increase in temperature. Such types of materials are highly sensitive in detecting small change in temperature. At higher temperatures, the temperature variation of ε_r in BFN ceramics is very large, which suggest their use in Bolometer applications.

v) BFN is an interesting material to study the origin (e.g. intrinsic or extrinsic) of HDC in complex perovskite systems.

vi) Defect structure in BFN system remains an important area to explain the various applications oriented properties of BFN system.

vii) The semiconducting nature of the BFN system suggests its use for optical application.

1.12 Motivation

Despite a great deal of work has been carried out in the search for lead-free HDC material based on BFN systems, it is still far-reaching and challenging to design BFN-based system with improved dielectric properties for electronic device applications. There are many factors like the grain size, the type and distribution of defects, microstructure of the sintered ceramics, processing conditions, purity of raw materials, and the synthesis routes used, aliovalent and isovalent substituents which affect the material properties. Due to the commercial interests on these materials for capacitor applications, different contributions to the dielectric properties of BFN ceramics are not completely explained in the open literature. The present work is focussed on understanding various effects of dopants and/or substitutions related to different relaxation phenomenon along with their defect chemistry. The present work is also focused on improving the dielectric properties of BFN system by suitable substitution, addition and using advanced processing techniques.

The literature data mainly reports the preparation of high dielectric constant ceramics by conventional routes. Microwave sintering of ceramics offers several potential advantages over conventional sintering. Microwave heating has the potential for energy and cost savings when compared with conventional heating. Besides that nearly theoretical density and uniform grains, which in turn improves the ceramics dielectric properties, can be achieved in microwave processed ceramics. Microwave processing of high dielectric constant based ceramics can reduce the dielectric loss since more the dielectric loss of a material more the efficiency of microwave processing technique. The presence of high dielectric loss in these high dielectric constant materials can be exploited for their synthesis with less processing temperature and time by microwave synthesis technique.

1.13 Objectives of the Present Thesis Work

a) Synthesis of $Ba(FeNb)_{0.5}O_3$ /BFN ceramics in single perovskite phase by conventional solid-state reaction (CSSR) route.

b) Optimization of BFN ceramics substituted with isovalent cation i.e. Pb^{2+}, and off-valent cation i.e. La^{3+} at the Ba-site of BFN ceramics to enhance the ferroelectricity (if existed) and lower the transition temperature.

c) Addition of metal oxides Cr_2O_3 and $MnCO_3$ in order to reduce the loss in the parent BFN ceramics

d) Studying and correlating dielectric relaxation phenomenon, conductivities, impedance spectroscopic phenomenon of all the substituted/added BFN ceramics

e) Studying the effect of all the substituted/added BFN ceramics on its band gap (E_g) for revealing its behaviour.

f) Studying leakage current behaviour of all the substituted/added BFN ceramics.

The following series of BFN based ceramics are synthesized by CSSR route:

Substitution of La^{3+} and Pb^{2+}

i. $Ba_{(1-x)}La_{2x/3}(FeNb)_{0.5}O_3$ (x=0,0.02,0.04,0.06,0.08)

ii. $Ba_{(1-x)}Pb_x(FeNb)_{0.5}O_3$ (x=0,0.02,0.04,0.06,0.08)

Addition of Cr_2O_3 and $MnCO_3$

iii. $Ba\,(FeNb)_{0.5}O_3$ – x wt% of $MnCO_3$ (x=0, 0.5,1.0,1.5,2.0)

iv. $Ba\,(FeNb)_{0.5}O_3$ – x wt% of Cr_2O_3 (x=0, 0.5,1.0,1.5,2.0)

g) Based on the observed highest dielectric properties, the following compositions of each series were taken for microwave (MW) sintering (for different duration):

i. $Ba(1-x)La_{2x/3}(FeNb)_{0.5}O_3$ (x=0.08)

ii. $Ba(1-x)Pb_x(FeNb)_{0.5}O_3$ (x=0.08)

iii. $Ba\ (FeNb)_{0.5}O_3$ – x wt% of $MnCO_3$ (x=0.5)

iv. $Ba\ (FeNb)_{0.5}O_3$ – x wt% of Cr_2O_3 (x=0.5)

h) Studying the effect of microwave sintering on the electrical properties of the above selected ceramics in detail.

References

[1] A. Safari, R.K. Panda, V.F. Janas, Ferroelectricity: Materials, Characteristics & Applications, Key Eng. Mater. 122-124 (1996) 35-70.

[2] R.J. Cava, Dielectric materials for applications in microwave communications, J. Mater. Chem. 11 (1) (2001) 54-62.

[3] S. Bhagavantam, P.V. Pantulu, Generalized symmetry and Neumann's principle, Proceedings of the Indian Academy of Sciences - Section A 66 (1) (1967) 33-39.

[4] K. Uchino, Ferroelectric Device, Marcel Dekker New York, 2000.

[5] S.N. Kumar, Synthesis and Characterization of $Sr_{0.53}Ba_{0.47}Nb_2O_6$ based Ferroelectric Composites for Pyroelectric Applications in: Department of Physics and Astronomy, Vol. Ph.D., National Institute of Technology, Rourkela, 2012.

[6] B.G. Hyde, S. Andersson, Inorganic Crystal Structures John Wiley & Sons, 1989.

[7] H.D. Megaw, Crystal Structures: A Working Approach (Studies in physics and chemistry), W.B. Saunders Co., Philadelphia 1973.

[8] B. Jaffe, W.R. Cook Jr., H. Jaffe, Piezoelectric Ceramics, Academic Press London and New York 1971.

[9] R.S. Roth, Classification of perovskite and other ABO_3-type compounds, J.Res. Nat. Bur. Stand. 58 (1957.) 75-88.

[10] R.C. Buchanan, Ceramic Materials for Electronics, Marcel Dekker, New York, 2004.

[11] A.J. Moulson , J.M. Herbert, Electroceramics: Materials, Properties, Applications, John Wiley & Sons, 2003.

[12] A.J. Moulson, J.M. Herbert, Dielectrics and Insulators, in: Electroceramics, John Wiley & Sons, Ltd, 2003, pp. 243-337.

[13] M. Stewart, M.G. Cain, D.A. Hall, Ferroelectric Hysteresis Measurement and Analysis, in: Technical Report CMMT (A) 152, National Physical Laboratory, Teddington UK, 1999.

[14] A.J. Moulson, J.M. Herbert, Elementary Solid State Science, in: Electroceramics, John Wiley & Sons, Ltd, 2003, pp. 5-93.

[15] U. Böttger, Dielectric Properties of Polar Oxides, in: Polar Oxides, Wiley-VCH Verlag GmbH & Co. KGaA, 2005, pp. 11-38.

[16] A.M. Badr, H.A. Elshaikh, I.M. Ashraf, Impacts of Temperature and Frequency on the Dielectric Properties for Insight into the Nature of the Charge Transports in the Tl2S Layered Single Crystals Journal of Modern Physics 2 (1) (2011) 12-25.

[17] E. Barsoukov, J.R. Macdonald, Impedance Spectroscopy: Theory, Experiment, and Applications, John Wiley & Sons, 2005.

[18] H. Föll, Electronic Materials, Christian-Albrechts-Universität zu Kiel, http://www.tf.uni-kiel.de/matwis/amat/elmat_en/index.html

[19] P. Kofstad, Nonstoichiometry, diffusion, and electrical conductivity in binary metal oxides, Wiley-Interscience, 1972

[20] D.M. Smyth, The Defect Chemistry of Metal Oxides, Oxford University Press, New York 2000.

[21] G.A. Samara, T. Sakudo, K. Yoshimitsu, Important Generalization Concerning the Role of Competing Forces in Displacive Phase Transitions, Phys. Rev. Lett. 35 (26) (1975) 1767-1769.

[22] M.T. Dove, A.P. Giddy, V. Heine, On the application of mean-field and landau theory to displacive phase transitions, Ferroelectrics 136 (1) (1992) 33-49.

[23] R.E. Cohen, Origin of ferroelectricity in perovskite oxides, Nature 358 (6382) (1992) 136-138.

[24] C. Kittel, Introduction to Solid State Physics, John Wiley & Sons, New York, 2005.

[25] S. Kojima, R. Ohta, T. Ariizumi, J. Zushi, Dynamic Polar Nanoregions a nd Broken Local Symmetry in Relaxor Ferroelectrics Probed by Inelastic Light Scattering in: XXIst International Symposium on the Jahn–Teller Effect 2012, Vol. 428 IOP Publishing, 2013 pp. 012027.

[26] M.E.X. Delgado, The Freezing Mechanisms of Perovskite Relaxor Ferroelectrics and The Thermodynamic Stability of Their Ferroelectric States, in: Physics, Vol. Doctor of Philosophy University of Illinois, Urbana-Champaign, 2009.

[27] B.S. Prakash, Investigations into the microstructure-property correlation in doped and undoped giant dielectric constant material $CaCu_3Ti_4O_{12}$, in: Materials Research Centre, Vol. Doctor of Philosophy, Indian Institute of Science, Bangalore, 2007, pp. 225.

[28] J. Nowotny, Electronic Ceramic Materials, Trans Tech Publications Ltd, http://www.scientific.net/KEM.66-67

[29] Broadband Single Layer Capacitor (GBBL), Johanson Technology Inc. , http://www.rfglobalnet.com/doc/broadband-single-layer-capacitor-gbbl-0001

[30] L.M. Levinson, H.R. Philipp, ZINC OXIDE VARISTORS - A REVIEW, Am. Ceram. Soc. Bull. 65 (4) (1986) 639-646.

[31] H.M. Chan, M.R. Harmer, D.M. Smyth, Compensating Defects in Highly Donor-Doped $BaTiO_3$, J. Am. Ceram. Soc. 69 (6) (1986) 507-510.

[32] J.M. Herbert, Barrier Layer Capacitor in: Ceramic Dielectrics and Capacitors, Vol. 6, Gordon & Breach Science Publishers 1985.

[33] T.B. Adams, D.C. Sinclair, A.R. West, Characterization of grain boundary impedances in fine- and coarse-grained $CaCu_3Ti_4O_{12}$ ceramics, Physical review B 73 (9) (2006) 094124.

[34] A.R. Von Hippel, Dielectrics and waves, Wiley; Chapman & Hall, New York; London, 1954.

[35] J.C. Maxwell, A Treatise on Electricity and Magnetism, Oxford University Press, 1873.

[36] P.K. Larsen, R. Metselaar, Electrical properties of yttrium iron garnet at high temperatures, Physical review B 14 (6) (1976) 2520-2527.

[37] P. Lunkenheimer, V. Bobnar, A.V. Pronin, A.I. Ritus, A.A. Volkov, A. Loidl, Origin of apparent colossal dielectric constants, Physical review B 66 (5) (2002) 052105.

[38] I.P. Raevski, S.A. Prosandeev, A.S. Bogatin, M.A. Malitskaya, L. Jastrabik, High dielectric permittivity in $AFe_{1/2}B_{1/2}O_3$ nonferroelectric perovskite ceramics (A=Ba, Sr, Ca; B=Nb, Ta, Sb), J. Appl. Phys. 93 (7) (2003) 4130-4136.

[39] M.A. Subramanian, D. Li, N. Duan, B.A. Reisner, A.W. Sleight, High Dielectric Constant in $ACu_3Ti_4O_{12}$ and $ACu_3Ti_3FeO_{12}$ Phases, J. Solid State Chem. 151 (2) (2000) 323-325.

[40] J. Wu, C.-W. Nan, Y. Lin, Y. Deng, Giant Dielectric Permittivity Observed in Li and Ti Doped NiO, Phys. Rev. Lett. 89 (21) (2002) 217601.

[41] D.C. Sinclair, T.B. Adams, F.D. Morrison, A.R. West, $CaCu_3Ti_4O_{12}$: One-step internal barrier layer capacitor, Appl. Phys. Lett. 80 (12) (2002) 2153-2155.

[42] T.B. Adams, D.C. Sinclair, A.R. West, Giant Barrier Layer Capacitance Effects in $CaCu_3Ti_4O_{12}$ Ceramics, Adv. Mater. (Weinheim, Ger.) 14 (18) (2002) 1321-1323.

[43] Z. Wang, X.M. Chen, L. Ni, X.Q. Liu, Dielectric abnormities of complex perovskite $Ba(Fe_{1/2}Nb_{1/2})O_3$ ceramics over broad temperature and frequency range, Appl. Phys. Lett. 90 (2) (2007) 022904-022903.

[44] Y. Li, P. Liang, X. Chao, Z. Yang, Preparation of $CaCu_3Ti_4O_{12}$ ceramics with low dielectric loss and giant dielectric constant by the sol-gel technique, Ceram. Int. 39 (7) (2013) 7879-7889.

[45] S. Maensiri, P. Thongbai, T. Yamwong, Giant dielectric response in (Li, Ti)-doped NiO ceramics synthesized by the polymerized complex method, Acta Mater. 55 (8) (2007) 2851-2861.

[46] S. Tangwancharoen, P. Thongbai, T. Yamwong, S. Maensiri, Dielectric and electrical properties of giant dielectric (Li, Al)-doped NiO ceramics, Mater. Chem. Phys. 115 (2-3) (2009) 585-589.

[47] C.-Y. Chung, Y.-H. Chang, G.-J. Chen, Y.-L. Chai, Preparation, structure and ferroelectric properties of Ba(Fe0.5Nb0.5)O3 powders by sol-gel method, J. Cryst. Growth 284 (1-2) (2005) 100-107.

[48] C. Liu, P. Liu, J.-p. Zhou, Y. He, L.-n. Su, L. Cao, H.-w. Zhang, Colossal dielectric constant and relaxation behaviors in Pr:$SrTiO_3$ ceramics, J. Appl. Phys. 107 (9) (2010) 094108.

[49] S. Saha, T.P. Sinha, Structural and dielectric studies of $BaFe_{0.5}Nb_{0.5}O_3$, J. Physi. Condens. Matter 14 (2002) 249-258.

[50] U. Intatha, S. Eitssayeam, J. Wang, T. Tunkasiri, Impedance study of giant dielectric permittivity in $BaFe_{0.5}Nb_{0.5}O_3$ perovskite ceramic, Current Applied Physics 10 (1) (2010) 21-25.

[51] N. Charoenthai, R. Traiphol, G. Rujijanagul, Microwave synthesis of barium iron niobate and dielectric properties, Mater. Lett. 62 (29) (2008) 4446-4448.

[52] W. Zhang, L. Li, X.M. Chen, Effects of oxygen vacancy on ferroelectricity in $Ba(Fe_{1/2}Nb_{1/2})O_3$ thin films grown by pulsed laser deposition, J. Appl. Phys. 106 (10) (2009) 104108.

[53] S. Ke, H. Huang, H. Fan, H.L.W. Chan, L.M. Zhou, Colossal dielectric response in barium iron niobate ceramics obtained by different precursors, Ceram. Int. 34 (4) (2008) 1059-1062.

[54] S. Eitssayeam, U. Intatha, K. Pengpat, T. Tunkasiri, Preparation and characterization of barium iron niobate ($BaFe_{0.5}Nb_{0.5}O_3$) ceramics, Current Applied Physics 6 (3) (2006) 316-318.

[55] G.H. Haertling, Ferroelectric Ceramics : History and Technology, Event (London) 818 (1999).

[56] W. Cai, C. Fu, J. Gao, X. Deng, Effect of Mn doping on the dielectric properties of $BaZr_{0.2}Ti_{0.8}O_3$ ceramics, J. Mater. Sci.: Mater. Electron. 21 (4) (2010) 317-325.

[57] T.R. Shrout, J. Fielding, Jr., "Relaxor ferroelectric materials", *IEEE Ultrasonics Symposium Proceedings* 2(1990) 711-720.

[58] D. Bochenek, Z. Surowiak, Influence of admixtures on the properties of biferroic $Pb(Fe_{0.5}Nb_{0.5})O_3$ ceramic, physica status solidi (a) 206 (12) (2009) 2857-2865.

[59] D. Bochenek, Z. Surowiak, J. Poltierova-Vejpravova, Producing the lead-free $BaFe_{0.5}Nb_{0.5}O_3$ ceramics with multiferroic properties, J. Alloys Compd. 487 (1-2) (2009) 572-576.

CHAPTER 2

Investigated Parameters

2.1 Introduction

This chapter describes synthesis route used and the basic principles of various experimental techniques used to characterize the materials under study. Various steps and processes, taking place during the material synthesis, are presented in detail. The characterization techniques involves: thermal analysis, structural analysis, morphology and density studies, dielectric, conductivity, impedance (wherever required), optical and leakage behaviour studies. The concepts of these experimental methods and techniques are briefly explained.

2.2 Synthesis of Ceramics

Among various methods of material synthesis such as conventional solid-state reaction (CSSR) process, mechanochemical synthesis, chemical co-precipitation, sol-gel process, hydrothermal synthesis, micro emulsion, combustion, thermal pyrolysis spray, molten salt etc., each method has its own advantages and disadvantages for achieving the quality product with respect to purity, homogeneity, reactivity, particle size etc. Based on reliability, reproducibility and economy, CSSR route is simple, convenient and low cost technique among other available synthesis methods. At the same time, the microwave processing of the ceramics can be utilized as an alternative approach for conventional sintering of ceramics because of the potential advantages such as rapid heating, penetrating radiation, more uniform microstructure & hence higher density. More importantly, microwave processing is material specific and the details of its heating mechanisms are explained in this chapter.

2.2.1 Convectional Solid State Reaction Route

By mixing two or more compounds, a solid solution is prepared and if the characteristics of the starting components are preserved, the mixture is formed. But, if the solid solutions of these compounds form one single compound then it does not retain the characteristics of its components. Solid state reaction route is used to prepare almost all polycrystalline materials [1]. High temperature is required to facilitate the reaction in the solids, as solids are generally unable to react at room temperature[1, 2]. In this route, the raw powders are ball milled and grinded first for uniform and homogeneous mixing of the precursors taken in stoichiometric proportions [3]. The size of the particles and the density of grinding media play an important role in the process of milling. Generally, acetone and zirconia balls are used as milling and grinding medium. The calcination temperatures were determined by thermal analysis of the raw powders after milling process.The phase formation of a compound takes place by solid-phase reaction, which involves the chemical reaction through atomic diffusion among grains at temperature below the melting points of the precursors [4]. In general, four physical processes are involved in the calcination of the raw materials:(i) linear expansion of the particles (ii) solid phase reaction (iii) contraction of the product and (iv) grain growth. The calcined powder were given a desired shape (called green compacts) by adding polyvinyl alcohol (PVA) as binder,which is a water soluble synthetic polymer with a monomer of (-CH_2-CHOH-) with excellent adhesive property to reduce the brittleness of green compacts. Hot press or uniaxial pressing technique is used to obtain the green compacts in the form of pellets with application of pressure ~60-65 MPa. Green compacts were densified through sintering process. There are various mechanisms of sintering in polycrystalline materials which lead to bonding and growth of necks between the particles and hence affecting the strength of the powder compact during sintering. These mechanisms are surface diffusion, lattice diffusion (from the surface), vapor transport, grain boundary diffusion, lattice diffusion (from the grain boundary) and plastic flow.Grain boundary diffusion and lattice diffusion are the most important densifying mechanisms in the polycrystalline ceramics as the diffusion from grain boundary to the pore permits both neck growth as well as densification process.Plastic flow by dislocation motion also leads to neck growth and densification, however this is more common in the sintering of metal powders. In addition to these mechanisms, the diffusion of the different ionic species making up the compound is coupled to preserve the stoichiometry and electro-neutrality of the compound. In sintering process the green compacts are heated to a temperature approximately 50-80% of the melting temperature[5]. In this way, a pellet does not melt and the particles join to reduce the porosity of the compact by ionic diffusion as shown in Fig.2.1

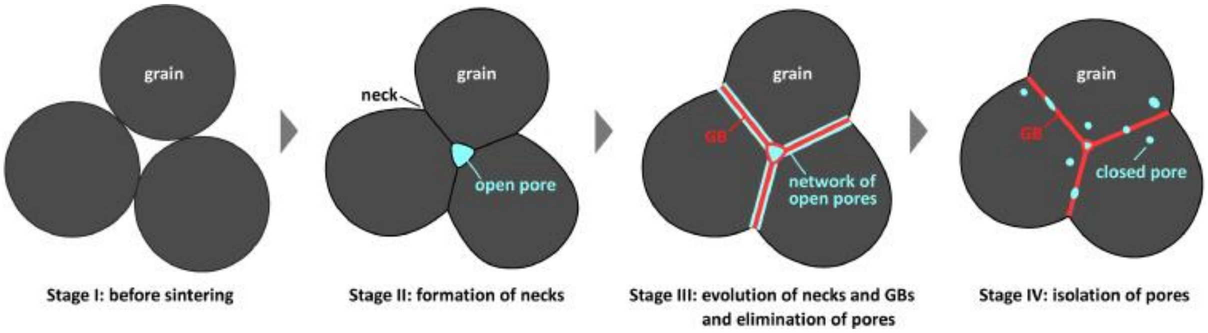

Fig. 2.1: Schematics of sintering process [6].

After sintering, the green pellets are ready for any type of characterizations succeeded by proper optimization or/else sintering temperature is varied for better densification is to be optimized again.

2.2.2 Microwave Processing Technique

Microwaves are the electromagnetic radiation with wavelengths between 1m to 1mm, or equivalently, with frequenciesbetween 300 MHz (0.3 GHz) to and 300 GHz. Although, the majority of the microwaves frequencies are dedicated for communications and radar purposes, the 915 MHz, 2.45 GHz, 5.8 GHz, and 20.2-21.1 GHz frequencies are specified for scientific, industrial, and medical applications [7, 8].

Generally, microwave ovens operate at 915 MHz and 2.45 GHz frequencies. This is due to the fact that the water molecules present in food show good microwave absorption at these frequencies and hence the relative easy availability of 915 MHz and 2.45 GHz microwave ovens resulted in their use in processing of ceramics[9]. The frequency and wavelength range, including microwave region, of electromagnetic waves are shown in Fig. 2.2. Material specific nature of microwaves helps this process to synthesize different materials for different purposes. Therefore, as shown in Table 2.1, microwaves can be absorbed, reflected or transmitted depending on the type of material.

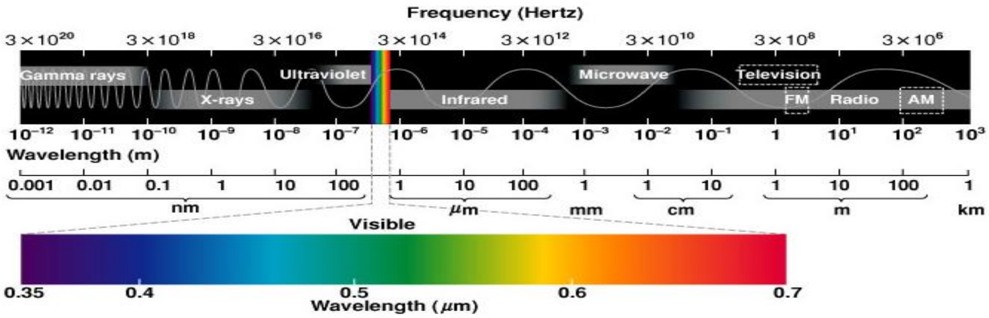

Fig. 2.2: The frequency and wavelength range of electromagnetic waves [10].

Table 2.1: Nature of microwave interaction with materials[11, 12].

Type of material	Interaction with MW	Reflectivity
Bulk Metals	Opaque	Good Reflector
Insulator	Absorb	Heat up effectively
Semi-Conductor	Permeable	Transparent

The advantages of microwave heating over conventional systems are:

- Rapid energy transfer
- Direct and indirect heating (almost all types of ceramics can be processed)
- Volumetric heating
- Uniformity of heating
- Considerably reduced processing times
- Reduced power consumption
- Enhanced diffusion processes
- Improved microstructure and densification
- Clean environment at the point of use (Green technology)

2.2.2.1 Microwave Heating Mechanism

Among all the polarization mechanisms discussed in the previous chapter, electronic and ionic polarization operates on timescales which are very much smaller than that required for microwave frequency field reversals and do not contribute to the microwave heating effect. However, dipolarpolarization results from the reorientation of polar molecules or other permanent dipoles in the material. As the timescale of dipolarpolarization operation is of the order of microwaves, therefore this polarisation phenomenon is related to microwave heating. The role of the space charge or interfacial polarisation results from interfacial phenomena in inhomogeneous materials is limited at microwave frequencies. Dipolar polarization is the phenomenon responsible for the majority of microwave heating effects observed in various systems.

Materials with high dielectric losses attenuate the microwaves. Such attenuation can be improved by the addition of small amounts of metallic powder, which reflects the microwaves and hinders loss-free propagation of the wave. The power density of absorbed microwaves, which explains the uniform heating in the material, may be expressed as:

$$P(W/m^3) = (electrical\ \ losses + magnetic\ \ losses) = \omega\varepsilon_0\varepsilon'' E_{rms}^2 + \omega\mu_0\mu'' H_{rms}^2 \qquad (2.1)$$

Where, ω= 2πf = angular frequency, ε_o = dielectric permittivity of vacuum, ε" = relative dielectric losses (polarization + conduction), E_{rms} = internal electrical field of the microwave, μ_o= magnetic permittivity in vacuum, μ" = relative magnetic losses and H_{rms} = internal magnetic field of the microwave. The magnetic losses are usually less relevant and the susceptibility of a polar material to microwave heating is mainly determined by the dielectric losses. The ability of a particular material to increase its temperature when exposed to microwaves can be described by the "loss tangent" tanδ = (ε"/ ε'). This loss factor measures the ability of the material to transfer microwave energy into heat and the dielectric constant measures the ability of the material to be polarized [13]. Fig. 2.3 shows the fundamental difference of the heating mechanism between microwave sintering and conventional sintering of a material.

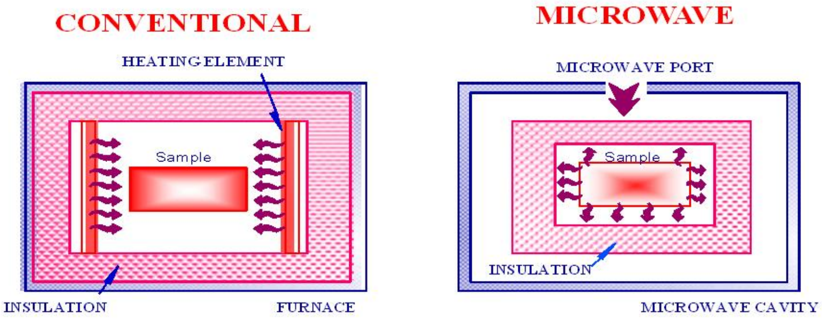

Fig. 2.3: Heat flow in conventional and microwave furnaces [10].

In conventional heating heat is generated by heating elements and transferred to samples via radiation, conduction, and convection. Whereas, in microwave sintering, the materials themselves absorb microwave energy, and then transform it into heat within their bodies [14, 15]. Microwave processing technique is material specific and has gained worldwide acceptance for its novelty method of processing and sintering of variety of materials.

2.3 Characterizing Techniques

For the present study, the following experimental techniques were used for characterizing various properties of the ceramics. Some of the characterizations are associated within synthesis process whereas maximum characterizations are after formation of the green pellets.

- Differential scanning calorimetry and thermo gravimetric analysis
- X-Ray diffraction study
- UV-Visible spectroscopy study
- Density measurements
- Scanning electron microscope
- Dielectric characterizations
- Conductivity study
- Impedance spectroscopic study
- Leakage current and polarization measurements

2.3.1 Differential Scanning Calorimetry / Thermo Gravimetric Analysis

Differential scanning calorimetry (DSC) provides information about thermal changes i.e. difference in the amount of heat required to increase the temperature of a sample and reference and measured as a function of temperature. In DSC, both the sample and the reference are maintained at nearly the same temperature throughout the experiment. Generally, the temperature program for a DSC analysis is designed such that the sample holder temperature increases linearly as a function of time. The basic principle of this technique is that when the sample undergoes a physical transformation such as phase transitions, more or less heat will flow to the sample holder than to the reference to maintain both at the same temperature. Therefore heat must flow in or out to the sample depends on whether the process is endothermic or exothermic. When the sample undergoes a phase transition from solid to liquid it requires more heat at the same rate as the reference. This absorption of heat corresponds to an endothermic peak in the DSC curve. Similarly when the sample becomes crystallized, less heat is required to raise the sample temperature and hence corresponds to an exothermic peak on the curve. By observing the difference in heat flow between the sample and reference, differential scanning calorimeters are able to measure the amount of heat absorbed or released during such transitions [16-18].The reference sample should have a well-defined heat capacity over the range of temperatures to be scanned. TGA is the mass change of a substance measured as function of temperature when the substance is subjected to a controlled temperature programme. Here, themass is lost if the substance contains a volatile fraction. The specimen powder is placed on a refractory pan (Alpha alumina or platinum). The pan is suspended from a high precision balance. A thermocouple is in close proximity to the specimen but not in contact, so as not to interfere with the free float of the balance. The balances are electronically compensated so that the specimen pan does not move when the specimen gains or losses weight. The measurement is normally carried out in air or in an inert atmosphere, such as He/Ar, and the changes in weight is recorded as a function of increase of temperature of testing samples. Sometimes the measurement is performed in neon oxygen atmosphere to slow down the oxidation process.

2.3.2 X-Ray Diffraction

X-ray diffraction/XRD characterization technique is a powerful, non-destructive analytical technique which reveals information about the crystal structure, atomic arrangements of materials, chemical composition, and physical properties of the materials under study. The principle of diffraction is that when the “the wavelength (λ) of X-ray comparable to the interplanar placing (d) of crystals, at particular angle (θ)”satisfies the Bragg law given in equation 2.2 and shown in Fig. 2.4

$$n\lambda = 2d\sin\theta \qquad (2.2)$$

Where, n is the order of diffraction where the effective diffraction takes place.

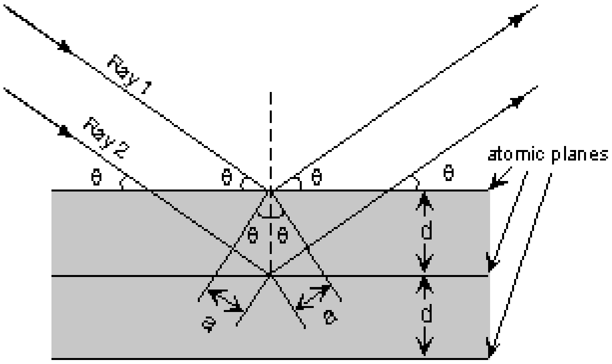

Fig. 2.4: X-ray Diffraction on the surface of a crystalline solid [19].

Various properties of the materials can be analysed by determining the lattice parameters accurately. The calculation of the lattice constants from the XRD/ 2θ positions or d-spacing values can be done using the following formula:

$$\frac{1}{d_{hkl}^{2}} = V^{2}[h^{2}b^{2}c^{2}\sin^{2}\alpha + k^{2}c^{2}a^{2}\sin^{2}\beta + l^{2}a^{2}b^{2}\sin^{2}\gamma]$$

$$= abc(1-\cos^{2}\alpha - \cos^{2}\beta - \cos^{2}\gamma + \cos\alpha\cos\beta\cos\gamma)^{1/2} \qquad (2.3)$$

Where, V is the volume of the unit cell, a, b, c, α, β and γ are lattice parameters and h, k, l are the Miller indices. The lattice parameters for all the studied compositions can be calculated by using the above formula. Since different types of defects may co-exist in crystalline materials then the problem of the separation of different types of defects and identification and quantitative estimation of the extent and distribution of each defects type arises.The different factors affecting the diffraction intensities can be grouped into a single expression for calculating the relative intensities of the reflections. For the powder method, the intensity (*I)* is given by

$$I = J\frac{1+\cos^2 2\theta}{4\sin^2\theta\cos\theta}F^2 A(\theta) \qquad (2.4)$$

Where, *J* is the multiplicity factor and *F* is the structure factor, which is given as

$$F = \Sigma_j f_j \exp 2\pi i(hx_j + ky_j + lz_j) \qquad (2.5)$$

Where, f_j= atomic scattering factor and

A (θ) = absorption coefficient = $\frac{1}{V}\int e^{-\mu x}dx$

Where, μ is the linear absorption coefficient of the specimen, *x* is the distance traversed by the beam and *V* is the volume of the crystal exposed to X-rays. A very important aspect of the intensity distribution among the reflections is to relate the extinction, which is a deciding factor for the symmetry elements involved in the material. The translations involved in these symmetry elements and centered lattices add a new periodicity in the patterns, which shows itself by extinguishing certain classes of X-ray spectra. Each type of extinction is a characteristic of a particular space group. Therefore, the absence of such characteristic spectra from the diffraction data is a major criterion for the determination of the lattice types and the space groups. We can obtain the following information from the X-ray diffraction analysis: (i) Quality and confirmation of the prepared samples, (ii) The interplanar spacing d of the reflections, (iii) The intensities of the reflections, (iv)The unit cell parameters and the lattice type

2.3.3 UV-Visible Spectroscopy

Ultraviolet-visible absorption spectroscopy (UV-Vis) study reveals the measurement of the attenuation of a beam of light after it passes through a sample or after reflection from a sample surface in the spectral range of 190-900 nm, i.e. in the visible and ultraviolet regions of the electromagnetic spectrum. When radiant energy is incident upon a solution then it may be absorbed, transmitted and/or reflected. In spectro-photometry, the absorbed light is determined. The relationship $E=h\upsilon$, where E is the transition energy from the stable to excited state, h is the Planck's constant, and υ is the frequency and the energy of ultraviolet and visible radiation corresponds to that required for electronic transitions of the outer electrons. Since these are the valence electrons of the molecules or ions, the reflectance spectrum gives the bonding characteristics of these particles.

The optical band gap of the sample can be calculated as follows. The obtained diffuse reflectance spectra can be converted to an equivalent absorption spectra using the Kubelka–Munk (KM) [20]. The KM function at any wavelength is given as:

$$F(R_\infty) = \frac{(1-R_\infty)^2}{2R_\infty} = \frac{\alpha}{s} \qquad (2.6)$$

Here, ‘$F(R_\infty)$’ is the remission or Kubelka–Munk function, ‘R_∞’ is the reflectance of the ceramics relative to the reference material ($R_\infty=(R_{sample}/\ R_{splectron})$), ‘α’ is the absorption coefficient and ‘s’ is the scattering coefficient. Typically, the scattering coefficient is weakly dependent on energy. Therefore, F (R_∞) can be assumed to be proportional to the absorption spectrum [21]. As suggested by Davis and Mott, the energy dependence of the absorption coefficient near the absorption edge can be expressed [22] by the following relation:

$$\alpha = \frac{(h\nu - E_g)^n}{h\nu} \qquad (2.7)$$

Here hν the photon energy and E_g the energy of the optical transition corresponding to the optical band gap. Value of the exponent ‘n’ denotes the nature of the sample transition. The value n = 1/2, 3/2, 2, 3 corresponds to the direct allowed, direct forbidden, indirect allowed, indirect forbidden transitions, respectively.

With an appropriate value of *n*, the plot of $(\alpha h\nu)^{1/n}$vs hν is linear near the absorption edge and the value of the optical band gap can be determined from the slope of the linear part. For the direct band gap *Eg*, we obtain the expression as:

$$[F(R_\infty)h\nu]^2 = C(h\nu - E_g) \qquad (2.8)$$

By plotting $[F(R_\infty)\ h\nu]^2$ vs. hν, the band gap $E_g$of a powder sample can be extracted easily.

2.3.4 Density Measurements

For better practical applications the ceramic materials should be well sintered in order to achieve near theoretical density after the sintering process. Theoretical density can be calculated with the help of lattice parameters, derived from structure analysis. The theoretical density 'ρ_{th}' can be defined as,

$$\rho_{th} = \frac{nM}{NV} \qquad (2.9)$$

Where, 'n'is the number of atoms per unit cell and M is the molecular weight. N is the Avogadro's number and V is thevolume of the unit cell.The experimental densities of the sintered samples can be measured using Archimedes principle. The experimental densities (ρ_{ex}) were calculated by using the following relation:

$$\rho_{ex} = \left[\frac{Dry\ weight}{Soaked\ weight - Suspended\ weight} \right] \times Density\ of\ the\ liquid \qquad (2.10)$$

Relative density (RD) of the samples can be calculated using the following relation

$$RD = \left(\frac{\rho_{ex}}{\rho_{th}}\right) \times 100\% \qquad (2.11)$$

2.3.5 Microscopy Technique

When an accelerated electrons beam is incident on a material then a number of interactions, as shown in Fig. 2.5, takes place. Secondary electrons and the back scattered electrons are used for the topography and the composition analysis of the material.Back scattered electrons are the electrons scattered either elastically or in elastically from the surface of the material. The secondary electrons are the electrons produced during ionization of atoms in the material due to incident (primary) electrons. Various electromagnetic radiations are produced due to spontaneous de-excitation of electrons in atoms. Secondary electrons / back scattered electrons are detected and these signals are used for imaging the topography / composition of the material.

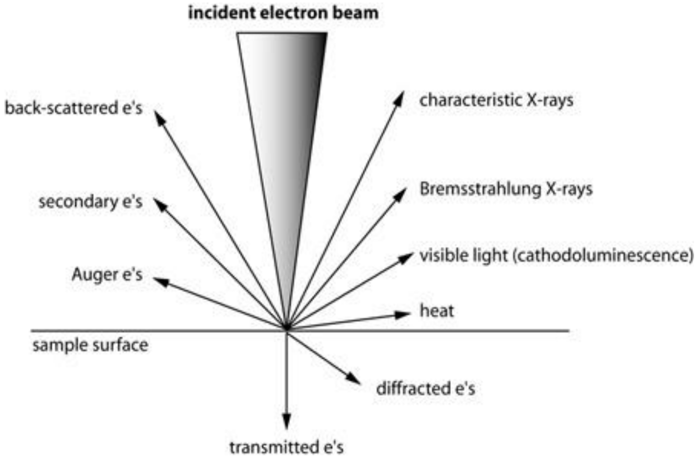

Fig. 2.5: Types of interactions between an accelerated electrons and a sample [23].

The scanning electron microscope (SEM) is produces image of a sample by scanning it with a focused beam of electrons. SEM can achieve resolution better than 1 nanometre. With this imaging technique we can get information about the topography, morphology, composition, and also about the crystallographic properties of samples.

2.3.6 Leakage Current & Polarization vs. Electric Field Characterization

The leakage current is primarily linked with the dielectric capacitors, used in the electronic devices, and which refer to the conduction of a small amount of current even when they are electrically turned off. Even though this off current is an order of magnitude less than the current through the device when it is on, this leakage current still slowly discharges the capacitor. Basically, leakage from a capacitor is linked with the imperfection of the dielectric materials used as capacitors and therefore also known as dielectric leakage. The nature of P-E hysteresis loop for materials possessing leakage current is shown in Fig. 2.6.

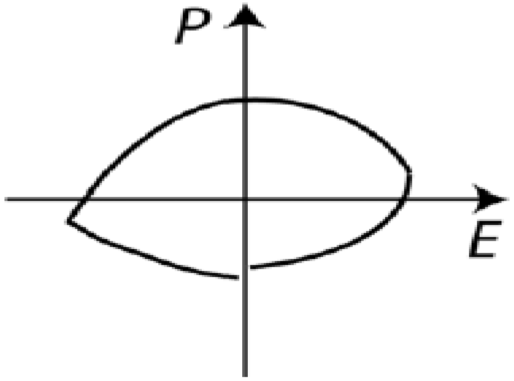

Fig. 2.6: Schematic diagram of leakage current dominant P-E hysteresis loop [24].

Time dependent leakage current has a direct relationship with the electrical conductivity and dielectric loss in the material. It is very difficult to observe the polarization hysteresis loops if leakage current is high in the ceramics and so why they are interlinked and compared in our present work.

2.3.7 Dielectric Characterizations

When a dielectric material is placed in an alternating a.c. field, different types of polarizations, discussed in chapter-1, get built up that account the dielectric constant of the material. A temporal phase shift is found to occur between the driving field and the resulting net polarization and a corresponding loss current component appears which account the dielectric loss of the sample. The polarization '*P'* as well as the electric displacement 'D' varies periodically with time. In general, *P* and *D* lag behind with the applied external electric field *E* with a phase angle δ so that

$$D = D_0 \cos(\omega t - \delta) = D_1 \cos \omega t + D_2 \sin \omega t \qquad (2.12)$$

Where, δ is the phase angle (normally slightly less than 90°) and

$$D_1 = D_0 \cos\delta \; and \quad D_2 = D_0 \sin\delta \qquad (2.13)$$

The ratio of the displacement vector to the electric field (D_0 / E_0) is frequency dependent for most of the dielectrics. Hence, we can introduce two frequency-dependent dielectric constants:

$$\varepsilon'(\omega) = (\frac{D_0}{E_0})\cos\delta \qquad (2.14)$$

$$\varepsilon''(\omega) = (\frac{D_0}{E_0})\sin\delta \qquad (2.15)$$

These two constants can be expressed in terms of a single complex dielectric constant,

$$\varepsilon^* = \varepsilon' - j\varepsilon'' \qquad (2.16)$$

As the applied voltage (*V*) varies periodically with time as: $V = V_0 e^{i\omega t}$, the total current is given by

$$I = \frac{dQ}{dt} = \frac{d(CV)}{dt} = j\omega CV = j\omega C_0 V \qquad (2.17)$$

Where, C and C_0 are the capacitance in a dielectric medium and vacuum, respectively.

Therefore,

$$I = j\omega C_0 V(\varepsilon' - j\varepsilon'') = \omega\varepsilon'' C_0 V + j\omega' C_0 V' = I_l + I_c \qquad (2.18)$$

The tangent loss is given by

$$\tan\delta = {}^{I_l}\!/_{I_c} = \frac{\varepsilon''}{\varepsilon'} \qquad (2.19)$$

The total current I through the capacitor can be resolved into two components, a charging current (I_c) in quadrature with voltage and conduction current I_l in phase with the voltage. The vector resolution of the total current is shown in Fig. 2.7

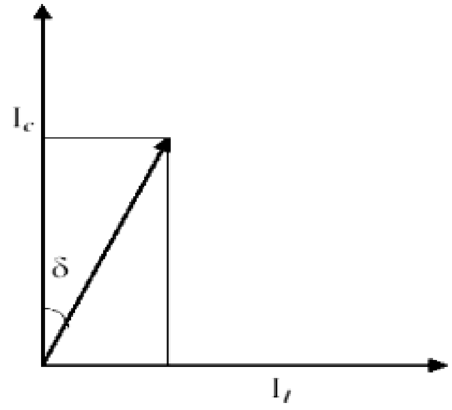

Fig. 2.7: The vector resolution of ac current in a capacitor [25].

Generally, LCR meters measure the various electrical parameters at different frequencies employing auto balancing bridge. Fig. 2.8 shows the schematic diagram of auto balancing bridge method. Z is the impedance of the material (in the form of electrode pellet), Z_1 and Z_2 are known impedance and Z_x is variable impedance. Z_x is varied until no current flows through G. Under balanced condition, Z can be calculated as

$$Z = \left(\frac{Z_2}{Z_1}\right) Z_\times \qquad (2.20)$$

Knowing the value of Z, the resistance component (R) and reactance component (X) can be calculated. Capacitance (C) and dielectric loss (tanδ) can be calculated using the following formula $C = 1 / 2\pi f X$ and dielectric loss: $\tan\delta = R / X$. Knowing the capacitance C, dielectric constant can be calculated as

$$\varepsilon_r = \frac{C \times d}{\varepsilon_o \times A} \qquad (2.21)$$

Where, ε_o: Permittivity of free space in farad per meter (8.854×10^{-12} *F/m*)

ε_r: Dielectric constant or relative permittivity of the sample.

A: Area of each plane electrode in square meters (m^2)

d: Thickness of the electrode ceramic sample in meters (*m*)

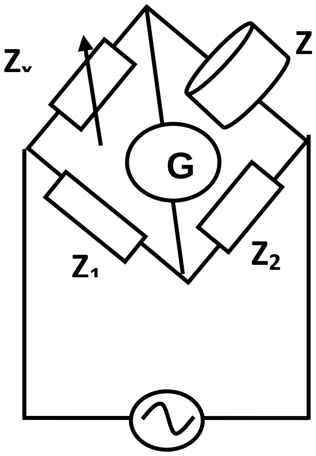

Fig. 2.8: Schematic diagram of auto balancing bridge.

2.3.8 Complex Impedance Study

The complex impedance analysis is a well-known technique of probing effectively the electro-ceramics in general, and dielectric materials in particular. This technique provides information about the nature of the various limiting processes taking during the charge transport within the electro-ceramics and also at the electrode/ceramic interfaces. It is also helpful in resolving the contributions to resistivity in the frequency domain of various processes such as: [i] the electrode effects, [ii] the bulk effects and [iii] the interfaces namely the grain boundaries etc.[26]. In *g*eneral the data in the complex plane could be represented in any of the four basic formalisms which are interrelated to each other. These four basic formalisms are complex impedance (Z*), complex admittance (Y*), complex permittivity (ε_r*) and the complex modulus (M*).

Complex impedance: $Z^* = Z' - jZ''$

Complex admittance: $Y^* = (Z^*)^{-1}$

Complex permittivity: $\varepsilon_r^* = (j\omega C_0 Z^*)^{-1}$

Complex electric modulus: $M^* = j\omega C_0 Z^* = M' + jM''$

Where, (Z', M', ε') and $(Z'', M'', \varepsilon'')$ are the real and imaginary components of impedance, modulus, and permittivity, respectively. $J = \sqrt{-1}$, and $\omega = 2\pi f$ is the angular frequency .

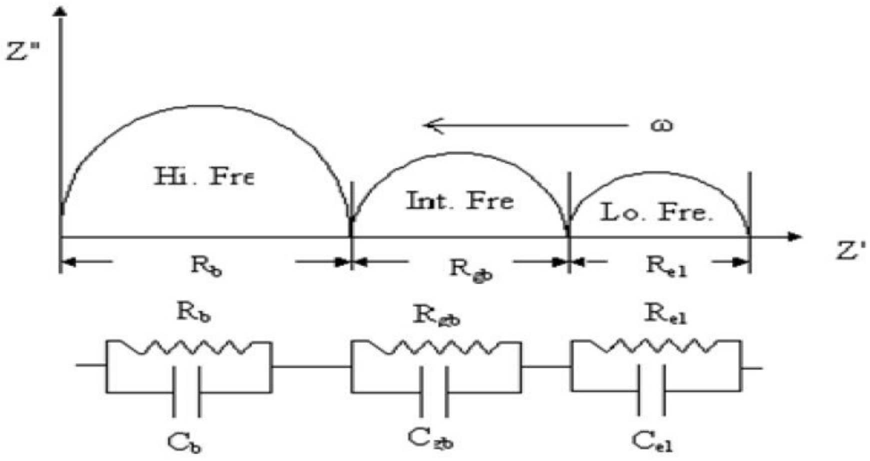

Fig. 2.9: (a) Nyquist plot showing grain, grain boundary and electrode interface effect[27].

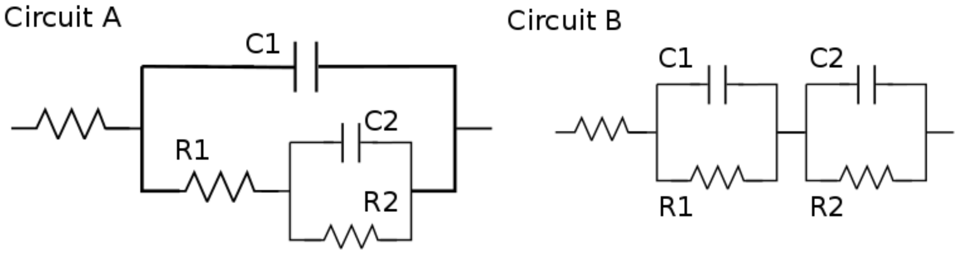

Fig. 2.9: Parallel and series combination of 2 parallel RC circuits, circuit A (b) and circuit B (c)[28].

The complex impedance plot (Cole-Cole or Nyquist plot or Z'vs. Z" plot) is represented by considering the relaxation times of various processes which are the consequences of different capacitive components. The aforementioned three processes give rise to three semi-circular arcs, shown in the Fig. 2.9. The relationship between the microstructure and the electrical properties can be obtained from complex impedance plots. In the complex impedance plots, the arc at the high frequency end refers to the bulk electrical conduction, the intermediate arc corresponds to conduction by the grain boundaries and the arc at the low frequency end corresponds to electrode processes. Predominantly, the grain and the grain boundary responses can be identified by the value of capacitance (C), associated with each semicircular arc, based on the brick layer model [29]. Fig. 2.9 (b) and (c) shows the equivalent circuit used for fitting the impedance spectra with two times constant.

Table 2.2: Phenomenon responsible for different capacitance values[30].

Capacitance(F)	10^{-12}	10^{-11}	10^{-11} - 10^{-8}	10^{-10} - 10^{-9}	10^{-9} - 10^{-7}	10^{-7} - 10^{-5}
Responsible phenomenon	Bulk	Secondary phase	Grain boundary	Bulk ferroelectric	Surface layer	Sample electrode interface

The values of the R-C circuit elements obviously depend on the individual components (i.e., grain and grain boundary effects), which is related to the microstructure and the electrical properties of the material. The apex of these semicircles position in the frequency spectrum depends on the relaxation times (τ), where $\tau \sim RC$, which follows the relation $\omega_{max}RC = 1$, where $\omega = 2\pi f$ and f is the applied frequency. Effectively large values of Z' at low frequencies or temperatures indicates a predominant effect of the polarizations which is consistent with large dielectric constant (ε') values of the materials.

The intercept of the semicircles at x-axis is used to calculate the resistance of grain (R_g), grain boundary (R_{gb}) and electrode interface (R_{el}) while their corresponding capacitance values obeyed the following general relation:

$$\omega_{\max} C_l R_l = 1 \qquad (2.22)$$

Where, l=grain/grain boundary/electrode interface and ω_{max} =frequency of maximum loss in the impedance spectrum

2.3.9 Conductivity Study

The causes of conductivity in many dielectrics are due to the motion of charges which gives rise to the conduction current and additionally polarizes the dielectric in turn contribute to dielectric loss. The ac conductivity (σ_{ac}) of the dielectric material is given by

$$\sigma_{ac} = \varepsilon_0 \varepsilon_r \omega \tan\delta \qquad (2.23)$$

The ac conductivity as a function of frequency can be explained on the basis of Jonscher's power law given as[31].

$$\sigma_{ac} = \sigma_{dc} + A\omega^n \qquad (2.24)$$

Here, σ_{ac} is the total conductivity, σ_{dc} is the frequency independent conductivity, the coefficient 'A' is the temperature dependent constant and the exponent 'n' is material related intrinsic factor [32]. The conductivity plots possess (i) frequency independent conductivity at low frequency side, generally referred as dc conductivity of the material, and (ii) frequency dependent conductivity at higher frequency region. The frequency at which the conductivity starts increasing is known as hopping frequency of the material. Generally, in the high resistance materials, at lower temperatures the frequency independent conductivity plateau is not clearly observed while at high temperature this plateau is clearly seen. The frequency independent plateau at lower frequencies and higher temperatures is attributed to the long-range translational motion of ions contributing to the dc conductivity (σ_{dc}). The dc conductivity follows temperature dependent Arrhenius relation as follows:

$$\sigma_{dc} = \sigma_0 \exp\left(-E_a / k_B T\right) \qquad (2.25)$$

The frequency independent ac conductivity at higher temperature can be explained by the jump relaxation model (JRM) [33]. According to this model, the conductivity at the lower frequencies region is associated with the successful hopping of ions to its neighbourhood vacant sites due to the available long time period; such successive jumps result in a long-range translational motion of ions contributing to dc conductivity. At higher frequencies, two competing relaxation processes namely: (i) the jumping ion to jump back to its initial position (correlated forward–backward–forward), i.e., unsuccessful hopping and (ii) the neighbourhood ions become relaxed with respect to the ion's position (the ions stay in the new site), i.e., successful hopping processes may be visualized. With the increase of the ratio of successful to unsuccessful hopping of ions, a dispersive conductivity at high frequencies is observed.

References

[1] A.J. Moulson , J.M. Herbert, Electroceramics: Materials, Properties, Applications, John Wiley & Sons, 2003.

[2] G.C.C. da Costa, A.Z. SimÃµes, A. Ries, C.R. Foschini, M.A. Zaghete, J.A. Varela, Phase formation and characterization of $BaBi_2Ta_2O_9$ obtained by mixed oxide procedure, Mater. Lett. 58 (11) (2004) 1709-1714.

[3] J.K. Beddow, Particle Characterization in Technology: Applications and Microanalysis, CRC Press, 1984. 265p., 1984.

[4] Y. Xu, Ferroelectric Materials and Their Applications, North-Holland, 1991.

[5] M.N. Rahaman, Sintering of ceramics, CRC Press, Boca Raton (FL); London; New York, 2008.

[6] T. Hiroya, Y. Akiyasu, S. Jun-ichi, O. Hiraku, K. Kohji, Strongly connected *ex situ* MgB_2 polycrystalline bulks fabricated by solid-state self-sintering, Supercond. Sci. Technol. 25 (11) (2012) 115022.

[7] D.E. Clark, W.H. Sutton, Microwave Processing of Materials, Annual Review of Materials Science 26 (1) (1996) 299-331.

[8] J.D. Katz, Microwave Sintering of Ceramics, Annual Review of Materials Science 22 (1) (1992) 153-170.

[9] N.R. Council, Microwave Processing of Materials, The National Academies Press, 1994.

[10] Sonia, Synthesis & Characterization of Modified Barium Titanate Ferroelectrics by Modified Solid State Reaction and Microwave Sintering Routes in: Department of Chemistry Vol. Doctor of Philosophy National Institute of Technology, Rourkela 2011, pp. 210.

[11] M. Oghbaei, O. Mirzaee, Microwave versus conventional sintering: A review of fundamentals, advantages and applications, J. Alloys Compd. 494 (1-2) (2010) 175-189.

[12] E.T. Thostenson, T.W. Chou, Microwave processing: fundamentals and applications, Composites Part A 30 (9) (1999) 1055-1071.

[13] W.H. Sutton, Microwave Processing of Ceramics, Am. Ceram. Soc. Bull. 68 (2) (1989) 376.

[14] A. Goldstein, N. Travitzky, A. Singurindy, M. Kravchik, Direct microwave sintering of yttria-stabilized zirconia at 2.45 GHz, J. Eur. Ceram. Soc. 19 (12) (1999) 2067-2072.

[15] V. Tsakaloudi, E. Papazoglou, V.T. Zaspalis, Microwave firing of MnZn-ferrites, Mater. Sci. Eng., B 106 (3) (2004) 289-294.

[16] J.A. Dean, Analytical Chemistry Handbook, McGraw-Hill Companies, 1995.

[17] D.A. Skoog, F.J. Holler, T.A. Nieman, Principles of Instrumental Analysis Saunders College Pub., 1998

[18] M.J. O'Neill, The Analysis of a Temperature-Controlled Scanning Calorimeter, Anal. Chem. 36 (7) (1964) 1238-1245.

[19] S.A. Nelson, X-Ray Crystallography, http://www.tulane.edu/~sanelson/eens211/x-ray.htm

[20] P. Kubelka, F. Munk, Z. Tech. Phys 12 (1931) 593.

[21] D.G. Barton, M. Shtein, R.D. Wilson, S.L. Soled, E. Iglesia, Structure and Electronic Properties of Solid Acids Based on Tungsten Oxide Nanostructures, The Journal of Physical Chemistry B 103 (4) (1999) 630-640.

[22] E.A. Davis, N.F. Mott, Conduction in non-crystalline systems V. Conductivity, optical absorption and photoconductivity in amorphous semiconductors, Philos. Mag. 22 (179) (1970) 0903-0922.

[23] D. Henry, Electron-Sample Interactions, http://serc.carleton.edu/research_education/geochemsheets/electroninteractions.html

[24] A. Gronotte, Development of new chemical processes to lead-free piezoelectric and ferroelectric materials, in: Department of Chemistry, Vol. Master of Science, Simon Fraser University, 2009.

[25] A.J. Moulson, J.M. Herbert, Elementary Solid State Science, in: Electroceramics, John Wiley & Sons, Ltd, 2003, pp. 5-93.

[26] A.K. Jonscher, Dielectric Relaxation in Solids, Chelsea Dielectrics Press Limited, London 1983.

[27] Dielectric Ceramics: Basic Principles, http://nptel.ac.in/courses/113104005/lecture24/24_3.htm

[28] Electrochemical Impedance Spectroscopy, http://www.lucasbard.com/eis101/07_multipleC.html

[29] J. Fleig, The influence of non-ideal microstructures on the analysis of grain boundary impedances, Solid State Ionics 131 (1-2) (2000) 117-127.

[30] J.T.S. Irvine, D.C. Sinclair, A.R. West, Electroceramics: Characterization by Impedance Spectroscopy, Adv. Mater. (Weinheim, Ger.) 2 (3) (1990) 132-138.

[31] A.K. Jonscher, The 'universal' dielectric response, Nature 267 (5613) (1977) 673-679.

[32] D.P. Almond, A.R. West, R.J. Grant, Temperature dependence of the a.c. conductivity of Nab-alumina, Solid State Commun. 44 (8) (1982) 1277-1280.

[33] K. Funke, Jump relaxation in solid electrolytes, Prog. Solid State Chem. 22 (2) (1993) 111-195.

CHAPTER 3

Materials and Methods

3.1 Introduction

This chapter describes the various steps involved in the synthesis of the selected ceramics by conventional and microwave processing techniques. Details of various instruments used for the different characterizations are also given.

3.2 Conventional Processing of the BFN Based Ceramics

The following series of BFN based ceramics are synthesized by the conventional solid state reaction (CSSR) route:

(v) $Ba_{(1-x)}La_{2x/3}(FeNb)_{0.5}O_3$ (x=0,0.02,0.04,0.06,0.08) [La^{3+} substituted series]

(vi) $Ba_{(1-x)}Pb_x(FeNb)_{0.5}O_3$ +4 wt % PbO (x=0,0.02,0.04,0.06,0.08) [Pb^{2+} substituted series]

(vii) Ba $(FeNb)_{0.5}O_3$ – x wt% of $MnCO_3$ (x=0, 0.5,1.0,1.5,2.0) [Mn added series]

(viii) Ba $(FeNb)_{0.5}O_3$ – x wt% of Cr_2O_3 (x=0, 0.5,1.0,1.5,2.0) [Cr added series]

In the present work, commercially available high purity (≥ 99%) starting reagents (powders) of barium carbonate ($BaCO_3$), iron oxide (Fe_2O_3), niobium pentoxide (Nb_2O_5), manganese carbonate ($MnCO_3$), chromium oxide (Cr_2O_3), lead oxide (PbO), lanthanum oxide(La_2O_3) were used as the starting materials for the synthesis of the BFN based high dielectric constant ceramics. The various steps of CSSR routes used for the synthesis of the BFN based ceramics are presented in Fig. 3.1 flow chart. These powders were thoroughly mixed and ball milled for 12 h in acetone using zirconia balls. Thermal analysis, DSC and TGA measurements of ball milled BFN samples were performed at a constant heating rate of 10 ˚C per minute by using Netzsch, STA 449C. The mixed powders were dried and conventionally calcined at different temperatures in air atmosphere. For single perovskite phase formation, the calcined powders were examined by X-ray diffractrometer. Single perovskite phase formation was confirmed for the BFN powders calcined at 1250 °C for 4 h. For additives, Cr_2O_3 and $MnCO_3$, (0.0, 0.5, 1.0, 1.5 and 2.0 wt %) were added to the base composition of the calcined BFN ceramics to form admixture? of Cr_2O_3 and $MnCO_3$ with the BFN ceramics, respectively. Whereas, La_2O_3 and PbO were taken in stoichiometric amount along with $BaCO_3$, Fe_2O_3 and Nb_2O_5 raw powders to form $Ba_{(1-x)}La_{2x/3}(FeNb)_{0.5}O_3$ and $Ba_{(1-x)}Pb_x(FeNb)_{0.5}O_3$ (x=0,0.02,0.04,0.06,0.08) compositions respectively. These calcined powders were mixed with 2wt. % polyvinyl alcohol as binder and then uniaxially pressed into disk shaped pellets of diameter ~1 cm. These green pellets were conventionally sintered in normal atmosphere for 4 h at 1350 °C with a heating rate of 5 °C/min. The microstructure and morphology was analyzed by scanning electron microscope. The ultraviolet visible (UV-Vis) diffuse reflectance spectra (DRS) in the range of 200 – 1100 nm was recorded using a UV-Vis spectrophotometer. The $BaSO_4$ was used as the reflectance standard material. The densities of the sintered samples were measured by using Archimedes principle. The sintered pellets were electroded using silver paste. The electrical measurements from RT to 400°C were performed in the 1 kHz to 1MHz frequencies rangeby using computer interfaced HIOKI 3532-50 LCR-HITESTER. The leakage current measurements were studied by using precision premier II (Radiant Technology). Polarization behaviour was also tested using the same precision premier II at low internal voltages.

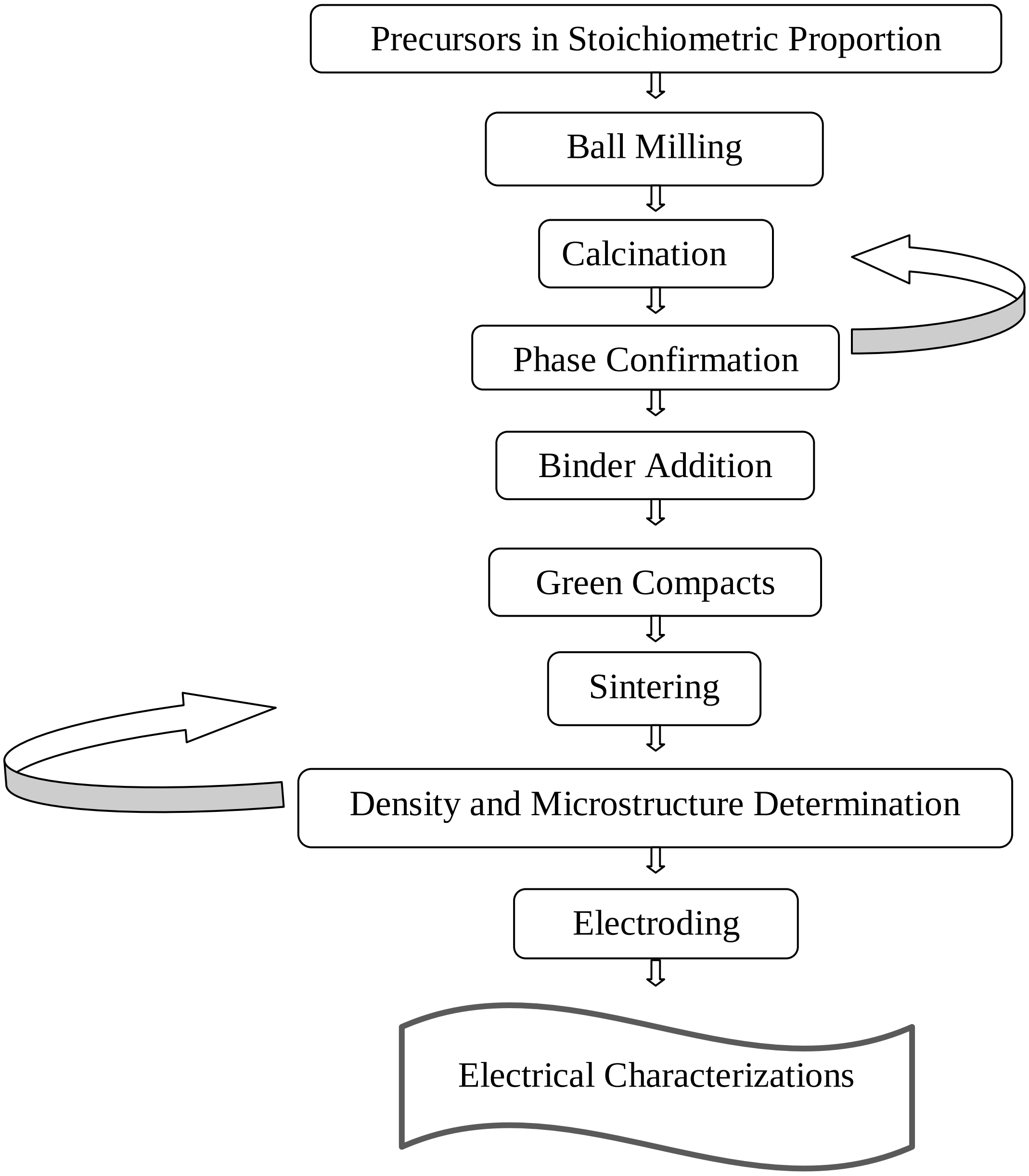

Fig.3.1: Flow chart of the steps involved in solid state reaction process.

Table 3.1: Details of conventionally processed BFN based ceramics.

Ceramic Composition	**Precursors**	**Optimized Calcination Temp.(^{o}C) for 4 h**	**Optimized Sintering Temp. (^{o}C) for 4 h**	**Sample Notation**
$Ba(Fe_{0.5}Nb_{0.5})O_3$/BFN	$BaCO_3$ Fe_2O_3 Nb_2O_5	1250	1350	BFN
$Ba_{(1-x)}La_{2x/3}(FeNb)_{0.5}O_3$ (x=0,0.02,0.04,0.06,0.08)	$BaCO_3$ La_2O_3 Fe_2O_3 Nb_2O_5	1250	1250	BLFN
$Ba_{(1-x)}Pb_x(FeNb)_{0.5}O_3$ +4 wt% PbO (x=0,0.02,0.04,0.06,0.08)	$BaCO_3$ PbO Fe_2O_3 Nb_2O_5	1200	1250	PBFN
Ba $(FeNb)_{0.5}O_3$ – x wt% of $MnCO_3$ (x=0.0, 0.5,1.0,1.5,2.0)	BFN calcined at 1250 ^{o}C added with $MnCO_3$	_	1300	-
Ba $(FeNb)_{0.5}O_3$ – x wt% of Cr_2O_3 (x=0.0, 0.5,1.0,1.5,2.0)	BFN calcined at 1250 ^{o}C added with Cr_2O_3	_	1300	-

3.3 Microwave Processing

The following BFN based ceramics were synthesized by the microwave processing technique.

(vi) $Ba(FeNb)_{0.5}O_3$

(vii) $Ba(1\text{-}x)La_{2x/3}(FeNb)_{0.5}O_3$ (x=0.08)

(viii) $Ba(1\text{-}x)Pb_x(FeNb)_{0.5}O_3$ (x=0.08)

(ix) Ba $(FeNb)_{0.5}O_3$ – x wt% of $MnCO_3$ (x=0.5)

(x) Ba $(FeNb)_{0.5}O_3$ – x wt% of Cr_2O_3 (x=0.5)

The above modified BFN compositions and the MW sintering parameters are mentioned in Table 3.2.

Table 3.2: Details of selected BFN based ceramics and MW sintering parameters.

Ceramic composition	**MW sintered (^oC)**	**sintering duration (min)**
$Ba(Fe_{0.5}Nb_{0.5})O_3$/BFN	1350	15, 30, 45
$Ba_{(1-x)}La_{2x/3}(FeNb)_{0.5}O_3$ (x=0.08)	1250	15, 30, 45
$Ba_{(1-x)}Pb_x(FeNb)_{0.5}O_3$ (x=0.08)	1250	15, 30, 45
Ba $(FeNb)_{0.5}O_3$ – x wt% of $MnCO_3$ (x=0.5)	1300	15, 30, 45
Ba $(FeNb)_{0.5}O_3$ – x wt% of Cr_2O_3 (x=0.5)	1300	15, 30, 45

3.3.1 Synthesis of BFN Based Ceramics by Microwave Processing Technique

For microwave processing, the above selected ceramics were taken for sintering in the microwave furnace. The steps followed for the preparation of the BFN based ceramics by MW processing techniques are presented in Fig. 3.2. For comparison purpose, the microwave sintering of the green pellets was performed for 15, 30 and 45 min, respectively at 1350 °C with a heating rate 30 °C/min. For this, pellets were taken in a zirconia crucible and placed inside a susceptor containing SiC slabs. Microwave furnace operating in multi-mode at 2.45 GHz frequency and 4.4 kW power was used for the sintering of the green pellets. The microwave furnace temperature was recorded by using a Raytek noncontact sensor (XRTG5). Schematic diagram of the microwave sintering system is shown in Fig. 3.3. For single perovskite phase formation, the sintered pellets were examined by X-ray diffractrometer using Cu Kα (1.5405 Ǻ) radiation. The microstructure and morphology was analyzed by scanning electron microscope. The densities of the sintered samples were measured by using Archimedes principle. The sintered pellets were electroded using silver paste. The electrical measurements from RT to 400°C were performed in the 1 kHz to 1 MHz frequencies rangeby using computer interfaced HIOKI 3532-50 LCR-HITESTER. The leakage current measurements were studied by using precision premier II (Radiant Technology). Polarization behaviour of the samples was also tested using the same precision premier II at low internal voltages.

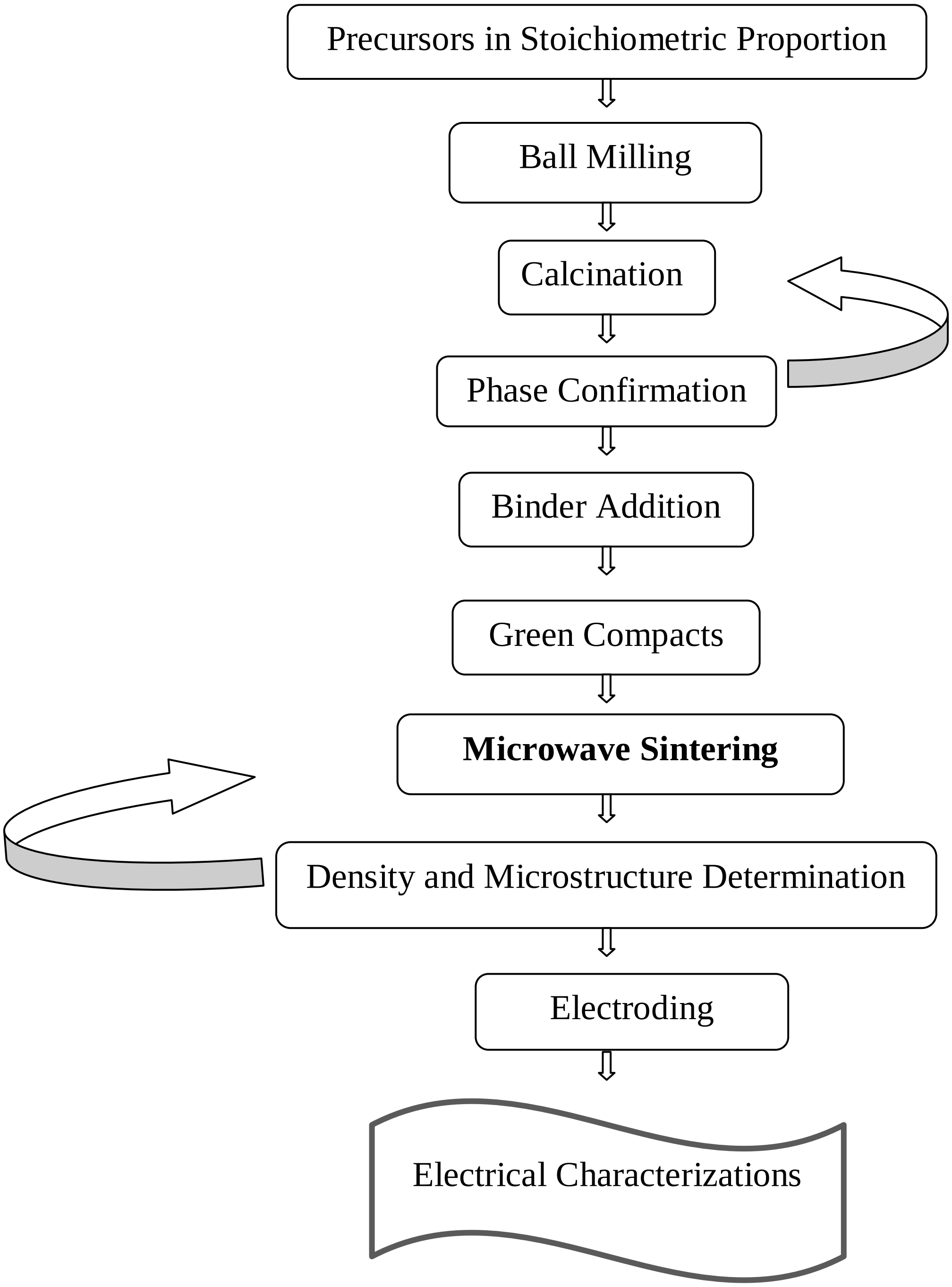

Fig. 3.2: Flow chart of the steps involved in microwave processing.

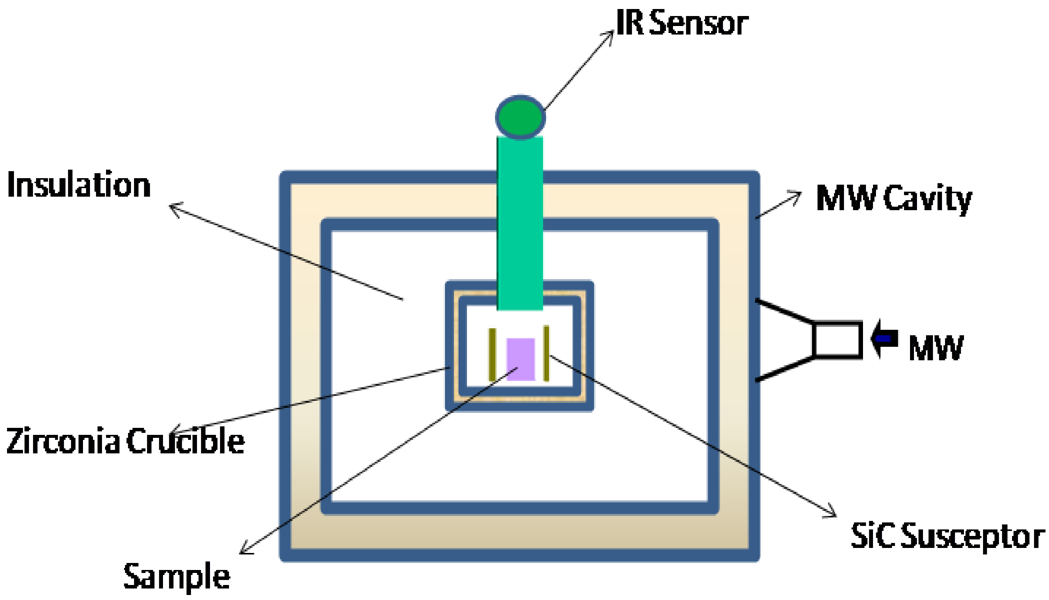

Fig. 3.3: Schematic diagram of microwave sintering system.

3.4 Investigated Parameters

Different experimental setups were used to investigate various properties of the entitled BFN based ceramics both in conventional and microwave techniques. This segment explains the details about the measurements that have been carried out in the instrument and their methods.

3.4.1 Thermal Analysis

Temperature program for a DSC analysis is designed such that the sample holder temperature increases linearly as a function of time. The reference sample should have a well-defined heat capacity over the range of temperatures to be scanned. Thermo gravimetric analysis (TGA) is the study of weight change of the specimen as a function of temperature. The specimen powder was placed on a refractory pan (Alpha alumina or platinum). The pan was suspended from a high precision balance. A thermocouple was in close proximity to the specimen but not in contact, so as not to interfere with the free float of the balance. The balances were electronically compensated to restrict the movement of specimen pan while gaining or loosing the weight. . The DSC/TGA experiments were done for all the sample by taking ~10 mg of the ball milled powder samples at a constant heating rate of 10 ˚C per minute by using Netzsch, STA 449C.

3.4.2 Phase Formation Study

X-ray diffraction patterns of all the samples were studied to observe the single perovskite phase formation. XRD analysis was performed on a PW 3020 Philips diffractrometer using Cu Kα (λ=0.15405 nm) radiation. The diffraction data was taken in the 2θ range from 20^o to $70^o/80^o$. Cu $K\alpha_2$ radiation was stripped from the collected XRD data by using standard software "X'pert high score. The crystal structure and the crystallographic parameters were indexed by using standard computer program "POWD".

3.4.3 Optical Property Study

The optical diffuse absorption spectra (DRS) in the UV–Vis region of the La and Pb based BFN ceramics were recorded by using UV-Vis spectrophotometer (Shimadzu UV-2450, Japan). Whereas, the diffuse reflectance spectra (DRS) of the Cr and Mn modified BFN ceramics were measured by using UV-vis spectrophotometer (Perkin Elmer, Lambda 35 UV-Vis spectrometer). The detail about the calculation of optical band gap is discussed in the previous chapter.

3.4.4 Density and Morphology Study

The experimental densities of the sintered samples were measured by Archimedes method. First the dry weights of the sintered samples were measured. Then these samples were immersed in a glass beaker containing kerosene and kept in desiccator connected with a suction pump to create vacuum till the liquid filled up the open pores completely by observing the beaker to become bubbles free. Then the samples were suspended in kerosene oil with the help of a specially designed hanging pan to hold the ceramic samples and the suspended weight was measured. The soaked weight of the ceramic samples (whose pores are filled with kerosene) was also measured and the experimental density was calculated by the following formula.

$$\rho_{ex} = \left[\frac{Dry\ weight}{Soaked\ weight - Suspended\ weight} \right] \times 0.81 (Density\ of\ \text{kerosene}) \qquad (3.1)$$

The SEM images were taken using JEOL SEM- 6480LV. The samples under study were non-conducting; therefore a thin layer of platinum/gold was coated using a sputter coater to avoid the potential build up. Average grain size of the samples was measured from the SEM images using linear intercept method by “ImageJ” software. In this method, the scale was set by comparing the length scale from the SEM images. Then the diagonal lines were drawn on a maximum number of grains (to minimize the error) and the lengths were calculated. The average grain size was calculated by dividing the total intercepted grain length by the number of grains.

3.4.5 Leakage Current and Polarisation Measurement

The time dependent leakage current and P-E loop behaviours of the BFN based ceramics were measured by using precision premier II (Radiant technology). The image of precision premier II is given in Fig. 3.4. The time dependent leakage current was measured at different selected voltages up to 20s. The polarization versus electric field loops were measured by using modified Sawyer –Tower circuit as shown in Fig 3.5 at different selected voltages of the BFN based ceramics.

Fig. 3.4: Image of precision premier II.

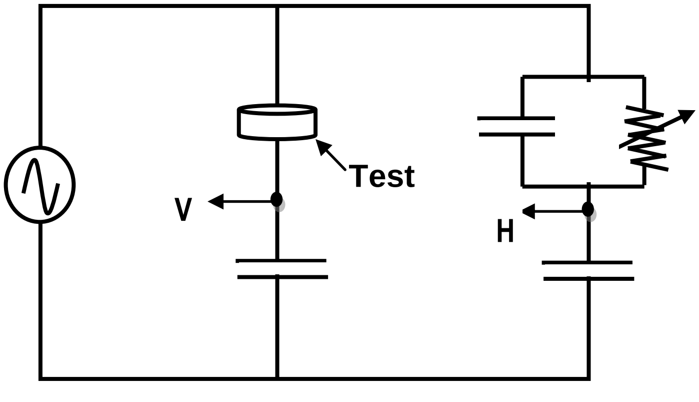

Fig. 3.5: Modified Sawyer-Tower circuit.

3.4.6 Dielectric Measurement

The temperature dependent dielectric constant and dielectric loss was measured over a wide range of temperature (30-400 ^{o}C) and at four different frequencies 1,10,100 and 1000 kHz by using HIOKI-LCR meter (3532-50 HI-TESTER). The RT data were taken over a frequency range (100 Hz to 1 MHz). The image of HIOKI-LCR meter (3532-50 HI-TESTER) is given in Fig. 3.6.

3.4.7 Impedance and Conductivity Measurements

The impedance and conductivity characteristics of BFN based ceramics were measured over a wide temperature (30-300 ^{o}C) and frequency range (100 Hz to 1 MHz) by using HIOKI-LCR meter (3532-50 HI-TESTER). Before measuring the impedance data, all the samples were polished and a thin layer of silver paint coated on both surfaces of the sample. Then the samples were heated slowly (2-3 °C/min) upto 170 °C. Amplitude of the AC signal was 100 mV. The data were taken by computer interface Lab VIEW programme. Z-view software was used for analysing the data and all the parameters related to this study were calculated and given in the results.

Fig. 3.6: Image of HIOKI-LCR meter (3532-50 HI-TESTER).

CHAPTER 4

Structural, Dielectric, Conductivity and Impedance Studies of $Ba(FeNb)_{0.5}O_3$ Ceramics Synthesized by CS and MWS Techniques

4.1 Introduction

In this work, polycrystalline $Ba(FeNb)_{0.5}O_3$/BFN ceramics were prepared by both conventional solid state reaction and microwave processing routes. The structural, microstructure and the electrical properties of the CS and MWS BFN ceramics are compared and discussed in detail.

4.2 Optimization of the Calcination and Sintering Temperatures

To ensure the single perovskite phase formation in the BFN ceramics, the calcination temperature of the parent $Ba(FeNb)_{0.5}O_3$ ceramics was optimized. It is very important to develop single perovskite phase in the synthesized materials as the presence of secondary phase in any ceramics always increases the conductivity and decreases the ceramic properties, which is undesirable for practical applications. Therefore, in the present section, the optimization of the calcination and sintering processes are discussed in detail.

4.2.1 Thermal Analysis

Fig 4.1 shows the DSC and TGA curves of ball milled and dried powders of $Ba(FeNb)_{0.5}O_3$ composition. The overall weight loss from the room temperature to $1250^{o}C$ is ~ 16.4%. The solid-state reactions in the uncalcined BFN powder are marked by two distinct weight losses, one above $600^{o}C$ and the other above $1100^{o}C$. Mass loss in the temperature region of ~600°C in the TGA curve can be attributed to the decomposition of the carbonate reactants. The calculated loss of CO_2 corresponds well with the weight loss indicated by the TGA curve above 600°C. The endothermic peak at 820°C corresponds to the transition of α-Fe_2O_3 to β-Fe_2O_3 as reported by Cahn and Lifshin[1]. The exothermic peak ~1135°C corresponds to solid-state reaction between $BaCO_3$, Fe_2O_3 and Nb_2O_5 precursors. No further weight loss above 1135°C indicates the completion of reaction between the precursors of BFN ceramics. These indicatives that the calcination of BFN ceramics should be performed at temperatures ~1200°C.

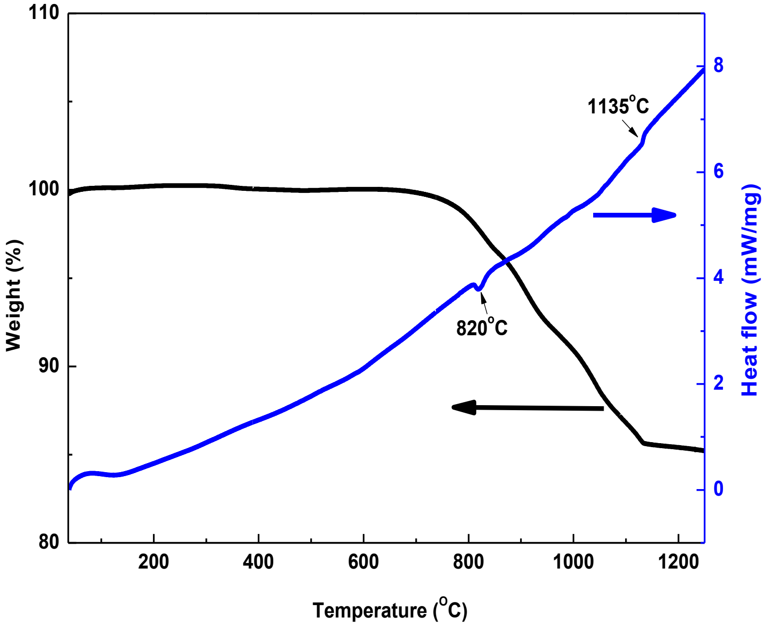

Fig. 4.1: DSC and TGA curves of ball milled BFN powders.

4.3 X-ray diffraction (XRD) studies

4.3.1 Optimization of the Calcination Process

Fig.4.2 shows the XRD patterns of the BFN powder calcined at 1200 and 1250 °C for 4 h, respectively. The single perovskite phase formation was confirmed at 1250°C, whereas at

1200°C small amount of secondary phase, marked by "*", was detected. This suggested that the calcination temperature of the BFN ceramics is 1250°C.

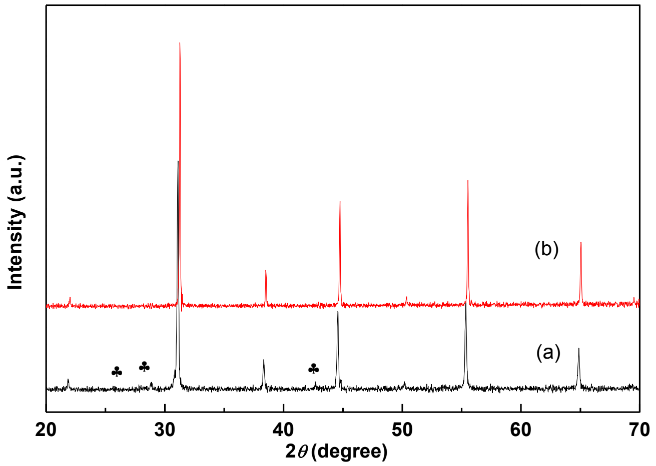

Fig. 4.2: XRD patterns of BFN powders calcined at (a) 1200°C and (b) 1250°C.

4.3.2 Rietveld Refinement

The cubic structure of BFN ceramics was structurally refined by using the crystallographic software FullProf [2] using the Rietveld-refinement method [3]. The results obtained from the Rietveld-refinement method have shown a good agreement between the observed XRD patterns and the theoretical results as shown in Fig. 4.2. Moreover, the difference between the profiles of the XRD patterns experimentally observed and theoretically calculated data's display small differences in scale of intensity as illustrated by a line (Y_{Observed} - $Y_{\text{Calculated}}$). The lattice parameters and atomic positions obtained from the Rietveld-refinement are presented in Table 4.1. The fitted parameters (R_p, R_{wp}, R_{exp}, and χ^2) suggest that the refinement results are well-reliable.

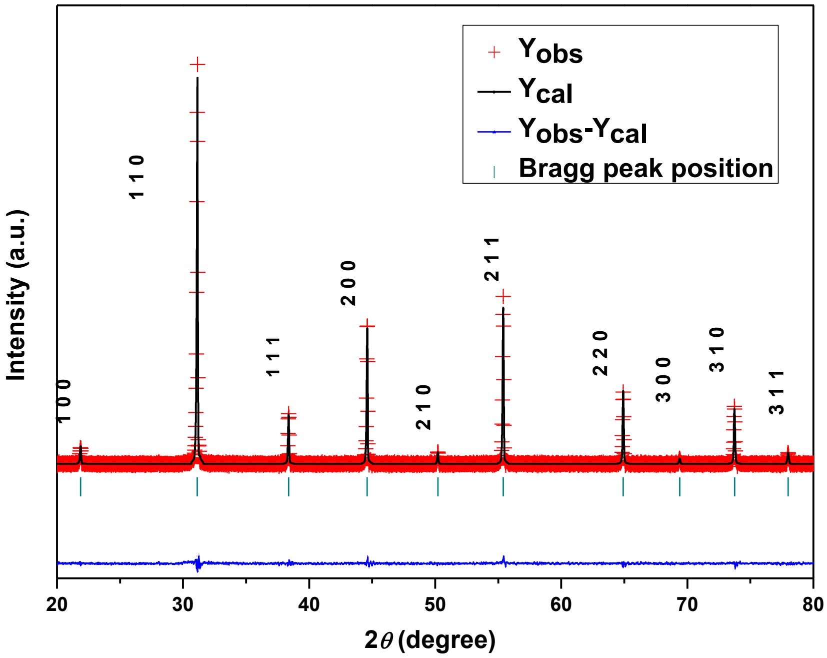

Fig. 4.3: Rietveld refinement of the BFN ceramics calcined at 1250°C.

Table 4.1: Crystallographic parameters obtained from Rietveld refinement of BFN system.

BFN cell parameters	**Refined Values**
Space group	Pm-3m
Cell parameter (Ȧ)	a=b=c= 4.0596 (2); α=β=γ=90°
Cell volume (Ȧ^3)	66.90
Cell Density (gm/cm^3)	6.41
Atomic Positions (x,y,z)	Ba: (0,0,0); Fe/Nb : (0.5,0.5,0.5); O:(0,0.5,0.5)
Wyckoff position	Ba:1a; Fe/Nb:1b; O:3c
R values (%)	R_p=7.27, R_{wp}=9.78, R_{exp}= 6.35, χ^2=2.37

4.3.3 XRD studies of the Conventional and Microwave Sintered BFN Ceramics

Fig. 4.4 shows the XRD patterns of the BFN ceramics conventionally sintered at 1350°C for 4hr and sintered by using microwave technique at 1350°C for 15, 30 and 45 min. Sharp and distinct XRD peaks were obtained for all the samples, which suggest the good crystalline and homogenous nature of the BFN ceramic samples sintered by both the techniques.. The XRD patterns were indexed in cubic crystal structure using a computer program 'POWD' where the standard deviation (SD= $\Sigma(d_{obs}-d_{cal})$, 'd' is inter-plane spacing) was found to be minimum [4].

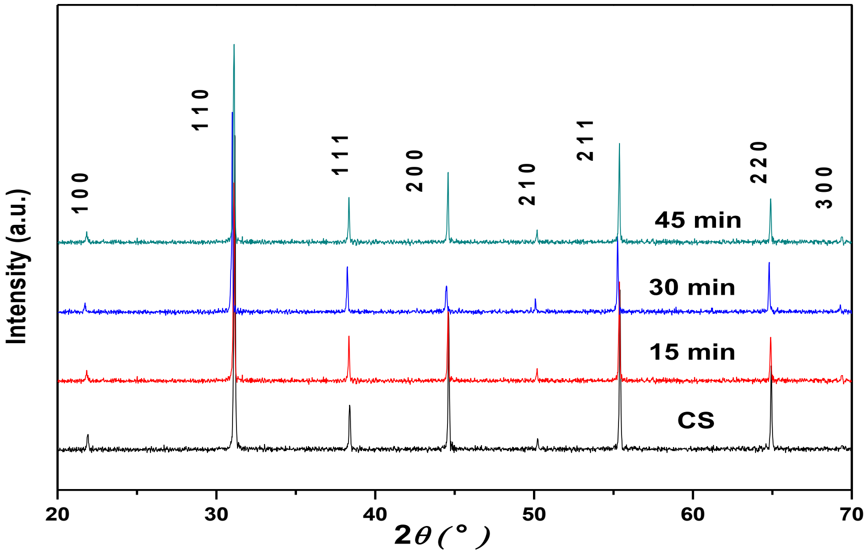

Fig. 4.4: XRD patterns of the BFN ceramics CS at 1350°C for 4hr and MWS at 1350°C for 15, 30, and 45 min.

4.4 Density and Surface Morphology Study

Fig. 4.5 shows the variation of experimental density (RD) with sintering temperature. Optimum density of the BFN ceramic samples, sintered conventionally, was observed at 1350°C. The green pellets of the BFN ceramics were also sintered in microwave furnace at

1350°C for 15, 30 and 45 min.

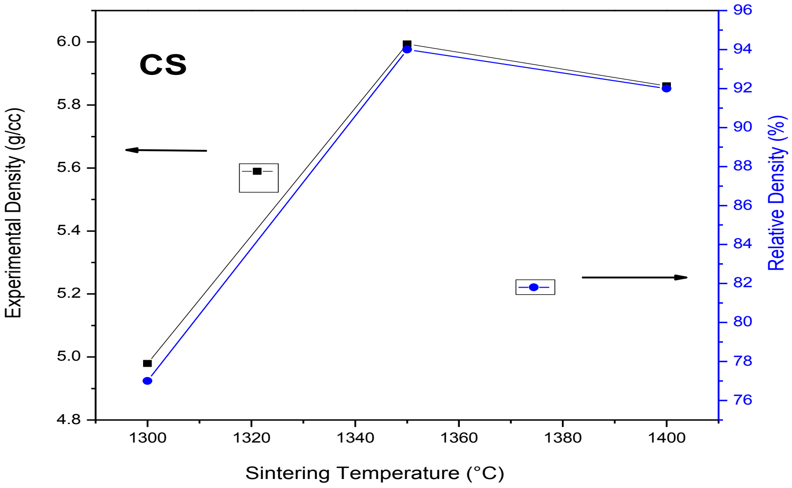

Fig. 4.5: Variation of experimental density with sintering temperature of the BFN ceramics sintered conventionally.

Fig. 4.6 shows the SEM micrographs of the BFN ceramics conventionally sintered (CS) at 1350°C for 4hr and microwave sintered (MWS) at 1350°C for 15, 30 and 45 min.. In all the specimens, dense microstructures with polyhedral grains were observed. Experimental densities, measured by Archimedes method, of CS and MWS BFN ceramics are given in Table 4.2. Experimental density of MWS ceramics was found to be nearer to that of conventionally sintered (CS) BFN samples (given in Table 4.2). MWS ceramic samples showed comparatively larger grains and the grain size increases with increase in soaking duration. Generally, high dielectric loss materials are good absorber of micro-waves [5]. Presence of Fe and high dielectric loss in the BFN ceramics makes this system good absorber of micro-waves. Hence, the grain size of MW sintered BFN ceramics increases with the increase in soaking time period [6]. Smaller grains were present at the grain boundaries, which confirmed the formation of larger grains during grain growth at the expense of smaller ones. The grain sizes of CS and

MWS sintered BFN ceramic samples are given in Table 4.2. The achievement of nearly equal experimental density in MWS BFN ceramics (in 30 minute soaking duration) as that of conventionally sintered (CS) BFN samples (in 4 hours soaking duration) showed the superiority of MWS process over conventional processing.

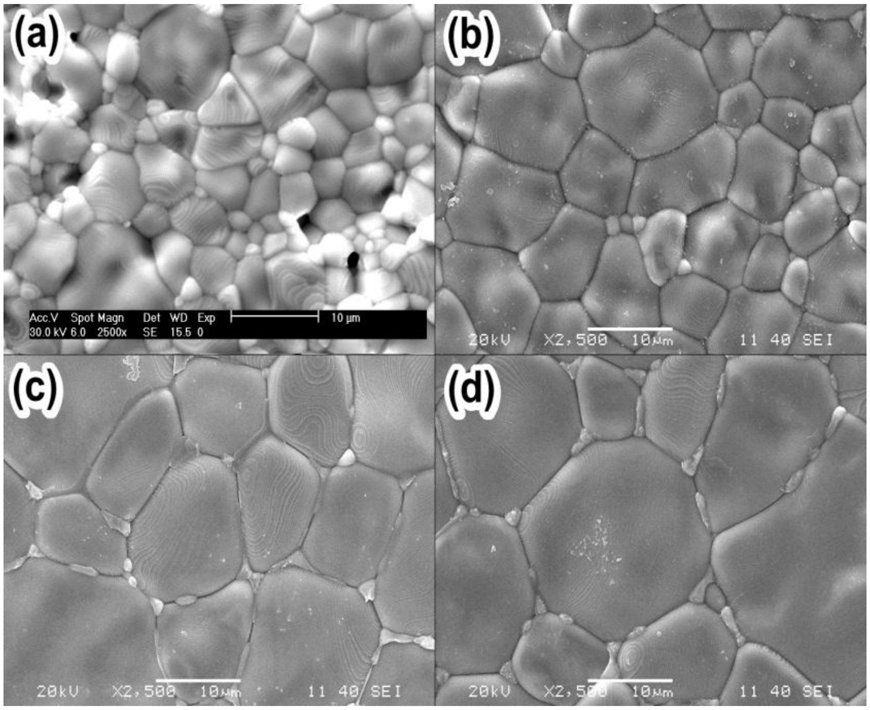

Fig. 4.6: Surface morphology of CS BFN ceramics for (a) 4hrs & MWS for (b) 15, (c) 30 & (d) 45 min at 1350°C, respectively.

Table 4.2: Grain size and experimental density of the BFN ceramics sintered conventionally and in a microwave furnace.

BFN ceramics sintered 1350°C	**Avg. grain size (µm)**	**Density (g/cm^3)**
Conventionally for 4h	6.32	5.97
15 min (MW)	8.19	5.84
30 min (MW)	12.43	5.99
45 min (MW)	16.95	5.93

4.5 Dielectric Studies

4.5.1 Frequency Variation of Dielectric Properties of CS and MWS BFN ceramics

Figs. 4.7 (a) & (b) show frequency dependence of real (ε') and imaginary (ε'') parts of the permittivity (ε*(ω) =ε'-jε'') at RT of CS and MWS BFN ceramics. The ε' decreases with the increase in frequency for all the samples and merges at higher frequencies and attain a value of ~100 at 1 MHz, which is a characteristic of high dielectric constant materials [7]. The dielectric loss (ε'') in a material is a combination of both dc conduction and ac relaxation processes [8]. Generally, the relaxation processes, observed in the case of dipolar materials, have a dispersion kink in the ε' spectrum accompanied by a relaxation peak in the ε'' spectrum [9]. Such type of dielectric behavior arises due to the inhomogeneity in the materials [10], internal barrier layer capacitor [11] and metal insulator interfacial effects [12]. In the present study, the origin of the relaxation process, observed near room temperature, is related with the theoretically fitted permittivity data using the following modified Cole-Cole equation [13, 14]:

$$\varepsilon^* = \varepsilon_\infty + (\varepsilon_0 - \varepsilon_\infty)/[1+(j\omega\tau)^{1-\alpha}] + \sigma^*/(j\varepsilon_0\omega^s) \qquad (4.1)$$

Where ε_0 is the static permittivity, ε_∞ is the permittivity at high frequency, τ is the mean relaxation time and β=1-α, (where α is the angle of semicircular arc). α=1 for Debye type relaxation. Further, the real and imaginary parts of the permittivity (ε*) can be written as,

$$\varepsilon^{'}(\omega) = \varepsilon_\infty + (\Delta\varepsilon/2)\{1 - \sinh\beta z/[\cosh\beta z + \cos\beta\pi/2]\} + \sigma_1/\varepsilon_0\omega^s \qquad (4.2)$$

$$\varepsilon''(\omega) = (\Delta\varepsilon/2)\{1-(\sin\beta\pi/2)/[\cos\beta z + \cos\beta\pi/2]\} + \sigma_{dc}/\varepsilon_0\omega^s \qquad (4.3)$$

Where z=ln(ωτ) and $\Delta\varepsilon = \varepsilon_0 - \varepsilon_\infty$. For purely ohmic conduction s=1. The experimental data at RT are fitted using Eq. 4.3 and the extracted fitted parameters ($\varepsilon_{0,}$ ε_{∞}, β, τ, s) are given in Table 4.4. The fitted α values, obtained for all samples at room temperature are less than 1, which confirmed a non-Debye type of relaxation process present in both the CS and MW sintered BFN samples. The characteristic loss peak observed in both the CS and MW sintered BFN ceramics does not fall at the same frequency. The characteristic loss peak at room temperature observed for all the MW sintered ceramics fall at around 10 kHz whereas for the CS ceramics, the characteristic loss peak is ~10^5 kHz. This hints that the relaxation processes responsible for MW sintered ceramics is not the same as that for the CS ceramics. It is well known that different types of relaxation processes fall in different frequency regions. At room temperature, the relaxation processes like space charge polarization, Maxwell-Wagner polarization show their loss peak below <10^5 Hz, whereas loss peak due to electronic and hopping polarizations are observed at or above 10^5 Hz [15]. This suggests that the hopping and electronic type relaxations are contributing to CS ceramics whereas; Maxwell-Wagner polarization contributing to the MW sintered BFN ceramics. The possible relaxation processes, which may be responsible for colossal dielectrics constant in both CS as well as in MW sintered BFN ceramics, are discussed below.

Generally, oxygen vacancies are produced in the ceramic materials processed at high temperature and in normal atmosphere [16]. This distorts the oxygen stoichiometry of the compound and produces some anionic as well as cationic defects in the processed samples. In the BFN system both the transition metals, iron (Fe) and niobium (Nb), have more than one oxidation states (Fe^{2+}, Fe^{3+}, Nb^{4+}, and Nb^{5+}). Electrons produced during the ionization of oxygen vacancies get trapped by the Fe^{3+} and Nb^{5+} cations, which promote electronic relaxation between the Fe^{3+} & Fe^{2+} or Nb^{5+} & Nb^{4+} ions. Similarly, electronic relaxation can also occur via oxygen vacancy as a medium in the form of Fe^{2+}-$V_O^{\bullet}$ - Fe^{3+} [17]. The relaxation processes in the CS and MW sintered BFN ceramics, shown in Fig. 4.7 (b), occurred in the different frequency regions. Since, the dielectric loss peak was observed around 10^5Hz for the CS ceramics; therefore the possible origin of the relaxation process in the CS ceramics may be due to the electronic relaxation of oxygen vacancies or relaxation between Fe^{3+}& Fe^{2+} or Nb^{5+}& Nb^{4+} ions. Whereas, the relaxation process observed in MW sintered ceramics was of Maxwell-Wagner type of relaxation. This confirmed that the processing conditions have great impact not only on the microstructures but also on the dielectric properties of the high dielectric constant materials.

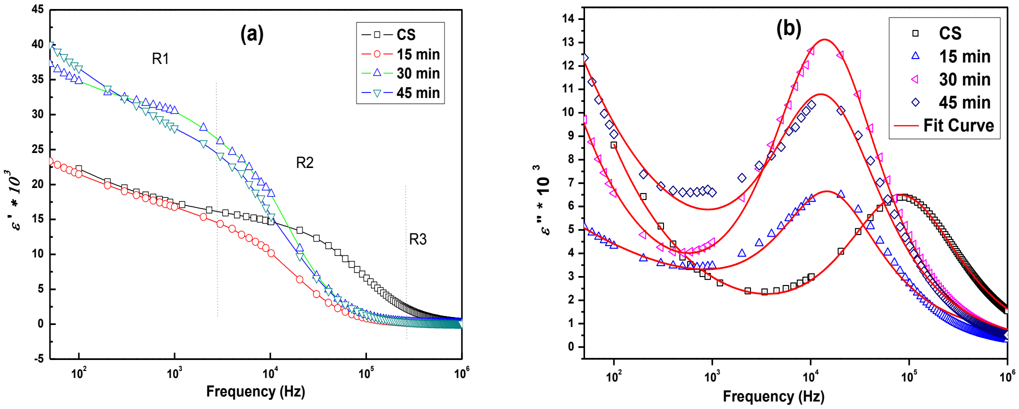

Fig. 4.7: Frequency variation of (a) real, and (b) imaginary parts of CS and MWS BFN ceramics.

Table 4.3: Dielectric constant and dielectric loss at room temperature of CS and MWS BFN ceramics.

BFN Ceramics sintered at 1350°C	**ε_r (RT) at 10 kHz**	**tanδ (RT) at 10 kHz**
4hrs (CS)	11569	0.31
15min (MWS	10063	0.51
30min (MWS	18650	0.65
45min (MWS)	15244	0.57

Table 4.4: Fitted parameters by using modified Cole-Cole relaxation equation of the CS and MWS BFN ceramics.

BFN ceramics sintered 1350 ^{0}C	**CS & MW sintered BFN at 1350 ^{0}C**	**$\Delta\varepsilon=\varepsilon_0-\varepsilon_\infty$**	**α**	**$\tau * 10^{-5}$ (s)**	**$\sigma_{dc} \times 10^{-6}$ (Sm^{-1})**	**S**
Conventionally for 4h	CS (4h)	14667	0.11	1.16	0.76	0.5
15 min (MW)	15 min	10738	0.02	6.42	0.11	0.2
30 min (MW)	30 min	29123	0.08	7.03	0.68	0.5
45 min (MW)	45 min	21715	0.10	7.21	0.45	0.4

4.5.2 Temperature Variation of Dielectric Properties of CS and MWS BFN ceramics

Figs. 4.8 (a) & (b) show the temperature dependence of dielectric constant (ε') and dielectric loss (tanδ) at different frequencies of the CS (4hr) and MWS (30 min). Here, because of the high dielectric constant, the BFN samples sintered in MW furnace for 30 min were taken for temperature dependent dielectric properties variation study.Two anomalies were observed in the ε' vs. temperature plot in all the samples i.e. a dielectric step was observed ~60^{o}C and a dielectric peak was observed ~350°C for both the CS and MWS samples.The dielectric peak observed at low frequency (1 kHz) ~350°C diminished with the increase in frequency (1 MHz), which suggests that the relaxation process must be originating from the extrinsic factors. Most of the ferroelectrics also exhibit similar type of dielectric relaxation in the paraelectric region

[18, 19]. The dielectric abnormalities observed in this temperature range is the result of the oxygen vacancies and the other point defects as reported earlier [20]. Concentration of oxygen vacancies and the used processing conditions influence the relaxation process [21]. The indexing of the calcined BFN powder pattern confirmed the centro-symmetric nature of BFN ceramic at room temperature. Literature reports also confirm that there is no structural phase transformations in the BFN ceramics from room temperature to 550^{o}C [22]. This confirmed that the origin of dielectric peak observed around 200^{o}C was not due to any structural transformation, but due to the formation of oxygen vacancies and related to other transition metal point defects. This confirmed BFN is a non ferroelectric ceramic.

The difference in the dielectric relaxations due to space charges present in the ferroelectric materials and the high dielectric constant (high-k) materials is that, space charges are present at the vicinity of room temperature in high-k materials [23], whereas effect of space charges can be observed far away from the room temperature in ferroelectric materials [19]. The space charges created during sintering process are confined to their defect sites, which promotes electronic relaxation among the defect sites. Generally, in high-k materials, thermal fluctuations are significantly high at room temperature such that the space charges are no more confined to their defect sites but extended to the whole sample, which makes the sample semiconducting. With the application of an electric field to these high-k materials, space charges moves inside the grains and forms different conducting regions near grain boundaries. This leads to Schottky type of barriers formation at the interfaces, which leads to high dielectric constant in these non-ferroelectric materials.

The interfacial or Maxwell-Wagner polarizations can be interpreted on the basis of semiconducting grains and insulating grain boundaries. There is a large difference in the processing conditions among the sintering processes used in the present study. In CS, the cooling rate was very small (~5°C / min) whereas in the MW sintering, a very fast cooling (~20 °C/min) takes place in normal atmosphere. It is well known that fast cooling in normal atmosphere after sintering produces semiconducting grains and insulating grain boundary [16]. Therefore, the Maxwell-Wagner polarization or interfacial polarization arises due to presence of different types of conducting processes present in the MW sintered BFN ceramics.

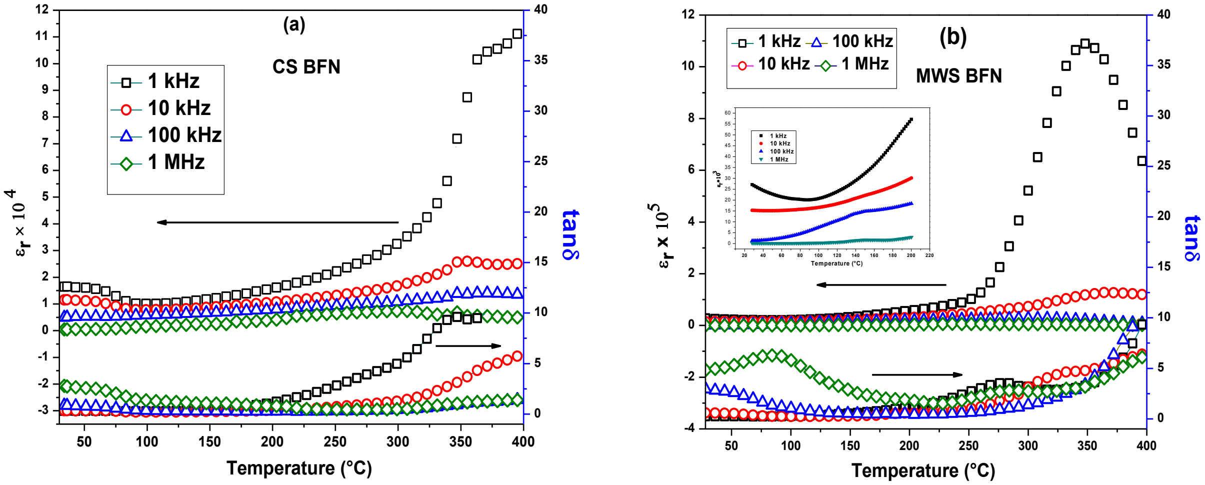

Fig. 4.8: Temperature dependence of dielectric constant and dielectric loss at different frequencies of (a) CS and (b) MWS for 4hr & 30 min respectively for BFN ceramics.

4.6 Frequency Variation of Conductivity & Impedance Spectroscopic Studies

4.6.1 Frequency Variation of Conductivity of CS BFN Ceramics

The ac conductivity study is a useful technique for investigating the charge carrier's nature and the ac conductivity response. Fig. 4.9 (a) shows the ac conductivity vs. frequency plots at various temperatures. In this plot, following different characteristics of ac conductivity were observed in different frequency and temperature regions

(a) At low temperature: conductivity followed the power law dependence i.e. $\sigma \sim \omega^s$

(b) At high temperature and at low frequencies, a frequency independent plateau region appeared in the conductivity spectrum and referred as dc conductivity (σ_{dc}),

(c) At high temperature and intermediate frequencies, a frequency dispersive conductivity regime appeared which was attributed to the presence of interfacial effect in the ceramics.

(d) At higher frequencies, a weak frequency dependent plateau region appeared which was attributed to the presence of grain in the ceramics.

The frequency variation ac conductivity can be explained by Jonscher's power law, given below: [24, 25]

$$\sigma(\omega) = \sigma_{dc} + a\omega^{S} \qquad (4.4)$$

Where, 'a' and 's' are the frequency and temperature dependent parameter. The total conductivity is a combination of low frequency dc conductivity (σ_{dc}) and the frequency dependent ac conductivity (σ_{ac}).

In the reprted study**, t**he experimental data did not fit well with the Jonscher's power law. Therefore, the double power law (given in Eqn. 5) was used for fitting the experimental data.

$$\sigma(\omega) = \sigma_{dc} + A\omega^{m} + B\omega^{n} \qquad (4.5)$$

Here, the coefficients A and B and exponents m ($0<m<1$) and n ($1<n<2$) are dependent on temperature and frequency. The use of double power law and interpretation of extracted parameters is explained earlier [26, 27]. This suggests the presence of three types of conduction processes at elevated temperature: (i) low frequency conductivity (σ_{dc}) is due to long-range ordering (frequency independent), (ii) mid frequency conductivity ($A\omega^{m}$) is due to the short-range hopping, and (iii) high frequency conduction ($B\omega^{n}$) is due to the localized relaxation hopping mechanism. The double power law confirms the jump relaxation model (JRM) [27]. According to this model, at low frequencies, the long range translational motion of ions is observed. Whereas in the frequency dispersive region the unsuccessful hopping (forward-backward-forward) of ions, moving back to its initial position and the successful localized hopping processes compete with each other.

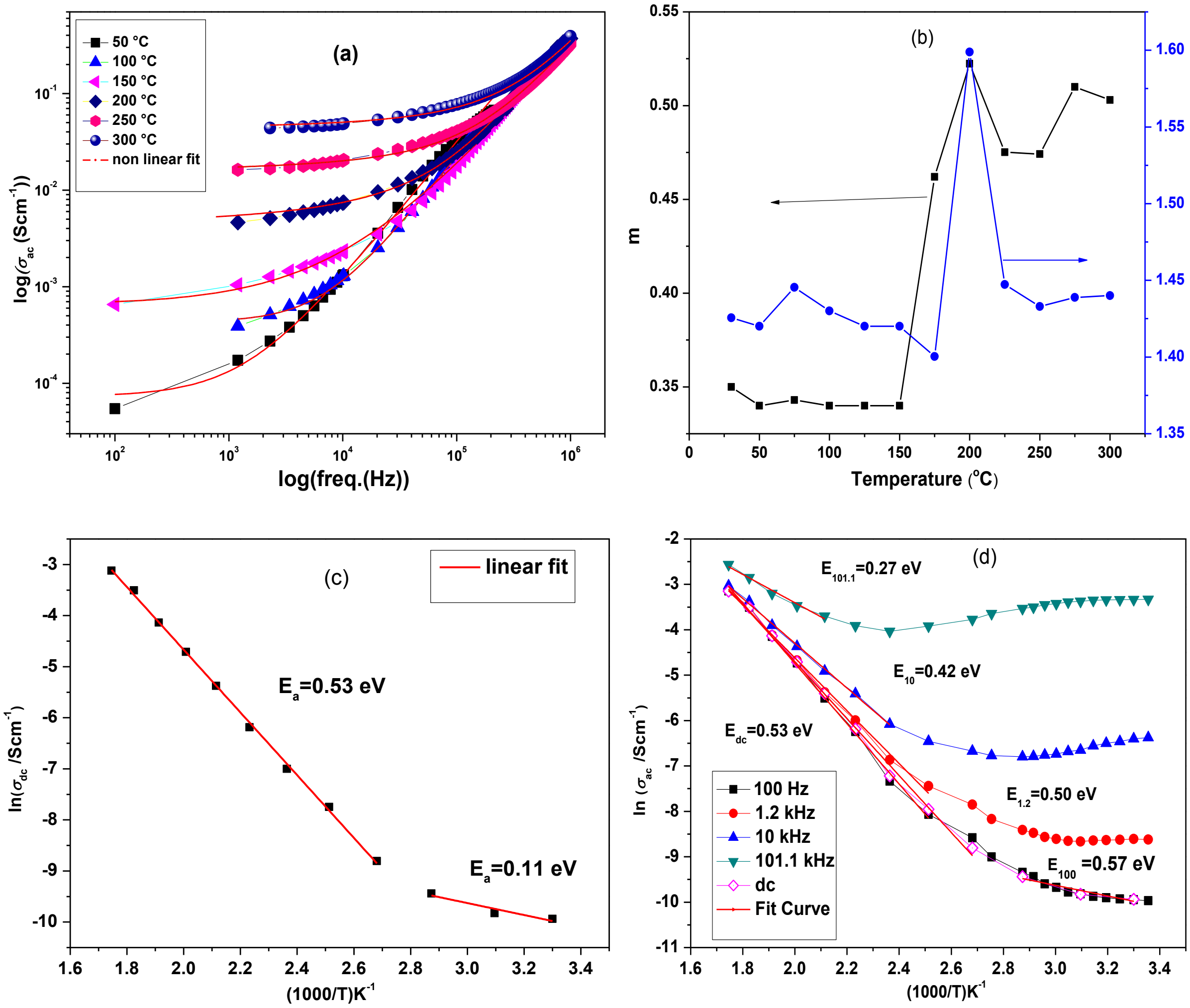

Fig. 4.9: (a) Variation of ac conductivity with frequency at different temperatures (b) temperature variation of extracted parameters, Arrhenius plots of (c) d.c. and (d) a.c. conductivities.

The experimental a.c. conductivity data was fitted by using the double power law and shown in Fig. 4.9 (a). The parameters extracted are A, B, m, n and σ_{dc}. The exponent's m and n are plotted in Fig. 4.9 (b). It is observed that the value of m ($0<m<1$) and n ($1<n<2$) first increases upto 200°C and then decreases with the increase of temperature. Since different hopping mechanisms have been reported by different researchers and these mechanisms predict different temperature and frequency dependencies of the exponent s ($0<s<1$), in the case of small polaron hopping, s increases with temperature, while for a large polaron hopping mechanism, s decreases with temperature. It can be seen in Fig. 4.9 (b) that the values of m are less than 1, and also m increases below 200°C and decreases above 200°C; hence, the conduction arises due to the short-range translation hopping assisted by both small polaron (T<200 °C) and large polaron (T>200 °C) hopping mechanisms. The values of n are found to vary between 1 and 2 and it increase with the increase of temperature. This indicates conduction mechanism is localized where back and forth hopping of electrons takes place between two charge defects.

Fig. 4.9 (c) shows the variation of dc conductivity with temperature. The dc conductivity follows temperature dependent Arrhenius behavior (given in Eqn. 4.6):

$$\sigma_{dc} = \sigma(0)\exp(-E_a / k_B T) \qquad (4.6)$$

Here, the slope of the dc conductivity changes with the increase in temperature, which indicates the involvement of multiple activation processes. In the lower temperature region, the dc conductivity is almost temperature independent and the corresponding low value of activation energy (~0.11 eV) suggests the presence of an intrinsic conduction phenomena taking place in the BFN samples [28]. At higher temperatures, the value of activation energy (0.53 eV) is closer to activation energy required for grain boundary conduction process. Low activation energy (~0.11 eV) corresponds to intrinsic conduction due to the release of a large number of space charges and other charge carriers in the BFN ceramics [28]. With the increase in temperature the dc conductivity increases. The obtained activation energy at higher temperature (~0.53 eV) is nearer to that of ionization of oxygen vacancies [29]. Therefore, movements of oxygen vacancies can be considered for the high temperature dc conduction in the BFN ceramics.

Fig. 4.9 (d) shows that the ac conductivity follows the temperature variation Arrhenius relation at different frequencies. The σ_{ac} strongly varies in high temperature regime whereas it remains unchanged at low temperature regime. The frequency dispersive nature of σ_{ac} in low temperature region is attributed to space charge effect [23].The value of the ac conductivity substantially increases with the increase in frequency. It can be seen that the ac conductivity value increases with the increase in frequency at a given temperature, which suggest that the polaron hopping may be taking place in the BFN system [30, 31]. With the increase in temperature, the dielectric relaxation becomes prominent and the σ_{ac} becomes less frequency dependent as all curves appear to merge together, which suggest that the relaxation mechanism is mainly governed by the hopping or trap-controlled ac conduction process [32]. At higher temperatures, the E_{ac} (ac activation energy) value is calculated by using the following equation.

$$\sigma_{ac} = \sigma(0)\exp(-E_a / k_B T) \qquad (4.7)$$

The calculated values of E_{ac} (ac activation energy) at 0.1, 1.2, 10, 101.1, 505.1 and 1000 kHz frequencies are 0.56, 0.53, 0.45, 0.37, 0.25 and 0.15 eV, respectively. The value of E_{ac} decreases with the increase of frequency. At low frequencies, the charge carriers exhibit long range hopping in order to overcome the high barrier width with large E_{ac}. While at the higher frequencies, the ac conductivity is accounted by the short range hopping.

4.6.2 Frequency variation of conductivity of MWS BFN ceramics

Fig. 4.10 (a) shows the frequency variation of ac conductivity at different temperatures of MWS BFN ceramics. With the increase in frequency and temperature, following characteristic features of the conductivity spectra are observed:

(a) Below 100°C- frequency dispersive conductivity in lower frequency region followed by a high frequency plateau region.

(b) Above 100°C- the high frequency plateau region gradually disappears and

(c) Above 130°C- the conductivity spectrum split into two dispersive regions with different natures and mechanisms. The low frequency region follows the Jonscher's power law while the intermediate frequency region follows the double power law.

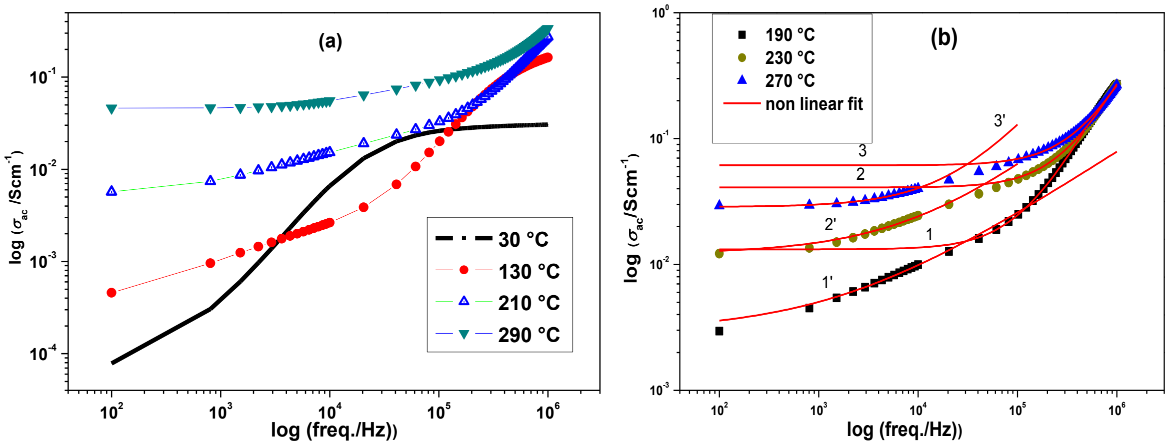

Fig. 4.10: (a) Variation of ac conductivity with frequency at different temperature, (b) Variation of ac conductivity with frequency fitted with single power law (1', 2' & 3') and double power law (1, 2 &3).

From the above explanation, following inference can be drawn: -Grain boundary and electrode interface effect becomes noticeable with the increase in temperature because of the increase in conductivity of the samples. Therefore, the high frequency plateau region is attributed to grain, the intermediate frequency region to grain boundary and the low frequency region to electrode interface. Presence of grain, grain boundary and electrode interface effect is confirmed in the impedance study.

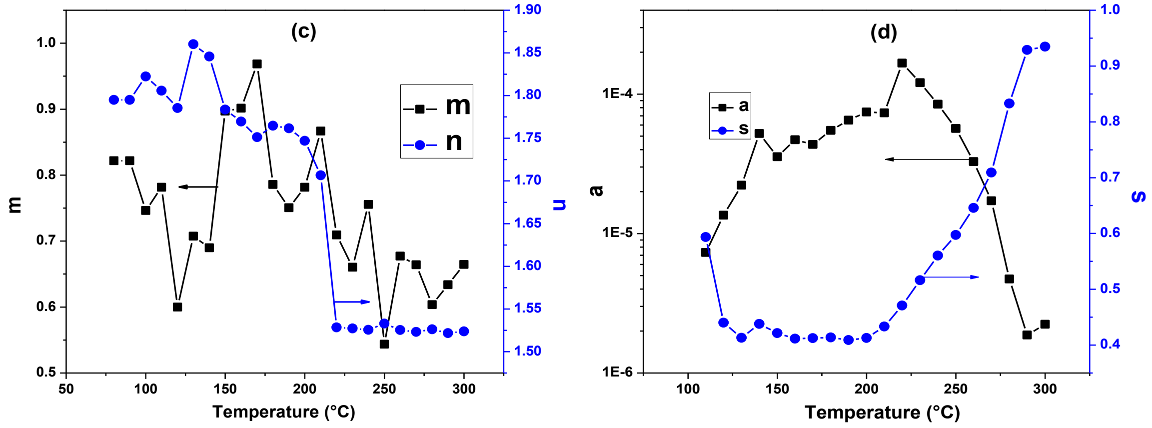

Fig. 4.10: Temperature variation of extracted parameters obtained from (c) double power law and (d) single power law.

The low frequency ac conductivity data is fitted with the Jonscher's power law and the intermediate frequency conductivity data is fitted with the double power law (Fig. 4.10 (b)). The notations 1, 2 and 3 are used for nonlinear fit at higher frequencies whereas; the 1', 2' and 3' notations are used for nonlinear fit at lower frequencies. Similar type of results are also reported in the high dielectric constant CCTO system [33]. The temperature variation of the adjustable parameters 'm', 'n', 'a' and's' are shown in Fig. 4.10 (c) & (d). The parameters 'm' and 'n' decreases with the increase of temperature above 150°C. The decrease of m (0<m<1) above 150°C suggests that the large polaron hopping mechanism contributes to the conduction process. Whereas, the value of "n" between 1 & 2 suggests that localized type of hopping mechanism is responsible for conduction process. Similarly, as shown in Fig. 4.10 (d) above 200°C, the value of ‘s’ ($0<s<1$), extracted from the lower frequency region (electrode interface), increases with the increase of temperature. This suggests that small polar hopping mechanism is responsible for the conduction process in lower frequency region.

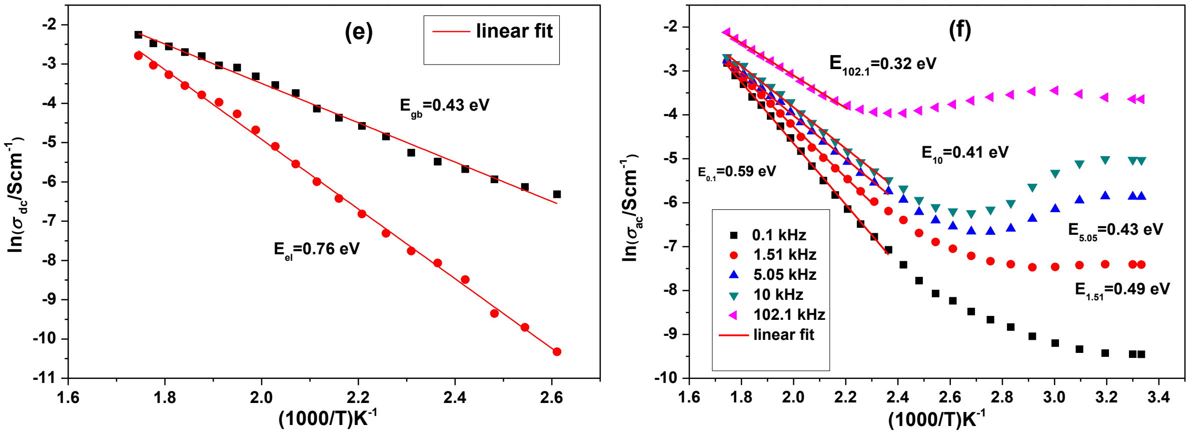

Fig. 4.10: Arrhenius plots of (e) dc and (f) ac conductivities.

Fig. 4.10 (e) shows that dc conductivity corresponding to electrode interface and grain boundary follows the Arrhenius behavior (eqn. 6). The conductivity of electrode interface is lower than that of the grain boundary, which suggests that resistance of electrode interface is higher than that of the grain boundary. The activation energies corresponding to grain boundary and electrode interface are 0.43 eV and 0.76 eV, respectively.

The temperature variation of ac conductivity at different frequencies also follows the Arrhenius relation, as shown in Fig. 4.10 (f). The σ_{ac} strongly varies at high temperature region above 140 °C whereas it remains unchanged in the low temperature region below 140 °C. The value of ac conductivity at a given temperature increases with the increase in frequency, which suggests that the polaron hopping is taking place in the system [30, 31]. At high temperatures i.e. above 140 °C, σ_{ac} becomes less frequency dependent and all the conductivity curves at different frequencies appears to merge. At higher temperatures, E_{ac} (ac activation energy) is calculated by using the Arrhenius equation (eqn. 4.7). The values of E_{ac} (ac activation energy) at 0.1, 1.51, 10 and 102.1 kHz frequencies are 0.59, 0.49, 0.43, 0.41, and 0.32 eV, respectively. The value of E_{ac} decreases with the increase in frequency. This is because at lower frequency the long range hopping involves to overcome the high barrier width while the lower activation energy at high frequency involves the short range or localized hopping.

4.6.3 Impedance Spectroscopic Studies of CS BFN Ceramics

Complex impedance spectroscopy (CIS) analysis has been mostly recognized for investigating the electrical properties of electro-ceramic materials. This analysis can distinguish the electrical inhomogeneities like grain, grain boundary and electrode interface effects present in the ceramic materials [34]. Each such electrical active region can be represented by a parallel combination of resistive, R and capacitive, C components. Therefore, the impedance of the system can be represented by the series combinations of such parallel R and C components. To extract this information, it is essential to model experimental data using an equivalent electrical circuit, i.e. some combination of resistors, capacitors and constant phase elements (CPEs) connected in series and/or parallel that give the same impedance response as that of the ceramic.

Fig. 4.11 (a) shows the complex impedance plot (Nyquist plot) of CS sintered BFN ceramics at selected temperatures between 30°C and 300°C. It was observed that with the increase in temperature the radius of the semicircles decreases. Depressed semicircular arcs were formed in the complex plane indicates a typical non-Debye type of relaxation which follows the empirical Cole-Cole formalism [13], given as

$$Z^*(\omega) = R/[1+(j\omega/\omega_0)^{1-\alpha}] \qquad (4.8)$$

Here, the exponent "α" represents the magnitude of departure from the ideal semicircular arc. For α→0, the above equation represents the classical Debye formalism. The distribution of relaxation phenomena is exhibited for α <1. This non ideal behavior can be attributed to several factors such as grain size distribution, grain orientation, grain boundaries, stress, strain phenomena and atomic defect distribution.

In this case, the equivalent circuit model consists of modified two parallel RC circuits connected in series. The equivalent circuit modeled here is suggested by a clear inspection of the ac conductivity data and the possible mechanisms, which can appear in the ceramics. From the ac conductivity data we observed two distinct regions, one at higher frequencies with frequency independent/weakly dependent on frequency/plateau region followed by lower frequency dispersive region. The resistance "R_g" is attributed to grain at high frequency and R_{gb} (lower frequency plateau region) and C_{gb} (frequency dispersive region) for grain boundary at lower frequencies. Further by inspection of the frequency variation modulus (M") and impedance (Z") data a CPE is included in the equivalent circuit. We have fitted the impedance data by using the equivalent circuit $R_g(R_{gb}QC_{gb})$.

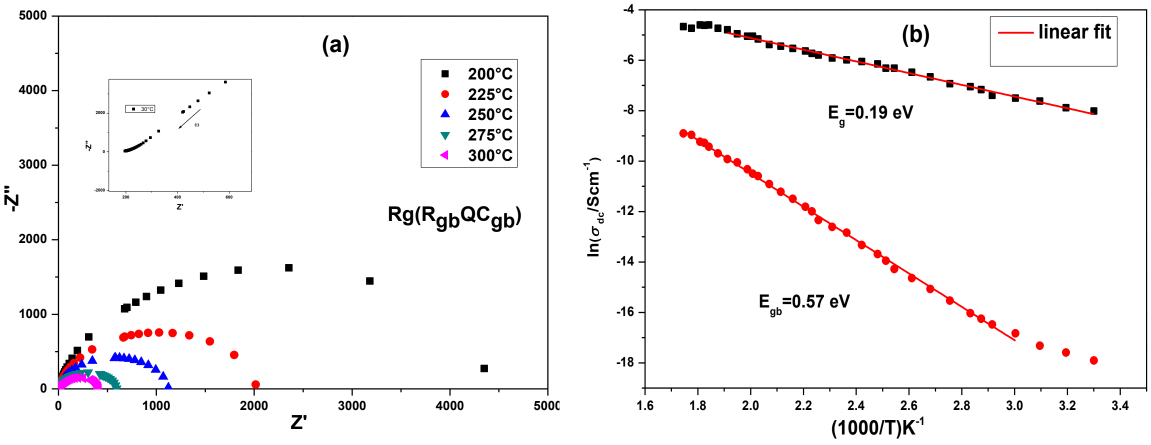

Fig. 4.11: (a) Nyquist plot of CS BFN ceramic at different temperatures and the inset fig shows the RT plot, and (b) temperature variation of grain & grain boundary conductivity.

The resistance of grain and grain boundary are extracted at different temperatures. The corresponding conductivities (σ=l/(A*R), where l=thickness & A=area of the sample) follows the temperature variation Arrhenius relation, as shown in Fig. 4.11 (b). The activation energy corresponding to grain and grain boundaries are ~ 0.19 eV and 0.57 eV, respectively. Oxygen vacancies are considered for the possible conduction mechanism in grain and grain boundary regions in the BFN ceramics. It is a well-known fact the release of oxygen from the bulk during the high temperature sintering and subsequent cooling makes the grains as semi conductive and the grain boundaries as insulating[35]. Since, the BFN ceramics are sintered at higher temperatures (1350°C) therefore the oxygen vacancies plays predominant role in the relaxation and conduction processes. The first and second ionization energies of oxygen vacancies are 0.1 and 0.6eV. The calculated values (0.19 & 0.57eV) of ionization energies suggest that first and second ionization energies of oxygen vacancies are responsible for the conduction processes in the BFN ceramics.

4.6.4 Impedance Spectroscopic Studies of MWS BFN Ceramics

The equivalent circuit for the MWS BFN ceramic is modeled considering the ac conductivity data. From the ac conductivity spectrum, the increase in conductivity with the increase in temperature helped to separate out the grain, grain boundary and the electrode interface effects. The capacitance of electrode interface effect is comparable to that of capacitance of grain boundary upto 170°C and above this temperature the capacitance of electrode interface effect is higher than that of the capacitance of grain boundary as can be seen in the Z' and Z" plot. Therefore we have used two equivalent circuits one upto 170 °C with $R_g(R_{gb}C)(R_{el}Q)$ and one above this temperature with $R_g(C(R_{gb}(R_{el}Q)))$ circuit. These two equivalent circuits are distinguished in the web report [36].

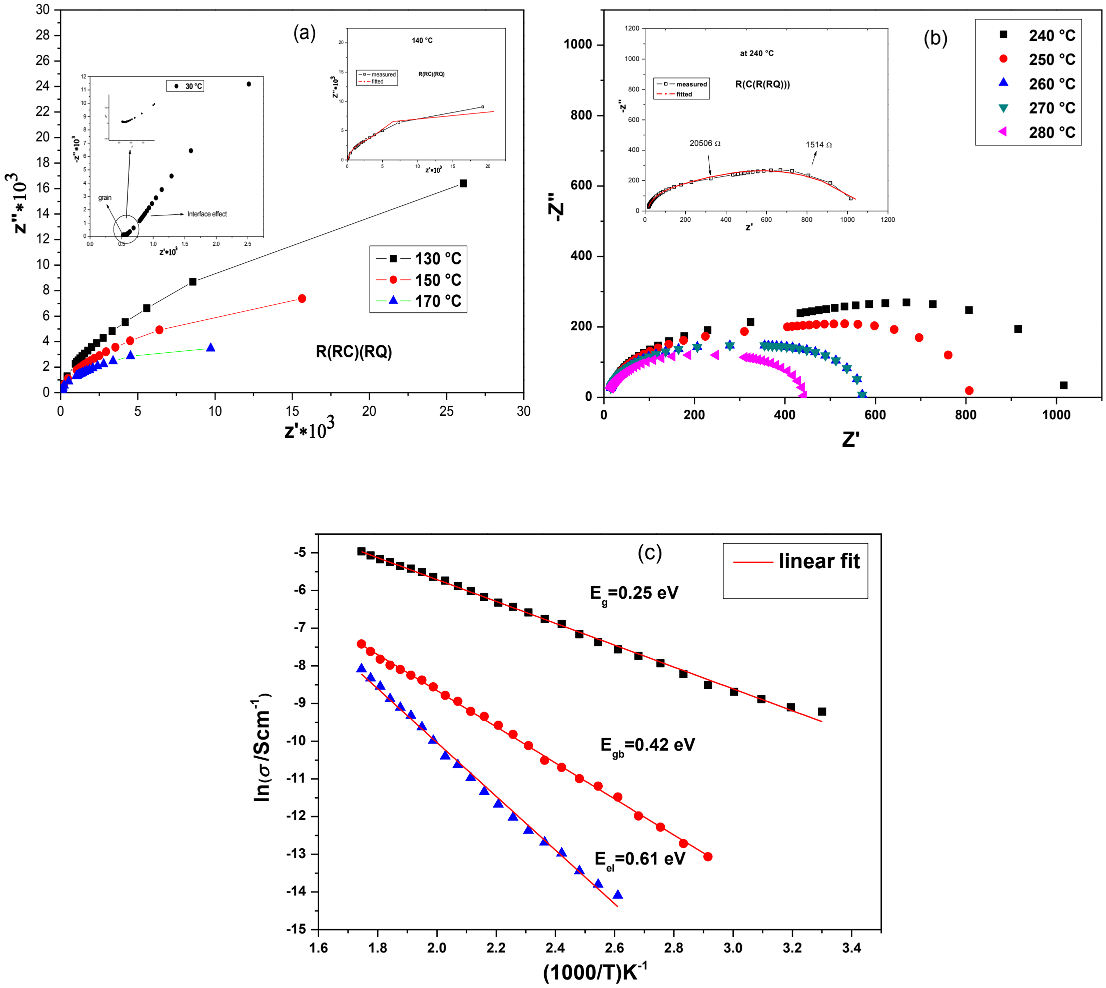

Fig. 4.12: Nyquist plots of MWS BFN ceramic at different temperature fitted with (a) $R_g(R_{gb}C)(R_{el}Q)$ equivalent circuit (b) $R_g(C(R_{gb}(R_{el}Q)))$ equivalent circuit (c), temperature variation of grain, grain boundary & the electrode interface conductivities.

Fig. 4.12 (a) and (b) show the cole-cole plots of the MWS BFN ceramics at selected range of temperatures. In Fig. 4.12 (a), it is shown that the experimental data is fitted well with the equivalent circuit $R_g(R_{gb}C)(R_{el}Q)$ up to 170°C and above this temperature the data is fitted well with the $R_g(C(R_{gb}(R_{el}Q)))$ circuit (Fig. 4.12 (b)). The inset in the Fig. 4.12 (a) shows the RT (30°C) Nyquist plot where the grain behavior is shown at higher frequencies and the interface effect is shown at lower frequency. With the increase in temperature, the high resistive interface becomes leaky interface because of the increase in conductivity which further enhances the capacitance of the interfaces. This leads to decrease in the radius of the semicircle decrease with the increase in temperature.

The resistance of grain, grain boundary and electrode interface effects are extracted at different temperatures. The corresponding conductivities, $\sigma = l/AR$, where l=thickness, A=area, and R=resistance of the sample follows the Arrhenius relation, as shown in Fig. 4.12 (c). The activation energy corresponding to grain, grain boundary and electrode interfaces are ~ 0.25, 0.41 and 0.62 eV, respectively. The obtained activation energies suggests oxygen vacancy plays important role for the conduction process at different regions such as grain, grain boundary and electrode interfaces.

4.7 Leakage Current and Polarization Measurement

Fig 4.13 (a) and (b) show the leakage current behaviour of the CS (for 4hr) and MW sintered (for 30 min) BFN samples. The current vs. time (I-t) response is measured at 50V applied voltage. There is not so much order of magnitude difference in the leakage current as a function of time (up to 20 s) for both the CS and MW sintered BFN samples. The value of leakage current is very high for conventional sintered ceramics i.e. ~1.29 x 10^{-6}A, whereas it

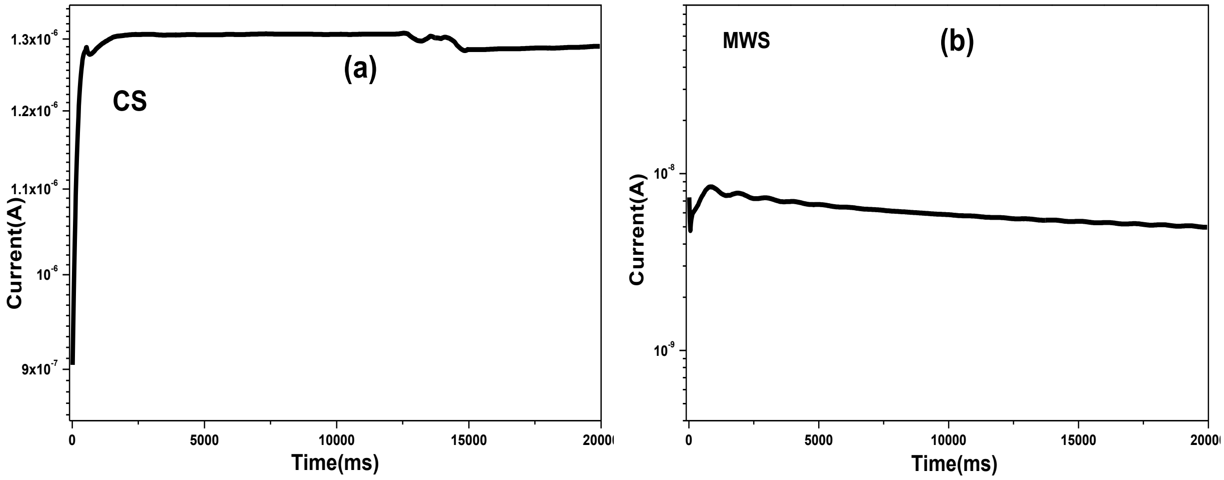

Fig. 4.13: Current-time (*I-t*) response of (a) CS and (b) MW sintered for 30 min BFN ceramics.

less for MW sintered ceramics i.e. ~4.98 x 10^{-9}A. The lower value of leakage current in the MW sintered BFN samples than the CS ones suggests the advantage of using MWS for these types of high dielectric constant systems.

Fig 4.14 (a) and (b) shows the polarization vs. voltage loops of the CS and MWS BFN samples, respectively. The loops are taken just below the breakdown voltages of the CS and MWS BFN samples. Loops of the CS and MWS BFN samples do not show polarization saturation, which confirms about the non-ferroelectric nature of these samples. Non-ferroelectric nature of the BFN samples can be explained on the basis of leakage current behavior [37, 38]. Unsaturated loops are observed for low value of applied field for both CS and MWS BFN samples. The lossy capacitor response [39] is observed in the hysteresis loops of both CS and MWS BFN samples indicates high leakage current in the sample [40].

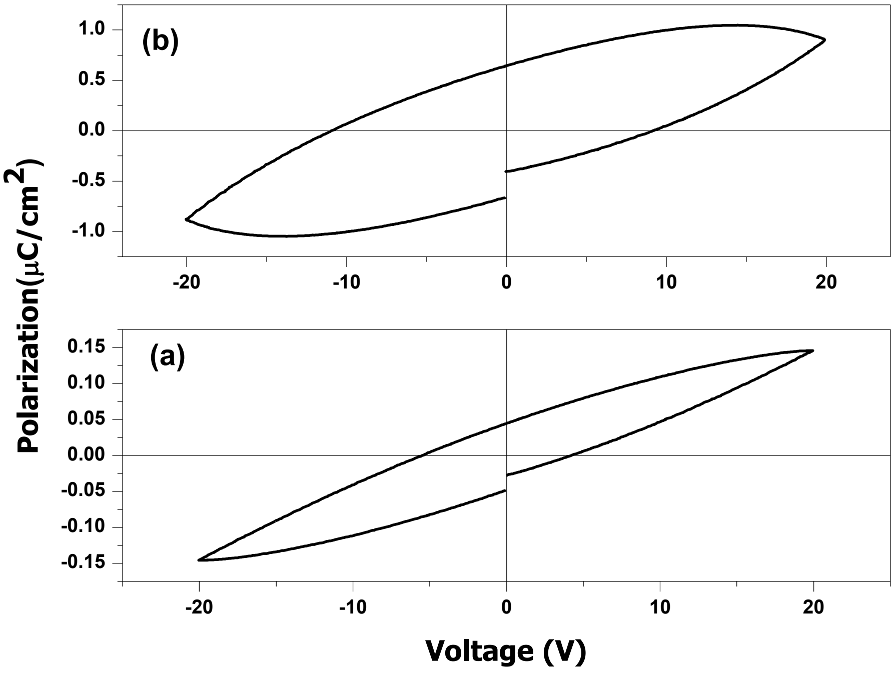

Fig. 4.14: Polarization vs. applied voltage of (a) CS, and (b) MWS BFN ceramics.

4.8 Chapter Summary

Effect of conventional and microwave sintering on the structural, morphological and dielectric properties of the BFN ceramic samples were studied and compared. Experimental density of the CS and MWS BFN samples was nearly same. Dense microstructures with large grains were obtained in MWS BFN ceramics. High dielectric constant, observed in MW sintered BFN ceramics, was attributed to the large grain size and the Maxwell-Wagner type interfacial polarization. A non-Debye type relaxation at room temperature was observed in both the CS and MW sintered BFN ceramics.

References

[1] R.W. Cahn, L. Eric, Concise encyclopedia of materials characterization, Pergamon Press, Oxford; New York 1993.

[2] J. Rodriguez Carvajal, FULLPROF: A Program for Rietveld Refinement and Pattern Matching Analysis, in: Abstracts of the Satellite Meeting on Powder Diffraction of the XV Congress of the IUCr, Toulouse, France, 1990, pp. 127.

[3] H.M. Rietveld, Line profiles of neutron powder-diffraction peaks for structure refinement, Acta Crystallographica 22 (1) (1967) 151-152.

[4] E. Wu, POWD, an interactive program for powder diffraction data interpretation and indexing, J. Appl. Crystallogr. 22 (5) (1989) 506-510.

[5] E.T. Thostenson, T.W. Chou, Microwave processing: fundamentals and applications, Composites Part A 30 (9) (1999) 1055-1071.

[6] Z. Xie, J. Yang, X. Huang, Y. Huang, Microwave processing and properties of ceramics with different dielectric loss, J. Eur. Ceram. Soc. 19 (3) (1999) 381-387.

[7] P. Lunkenheimer, R. Fichtl, S.G. Ebbinghaus, A. Loidl, Nonintrinsic origin of the colossal dielectric constants in $CaCu_3Ti_4O_{12}$, Phys. Rev. B: Condens. Matter 70 (17) (2004) 172102

[8] V.T. Truong, S.Z. Riddell, R.F. Muscat, Polypyrrole Based Microwave Absorbers, J. Mater. Sci. 33 (20) (1998) 4971-4976.

[9] C.C. Wang, H.B. Lu, K.J. Jin, G.Z. Yang, Temperature-dependent dielectric strength of a maxwell wagner type relaxation, Mod. Phys. Lett. B 22 (13) (2008) 1297-1305.

[10] J. Liu, C.-G. Duan, W.-G. Yin, W.N. Mei, R.W. Smith, J.R. Hardy, Large dielectric constant and Maxwell-Wagner relaxation in $Bi_{2/3}Cu_3Ti_4O_{12}$, Phys. Rev. B: Condens. Matter 70 (14) (2004) 144106.

[11] T.-T. Fang, H.-K. Shiau, Mechanism for Developing the Boundary Barrier Layers of $CaCu_3Ti_4O_{12}$, J. Am. Ceram. Soc. 87 (11) (2004) 2072-2079.

[12] I. Ahmad, M.J. Akhtar, M. Younas, M. Siddique, M.M. Hasan, Small polaronic hole hopping mechanism and Maxwell-Wagner relaxation in $NdFeO_3$, J. Appl. Phys. 112 (7) (2012) 074105-074107.

[13] K.S. Cole, R.H. Cole, Dispersion and Absorption in Dielectrics I. Alternating Current Characteristics, J. Chem. Phys. 9 (4) (1941) 341-351.

[14] G. Georgoussis, A. Kanapitsas, P. Pissis, Y.V. Savelyev, V.Y. Veselov, E.G. Privalko, Structure-property relationships in segmented polyurethanes with metal chelates in the main chain, Eur. Polym. J. 36 (2000) 1113 -1126.

[15] P. Cheng, S. Li, L. Zhang, J. Li, Characterization of intrinsic donor defects in ZnO ceramics by dielectric spectroscopy, Appl. Phys. Lett. 93 (1) (2008) 012902-012903.

[16] P.R. Bueno, M.A. Ramirez, J.A. Varela, E. Longo, Dielectric spectroscopy analysis of $CaCu_3Ti_4O_{12}$ polycrystalline systems, Appl. Phys. Lett. 89 (19) (2006) 191117-191113.

[17] M.H.R. Lankhorst, H.J.M. Bouwmeester, H. Verweij, Thermodynamics and Transport of Ionic and Electronic Defects in Crystalline Oxides, J. Am. Ceram. Soc. 80 (9) (1997) 2175-2198.

[18] C. Elissalde, J. Ravez, Ferroelectric ceramics: defects and dielectric relaxations, J. Mater. Chem. 11 (8) (2001) 1957-1967.

[19] O. Bidault, P. Goux, M. Kchikech, M. Belkaoumi, M. Maglione, Space-charge relaxation in perovskites, Phys. Rev. B: Condens. Matter 49 (12) (1994) 7868-7873.

[20] Z. Wang, X.M. Chen, L. Ni, X.Q. Liu, Dielectric abnormities of complex perovskite $Ba(Fe_{1/2}Nb_{1/2})O_3$ ceramics over broad temperature and frequency range, Appl. Phys. Lett. 90 (2) (2007) 022904-022903.

[21] C. Ang, Z. Yu, Oxygen-vacancy-related low-frequency dielectric relaxation and electrical conduction in Bi : $SrTiO_3$, Phys. Rev. B: Condens. Matter 62 (1) (2000) 228-236.

[22] M. Ganguly, S. Parida, E. Sinha, S.K. Rout, A.K. Simanshu, A. Hussain, I.W. Kim, Structural, dielectric and electrical properties of $BaFe_{0.5}Nb_{0.5}O_3$ ceramic prepared by solid-state reaction technique, Mater. Chem. Phys. 131 (1-2) (2011) 535-539.

[23] M. Maglione, Polarons, free charge localisation and effective dielectric permittivity in oxides, in: arXiv e-prints : 1006.3719, 2010, pp. 3719.

[24] A.K. Jonscher, Dielectric Relaxation in Solids, Chelsea Dielectrics Press Limited, London 1983.

[25] A.K. Jonscher, The 'universal' dielectric response, Nature 267 (5613) (1977) 673-679.

[26] A. Mandanici, M. Cutroni, C. Cramer, K. Funke, P. Mustarelli, C. Tomasi, Microwave dielectric spectroscopy and dynamical processes in superionic glasses, in: AIP Conf. Proc., Vol. 513, Aip, 2000, pp. 150-153.

[27] N. Ortega, A. Kumar, P. Bhattacharya, S.B. Majumder, R.S. Katiyar, Impedance spectroscopy of multiferroic $PbZr_xTi_{1-x}O_3$ / $CoFe_2O_4$ layered thin films, Physical review B 77 (1) (2008) 014111.

[28] M.M. Kumar, Z.G. Ye, Dielectric and electric properties of donor- and acceptor-doped ferroelectric $SrBi_2Ta_2O_9$, J. Appl. Phys. 90 (2) (2001) 934-941.

[29] S.A. Long, R.N. Blumenthal, Ti-Rich Nonstoichiometric $BaTiO_3$: II, Analysis of Defect Structure, J. Am. Ceram. Soc. 54 (11) (1971) 577-583.

[30] N.A. Sabu, Priyanka, K. P., S. Thankachan, A.T. Sunny, E.M. Mohammed, O.P. Jaseentha, T. Varghese, Dielectric Studies Of Nanocrystalline Manganese Tungstate, Nanosystems: Physics, Chemistry, Mathematics 4 (3) (2013) 357–362.

[31] V. SHARMA, R. SAMKARIA, Structural And Dielectric Properties of $MgAl_{2-2x}Y_{2x}O_4$ Nanoparticles, in: International Conference on Ceramics, Vol. 22, World Scientific Publishing Company, Bikaner, India, 2013, pp. 361-364.

[32] S.-J. Lee, K.-Y. Kang, S.-K. Han, Low-frequency dielectric relaxation of BaTiO3 thin-film capacitors, Appl. Phys. Lett. 75 (12) (1999) 1784-1786.

[33] L. Zhang, Electrode and grain-boundary effects on the conductivity of CaCu3Ti4O12, Appl. Phys. Lett. 87 (2) (2005) 022907.

[34] J.T.S. Irvine, D.C. Sinclair, A.R. West, Electroceramics: Characterization by Impedance Spectroscopy, Adv. Mater. (Weinheim, Ger.) 2 (3) (1990) 132-138.

[35] J. Xu, M. Itoh, Unusual Dielectric Relaxation in Lightly Doped n-Type Rhombohedral BaTi0.85Zr0.15O3:Ta Ferroelectric Ceramics, in: arXiv:cond-mat/0503248, 2005.

[36] Electrochemical Impedance Spectroscopy, in. http://www.lucasbard.com/eis101/07_multipleC.html

[37] L. Zheng, C. Lin, H. Xu, S. Zou, O. Masanori, Leakage behavior and distortion of the hysteresis loop in ferroelectric thin films, Science in China Series E: Technological Sciences 40 (2) (1997) 126-134.

[38] A. Gronotte, Development of new chemical processes to lead-free piezoelectric and ferroelectric materials, in: Department of Chemistry, Vol. Master of Science, Simon Fraser University, 2009.

[39] M. Stewart, M.G. Cain, D.A. Hall, Ferroelectric Hysteresis Measurement and Analysis, in: Technical Report CMMT (A) 152, National Physical Laboratory, Teddington UK, 1999.

[40] P. Manimuthu, C. Venkateswaran, Evidence of ferroelectricity in $SrFeO_{3-d}$, J. Phys. D: Appl. Phys. 45 (1) (2012) 015303.

CHAPTER 5

Structural, Morphological, Optical and Electrical Studies of La^{3+} and Pb^{2+} Modified BFN Ceramics

5.1 Introduction

Aliovalent (La^{3+}) and isovalent (Pb^{2+}) ions are substituted at the A-site (in the ABO_3 structure) of the BFN ceramics. La^{3+} ion dopants are used for stabilizing the temperature as well as shifting the Curie temperature (T_c) in ferroelectric materials towards lower temperature side [1]. Whereas, lead (Pb^{2+}) ion dopants are used for increasing the dielectric properties and decreasing the processing temperatures of the BFN based ceramics. In the present work, $Ba_{1-x}La_{2x/3}(FeNb)_{0.5}O_3$ /BLFN (x= 0, 0.02, 0.04, 0.06, 0.08), and $Ba_{1-x}Pb_x(FeNb)_{0.5}O_3$/PBFN (x= 0, 0.02, 0.04, 0.06, 0.08) ceramic systems are synthesized by solid state reaction route and studied for their structural, microstructural, dielectric and optical properties.

5.2 XRD Analysis

The X-ray diffraction study of the calcined and sintered BLFN and PBFN (x= 0, 0.02, 0.04, 0.06, 0.08) ceramics are carried out.

5.2.1 XRD Analysis of the La-modified BLFN Ceramics

Fig. 5.1 shows the XRD patterns of the calcined and the inset figure shows the XRD patterns of the sintered BLFN (x= 0, 0.02, 0.04, 0.06, 0.08) ceramics. Developments and retention of single perovskite phase is confirmed by the XRD patterns of the calcined and sintered BLFN samples, respectively. Cubic structure is observed for all the BLFN ceramic samples and the corresponding lattice parameters are given in Table 5.1. There is no change in the crystal structure with the different doping concentrations of La_2O_3 into the BFN ceramics.

But, the lattice parameter and the unit cell volume of the BLFN ceramics slightly decreased as compared to the parent BFN ceramics. This may related to the fact that the radii of the Ba^{2+} (0.161 nm) ions is larger than the substituted La^{3+} (0.136 nm) ions in Ba-site of the Ba(FeNb)$_{0.5}$O$_3$ ceramics. The tolerance factor of the BLFN ceramics are ~1.0407, 1.0359, 1.0310, 1.0261 and 1.0213 for x=0, 2, 4, 6 and 8%, respectively. The value of tolerance factor tends towards "1" with the increase of La content in the BLFN ceramics. Tolerance factor 1 corresponds to cubic structure and which justifies the observed experimental structure analysis.

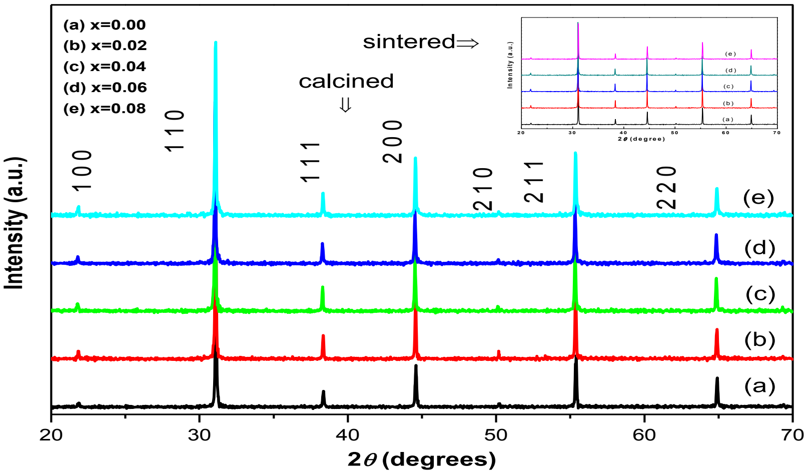

Fig. 5.1: XRD patterns of Ba$_{1-x}$La$_{2x/3}$(FeNb)$_{0.5}$O$_3$ ceramics with x=0 (a), 2 (b), 4 (c), 6 (d) & 8 % (e) calcined at 1250°C for 4h. The inset figure shows the XRD patterns of sintered ceramics.

Table 5.1: Lattice parameters of the BLFN ceramics.

Samples	**BFN**	**BLFN2**	**BLFN4**	**BLFN6**	**BLFN8**
Lattice parameter(Å)	a=b=c=4.0604 α=β=γ=90°	a=b=c= 4.0520 α=β=γ=90°	a=b=c= 4.0541 α=β=γ=90°	a=b=c= 4.0538 α=β=γ=90°	a=b=c= 4.0515 α=β=γ=90°
Volume (Å^3)	66.94	66.52	66.63	66.61	66.50

5.2.2 XRD Analysis of the PBFN Ceramics

Fig. 5.2: shows the XRD patterns of the calcined and the inset figure shows the XRD patterns of the sintered PBFN (x= 0, 0.02, 0.04, 0.06, 0.08) ceramics. There is no indication of the presence of any secondary phase peaks in both the calcined and sintered ceramics. This shows that there is a complete replacement of the Ba^{2+} ions with the Pb^{2+} ions. The XRD peaks were indexed in different crystal systems and the lattice parameters were calculated by considering the best agreement between observed (obs) and calculated (cal) interplanar spacing d (i.e. $\Sigma\Delta d = \Sigma\ (d_{obs} - d_{cal})$) as minimum by using a standard computer program (POWD) and are given in Table 5.2. Here also, all the samples show cubic structure like the parent BFN ceramics. The tolerance factor of Pb doped BFN perovskite ceramics is calculated as ~1.0407, 1.0399, 1.0391, 1.0382 and 1.0374 for x=0, 2, 4, 6 and 8%, respectively.

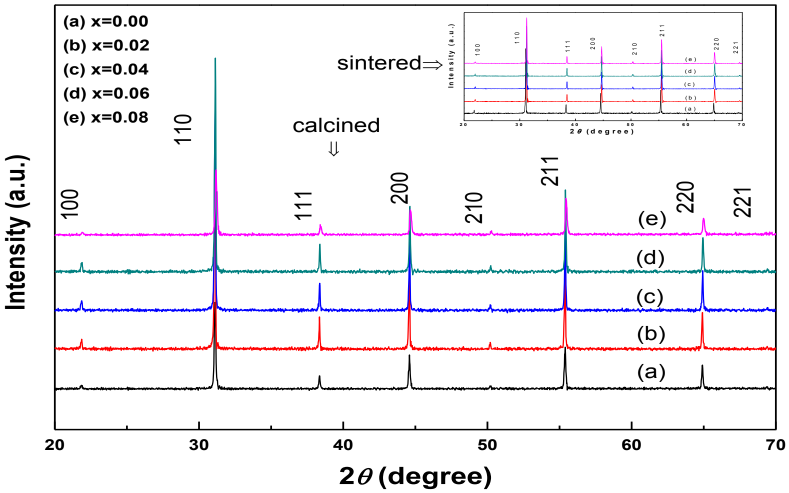

Fig. 5.2: XRD patterns of the $Ba_{1-x}Pb_x(FeNb)_{0.5}O_3$ ceramics with x=0 (a), 2 (b), 4 (c), 6 (d) & 8 % (e) calcined at 1200°C for 4h. The inset figure shows the XRD patterns of the sintered ceramics.

Table 5.2 Lattice parameters of PBFN ceramics.

Samples	**BFN**	**PBFN2**	**PBFN4**	**PBFN6**	**PBFN8**
Lattice parameter(Å)	a=b=c=4.0604 α=β=γ=90°	a=b=c= 4.0611 α=β=γ=90°	a=b=c= 4.0600 α=β=γ=90°	a=b=c= 4.0587 α=β=γ=90°	a=b=c= 4.0557 α=β=γ=90°
Volume (Å ^{3})	66.94	66.98	66.92	66.86	66.71

5.3 Density and Morphological Study

5.3.1 Density and Morphological Study of BLFN Ceramics

Fig. 5.3 shows the SEM micrographs of the sintered BLFN ceramics. All the sintered BLFN ceramics show dense and almost non-uniform microstructures. Distribution of grains of BLFN ceramics is more uniform than the parent BFN ceramics. The abnormality in the grain growth decreases with the increase in La content in the BLFN ceramics. Decrease in grain size with the increase of La doping concentration in the BLFN ceramic samples suggets that La acts as grain growth inhibitors in the BLFN ceramics [2, 3].

The experimental densities and average grain size of all the BLFN ceramics are given in the Table 5.3. Highest value of the exprimental density is observed for the 8% La doped BLFN ceramics. The density of all the BLFN ceramic samples is higher than the parent BFN ceramics. This can be explained on the basis of ionic diffusion rate. The ionic radii of Ba^{2+} and La^{3+} are 0.161 and 0.136 nm, respectively [4], which indicates that the smaller ionic radius of La^{3+} enhances the diffusion rate [5] and may enhances the density. The sintering temperature of La modified ceramics are lower (1250°C) than that of the parent (1350°C) BFN system. The reduction in sintering temperature with La was attributed to the liquid phase effect. Similar type of result is observed in other La doped ceramics [6].

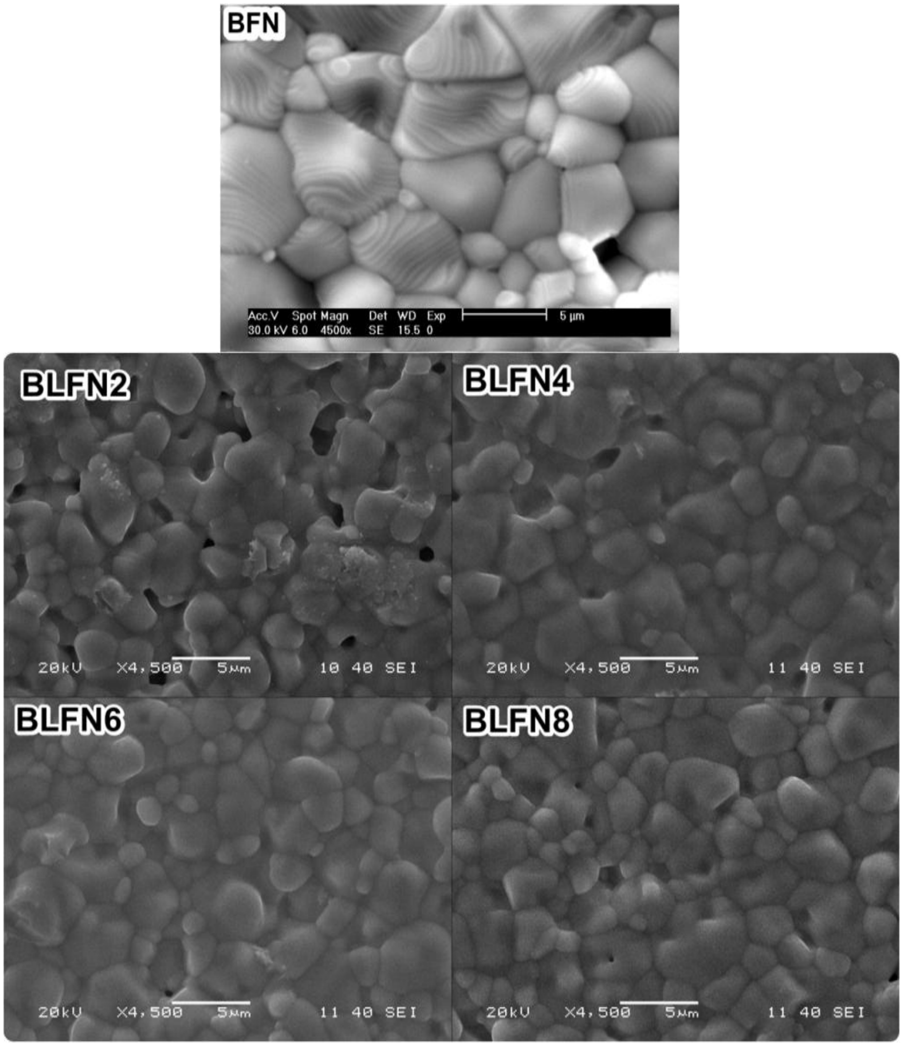

Fig. 5.3: SEM micrographs of BLFN ceramics.

Table 5.3: Density and grain size parameters of BLFN ceramics.

Samples	**BFN**	**BLFN2**	**BLFN4**	**BLFN6**	**BLFN8**
Avg. Grain size(µm)	6.32	3.41	3.13	2.51	2.42
Density(g/cc)	5.97	5.94	6.01	5.99	6.08

5.3.2 Density and Morphological Study of the PBFN Ceramics

Fig. 5.4 shows the SEM micrographs of the sintered $Ba_{1-x}Pb_x(FeNb)_{0.5}O_3$ (x= 0, 0.02, 0.04, 0.06, 0.08) ceramics. With the increase of the Pb content in the PBFN ceramics, the spherical nature of the grains increases. Moreover, the distribution of the grains is non-uniform. The decrease of grain size in the PBFN ceramics suggests formation of liquid phase which can inhibit the grain growth [7]. The values of the average grain size and the experimental densities are given in Table 5.4. The density of the PBFN ceramic samples is higher than that of the parent BFN ceramics, which indicates that the smaller ionic radius of Pb^{2+} (0.149 nm) compared to Ba^{2+} (0.161 nm) enhanced the diffusion coefficient [5].

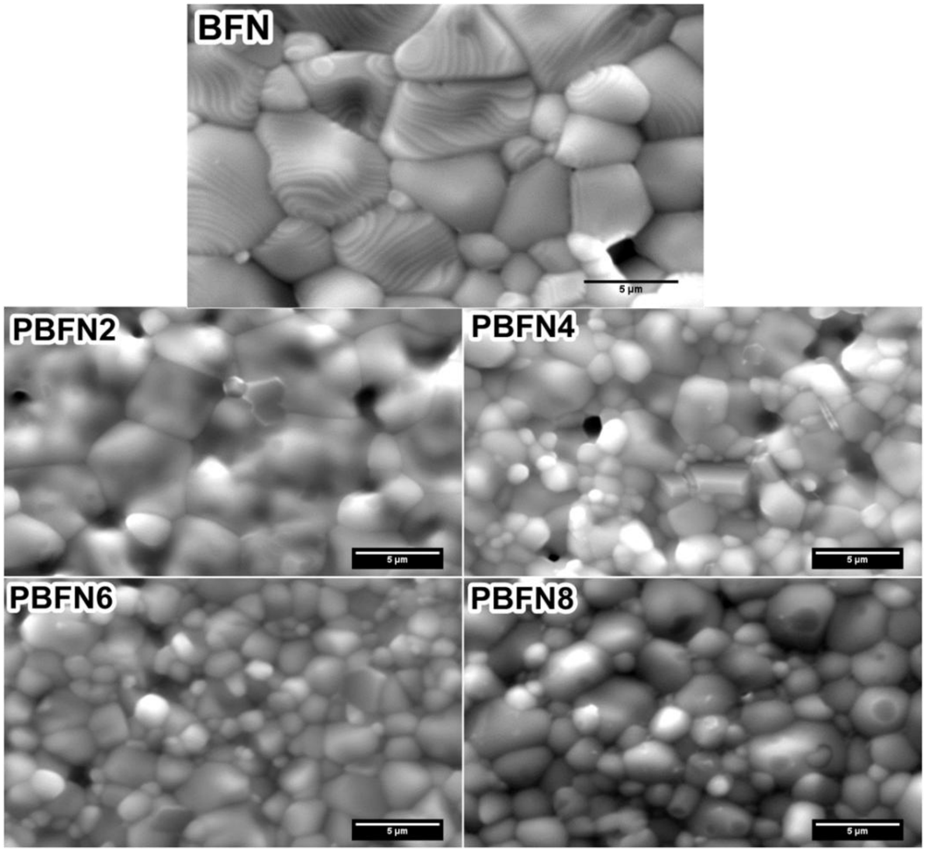

Fig. 5.4: SEM micrographs of PBFN ceramics

Table 5.4: Density and grain size parameters of PBFN ceramics.

Samples	BFN	PBFN2	PBFN4	PBFN6	PBFN8
Avg. Grain size(μm)	6.32	4.56	2.52	2.28	3.18
Density(g/cc)	5.97	6.16	6.12	6.19	6.29

5.4 Dielectric Analysis

5.4.1 RT Frequency Dependent Dielectric Properties of BLFN Ceramics

Figs. 5.5 (a) & (b) show the room temperature frequency dependence of the real (ε') and imaginary (ε'') parts of the permittivity of all the BLFN ceramics. The frequency variation of ε' exhibits a plateau region followed by a dispersive region. Whereas, with the increase in the content of La in the BLFN ceramics, the ε' exhibit a frequency dispersive nature instead of a plateau region. Further at higher frequencies all curves merges together. Corresponding to the dispersive kink in the ε' plot, a relaxation peak is observed in the loss spectrum (Fig. 5.5(b)). Such type of behaviour is a characteristic of dipolar materials. Generally space charge polarisation in a dielectric material is present upto 100 kHz frequency [8]. La enriched samples exhibits two dispersion in the ε' plot, one around 10^3 Hz and the other one at 10^5 Hz. A large fall of the order of $\sim 10^2$ in ε' is observed at 10^6 Hz frequency compared to 10^2 Hz. This may be due to the space charges fails to respond at high frequencies (1 MHz), which suggest that the high frequency dielectric constant arises due to grain or lattice effect [8]. At RT, the highest value of ε' (~9, 49,000 at 100 Hz) is observed for La (8%) doped BLFN ceramics.

The dielectric loss (ε'') spectrum significantly changes with the increase in La content in the BLFN ceramics. The dielectric loss is a combination of both pure dielectric relaxation and dc conduction processes [9, 10]. A the low frequency tail region in the ε” plot is dominated by dc conductivity. Thermally activated motion of defects or vacancies contributes to the overall dielectric relaxation at higher temperatures [11]. In the BLFN based ceramics thermally activated dielectric relaxation is noticeable even at room temperature [12]. In the present study, the dc conductivity and the ac relaxation processes (space charge or interfacial polarisation) convolved together and the nature of the spectrum broadened at room temperature. The low frequency relaxation and the diffuseness in the loss spectrum can be explained on the basis of La content in the BLFN ceramics. Effective number of charge carriers increases by different compensation mechanism with the increase in La content in the BLFN ceramics [13]. These charge carriers plays important role in dielectric relaxation as well as conduction processes. The space charge polarisation is considered to explain the high dielectric constant in the BLFN ceramics [12, 14].

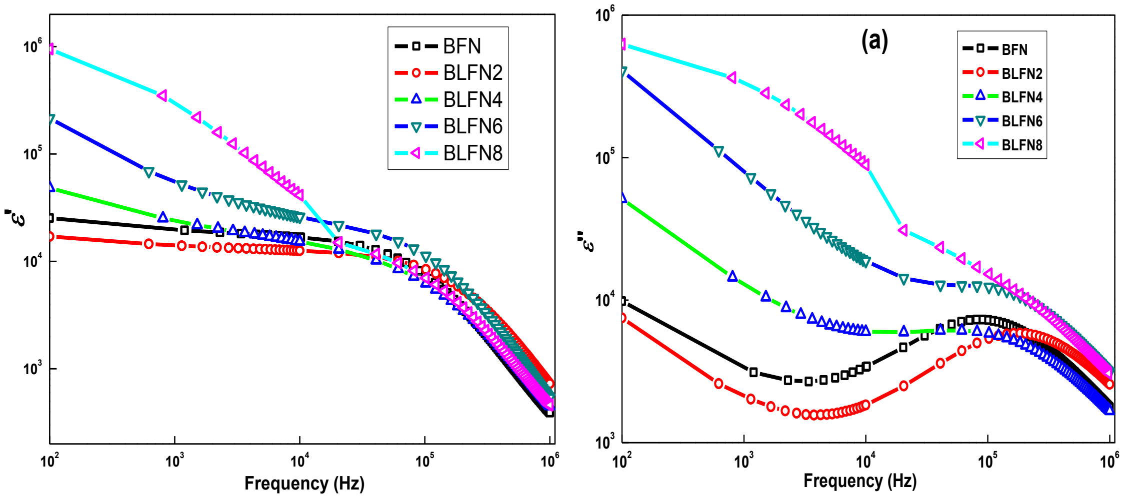

Fig. 5.5: Room temperature frequency variation of (a) dielectric constant and (b) dielectric loss of the BLFN ceramics.

5.4.2 RT Frequency Dependent Dielectric Properties of PBFN Ceramics

The frequency variation of dielectric constant and dielectric loss of the PBFN ceramics at room temperature are shown in Figs. 5.6 (a) and (b). The observed nature is similar to that of pure BFN and La doped BLFN ceramics. The dispersive nature of ε' at higher frequencies is accompanied with a corresponding peak in the loss spectrum. The large difference in dielectric constant at lower frequency (100 Hz) and higher frequency (1 MHz) confirms that more than one type of polarization processes contribute to the overall dielectric constant. For all the PBFN ceramics, the dielectric constant value decreased to a value ~10^2 at 1 MHz from ~10^5 at 100 Hz frequency.

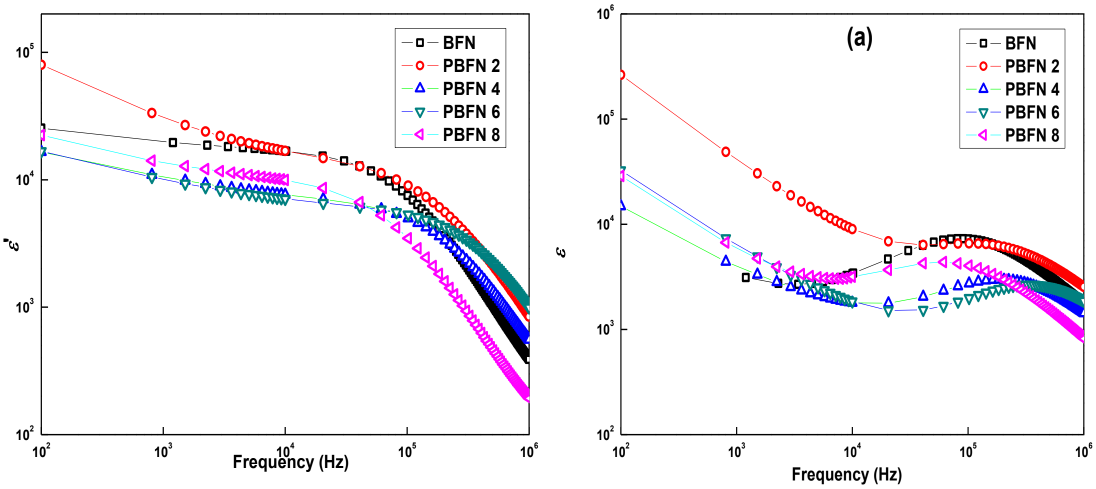

Fig. 5.6: Room temperature frequency variation of (a) dielectric constant and (b) dielectric loss of the PBFN ceramics.

5.4.3. Temperature Dependent Dielectric Properties of BLFN Ceramics

Figs. 5.7 (a) and (b) show the variation of dielectric constant and dielectric loss with temperature at 10 kHz frequency of all the BLFN ceramics. The dielectric constant increases with the increase in temperature and also with the increase in La content in the BLFN ceramics. La acts as a donor and generates different types of point defects in the BLFN ceramics. In order to make the system neutral, different types of charge compensation mechanism such as electronic, A-site and B-site cations vacancies, oxygen vacancies or self-compensation mechanisms may generate and can change the stoichiometry of the BLFN ceramics. In turn these charge compensation mechanisms may contribute for the large polarization and high dielectric constant in the BLFN ceramics [13, 15-17]. The highest value of dielectric constant is observed for 8% La content in the BLFN ceramics and the values of dielectric properties for all the BLFN samples are given in Table 5.3.

Two types of compensation mechanisms are proposed for incorporation of La in the BFN ceramics such as A-site vacancies and electronic compensation mechanisms. Electronic charge compensation mechanisms, which may develop in the BLFN ceramics is given in eqns.1 and 2.

$$BaO + La_2O_3 \rightarrow Ba_{Ba}^{\times} + 2La_{Ba}^{\bullet} + V_{Ba}^{''} + 4O_O^{\times} \qquad (5.1)$$

$$2BaO + La_2O_3 \rightarrow 2Ba_{Ba}^{\times} + 2La_{Ba}^{\bullet} + 4O_O^{\times} + \frac{1}{2}O_2 + 2e' \qquad (5.2)$$

A small amount of oxygen loss during synthesis process may make these samples semiconducting by releasing electrons as follows

$$O_O^X \rightarrow \frac{1}{2}O_2 + V_O^{\bullet} + e' \qquad (5.3)$$

,

$$O_O^X \rightarrow \frac{1}{2}O_2 + V_O^{\bullet\bullet} + 2e' \qquad (5.4)$$

These released electrons from different types of compensation mechanisms can be trapped by the iron or niobium ions in the BLFN ceramics as follows:

$$Fe^{3+} + e^{'} \leftrightarrow Fe^{2+} \qquad (5.5)$$

$$Nb^{5+} + e^{'} \leftrightarrow Nb^{4+} \qquad (5.6)$$

The electronic charge compensation can be considered in the BLFN ceramics due to their high temperature synthesis. During high temperature synthesis, oxygen loss from the bulk ceramics can make the grains semiconducting and subsequent cooling after sintering, re-oxidation occurs along grain boundaries, which can make it insulating [18]. The absorbed oxygen along grain boundaries behave as electron traps or acceptors and also attract electrons from the n-type semiconducting grains and forms depletion layer at the boundaries[18]. Resultant electrons are easily captured by the Fe^{3+} and Nb^{5+} ions as shown in eqns. 4 & 5, respectively, which lead to increase of polarization and hence increase in dielectric constant in the BLFN ceramics.

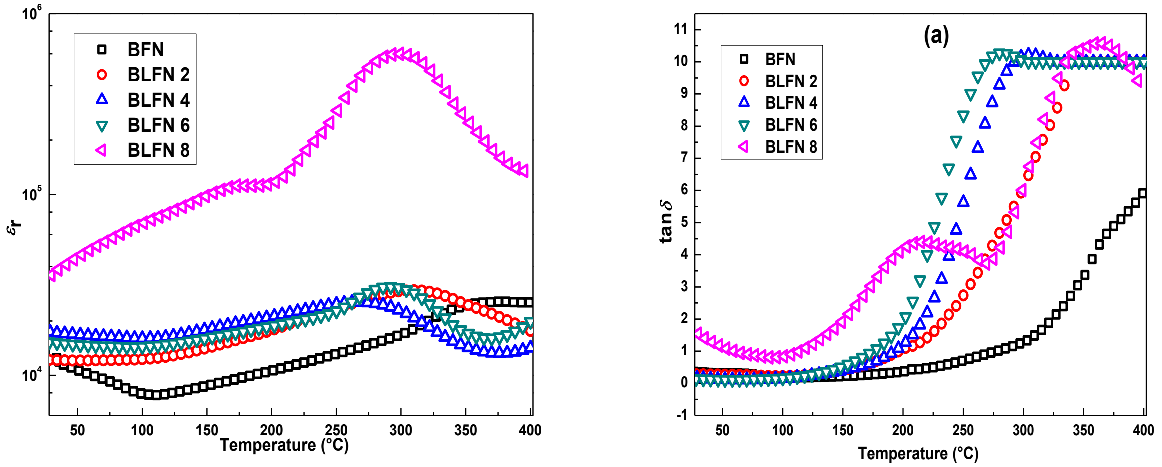

Fig. 5.7 Temperature variation of (a) dielectric constant and (b) dielectric loss at 10 kHz frequency of the BLFN ceramics.

Table 5.5 Dielectric parameters of BLFN ceramics.

Samples	**BFN**	**BLFN2**	**BLFN4**	**BLFN6**	**BLFN8**
ε_r (10 kHz)	11569	12146	17265	15220	35844
tanδ (10 kHz)	0.329	0.293	0.162	0.138	1.492

5.4.3.1 Dielectric Relaxation Mechanisms (Origin of HDC in BLFN Ceramics)

Both intrinsic as well as the extrinsic factors are used to explain the cause of HDC in the BLFN ceramics. It is a well-established fact that unlike in ferroelectric materials, the HDC materials shows space charge or microscopic Maxwell-Wagner interfacial polarization effect at RT under an applied ac field [12]. HDC materials have inner surface of grains which have enough number of trapping states or localized states, which can attract the electrons from the semiconducting grains. These inner surfaces of the grains can behave as electrodes and the thin grain boundary layers can behave as insulator for the boundary layer capacitor under the applied ac field, which ultimately enhances the dielectric constant with the increase in temperature, space charges are depleted at the grain boundaries and there can appear macroscopic Maxwell-Wagner type interfacial polarization. This accounts the increase of dielectric constant with the increase in temperature in the BLFN ceramics. It can be seen that peaks in dielectric plots near 300°C is observed for all the BLFN ceramics. Such type of dielectric relaxation can be explained on the basis of the dipolar nature induced by defects.

5.4.4 Temperature Dependent Dielectric Properties of PBFN Ceramics

The temperature variation of dielectric constant and dielectric loss at 10 kHz frequency of the Pb doped PBFN ceramic is shown in Figs. 5.8 (a) and (b). As shown, the dielectric constant of all the Pb modified PBFN ceramics are higher than compared to parent BFN ceramics. Maximum value of dielectric constant is observed in 8% of Pb doped PBFN ceramics. ε_r value of 2 % doped PBFN ceramic is higher than that of 4 and 6 % doped PBFN ceramics. This may be due to the fact that for smaller doping concentration (2%) of Pb, due to PB loss the stoichiometry will be more disturbed and the defects will be more whereas for doping concentration of Pb, BPFN ceramic can maintain stoichiometry with optimal characteristics [19]. Again ε_r increases with the increase in temperature for all the PBFN compositions and is higher than the parent PBFN ceramics. Corresponding dielectric loss values of PBFN ceramics is higher than that of parent BFN ceramics (Fig. 5.8(b)). The values of dielectric properties of all the PBFN ceramics at RT are given in Table 5.6.

It is reported that oxygen vacancies plays important role in the dielectric relaxation in most of perovskite ceramics. In PbO contained ceramics, lead loss is inevitable or difficult to control during high temperature processing. In the defect equilibrium reaction, Pb vacancy is compensated by V_o, since both of these forms a neutral complex (V''_{Pb}-V''_O), as shown in the following equation.

$$Pb_{Pb}^{X} + O_{O}^{X} \leftrightarrow PbO(g) + V_{Pb}^{''} + V_{O}^{\bullet\bullet} \qquad (5.7)$$

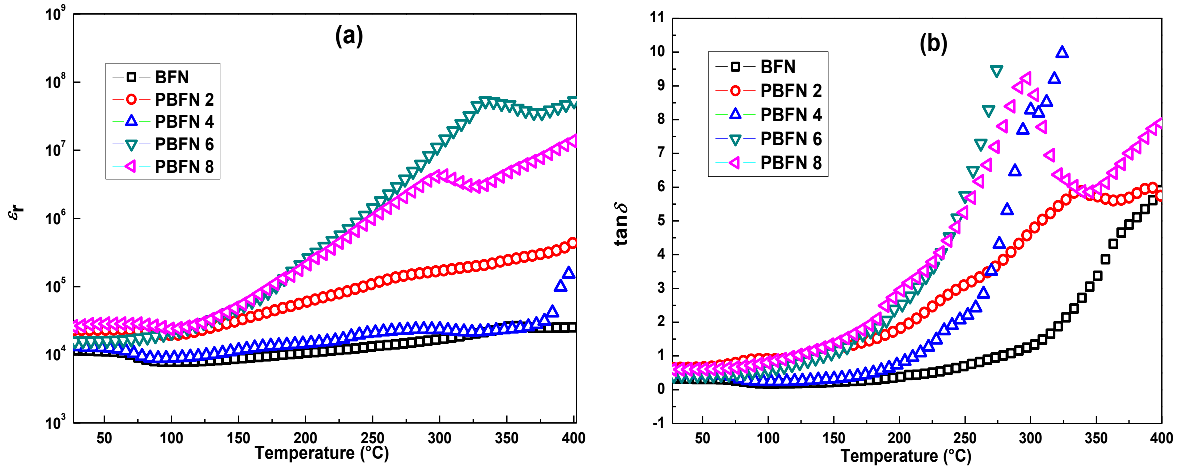

Fig. 5.8 Temperature variation of (a) dielectric constant and (b) dielectric loss at 10 kHz frequency of the PBFN ceramics.

Table 5.6 Dielectric parameters of the PBFN ceramics

Samples	**BFN**	**PBFN2**	**PBFN4**	**PBFN6**	**PBFN8**
ε_r (10 kHz)	11569	22957	13196	15783	25999
tanδ (10 kHz)	0.32	0.64	0.45	0.41	0.59

5.5 Leakage Current and Polarization Studies

5.5.1 Leakage Current and Polarization vs. Voltage Studies of BLFN and PBFN ceramics

It is well known that leakage current (I) in a material mainly depends on three factors such as (i) time period (t), (ii) voltage (V) & (iii) temperature (T). The values of leakage current for both the La and Pb modified BFN ceramics were measured at 50V for 20sec time period. The behavior of I-t in both the La and Pb modified BFN ceramics, respectively is same as that of parent BFN ceramics, i.e. there is no large change in the value of the current over the observed time period. However, there is a change in the values of leakage current with La and Pb- modifications in the BFN ceramics and these values are listed in Table 5.7

Table 5.7 Leakage current values of the La and Pb- modified (with x=0, 2, 4, 6 & 8 %) BFN ceramics

Samples	0%	2%	4%	6%	8%
Leakage current(A) in BLFN	1.29×10^{-6}	1.16×10^{-6}	7.71×10^{-7}	7.16×10^{-6}	1.28×10^{-6}
Leakage current(A) in PBFN		1.00×10^{-6}	9.87×10^{-7}	1.64×10^{-6}	3.01×10^{-6}

As the observed leakage current values are of the order of ~10^{-6} to 10^{-7}A, which is very high for a dielectric material. The ferroelectric/non-ferroelectric nature of the BLFN and PBFN ceramics was ascertained by the polarization vs. voltage loops measurements and shown in Figs. 5.9(a) and (b). The behaviour of polarization with small applied voltage of 5V and 10 V, respectively for La and Pb modified BFN ceramics shows no saturations in their loops and confirms high leakage current behavior [20, 21] contributes to the observed loop, which is of non-ferroelectric nature.

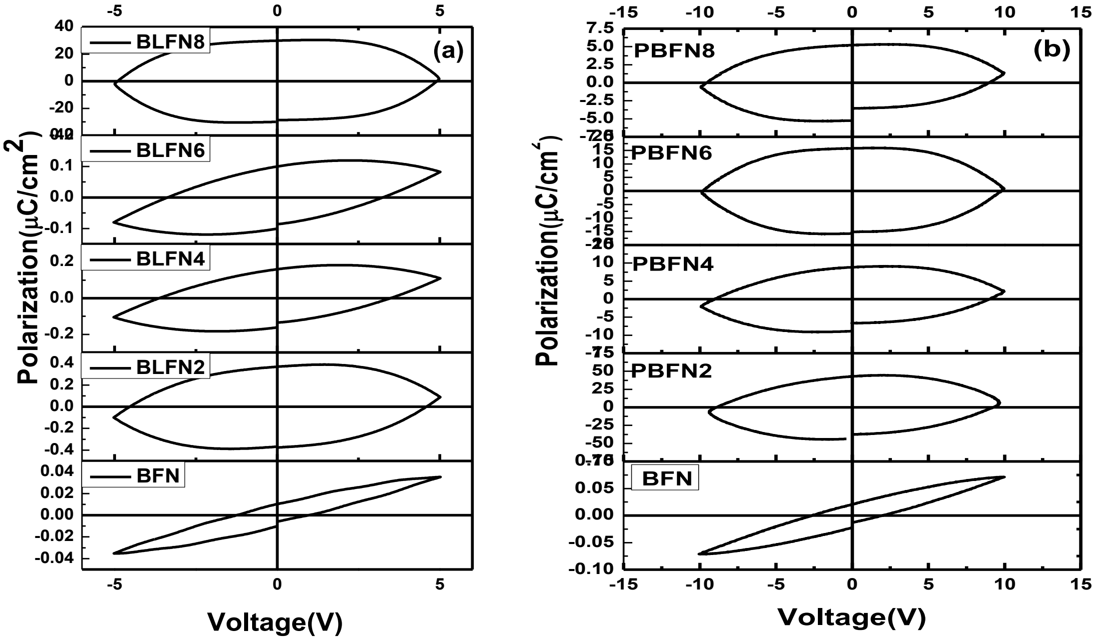

Fig. 5.9 RT variation of polarization with applied voltage of (a) BLFN and (b) PBFN ceramics.

5.6 Optical Properties Study

5.6.1 UV-Vis Optical Properties Study of the BLFN Ceramics

Fig. 5.10 (a) shows the optical diffuse absorbance spectra of all the La-doped BLFN ceramics in the UV–Vis region. A broad diffuse absorption band within the 200-910 nm wavelength range is observed in all the BLFN ceramics. The spectra of the all the BLFN ceramics exhibit three broad bands, centered at ~264, 480 and 890 nm wavelengths, respectively. The absorption band decreases with the increase in La concentration in the BLFN ceramics. The band gap absorption edge of the La-doped BLFN (x=0 to 8%) ceramics is determined to be ~985 nm. The band gap for all ceramics are calculated by using the Kubelka–Munk (KM) function [22], as discussed in Chapter 2. Fig. 5.10 (b) shows the optical band gaps (E_g) of the BLFN ceramics. The 'E_g' for all the BLFN ceramics is found to be ~1.3 eV. Here, no significant change in the band gap is observed with the variation of the La doping concentration in the BLFN ceramics. However, the observed low optical band gap is comparable to the other ceramic and polymer compounds [23]. The smaller band gap of the BLFN ceramics indicates a possibility of utilizing these materials for photo-catalysis process in the solar cells applications. Since, low band gap and wide UV-Vis absorption spectra are required for a material to be used in the photo-catalytic applications.

The observed low optical band gap in the BLFN ceramics again suggests the semiconducting nature of these ceramics. Oxygen vacancies, which contribute in the dielectric relaxation process in the BLFN ceramics, may be associated with the lowering of the optical band gap[24]. It is reported that the vacancy enriched materials can possess a band of electronic states just below the conduction band gap [24]. These mini band gaps, corresponding to the oxygen vacancies, can lie just below the conduction band minimum and hence responsible for lowering down the band gap in the BLFN ceramics.

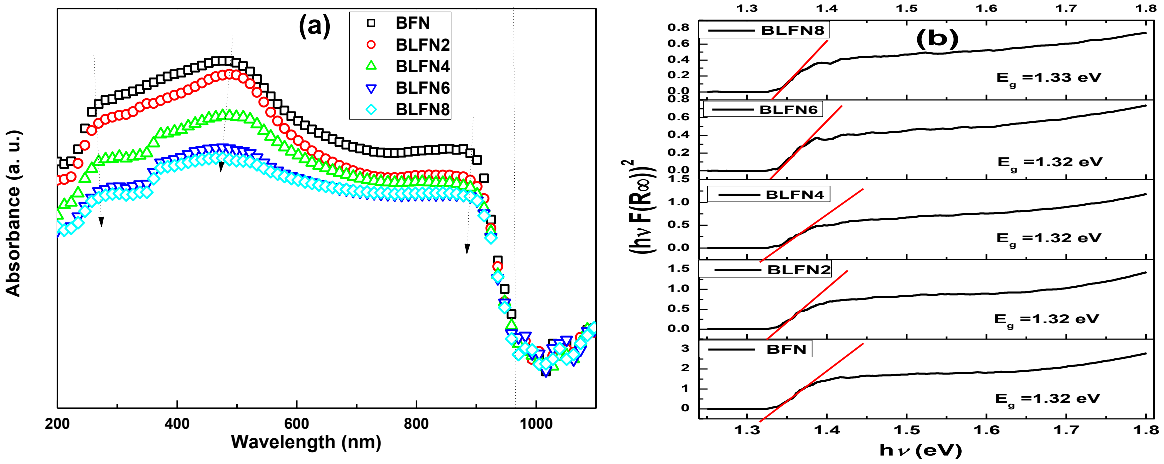

Fig.5.10 (a) UV-Vis diffuse absorbance spectra and (b) estimated band-gap energy of the BLFN ceramics with x=0 to 8%.

5.6.2 UV-Vis Optical Properties Study of the PBFN Ceramics

Fig. 5.11 (a) shows the optical diffuse absorbance spectra of all the Pb-doped PBFN ceramics in the UV–Vis region. Broad diffuse absorption band within the 200-910 nm wavelengths range is observed in all the PBFN ceramics. The spectra of the entire PBFN ceramics exhibit three broad bands, centered at ~260, 480 and 890 nm wavelengths, respectively. The absorption band decreases (except for the 2% Pb doping) with the increase in Pb doping concentration in the PBFN ceramics. The optical band gap is calculated by using the Kubelka–Munk (KM) function.

Fig. 5.11 (b) shows the optical band gap (E_g) of the PBFN ceramics. The ‘E_g’ value is found to be ~1.324,1.324,1.318,1.315 & 1.318eV for 0,2,4,6 & 8 %, respectively of the Pb doping concentration in the PBFN ceramics. There is no significant change in the value of the band gap is observed in the Pb doped PBFN ceramics. However, the observed low optical band gap is comparable to the other ceramic and polymer compounds. The narrow band gap, observed in PBFN ceramics again suggests the semiconducting nature of these ceramics.

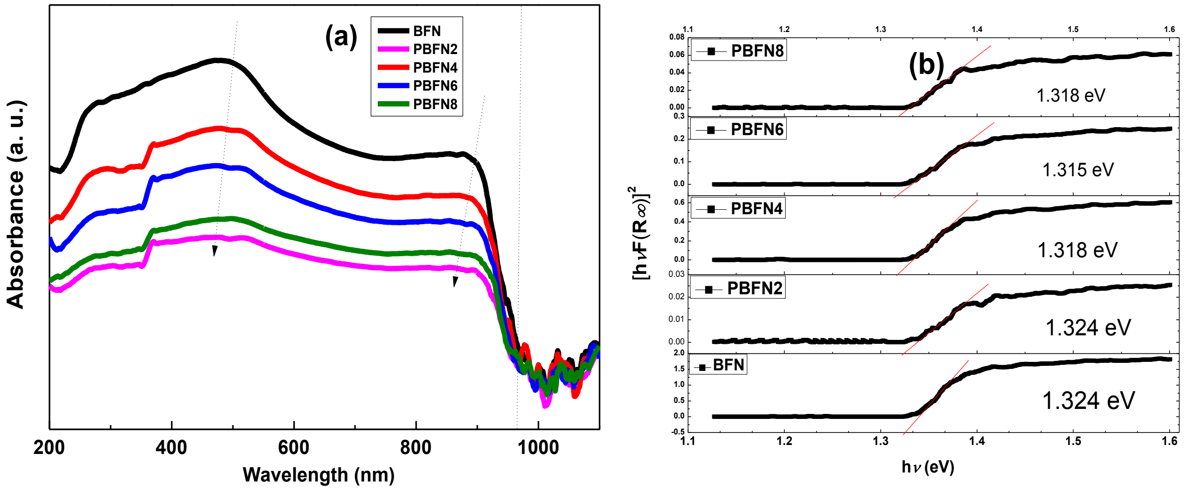

Fig.5.11 (a) UV-Vis diffuse absorbance spectra and (b) estimated band-gap energy of the PBFN ceramics with x=0 to 8%.

5.7 Chapter Summary

La and Pb modified BFN ceramics were synthesized by conventional solid state reaction route . The XRD study confirmed the single phase with cubic structure without any trace of secondary phase. The average grain size decreased with the incorporation of La and Pb in the BFN ceramics and suggested the grain growth inhibitors nature of the dopants. The experimental densities of the La and Pb modified BFN ceramics increased compared to the parent BFN ceramics and the highest experimental densities were obtained for both the 8% La and Pb modified BFN ceramics. Room temperature highest dilectric constant (at 1kHz frequency) ~ 35844 for La and ~ 25999 for Pb modified BFN ceramics were obtained for $x = 0.08$. Polarization with applied voltage showed no saturation in the loops with high leakage in both the BLFN and PBFN ceramics. The narrow optical band gap observed in both the BLFN and PBFN ceramics suggested their semiconducting nature and usefulness for photo-catalytic applications in solar cells.

References

[1] F.D. Morrison, D.C. Sinclair, A.R. West, Electrical and structural characteristics of lanthanum-doped barium titanate ceramics, J. Appl. Phys. 86 (11) (1999) 6355-6366.

[2] A.M. Ruiz, A. Cornet, J.R. Morante, Study of La and Cu influence on the growth inhibition and phase transformation of nano-TiO2 used for gas sensors, Sensors and Actuators B: Chemical 100 (1-2) (2004) 256-260.

[3] M.M. Vijatovic, B.D. Stojanovic, J.D. Bobic, T. Ramoska, P. Bowen, Properties of lanthanum doped BaTiO3 produced from nanopowders, Ceram. Int. 36 (6) (2010) 1817-1824.

[4] R.D. Shannon, Revised effective ionic radii and systematic studies of interatomic distances in halides and chalcogenides, Acta Crystallographica Section A 32 (5) (1976) 751-767.

[5] K. Huang, Statistical Mechanics 2nd edition ed., John Wiley and Sons, New York, 1987, New York, 1987.

[6] R.K. Bhuyan, T.S. Kumar, D. Goswami, A.R. James, D. Pamu, Liquid phase effect of La2O3 and V2O5 on microwave dielectric properties of Mg2TiO4 ceramics, Journal of Electroceramics 31 (1-2) (2013) 48-54.

[7] L. Zhou, A. Zimmermann, Y.-P. Zeng, F. Aldinger, Effects of PbO content on the sintering behavior, microstructure, and properties of La-doped PZST antiferroelectric ceramics, J. Mater. Sci.: Mater. Electron. 15 (3) (2004) 145-151.

[8] V. Shrivastava, A.K. Jha, R.G. Mendiratta, Dielectric studies of La and Pb doped $SrBi_2Nb_2O_9$ ferroelectric ceramic, Mater. Lett. 60 (12) (2006) 1459-1462.

[9] G. Georgoussis, A. Kanapitsas, P. Pissis, Y.V. Savelyev, V.Y. Veselov, E.G. Privalko, Structure-property relationships in segmented polyurethanes with metal chelates in the main chain, Eur. Polym. J. 36 (2000) 1113 -1126.

[10] A.S. Roy, K.R. Anilkumar, M.V.N.A. Prasad, Studies of AC conductivity and dielectric relaxation behavior of CdO-doped nanometric polyaniline, J. Appl. Polym. Sci. 123 (4) (2011) 1928-1934.

[11] T. Wu, Y. Pu, K. Chen, Dielectric relaxation behavior and energy storage properties in $Ba_{0.4}Sr_{0.6}Zr_{0.15}Ti_{0.85}O_3$ ceramics with glass additives, Ceram. Int. 39 (6) (2013) 6787-6793.

[12] M. Maglione, Polarons, free charge localisation and effective dielectric permittivity in oxides, in: arXiv e-prints : 1006.3719, 2010, pp. 3719.

[13] F. Morrison, A. Coats, D. Sinclair, A. West, Charge Compensation Mechanisms in La-Doped BaTiO3, Journal of Electroceramics 6 (3) (2001) 219-232.

[14] S.K. Kar, P. Kumar, Permittivity and modulus spectroscopic study of BaFe0.5Nb0.5O3 ceramics

Processing and Application of Ceramics 7 (4) (2013) 181-187.

[15] A.R. West, T.B. Adams, F.D. Morrison, D.C. Sinclair, Novel high capacitance materials:- BaTiO3:La and CaCu3Ti4O12, J. Eur. Ceram. Soc. 24 (6) (2004) 1439-1448.

[16] N.G. Eror, U. Balachandran, Self-compensation in lanthanum-doped strontium titanate, J. Solid State Chem. 40 (1) (1981) 85-91.

[17] F.D. Morrison, D.C. Sinclair, A.R. West, Doping mechanisms and electrical properties of La-doped BaTiO3 ceramics, International Journal of Inorganic Materials 3 (8) (2001) 1205-1210.

[18] Jun Xu, M. Itoh, Unusual Dielectric Relaxation in Lightly Doped n-Type Rhombohedral BaTi0.85Zr0.15O3:Ta Ferroelectric Ceramics, in: arXiv:cond-mat/0503248, 2005.

[19] A. Megriche, M. Troccaz, Effects of Excess PbO Addition on the Properties of Ferroelectric Doped PZT Ceramics, Mater. Res. Bull. 33 (4) (1998) 569-574.

[20] L. Zheng, C. Lin, H. Xu, S. Zou, O. Masanori, Leakage behavior and distortion of the hysteresis loop in ferroelectric thin films, Science in China Series E: Technological Sciences 40 (2) (1997) 126-134.

[21] A. Gronotte, Development of new chemical processes to lead-free piezoelectric and ferroelectric materials, in: Department of Chemistry, Vol. Master of Science, Simon Fraser University, 2009.

[22] P. Kubelka, F. Munk, Z. Tech. Phys 12 (1931) 593.

[23] L.M. Campos, A. Tontcheva, S. Gunes, G. Sonmez, H. Neugebauer, N.S. Sariciftci, F. Wudl, Extended Photocurrent Spectrum of a Low Band Gap Polymer in a Bulk Heterojunction Solar Cell, Chem. Mater. 17 (16) (2005) 4031-4033.

[24] I. Justicia, P. Ordejón, G. Canto, J.L. Mozos, J. Fraxedas, G.A. Battiston, R. Gerbasi, A. Figueras, Designed Self-Doped Titanium Oxide Thin Films for Efficient Visible-Light Photocatalysis, Adv. Mater. (Weinheim, Ger.) 14 (19) (2002) 1399-1402.

CHAPTER 6

Structural, Morphological and Electrical Studies of Cr and Mn Added BFN Ceramics

6.1 Introduction

Low contents of additives in the perovskite ceramics can act as a sintering aid, reduce dissipation factor, and can enhance dielectric and electrical properties. In this chapter, the structural, morphological, and electrical properties of the Cr_2O_3(0.0, 0.5, 1.0, 1.5 & 2.0 wt %) and $MnCO_3$(0.0, 0.5, 1.0, 1.5 & 2.0 wt %) added BFN ceramics, synthesized by the conventional solid state reaction route, are presented and discussed in detail.

6.2 XRD Analysis

6.2.1 XRD Analysis of the Cr-added BFN Ceramics

Fig. 6.1 shows the XRD patterns of the calcined Cr-modified BFN ceramics. The samples show single perovskite phase upto 1.0 wt% addition, whereas a trace of unidentified phase develops in the 1.5 and 2.0 wt% addition of Cr_2O_3 in the BFN ceramics. This indicates that chromium (ionic radius ~0.062 nm), can go to the B-site (ionic radii of Fe ~0.065 nm and of Nb ~0.064 nm) in the BFN system and form a complete solid solution for ≤ 1.0 wt% addition Cr_2O_3 in the BFN system. Indexing, lattice parameters etc. of the XRD data is carried out by using a standard computer program (POWD) [1]. Lattice parameters are calculated by considering the best agreement between observed (obs) and calculated (cal) interplanar spacing d (i.e. $\Sigma\Delta d = \Sigma\ (d_{obs} - d_{cal})$) as minimum and are tabulated in Table 6.1. All Cr-modified BFN ceramics are found to be having cubic structure.

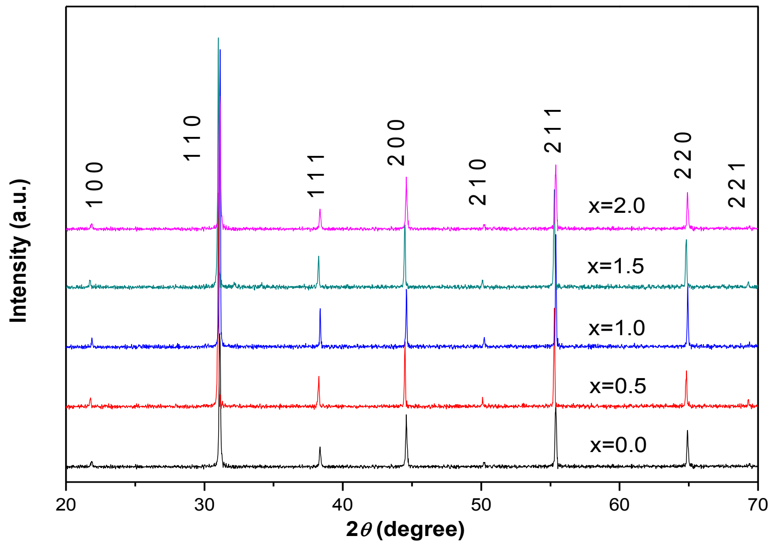

Fig. 6.1: XRD patterns of the Cr added (0.0, 0.5, 1.0, 1.5 & 2.0 wt %) BFN ceramics sintered at 1300°C for 4h.

Table 6.1: Lattice parameters of Cr-added BFN ceramics

Samples	**BFN**	**Cr0.5-BFN**	**Cr1.0-BFN**	**Cr1.5-BFN**	**Cr2.0-BFN**
Lattice parameter(Å)	a=b=c= 4.0604; α=β=γ=90°	a=b=c= 4.0671; α=β=γ=90°	a=b=c=4.0599; α=β=γ=90°	a=b=c=4.0678; α=β=γ=90°	a=b=c= 4.0616; α=β=γ=90°
Volume ($Å^3$)	66.94	67.28	66.92	67.31	67.0

6.2.2 XRD Analysis of the Mn-added BFN Ceramics

Fig. 6.2 shows the retention of single phase in all the calcined Mn-added BFN samples. This indicates that the small amount of Mn is completely dissolved or distributed in the BFN ceramics. The XRD peaks are indexed in different crystal systems and the lattice parameters are calculated by considering the best agreement between observed (obs) and calculated (cal) interplanar spacing d (i.e. $\Sigma\Delta d = \Sigma\ (d_{obs} - d_{cal})$) as minimum by using a standard computer program (POWD) [1] and are tabulated in Table 6.2. All Mn-doped BFN ceramics are having cubic structure.

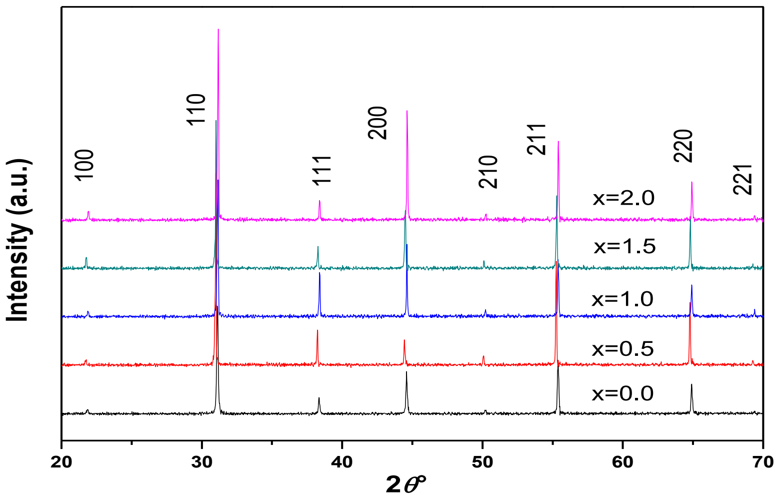

Fig. 6.2: XRD patterns of Mn added (0.0, 0.5, 1.0, 1.5 & 2.0 wt %) BFN ceramics sintered at 1300°C for 4h.

Table 6.2: Lattice parameters of the Mn-added BFN ceramics.

Samples	BFN	Mn0.5-BFN	Mn1.0-BFN	Mn1.5-BFN	Mn2.0-BFN
Lattice parameter(Å)	a=b=c= 4.0604; α=β=γ=90°	a=b=c= 4.0694; α=β=γ=90°	a=b=c=4.0599; α=β=γ=90°	a=b=c=4.0674; α=β=γ=90°	a=b=c= 4.0591; α=β=γ=90°
Volume (Å^3)	66.94	67.39	66.92	67.29	67.29

6.3 Density and Morphological Study

6.3.1 Density and Morphological Study of the Cr-added BFN Ceramics

Fig. 6.3 shows the SEM micrographs of all the Cr modified BFN ceramics. All sintered ceramics show dense and almost non-uniform microstructures. The grain size of all the Cr-added BFN samples is higher than that of parent BFN ceramics. The abnormality in grain growth decreases with the increase in Cr content in the BFN ceramics (Table 6.3). There is a significant difference in average grain size with increase in Cr concentration. Increase in Cr content in the ceramic probably segregate at grain boundary which might decrease the grain boundary mobility leading to a decrease in the grain size. Similar type results are reported in Cr_2O_3 doped ceramics [2]. It is reported that small content of Cr_2O_3 (<0.6 wt %) promotes the grain growth [3] and accelerate densification in the microstructure [4]. This indicates that the small content of Cr (0.5 wt %) in the BFN system acts as grain growth promoter, whereas Cr addition (≥1.0 wt %) acts as growth inhibiter.

Experimental density (given in Table 6.3) of the Cr added BFN ceramics is nearly same as that of the parent BFN ceramics. With the addition Cr in the BFN system, the sintering temperature reduces from 1350 to 1300°C with enhanced microstructural properties. Similar results are observed in various other ceramics. It is reported that the addition of Cr_2O_3 in the parent BFN ceramics leads to the formation of liquid phase and reduces the sintering temperature [5-7], and therefore acts as sintering aid.

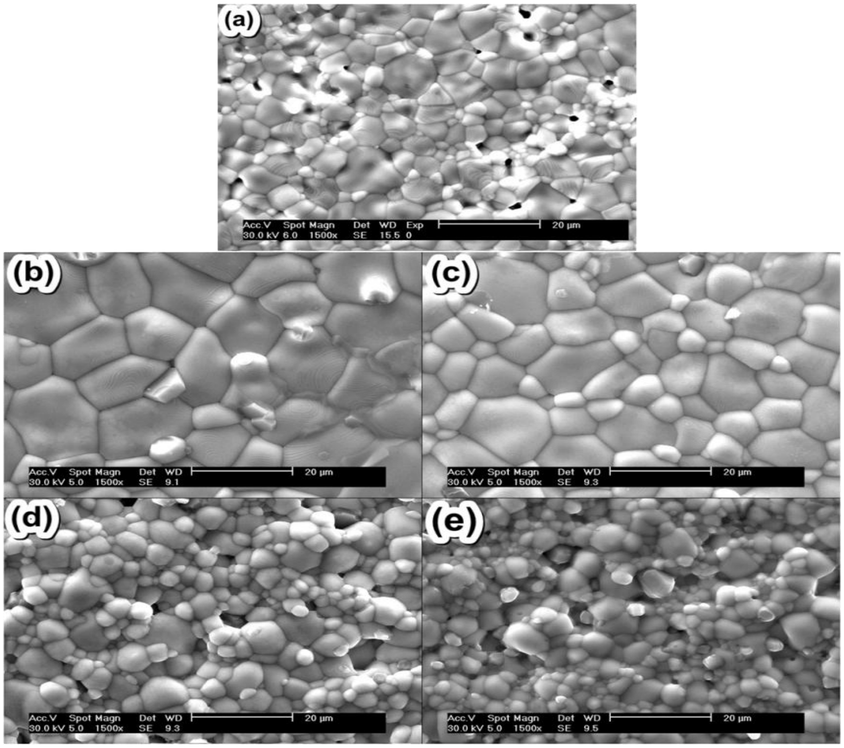

Fig. 6.3: SEM micrographs of the Cr added (0.0, 0.5, 1.0, 1.5 & 2.0 wt %) BFN ceramics sintered at 1300°C for 4h.

Table 6.3: Density and grain size parameters of the Cr-added BFN ceramics.

Samples	**BFN**	**Cr0.5-BFN**	**Cr1.0-BFN**	**Cr1.5-BFN**	**Cr2.0-BFN**
Avg. Grain size(μm)	6.32	11.83	10.76	7.33	5.93
Density(g/cc)	5.97	6.08	6.04	6.03	6.06

6.3.2 Density and Morphological Study of the Mn-added BFN Ceramics

The SEM micrographs of the Mn-added BFN ceramics are shown in Fig.6.4. Close packing of grains with non-uniform microstructures is observed. There is a substantial increase of non-uniformity grain size is observed after the Mn addition in the BFN ceramics. Similar results are observed in which Mn promotes the grain size [8-10]. Small content of Mn (0.5 wt %) addition in the BFN system produces larger grain size compared to other compositions. It is reported that addition of small amount of additives significantly enhanced the grain size due to formation of small amount of liquid phase in the ceramics [11]. This may be the reason for which small content of Mn (0.5 wt %) in BFN system enhanced the grain size. Further additions of Mn in the ceramic segregate at the grain boundary and inhibit the grain growth [12, 13]. The values of grain size and experimental densities are given in Table 6.4. The experimental density of Mn (0.5 at %) added BFN ceramics are comparatively higher than other Mn added BFN ceramics. Addition of Mn in the BFN system leads to the reduction of sintering temperature from 1350 to 1300°C, which indicated the sintering aid nature of Mn. Similar results are observed in other perovskite ceramics where the addition of Mn lowered the sintering temperature [14, 15].

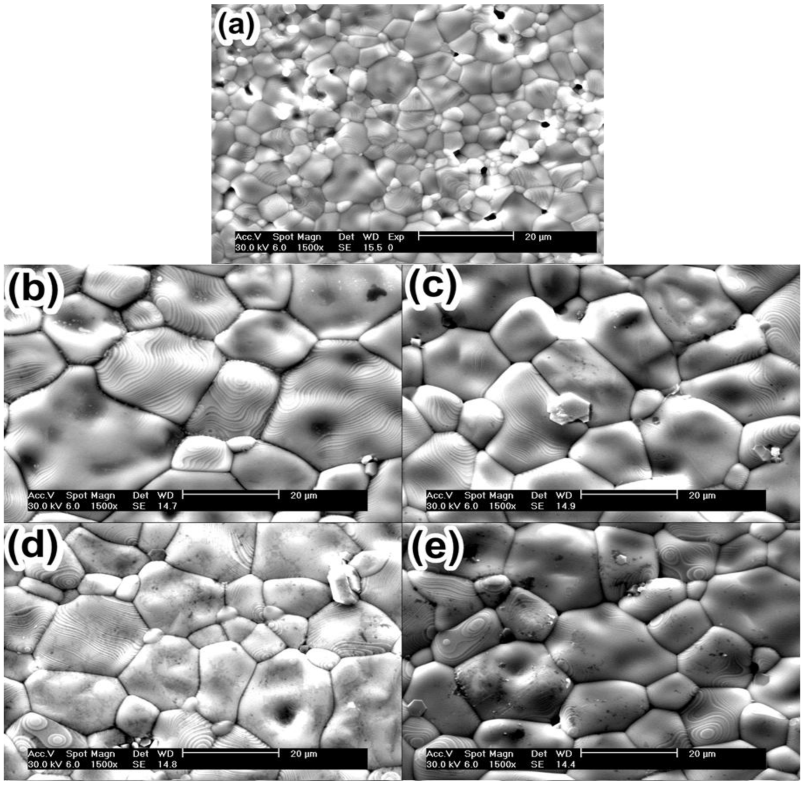

Fig. 6.4: SEM micrographs of the Mn added (0.0, 0.5, 1.0, 1.5 & 2.0 wt %) BFN ceramics sintered at 1300°C for 4h.

Table 6.4: Density and grains size parameters of the Mn-added BFN ceramics.

Samples	BFN	Mn0.5-BFN	Mn1.0-BFN	Mn1.5-BFN	Mn2.0-BFN
Avg. Grain size(μm)	6.32	27.01	18.20	20.23	20.88
Density(g/cc)	5.97	6.02	5.99	6.01	6.01

6.4 Dielectric property analysis

6.4.1 RT Frequency Dependent Dielectric Properties of the Cr-added BFN Ceramics

Fig. 6.5 (a) & (b) shows the frequency dependence of dielectric constant (ε') and dielectric loss (tanδ) at room temperature of the Cr-modified BFN ceramics. Both, ε' and tanδ obeys the similar type of behaviour as that of pure BFN ceramics. For low content of Cr (≤ 1.5 wt %) addition, a low frequency dispersion is observed whereas for 2.0 wt % Cr addition, a clear plateau region is observed. Above 10^5 Hz frequency, the value of dielectric constant drastically decreases to ~10^2 for all the compositions. The decrease in the dielectric constant with the increase in frequency suggests that more than one type of polarisation mechanism are presents in these systems [16, 17].

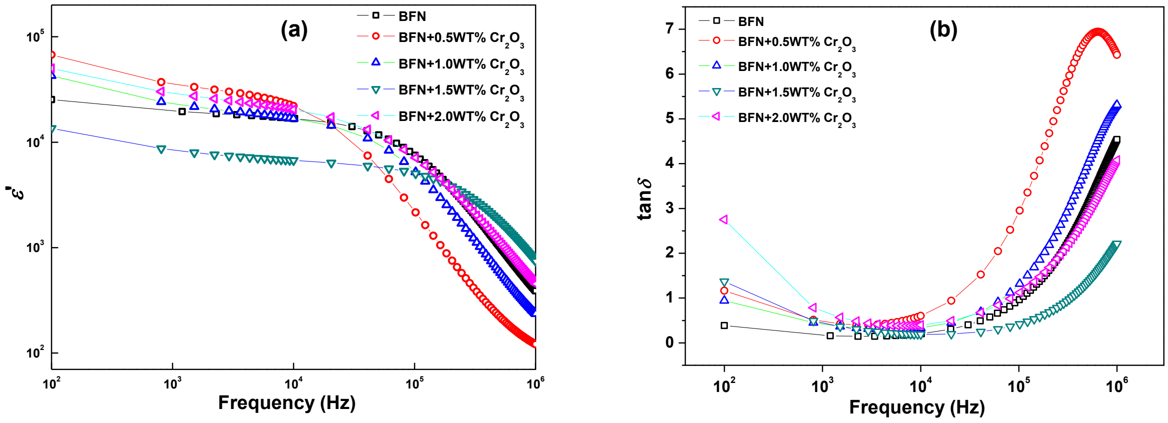

Fig. 6.5: Room temperature frequency variation of (a) dielectric constant and (b) dielectric loss of the Cr-added BFN ceramics.

6.4.2 Temperature Dependent Dielectric Properties of the Cr-added BFN Ceramics

Fig. 6.6 (a) shows the temperature dependence of dielectric constant at 10 kHz of Cr-added BFN ceramics. Incorporation of Cr in the BFN ceramics strongly enhances the dielectric constant and is more than that of parent BFN ceramics. Dielectric abnormalities are observed ~ 70°C and 300°C, respectively for all the samples. The dielectric abnormalities may be assigned to the extrinsic mechanism, the point defects and oxygen vacancies, present in the Cr-modified BFN ceramics [18]. The dielectric anomaly observed ~70 °C in dielectric may be the result of local disorder in the lattice due to the fluctuation of valence states of Fe (Fe^{+3}↔Fe^{+2}) in the Cr-modified BFN ceramics [19]. The increase of dielectric constant with the increase of temperature in a dielectric material is generally related to the increase of trapped charge carriers at the grain boundaries [20]. The high temperature (~300°C) dielectric anomaly can be attributed to defects and vacancies. At high frequency (1 MHz), space charges fail to respond and because of these the dielectric anomaly is suppressed. Similar type of dielectric behavior is also observed in the BFN ceramics.

Hetero-valent admixture can generate ionic or atomic defects and oxygen vacancies through charge compensation mechanism in the BFN ceramics[21]. Admixture like Cr can act as acceptor dopant in the BFN system if substituted for Fe or Nb in the lattice or placed in the interstitial positions. Admixture of Cr in the BFN ceramics can give rise to various defect reactions, written in the form of Kroger-Vink notation.

If Cr is substituted for Nb and generates niobium vacancies (V_{Nb}) then,

$$BaFe_{0.5}Nb_{0.5}O_3 + 0.5Cr_2O_3 \rightarrow BaFe_{0.5}Nb_{0.5-0.6x}Cr_xO_3 + 0.3xNb_2O_5 \qquad (6.1)$$

and,

$$Ba^{2+}Fe_{0.5}^{3+}Nb_{0.5-0.6x}^{5+}Cr_x^{3+}O_3^{-2}\ (0.6xV_{Nb}^{'''''}) \qquad (6.2)$$

Similarly, if Cr is substituted for Fe and generates V_{Fe} then,

$$BaFe_{0.5}Nb_{0.5}O_3 + 0.5Cr_2O_3 \rightarrow BaFe_{0.5-x}Cr_xNb_{0.5}O_3 + 0.5xFe_2O_3, \qquad (6.3)$$

and,

$$Ba^{2+}Fe^{3+}{}_{0.5-x}Cr^{3+}{}_{x}Nb^{5+}{}_{0.5}O^{-2}{}_{3}\ (xV_{Fe}) \qquad (6.4)$$

If excess amount of Cr is added to the parent BFN ceramics then the interstitial positions are filled by Cr which can act as donor defects and release electrons. Ionization of Cr ion can be written as

$$Cr_{Cr} = Cr^{\bullet} + e^{'} \qquad (6.5)$$

Acceptor defects are created with addition of Cr can act as trap states for free electron for which dielectric constant decreases with increase in Cr content near RT. However the increase in dielectric constant with increase in temperature is attributed the release of free electrons at high temperature as given in eqn. 6.5.

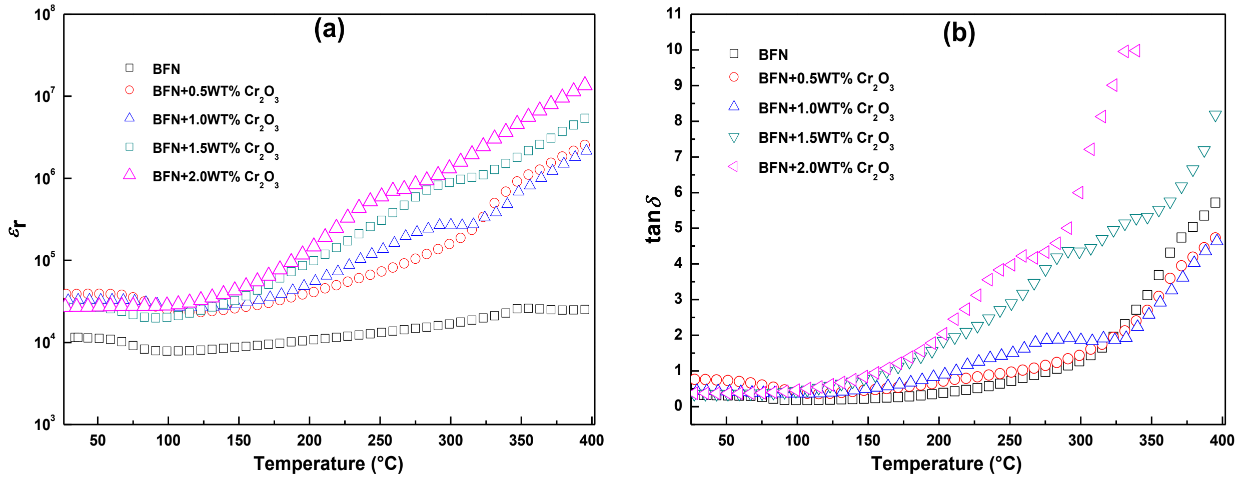

Fig. 6.6: Temperature variation of (a) dielectric constant and (b) dielectric loss at 10 kHz frequency of the Cr-added ceramics.

Table 6.5: Dielectric parameters of the Cr-added BFN ceramics.

Samples	**BFN**	**Cr0.5-BFN**	**Cr1.0-BFN**	**Cr1.5-BFN**	**Cr2.0-BFN**
ε' (10 kHz)	11569	38832	32575	26704	26941
tanδ (10 kHz)	0.32	0.76	0.43	0.35	0.37

6.4.3 RT Frequency Dependent Dielectric Properties of the Mn-added BFN Ceramics

Fig. 6.7(a) & (b) show the frequency dependence of dielectric constant and dielectric loss of the Mn-added BFN ceramics. The value of ε' decreases drastically with the increase of Mn added concentration in the BFN ceramics. For the higher content of Mn (≥1.0 wt %) in the BFN ceramics, the dielectric relaxation is strongly suppressed. The dielectric characteristic, observed for 0.5 wt % of Mn-doped BFN ceramics, is clearly distinguishable from other Mn content addition in the BFN ceramics as shown in Fig. 6.7(a) and (b). The reason behind the suppression of dielectric relaxation with content of Mn in BFN system is explained in the next section.

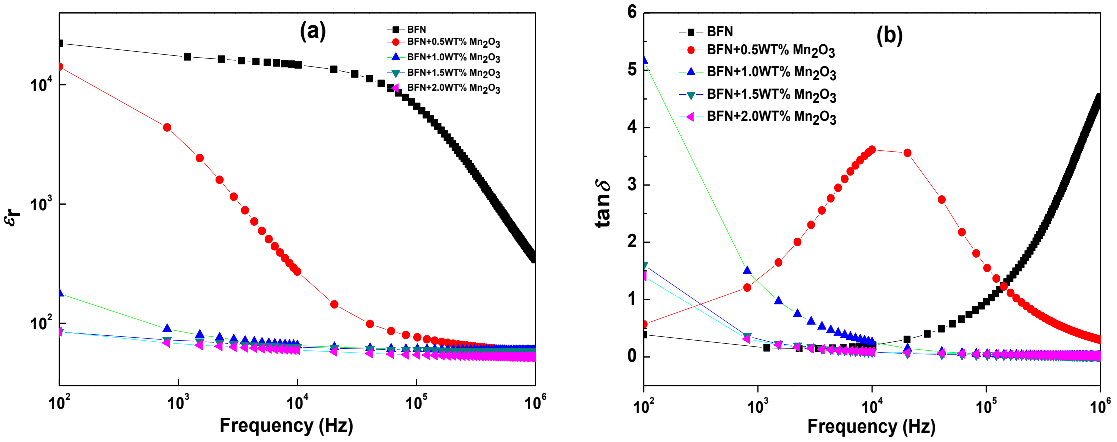

Fig. 6.7: Room temperature frequency variation of (a) dielectric constant and (b) dielectric loss of the Mn-added BFN ceramics.

6.4.4 Temperature Dependent Dielectric Properties of the Mn-added BFN Ceramics

Fig. 6.8 (a) shows the temperature variation of dielectric constant at 10 kHz frequency of Mn added BFN ceramics. At room temperature, with the addition of Mn in the BFN ceramics the dielectric constant decreases. The ε' is significantly decreased for higher contents of Mn (1.0, 1.5&2.0 wt %) and remain independent with temperature up to 125°C. Above 300°C, the ε' of Mn-added BFN samples is higher than that of parent BFN ceramics. Corresponding to the step changes in ε' plot, a peak is observed in dielectric loss plot (Fig. 6.8(b)). The dielectric loss peak shifts towards right or higher temperature with the increase of Mn-content in the BFN ceramics.

In the Mn added BFN samples (1.0, 1.5 and 2.0 wt% $MnCO_3$) dielectric constant is suppressed below 125°C and later increases sharply with the increase in temperature. This may be associated to the release of electrons during ionization of oxygen vacancies, captured by Mn^{2+} ions. This process reduces the electronic hopping relaxation and dielectric constant. Further the defect complexes ($(Mn''_{Nb}-V^{\bullet\bullet}_{o})$ or $(2Mn'_{Fe}-V^{\bullet\bullet}_{o})$) associated with Mn and oxygen vacancy are highly immobile below 125°C which suppresses the oxygen vacancy migration and the dielectric constant. Above 125°C the dielectric relaxation in the Mn added BFN ceramics can be explained by mobile oxygen vacancies. It was reported that concentration of mobile oxygen vacancies may increases at higher temperature for Mn rich BT system due to dissociation of the defect complex associated with oxygen vacancy and manganese ion [22]. Therefore it is a possibility of dissociation of the defect complex above 125° C and movement of oxygen vacancies, which can contribute to the high dielectric constant in BFN system. Again as per the space charge model, a thermally activated process can be considered for explaining the high temperature high dielectric constant in the Mn added BFN ceramics [23, 24].

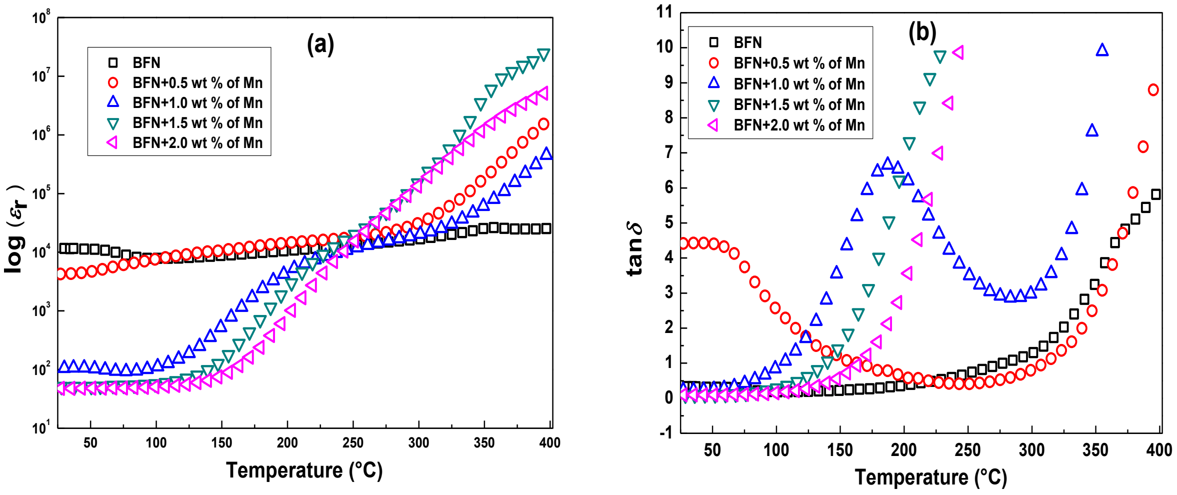

Fig. 6.8: Temperature variation of (a) dielectric constant and (b) dielectric loss at 10 kHz frequency of the Mn-added ceramics.

Table 6.6: Dielectric values of Mn-added BFN ceramics.

Sample	**BFN**	**Mn0.5-BFN**	**Mn1.0-BFN**	**Mn1.5-BFN**	**Mn2.0-BFN**
ε' (10 kHz)	11569	4245	106	51	53
tanδ (10 kHz)	0.3129	4.4094	0.225	0.084	0.092

6.5 Leakage Current and Polarization Studies

Like La and Pb doped BFN ceramics, the values of leakage current (I) for both the Cr and Mn added BFN ceramics is also measured at 50V up to a time period (t) of 20sec. The I-t behavior of the Cr and Mn added BFN ceramics is same as that of the parent BFN ceramics. Change in the value of the current with time is minimal; however, there is a change in the values of the leakage current (given in Table 6.7) with the variation of Cr and Mn – addition content in the BFN ceramics.

Table 6.7: Leakage current values of Cr and Mn- modified (with x=0, 2, 4, 6 & 8 %) BFN ceramics

Samples	**0.0wt%**	**0.5wt%**	**1.0wt%**	**1.5wt%**	**2.0wt%**
Leakage current(A) in Cr-BFN	1.29 x 10^{-6}	5.85 x 10^{-7}	6.77 x 10^{-7}	1.57 x 10^{-6}	1.40 x 10^{-6}
Leakage current(A) in Mn-BFN		2.09 x 10^{-5}	6.72 x 10^{-6}	1.47 x 10^{-6}	9.78 x 10^{-7}

The leakage current values of both the Cr and Mn added BFN samples decreases in comparison to the parent BFN ceramics. But, the overall leakage current is of the order ~10^{-6} to 10^{-7}A which is high for a material to be used as a dielectric application. The polarization vs. electric field (P-E) loop behaviour with small applied voltages of 3V and 50 V for Cr and Mn added BFN ceramics, respectively were carried out and shown in Fig. 6.9(a) and (b). No saturation in the P-E loops confirms the existence of non-ferroelectricity in these ceramics.

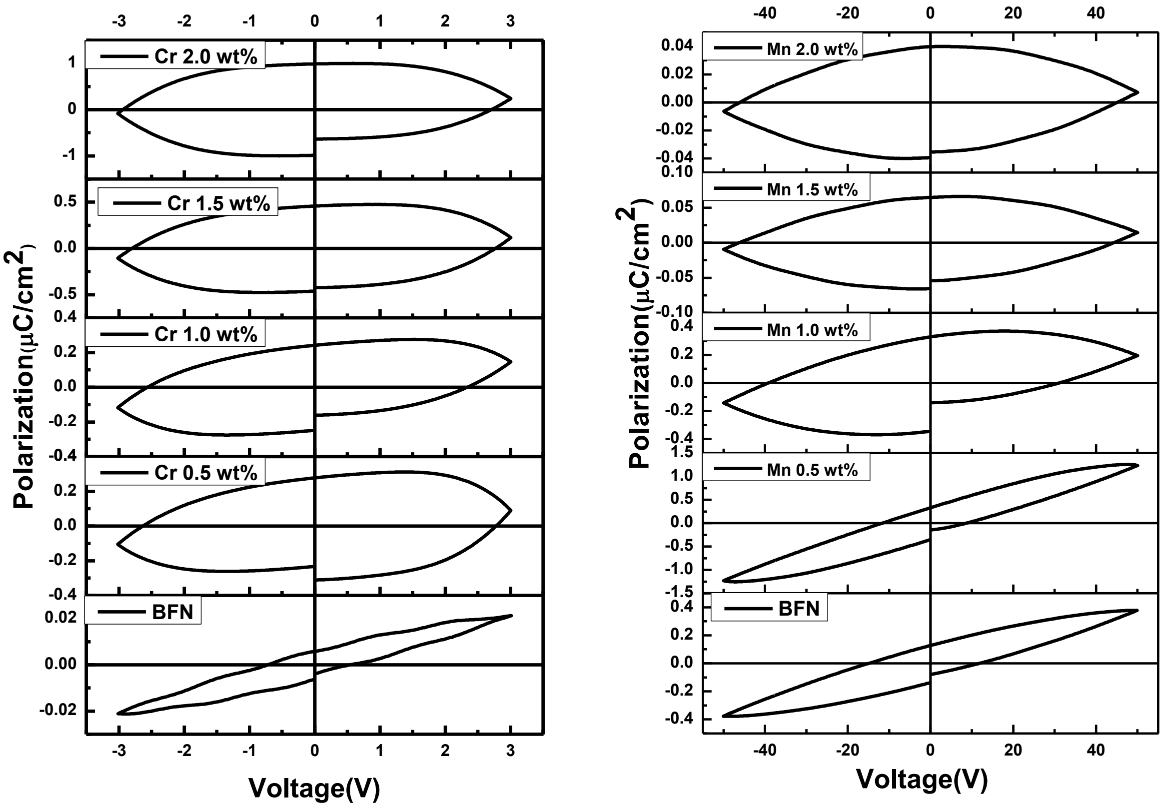

Fig. 6.9: RT variation of the polarization with applied voltage of (a) Cr and (b) Mn modified BFN ceramics.

6.6 Optical Properties Study

6.6.1 UV-Vis Optical Properties Study of the Cr-added BFN Ceramics

Fig. 6.10(a) shows the optical diffuse reflectance spectra (DRS) of all the Cr-added BFN samples in the UV–Vis region. Reflectance percentage is lowered in the 400-600nm and 800-1100nm wavelength ranges in comparison to 600-800nm wavelength range. The reflectance percentage decreases with the increase in Cr addition content in the BFN ceramics. The optical band gap of all the Cr-added BFN samples is calculated by using the Kubelka–Munk (KM) function. Fig. 6.10(b) shows that the optical band gap (E_g) of all the Cr-added BFN samples is evaluated by extrapolating the linear part of the curve $[F(R_\infty)h\nu]^2$ onto the photon energy axis. The E_g of all the Cr-added BFN samples is found to be ~1.5 eV. There is no significant change in the reflectance spectra after the addition of Cr in the BFN ceramics. The observed low optical band gap of the Cr-added BFN samples is comparable to other ceramic and polymer compound [25]. The band gap of Cr (0.0, 0.5, 1.0, 1.5 &2.0 wt %) added BFN ceramics are 1.53, 1.52, 1.52, 1.45 and 1.45 eV, respectively. The narrow band gap in the Cr added BFN ceramics indicates a possibility of utilizing more visible light for photo-catalysis. Vacancy enriched materials can have a band of electronic states just below the conduction band [26]. Lower band gap in the systems like ZnO, TiO_2 etc. is associated with the oxygen vacancies [27]. Since, the oxygen defect states remain close to the conduction band, the electrons captured by the oxygen defects can be promoted to the surface by visible light absorption [28, 29]. This suggests that the oxygen vacancies in the Cr-added BFN may be responsible for the observed low band gaps.

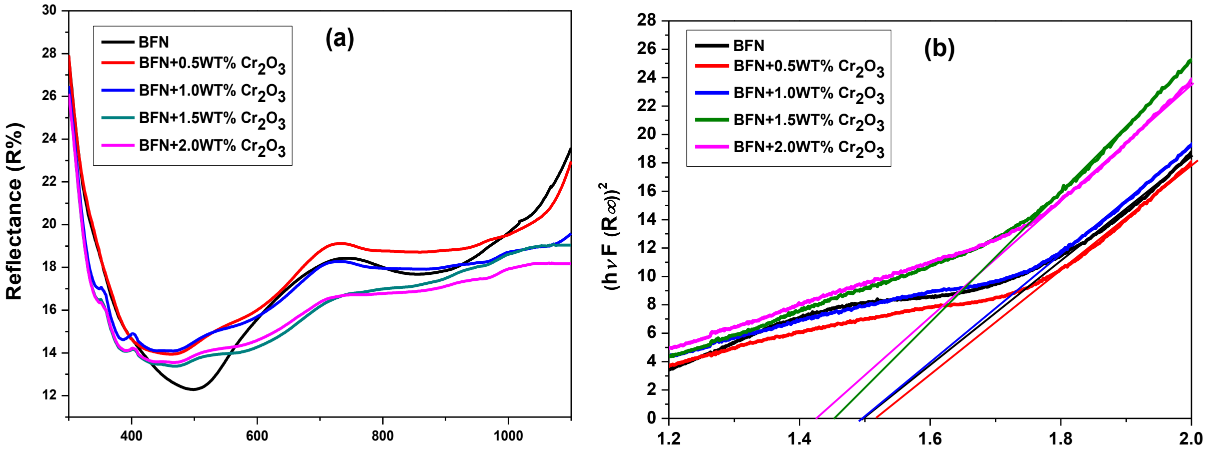

Fig. 6.10: (a) UV-Vis reflectance spectra and (b) Estimated band-gap energy of the Cr-added BFN ceramics.

6.6.2 UV-Vis Optical Properties Study of the Mn-added BFN Ceramics

Fig. 6.11(a) shows the optical diffuse reflectance spectra (DRS) in the UV–Vis region of the Mn-added BFN ceramics. The reflectance percentage attains minima near 490 nm and 890 nm wavelengths. The reflectance percentage decreases with the increase in the Mn addition content in the BFN ceramics.

The optical band gap is calculated by using the Kubelka–Munk (KM) function. As per this, the optical band gap (E_g) of the Mn added BFN ceramics is evaluated by extrapolating the linear part of the curve $[F\,(R_\infty)h\nu]^2$ onto the energy axis, as shown in Fig. 6.11(b). The band gap of the Mn (0.0, 0.5, 1.0, 1.5 & 2.0 wt %) added BFN ceramics is 1.53, 1.52, 1.52, 1.45 & 1.45 eV, respectively. The origin of narrow band gap in the Mn-added BFN ceramics may be termed as a material characteristic or oxygen vacancy induced phenomena, which need further study. The narrow band gap, observed in the Mn added BFN ceramics, suggest the utility of these compounds photo-catalysis and other applications.

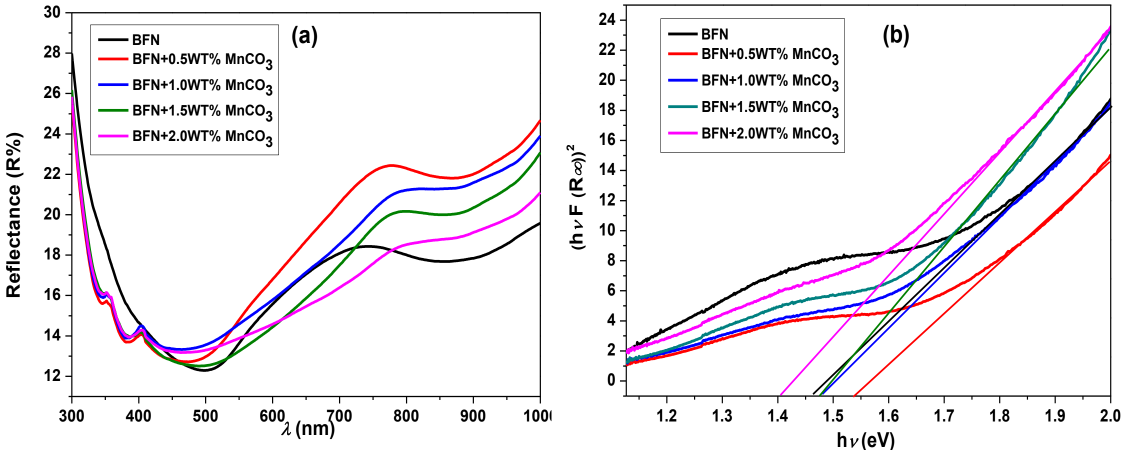

Fig. 6.11: (a) UV-Vis reflectance spectra and (b) Estimated band-gap energy of the Mn-added BFN ceramics.

6.7 Chapter Summary

Cr and Mn (0.0, 0.5, 1.0, 1.5 & 2.0 wt %) added BFN ceramics were synthesized by conventional solid state reaction route . The XRD study on both the Cr and Mn (0.0, 0.5, 1.0, 1.5 & 2.0 wt %) modified BFN ceramics showed single perovskite phase with cubic structure. A negligible trace of secondary phase oapeared in the higher % of Cr-added BFN samples. The average grain size increased for all the Mn and Cr added BFN samples (except for Cr2.0-BFN aded modified samples). Experimental densities of the Mn and Cr added BFN samples was nore compared to parent BFN ceramics. Room temperature dilectric constant was found to be maximum for 0.5wt% Cr and Mn added BFN sampless. The polarization with applied voltage showed no saturation in the loops. The leakage current decreased in both the Cr and Mn added BFN ceramics compared to parent BFN ceramics. The narrow optical band gap in the Mn and Cr added BFN samples suggested about their semiconducting nature.

References

[1] E. Wu, POWD, an interactive program for powder diffraction data interpretation and indexing, J. Appl. Crystallogr. 22 (5) (1989) 506-510.

[2] F.M. Filho, A.Z. Simoes, A. Ries, L. Perazolli, E. Longo, J.A. Varela, Nonlinear electrical behaviour of the Cr_2O_3, ZnO, CoO and Ta_2O_5-doped SnO_2 varistors, Ceram. Int. 32 (3) (2006) 283-289.

[3] W. Long, L. Yi-Yeh, L. Chich-Kow, W. Tien-Shou, Effect of Cr_2O_3 Additives on Microstructure and Electrical Properties of Nd-Modified $PbTiO_3$ Ceramics, Japanese Journal of Applied Physics 31 (12R) (1992) 3913.

[4] L. Wu, L. Yi-Yeh, C.K. Liang, Microstructure and properties of Cr_2O_3 doped lead titanate piezoceramics, in: Applications of Ferroelectrics, 1992. ISAF '92., Proceedings of the Eighth IEEE International Symposium on, IEEE, Greenville, SC 1992, pp. 529-532.

[5] D.-H. Riu, Y.-M. Kong, H.-E. Kim, Effect of Cr_2O_3 addition on microstructural evolution and mechanical properties of Al_2O_3, J. Eur. Ceram. Soc. 20 (10) (2000) 1475-1481.

[6] X.H. Jin, L. Gao, Y.R. Chen, Q.M. Yuan, Influence of Cr_2O_3 on the sintering, microstructure and mechanical performances of ZTM-Al_2O_3, J. Mater. Sci. Lett. 20 (3) (2001) 253-256.

[7] S. Maitra, S. Pal, S. Nath, A. Pandey, R. Lodha, Role of MgO and Cr_2O_3 additives on the properties of zirconia-mullite composites, Ceram. Int. 28 (7) (2002) 819-826.

[8] G. Fan, W. Lu, X. Wang, F. Liang, Effects of manganese additive on piezoelectric properties of $(Bi_{1/2}Na_{1/2})TiO_3$-$BaTiO_3$ ferroelectric ceramics, J. Mater. Sci. 42 (2) (2007) 472-476.

[9] H. Nagata, T. Takenaka, Additive effects on electrical properties of $(Bi_{1/2}Na_{1/2})TiO_3$ ferroelectric ceramics, J. Eur. Ceram. Soc. 21 (10-11) (2001) 1299-1302.

[10] V. Tsakaloudi, E. Eleftheriou, M. Stoukides, V. Zaspalis, Electromagnetic properties of Mn-doped NiCuZn-ferrites, J. Magn. Magn. Mater. 318 (1-2) (2007) 58-64.

[11] S. Bernik, P. Zupancic, D. Kolar, Influence of Bi_2O_3/TiO_2, Sb_2O_3 and Cr_2O_3 doping on low-voltage varistor ceramics, J. Eur. Ceram. Soc. 19 (6-7) (1999) 709-713.

[12] S. Ramesh, W.J. Kelvin Chew, C.Y. Tan, P. J., A.M. Noor, M.A. Hassan, U. Sutharsini, M. Satgunam, W.D. Teng, Influence Of Manganese On The Sintering Properties Of Tetragonal Zirconia Ceram.-Silik. 57 (1) (2013) 28-32

[13] U. Ichiro, Effects of Additives on Piezoelectric and Related Properties of PbTiO3 Ceramics, Japanese Journal of Applied Physics 11 (4) (1972) 450.

[14] S.-M. Lee, S.-H. Lee, C.-B. Yoon, H.-E. Kim, K.-W. Lee, Low-temperature sintering of MnO_2-doped PZT-PZN Piezoelectric ceramics, Journal of Electroceramics 18 (3-4) (2007) 311-315.

[15] I.-Y. Kang, I.-T. Seo, Y.-J. Cha, J.-H. Choi, S. Nahm, T.-H. Sung, J.-H. Paik, Low temperature sintering of ZnO and MnO_2-added (Na0.5K0.5)NbO3 ceramics, J. Eur. Ceram. Soc. 32 (10) (2012) 2381-2387.

[16] V. Shrivastava, A.K. Jha, R.G. Mendiratta, Dielectric studies of La and Pb doped $SrBi_2Nb_2O_9$ ferroelectric ceramic, Mater. Lett. 60 (12) (2006) 1459-1462.

[17] P. Kumar, B.P. Singh, T.P. Sinha, N.K. Singh, AC conductivity and dielectric relaxation in $Ba(Sm_{1/2}Nb_{1/2})O_3$ ceramic, Physica B: Condensed Matter 406 (2) (2011) 139-143.

[18] Z. Wang, X.M. Chen, L. Ni, X.Q. Liu, Dielectric abnormities of complex perovskite $Ba(Fe_{1/2}Nb_{1/2})O_3$ ceramics over broad temperature and frequency range, Appl. Phys. Lett. 90 (2) (2007) 022904-022903.

[19] M.M. Kumar, Z.G. Ye, Dielectric and electric properties of donor- and acceptor-doped ferroelectric $SrBi_2Ta_2O_9$, J. Appl. Phys. 90 (2) (2001) 934-941.

[20] S.M. Shaban, B.S. Mahdi, R.M.S. Al-Haddad, AC conductivity and dielectric behaviour of $CuZnSnO_4$ compound prepared by powder technology Indian J. Pure Appl. Phys. 51 (11) (2013) 784-787.

[21] C.-Y. Chung, Y.-H. Chang, G.-J. Chen, Effects of lanthanum doping on the dielectric properties of $Ba(Fe_{0.5}Nb_{0.5})O_3$ ceramic, J. Appl. Phys. 96 (11) (2004) 6624-6624.

[22] S.H. Cha, Y.H. Han, Effects of Mn doping on dielectric properties of Mg-doped $BaTiO_3$, J. Appl. Phys. 100 (10) (2006) 104102.

[23] O. Bidault, P. Goux, M. Kchikech, M. Belkaoumi, M. Maglione, Space-charge relaxation in perovskites, Phys. Rev. B: Condens. Matter 49 (12) (1994) 7868-7873.

[24] M. Maglione, Polarons, free charge localisation and effective dielectric permittivity in oxides, in: arXiv e-prints : 1006.3719, 2010, pp. 3719.

[25] L.M. Campos, A. Tontcheva, S. Gunes, G. Sonmez, H. Neugebauer, N.S. Sariciftci, F. Wudl, Extended Photocurrent Spectrum of a Low Band Gap Polymer in a Bulk Heterojunction Solar Cell, Chem. Mater. 17 (16) (2005) 4031-4033.

[26] I. Justicia, P. Ordejón, G. Canto, J.L. Mozos, J. Fraxedas, G.A. Battiston, R. Gerbasi, A. Figueras, Designed Self-Doped Titanium Oxide Thin Films for Efficient Visible-Light Photocatalysis, Adv. Mater. (Weinheim, Ger.) 14 (19) (2002) 1399-1402.

[27] B. Santara, P.K. Giri, K. Imakita, M. Fujii, Evidence for Ti Interstitial Induced Extended Visible Absorption and Near Infrared Photoluminescence from Undoped TiO_2 Nanoribbons: An In Situ Photoluminescence Study, The Journal of Physical Chemistry C 117 (44) (2013) 23402-23411.

[28] J. Ravichandran, W. Siemons, H. Heijmerikx, M. Huijben, A. Majumdar, R. Ramesh, An Epitaxial Transparent Conducting Perovskite Oxide: Double-Doped $SrTiO_3$, Chem. Mater. 22 (13) (2010) 3983-3987.

[29] X. Pan, M.-Q. Yang, X. Fu, N. Zhang, Y.-J. Xu, Defective TiO_2 with oxygen vacancies: synthesis, properties and photocatalytic applications, Nanoscale 5 (9) (2013) 3601-3614.

CHAPTER 7

Structural, Morphological and Electrical Studies of the MW Processed BFN Based Ceramics

7.1 Introduction

The BFN based ceramics, synthesized by conventional route and showing best dielectric properties were selected to study the effect of microwave sintering on their different properties. The studied samples are (i) $Ba_{(1-x)}La_{2x/3}(FeNb)_{0.5}O_3$ (x=0.08), (ii) $Ba_{(1-x)}Pb_x(FeNb)_{0.5}O_3$ (x=0.08), (iii) $Ba(FeNb)_{0.5}O_3$ – x wt% of $MnCO_3$ (x=0.5) and (iv) $Ba(FeNb)_{0.5}O_3$ – x wt% of Cr_2O_3 (x=0.5). The detail microwave sintering process is given in the Chapter 3. The structural, morphological and electrical properties of these microwave sintered samples are investigated and compared with the same ceramics processed conventionally.

7.2 XRD Patterns of the La, Pb, Cr and Mn Modified BFN Ceramics

X-ray diffraction study is carried out for all the BFN based MWS samples. The BFN based samples are sintered for 15, 30 and 45 min duration, respectively at the sintering temperature, optimized conventionally. With the increase of sintering time, the chances of getting secondary phase increases in the XRD pattern. Therefore, in the present study we have given the XRD patterns of the BFN based samples sintered for 45 minutes (maximum soaking duration). Figs. 7.1 (a) and (b) show the XRD patterns of the La (x=0.08) and Pb (x=0.08) modified BFN ceramics MWS at 1250°C for 45 min., respectively. Figs. 7.1 (c) and (d) show the XRD patterns of the Cr (x=0.5 wt %) and Mn (x=0.5wt %) modified BFN ceramics MWS at 1300°C for 45 min, respectively. XRD patterns of all the MWS BFN based ceramics showed the formation of single perovskite phase without any trace of secondary phase peaks. These XRD patterns of the MWS BFN based ceramics are indexed by standard computer programme

(POWD). The best agreement between the observed and the calculated'd' spacing was (minimum) taken for determining the structure. The structure is cubic for all the MWS BFN based ceramics. This indicates that the low contents of La and Pb completely diffuse into the BFN structure and formed a homogeneous solid solution. The XRD patterns of the MWS Cr (0.5 wt %) and Mn (0.5 wt %) admixture BFN ceramic also show the single perovskite phase without any trace of secondary phase peaks. This indicates that the Cr and Mn additives get completely dissolved in the BFN lattice.

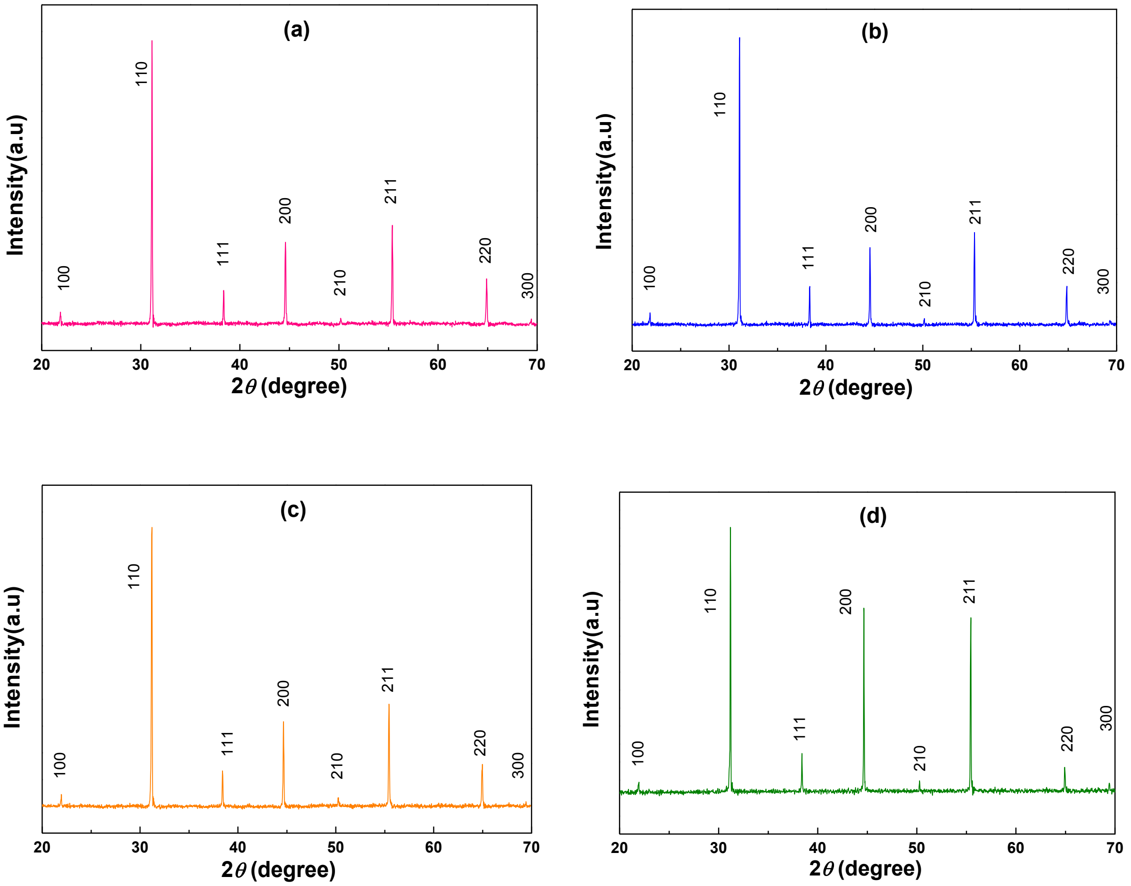

Fig. 7.1: (a) XRD patterns of the La (x=0.08) and (b) Pb (x=0.08) (c) Cr (x=0.5wt %) and (d) Mn (x=0.08) modified MWS BFN ceramics.

7.3 SEM Study of the MWS La, Pb, Cr and Mn Modified BFN Ceramics

Figs. 7.2 (a), (b), (c) and (d) show the surface micrographs of the La, Pb, Cr and Mn modified BFN ceramics sintered in a microwave furnace for different times. The average grain size of all these MWS ceramics are given in Table 7.1. The average grain size of La and Pb modified BFN ceramics increases with the increase of sintering time duration. This indicates increase in sintering time duration the grain size of the samples increases [1]. The grain size of MWS BFN + Mn (0.5 wt %) sample lower than that of CS, indicates fast processing in MW inhibit the unwanted grain growth [2]. However, for the MWS Cr added BFN ceramics the grain size is significantly lower than the corresponding CS samples. This indicates that there may be a significant interaction between MW and Cr in BFN system, which needs further investigation to account the detailed mechanism.

Experimental density of all the MWS BFN based ceramics increases with the increase in sintering time. All the BFN based MWS samples (except Mn added samples), sintered for 45 min, show higher density than that of the corresponding CS samples. This indicates that through MWS process we can get better sintered BFN based ceramics in small time period.

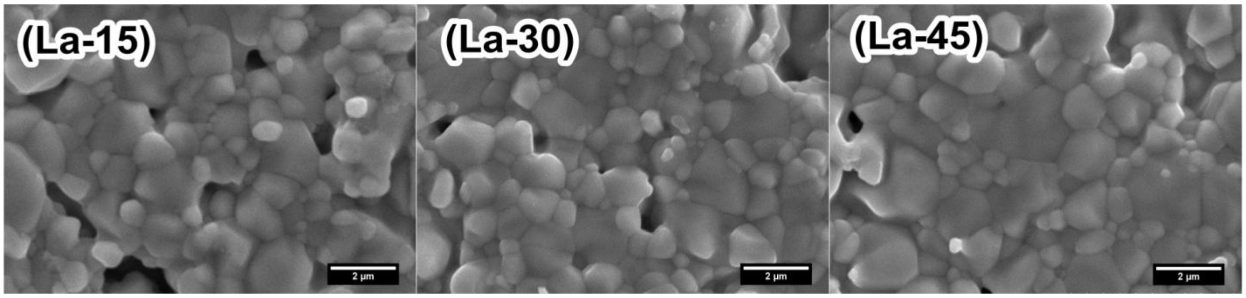

Fig. 7.2: (a) SEM micrographs of the La (x=0.08) modified BFN ceramics MWS at 1250°C for 15, 30 and 45 min.

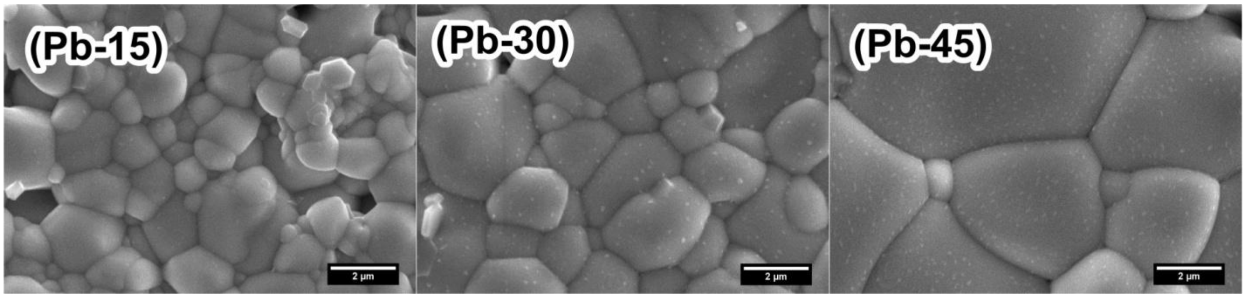

Fig. 7.2: (b) SEM micrographs of the Pb (x=0.08) modified BFN ceramics MWS at 1250°C for 15, 30 and 45 min.

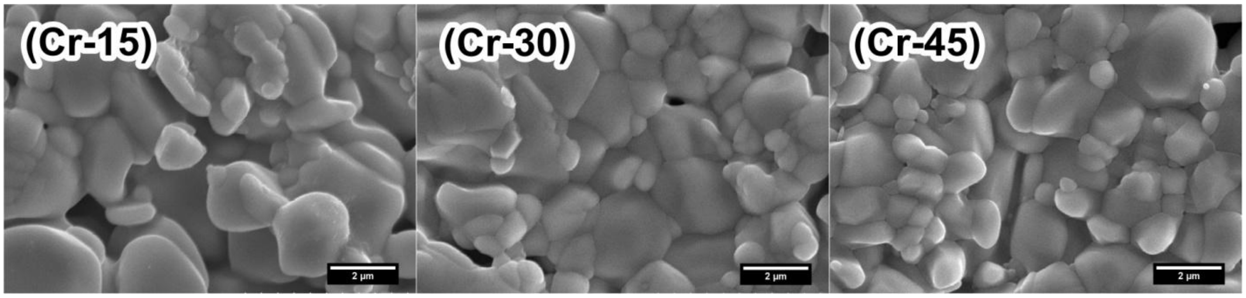

Fig. 7.2: (c) SEM micrographs of the Cr (x=0.05) added BFN ceramics MWS at 1300°C for 15, 30 and 45 min.

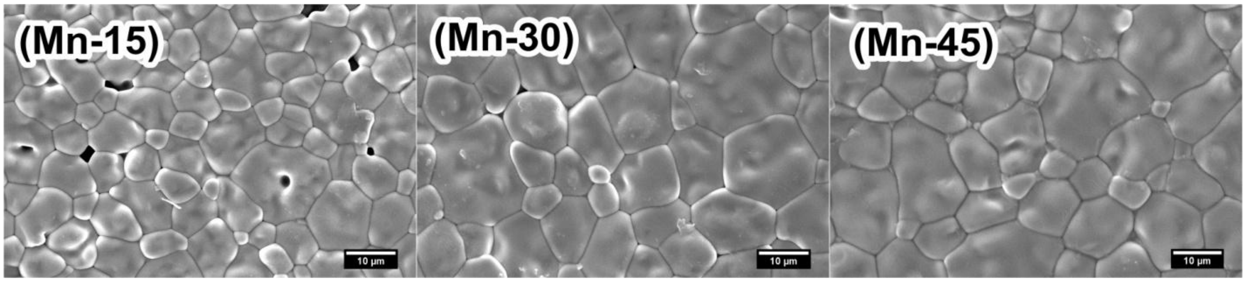

Fig. 7.2: (d) SEM micrographs of the Mn (x=0.05) added BFN ceramics MWS at 1300°C for 15, 30 and 45 min.

Table 7.1: Avg. Grain size of the CS and MWS La, Pb, Cr and Mn modified BFN ceramics.

Modification	Average Grain size(μm)			
	CS	**15min**	**30min**	**45min**
La (x=0.08)	2.42	1. 22	1.37	2.25
Pb (x=0.08)	3.18	2. 39	2.90	3.62
Cr (x=0.5 wt %)	11.83	2. 62	2.81	3.01
Mn (x=0.5 wt %)	27.01	12.32	18.35	18.46

Table 7.2: Experimental densities of CS and MWS La, Pb, Cr and Mn modified BFN ceramics

Modification	Density(g/cc)			
	CS	**15 min**	**30 min**	**45 min**
La (x=0.08)	6.08	5.91	5.97	6.15
Pb (x=0.08)	6.29	5.99	6.02	6.35
Cr (0.5 wt %)	6.08	5.93	5.97	6.05
Mn (0.5 wt %)	5.99	5.96	6.03	5.98

7.4 Dielectric Study of MWS BFN Based Ceramics

7.4.1 Frequency Variation of the Dielectric Properties of the MWS La, Pb, Cr and Mn Modified BFN Ceramics

Figs. 7.3 (a) & (b) show the frequency variation of the dielectric constant (ε') and the dielectric loss (ε") of the La modified BFN ceramics MWS for 15, 30 and 45 min sintering durations, respectively. Two dispersive regions are observed in the ε' spectrum, one below 10 kHz and another one above it. Corresponding to the high frequency dispersion in the ε' plot, relaxation peaks are observed in the ε" plot. The broadening in the ε" plot indicates presence of non Debye type relaxation in the system.

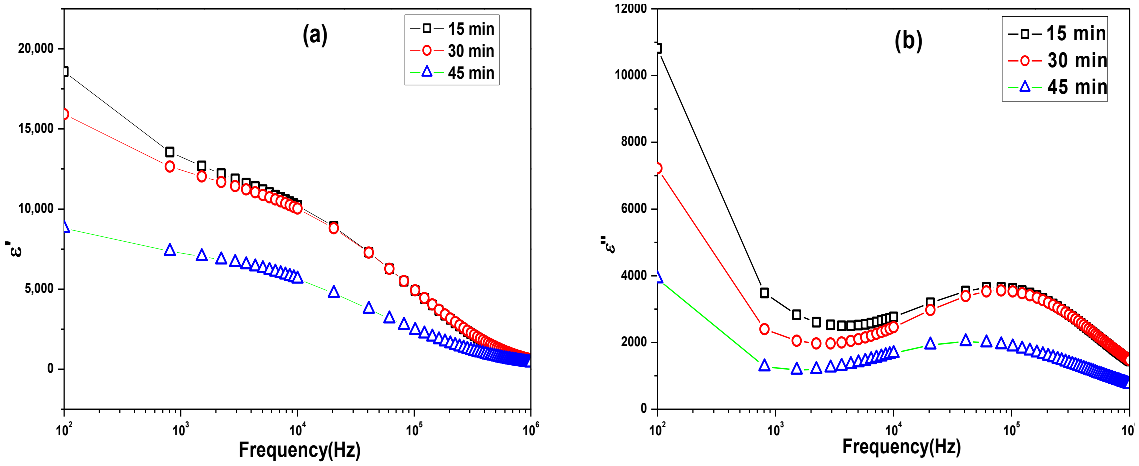

Fig. 7.3: Room temperature frequency variation of (a) dielectric constant and (b) dielectric loss of the La (x=0.08) modified MWS BFN ceramics.

Figs. 7.3 (c) & (d) show the frequency variation of the dielectric constant (ε') and dielectric loss (ε") of the Pb modified BFN ceramics MWS for 15, 30 and 45 min sintering durations, respectively. Similar types of dielectric behaviour is observed in the case of La modified BFN ceramic samples. The broadening in the ε" plot suggest the non intrinsic dielectric origin in the MWS Pb modified BFN ceramics.

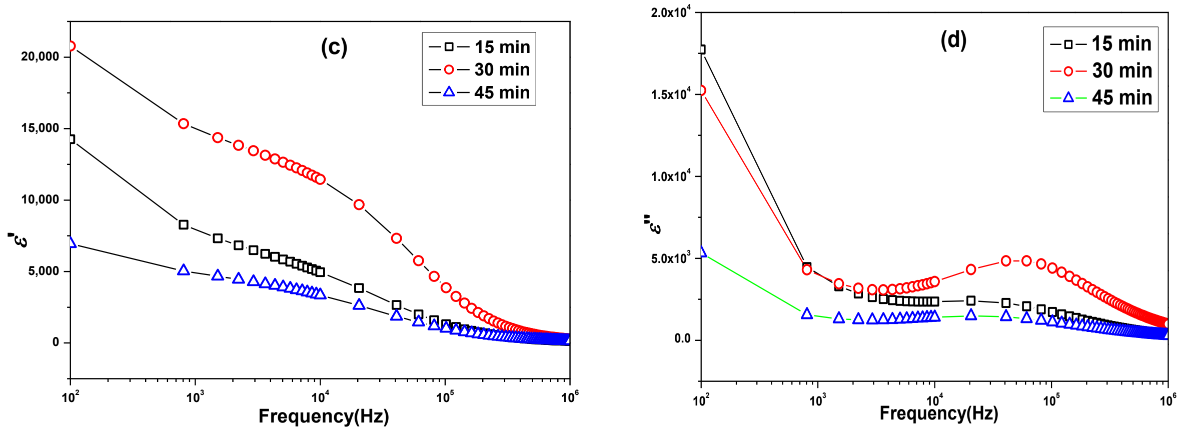

Fig. 7.3: Room temperature frequency variation of (c) dielectric constant and (d) dielectric loss of the Pb (0.08) modified MWS BFN ceramics.

Figs. 7.3 (e) & (f) shows the frequency variation of the dielectric constant (ε') and dielectric loss (ε") of the Cr added BFN ceramics MWS for 15, 30 and 45 min sintering durations, respectively. Similar dielectric behaviour as in case of La and Pb modified BFN ceramics is observed. The value of ε' increases with the increase in sintering time duration. This can be associated to the increase in grain size with the increase in sintering time duration.

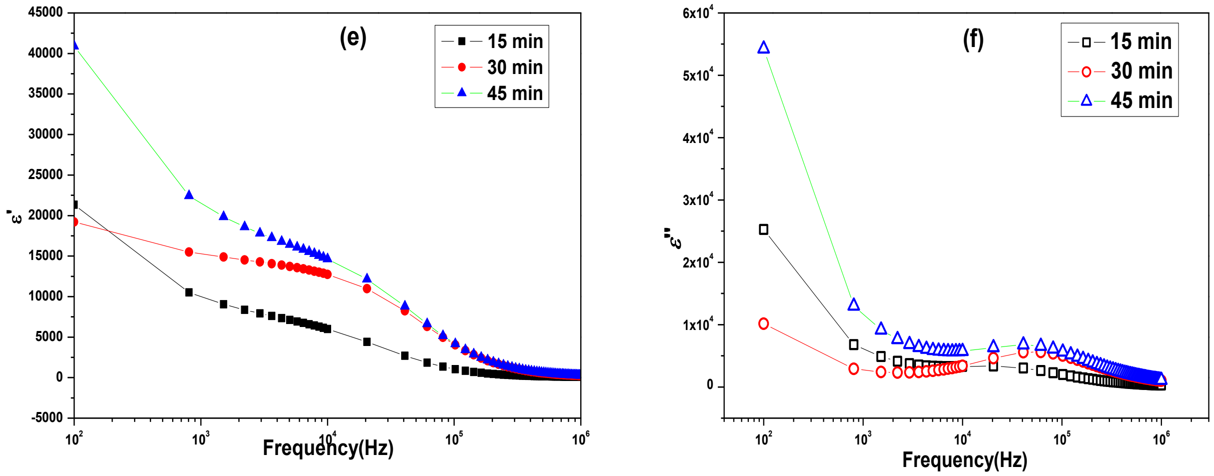

Fig. 7.3: Room temperature frequency variation of (e) dielectric constant and (f) dielectric loss of the Cr (0.5 wt %) modified MWS BFN ceramics.

Figs. 7.3 (g) & (h) show the frequency variation of the dielectric constant (ε') and dielectric loss (ε") of the Mn added BFN ceramics MWS for 15, 30 and 45 min sintering durations, respectively. In the ε' plots, a low frequency dispersion is followed by high frequency plateau region. There is no such low frequency plateau region is observed in the ε" plots. Corresponding to dispersion in the ε' plot, relaxation peak are observed in the ε" plots. The relaxation peaks for all the Mn added BFN ceramics samples lies below 10 kHz frequency. This indicates that the Maxwell-Wagner type of interfacial polarisation [3] is responsible for dielectric relaxation and high dielectric constant in Mn added BFN ceramics samples.

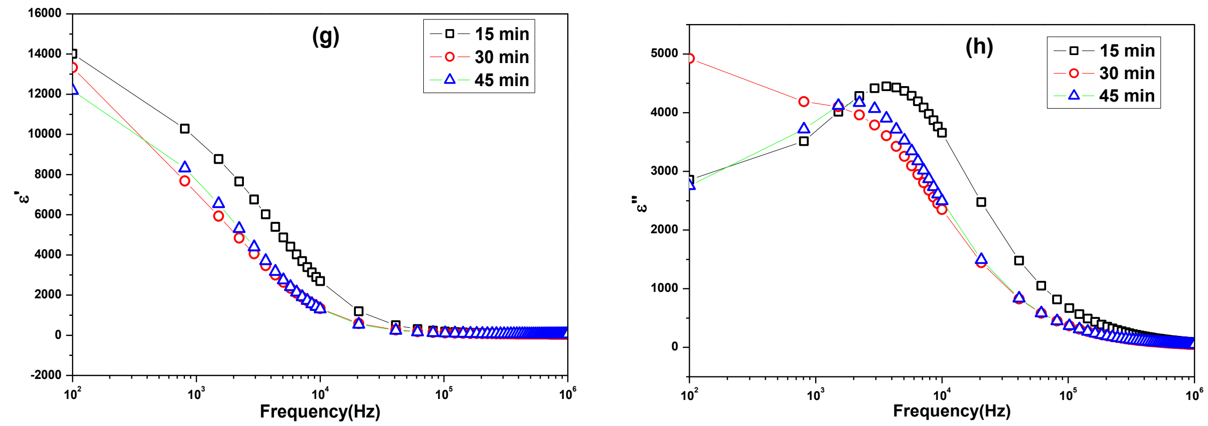

Fig. 7.3: Room temperature frequency variation of (g) dielectric constant and (h) dielectric loss of the Mn (0.5 wt %) modified MWS BFN ceramics.

The salient observations and the possible mechanisms, which may account the observed dielectric properties of the MWS La, Pb, Cr and Mn modified BFN ceramics are given below:

(i) The nature of the frequency variation of ε' and ε'' is almost similar for all the MWS La, Pb, Cr and Mn modified BFN ceramics sintered for different time periods.

(ii) In all the MWS La, Pb, Cr and Mn modified BFN ceramics two dispersive regions are observed in the ε' vs. frequency spectrum. These two dispersive regions are observed one at below 10 kHz and another at above 10 kHz frequencies, respectively, which indicates that two different types of relaxation mechanism are present in these ceramics. Moreover, this further suggests that in the MWS La, Pb, Cr and Mn modified BFN ceramics, the space charge polarisation is present below 10 kHz [4] and the interfacial Maxwell-Wagner type polarisation is present above 10 kHz [5-7] frequencies. The interfacial Maxwell-Wagner type polarisation can be explained on the basis of oxygen loss from the lattice during high temperature sintering of the ceramics, which can make the sintered system semiconducting. The loss of oxygen is associated with the release of electrons which may promote Fe^{3+}-Fe^{2+} hopping type polarisation, shown in below equations. Further the ε" peak of all the MWS La, Pb, Cr and Mn modified BFN ceramics falls ~10^5 Hz frequency, which indicates that both the Maxwell-Wagner type [3] and the hopping types of polarisations [8] are present in these ceramics:

$$O_O^X \rightarrow \frac{1}{2} O_2 + V_O^{\bullet} + e' \quad , \quad Fe^{3+} + e' \leftrightarrow Fe^{2+}$$

(iii) In the Mn added BFN ceramics only one dispersive region, below 10 kHz frequency, is observed in the ε' vs. frequency spectrum. In the 10kHz to 1MHz frequency region, the ε' value remains constant with a value ~10^2, which suggest the presence of Maxwell-Wagner type interfacial polarisation in this system [3].

(iv) In all the MWS La, Pb, Cr and Mn modified BFN ceramics, the value ε' drops to a value ~10^2 at 1 MHz frequency from 10^4 at 100 Hz frequency. The sudden large decrease in the ε' value with the increase of frequency suggest the presence of intrinsic or grain polarisation in these ceramics [9].

(v) In all the MWS La, Pb, Cr and Mn modified BFN ceramics, corresponding to the dispersion in the ε' vs. frequency plots a relaxation peak is observed in the ε" vs. frequency plots. The observed broadening in the ε" vs. frequency spectrum of all the MWS La, Pb, Cr and Mn modified BFN ceramics indicate the presence of non-Debye type of relaxation in these ceramics [10].

(vi) The low frequency dispersion in the ε" vs. frequency spectrum, observed in the MWS La, Pb doped and Cr added BFN ceramics, can be attributed to dc conductivity of these systems [11, 12].

(vii) In all the MWS La, Pb, Cr and Mn modified BFN ceramics the variation of ε' and ε" with sintering time duration, respectively can be attributed to the average grain size and interaction of MW with the sintered ceramics.

7.4.2 Temperature variation of the dielectric properties of the MWS La, Pb, Cr and Mn Modified BFN Ceramics

Figs. 7.4 (a) and (b) show the temperature variation of the dielectric constant and dielectric loss of the La (x=0.08) modified BFN ceramics MWS for 15, 30 and 45 min sintering durations, respectively. La doped BFN ceramic samples, MWS for 45 min, possess highest dielectric constant ~38384 at RT. The value of ε_r of MWS is nearly equal to that of the corresponding CS ceramic samples. The dielectric loss (tanδ) of the MWS La modified BFN ceramic samples is lower in comparison to the corresponding CS ceramic samples. Moreover there is not much change in the values of ε_r and tanδ upto 100°C, which indicates the superiority of MWS process over CS process and the usefulness of this compound for dielectric applications. The increase in dielectric constant with sintering time duration is attributed to the increase in grain size [1, 13].

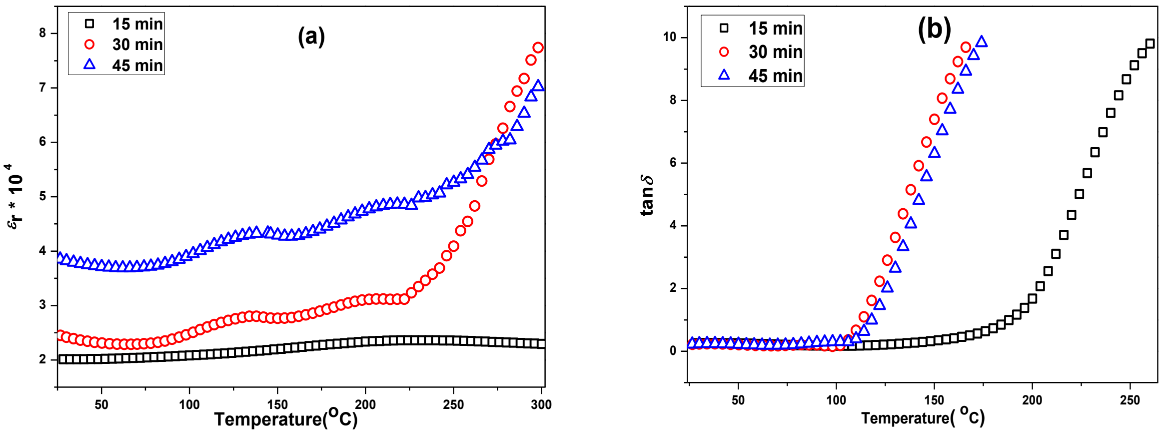

Fig. 7.4: Temperature variation of (a) dielectric constant and (b) dielectric loss at 10 kHz frequency of the La (x=0.08) modified MWS BFN ceramics at different sintering duration.

Table 7.3: Room temperature dielectric constant and dielectric loss of the CS and MWS ceramics.

Modification	**ε_r**			**tanδ**			**CS**	
	15 min	**30 min**	**45 min**	**15 min**	**30 min**	**45 min**	**ε_r**	**tanδ**
La (x=0.08)	20106	24334	38384	0.25	0.23	0.23	35844	1.49
Pb (x=0.08)	15006	21023	23144	0.40	0.34	0.38	25999	0.59
Cr (0.5 wt %)	11313	14623	17363	0.26	0.25	0.34	38832	0.76
Mn (0.5 wt %)	2230	3612	2404	4.09	1.74	3.84	4245	4.41

Figs. 7.4 (c) and (d) show the temperature variation of ε_r and tanδ of the Pb modified (x=0.08) BFN ceramics MWS for 15, 30 and 45 min sintering durations, respectively. The value of ε_r increases with the increase in sintering time duration. The dielectric plots of the Pb modified (x=0.08) BFN ceramics MWS for 30 and 45 min sintering durations possesses dielectric anomaly near 160 and 210°C, respectively. The value of tanδ of the Pb modified system remains independent of temperature upto ~110°C and lower in comparison to that of the corresponding CS samples. The dielectric properties of the MWS and CS Pb (x=0.08) modified BFN ceramics are given in Table 7.3.

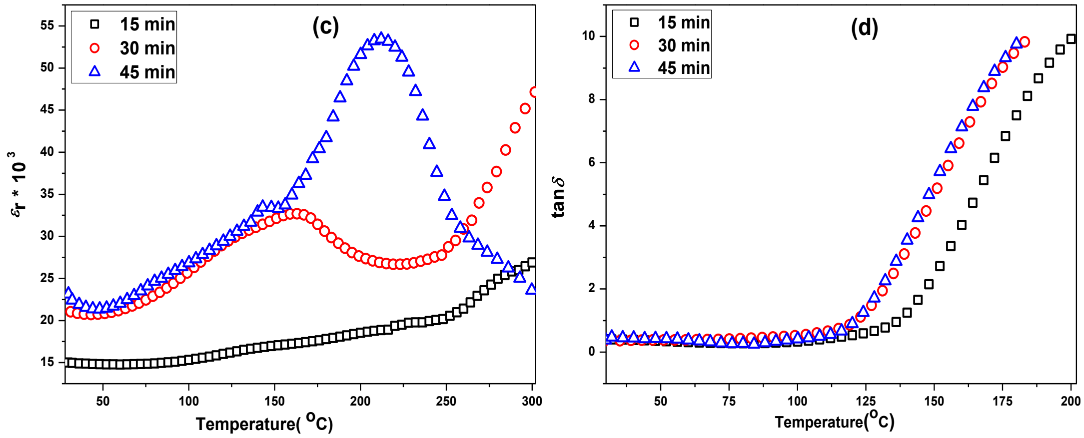

Fig. 7.4: Temperature variation of (c) dielectric constant and (d) dielectric loss at 10 kHz frequency of the Pb (x=0.08) modified MWS BFN ceramics at different sintering duration.

Figs. 7.4 (e) and (f) show the temperature variation of ε_r and tanδ of the Cr (x=0.5 wt %) modified BFN ceramics MWS for 15, 30 and 45 min sintering durations, respectively. The room temperature dielectric values of these MWS ceramics are given in Table 7.3. ε_r is highest for the Cr (x=0.5 wt %) added BFN ceramics MWS for 45 min. ε_r value is lower in comparison to the corresponding CS ceramics. The tanδ value remains independent of temperature up to

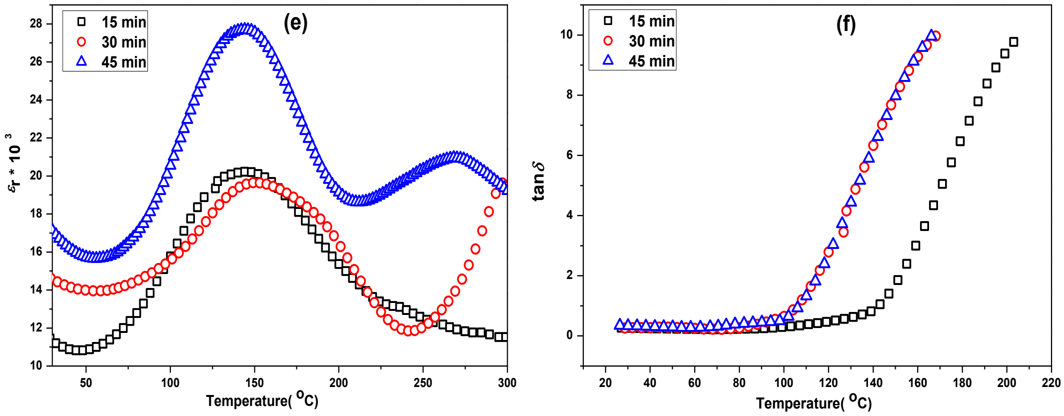

Fig. 7.4: Temperature variation of (e) dielectric constant and (f) dielectric loss at 10 kHz frequency of the Cr-added MWS BFN ceramics at different sintering duration.

~100°C. The low value of ε_r in comparison to the corresponding CS ceramics can be attributed to the small grain size of MWS samples. The decrease in dielectric constant is directly related to increase in grain size as reported in literature [14].

Figs. 7.4 (g) and (h) show the temperature variation of ε_r and $\tan\delta$ of Mn (x=0.5 wt %) modified BFN ceramics MWS for 15, 30 and 45 min sintering durations, respectively. The room temperature dielectric values of these MWS ceramics are given in Table 7.3. The value of ε_r increases linearly with the increase in temperature for all the MWS samples. The value of $\tan\delta$ first decreases to a minimum value and then increases at higher temperature. Large temperature coefficient of capacitance hints towards the use of these ceramics for bolometer and temperature detector application.

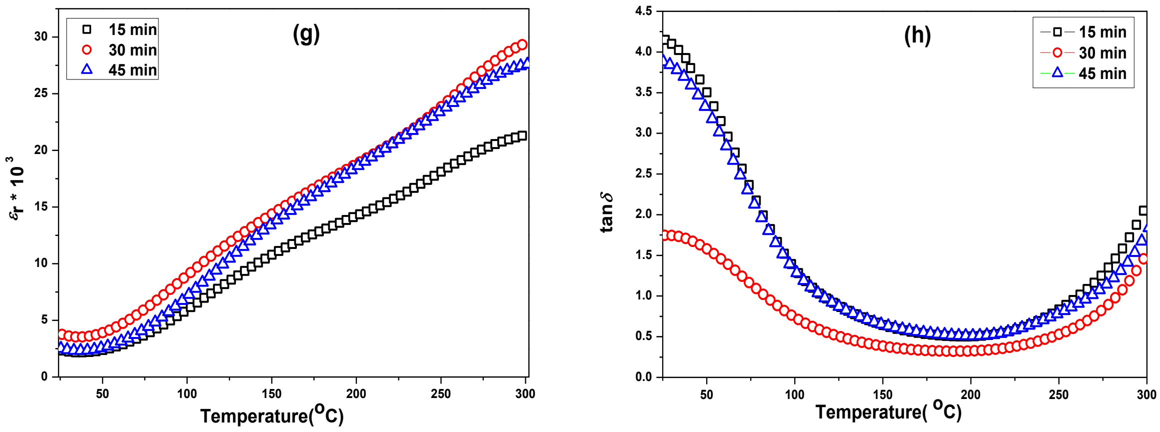

Fig. 7.4: Temperature variation of (a) dielectric constant and (b) dielectric loss at 10 kHz frequency of the Mn-added MWS BFN ceramics at different sintering duration.

7.5 Leakage Current and Polarization Studies

The values of leakage current (I), measured at 50V up to a time period (t) of 20sec, of the MWS La, Pb, Cr and Mn modified BFN ceramics are given in Table 7.4. High value of leakage current is observed for both the La and Pb modified MWS BFN ceramics, compared to the corresponding CS ones. The value of the leakage current of the MWS Cr modified BFN system has greatly reduced.

Table 7.4: Room temperature leakage current values of the MWS and CS BFN based ceramics.

Modification		**La** **(x=0.08)**	**Pb** **(x=0.08)**	**Cr** **(x=0.5 wt %)**	**Mn** **(x=0.5 wt %)**
Leakage current(A)	MWS	$2.56\text{x}10^{-4}$	$2.52\ \text{x}10^{-4}$	$8.80\ \text{x}10^{-10}$	$1.25\ \text{x}10^{-5}$
	CS	$1.28\ \text{x}10^{-6}$	$3.01\ \text{x}10^{-6}$	$5.85\ \text{x}10^{-7}$	$2.09\ \text{x}10^{-5}$

The polarizations vs. voltage loop behaviour of all the MWS La, Pb, Cr and Mn modified BFN ceramics are shown in Fig. 7.5. Development of no saturation in all these loops confirms the non-ferroelectric nature of these ceramics. The polarization vs. voltage loops indicates that the leakage current contribution [15] is present in the La, Pb and Cr modified BFN samples, whereas the loop corresponding to the Mn modified BFN system can be termed as the lossy one [16].

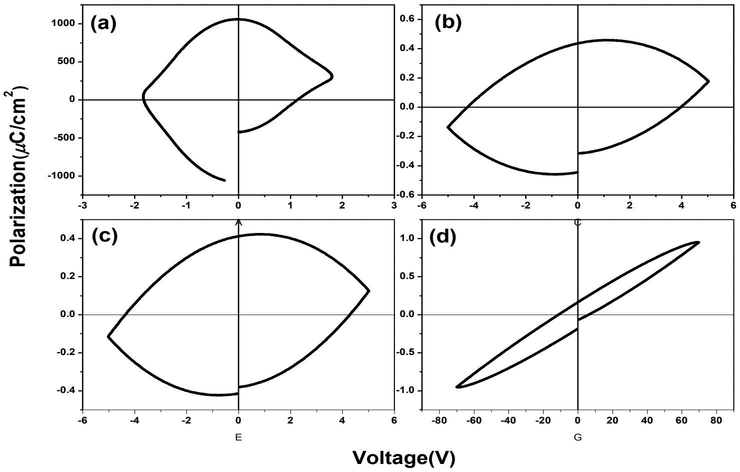

Fig. 7.5: Polarization vs. voltage loops of MWS (a) La (x=0.08), (b) Pb (x=0.08), (c) Cr (x=0.5 wt %) and (d) Mn (x=0.5 wt %) ceramics.

7.5 Chapter Summary

Selected compositions of the La, Pb, Cr and Mn modified BFN ceramics were sintered in a MW furnace. The microstructure formed during the sintering process influence the dielectric and electrical properties of the ceramics. Therefore, the selected compounds with better dielectric properties were sintered in a MW furnace. The following conclusions are drawn from the above study.

The XRD patterns confirmed formation of single phase with cubic structure for all the MWS ceramics. The grain size of the MWS ceramics increased with increase in sintering time. Except Cr added BFN ceramics, all samples exhibited nearly same grain size as that of CS. The density of all the MWS samples sintered for 45 min (except Mn added BFN ceramics) exhibited higher density than the corresponding CS ceramic samples.

The dielectric properties study confirmed very high value of dielectric constant (ε_r) ($\sim 10^4$) for all the samples (except Mn added BFN ceramics) at room temperature. The RT dielectric loss of all the MWS ceramics was lower compared to the corresponding CS ceramic samples. This indicated that the MW sintering can serve as an effective technique for reducing the dielectric loss with better dielectric properties in less processing time.

References

[1] K.V.R. Prasad, A.R. Raju, K.B.R. Varma, Grain size effects on the dielectric properties of ferroelectric $Bi_2VO_{5.5}$ ceramics, J. Mater. Sci. 29 (10) (1994) 2691-2696.

[2] D.K. Agrawal, Microwave processing of ceramics, Curr. Opin. Solid State Mater. Sci. 3 (5) (1998) 480-485.

[3] P. Cheng, S. Li, L. Zhang, J. Li, Characterization of intrinsic donor defects in ZnO ceramics by dielectric spectroscopy, Appl. Phys. Lett. 93 (1) (2008) 012902-012903.

[4] V. Shrivastava, A.K. Jha, R.G. Mendiratta, Dielectric studies of La and Pb doped $SrBi_2Nb_2O_9$ ferroelectric ceramic, Mater. Lett. 60 (12) (2006) 1459-1462.

[5] J. Liu, C.-g. Duan, W.N. Mei, R.W. Smith, J.R. Hardy, Dielectric properties and Maxwell-Wagner relaxation of compounds $ACu_3Ti_4O_{12}$ ($A = Ca,Bi_{2/3},Y_{2/3},La_{2/3}$), J. Appl. Phys. 98 (9) (2005) 093703-093705.

[6] C.C. Wang, H.B. Lu, K.J. Jin, G.Z. Yang, Temperature-dependent dielectric strength of a maxwell wagner type relaxation, Mod. Phys. Lett. B 22 (13) (2008) 1297-1305.

[7] N. Bona, A. Ortenzi, S. Capaccioli, Advances in understanding the relationship between rock wettability and high-frequency dielectric response, Journal of Petroleum Science and Engineering 33 (1-3) (2002) 87-99.

[8] A.N. Papathanassiou, J. Grammatikakis, I. Sakellis, S. Sakkopoulos, E. Vitoratos, E. Dalas, Hopping charge transport mechanisms in conducting polypyrrole: Studying the thermal degradation of the dielectric relaxation, Appl. Phys. Lett. 87 (15) (2005) 154107.

[9] D.K. Mahato, A. Dutta, T.P. Sinha, Dielectric relaxation in double perovskite oxide, Ho_2CdTiO_6, Bull. Mater. Sci. 34 (3) (2011) 455-462.

[10] K.S. Cole, R.H. Cole, Dispersion and Absorption in Dielectrics I. Alternating Current Characteristics, J. Chem. Phys. 9 (4) (1941) 341-351.

[11] G. Georgoussis, A. Kanapitsas, P. Pissis, Y.V. Savelyev, V.Y. Veselov, E.G. Privalko, Structure-property relationships in segmented polyurethanes with metal chelates in the main chain, Eur. Polym. J. 36 (2000) 1113 -1126.

[12] A.S. Roy, K.R. Anilkumar, M.V.N.A. Prasad, Studies of AC conductivity and dielectric relaxation behavior of CdO-doped nanometric polyaniline, J. Appl. Polym. Sci. 123 (4) (2011) 1928-1934.

[13] H.T. Martirena, J.C. Burfoot, Grain-size effects on properties of some ferroelectric ceramics, Journal of Physics C: Solid State Physics 7 (17) (1974) 3182.

[14] I. Norezan, A.K. Yahya, M.K. Talari, Effect of $(Ba_{0.6}Sr_{0.4})TiO_3$ (BST) Doping on Dielectric Properties of $CaCu_3Ti_4O_{12}$ (CCTO), Journal of Materials Science & Technology 28 (12) (2012) 1137-1144.

[15] A. Gronotte, Development of new chemical processes to lead-free piezoelectric and ferroelectric materials, in: Department of Chemistry, Vol. Master of Science, Simon Fraser University, 2009.

[16] M. Stewart, M.G. Cain, D.A. Hall, Ferroelectric Hysteresis Measurement and Analysis, in: Technical Report CMMT (A) 152, National Physical Laboratory, Teddington UK, 1999.

CHAPTER 8

Conductivity and Impedance Spectroscopic Study of the CS & MWS Modified BFN Ceramics

8.1 Introduction

In this chapter, the conductivity and impedance spectroscopic studies of (i)Ba(1-x)$La_{2x/3}(FeNb)_{0.5}O_3$ (x=0.08)/BLFN, (ii) Ba(1-x)$Pb_x(FeNb)_{0.5}O_3$ (x=0.08)/PBFN, (iii) Ba $(FeNb)_{0.5}O_3$ – x wt% of $MnCO_3$ (x=0.5)/Mn-BFN and (iv) Ba $(FeNb)_{0.5}O_3$ – x wt% of Cr_2O_3 (x=0.5)/Cr-BFN ceramics (conventionally and microwave sintered, respectively) are investigated and discussed in detail.

8.2 Conductivity Study

The ac conductivity measurement is a useful technique for investigating the charge carrier's nature, conduction and relaxation mechanism. The frequency variation of ac conductivity can be explained by Jonscher's power law (JPL): [1, 2]

$$\sigma(\omega) = \sigma_{dc} + a\omega^S \qquad (8.1)$$

Where, σ_{dc} is the dc conductivity, which represents the frequency independent plateau region at low frequency region, and **a** and **s (0<s <1)** are the frequency and temperature dependent parameters. But, the conductivity behavior of certain materials cannot be explained by the Jonscher's power law. For these kind of materials, the value of s is greater than 1 [3] and the double power law is applicable. The double power law is favorable to the jump relaxation model (JRM), given by Funke [4]. According to this model, at low frequencies the long range translational motion of ions is dominant. In the low frequency region, two processes: the unsuccessful hopping (forward-backward-forward) of ions, moving back to its initial position and the successful localized hopping, compete with each other. The double power law is given as:

$$\sigma(\omega) = \sigma_{dc} + A\omega^m + B\omega^n \qquad (8.2)$$

Where, the coefficients A & B and exponents ‘m’ & ‘n’ are dependent on the temperature and frequency. The value of ‘m’ and ‘n’ are $0<m<1$, $1<n<2$. The use of double power law and interpretation of extracted parameters is explained earlier [5, 6].

8.2.1 AC and DC Conductivity Study of the CS BLFN Ceramic

Fig. 8.1(a) shows the frequency variation of the ac conductivity (σ_{ac}) at various temperatures of the BLFN ceramics. The σ_{ac} contains both the frequency independent i.e. the dc conductivity (σ_{dc}) part in the low frequency region and the frequency dependent part in the high frequency region. The σ_{ac} spectrum of the BLFN ceramics obeys the double power law. Fig. 8.1(b) shows the temperature variation of the extracted parameters, m ($0<m<1$) and n ($1<n<2$), mentioned in equation 8.2.

The variation of the dc conductivity (σ_{dc}) with the inverse of the absolute temperature of the BLFN ceramics is shown in Fig. 8.1(c). The σ_{dc} variation with temperature follows the Arrhenius behavior. Activation energies ~0.60eV (>120 °C) and 0.08(<120 °C) eV are observed for the BLFN ceramic samples. The value of m and n justifies the use of the double power law to explain the conductivity behavior of the BLFN ceramics.

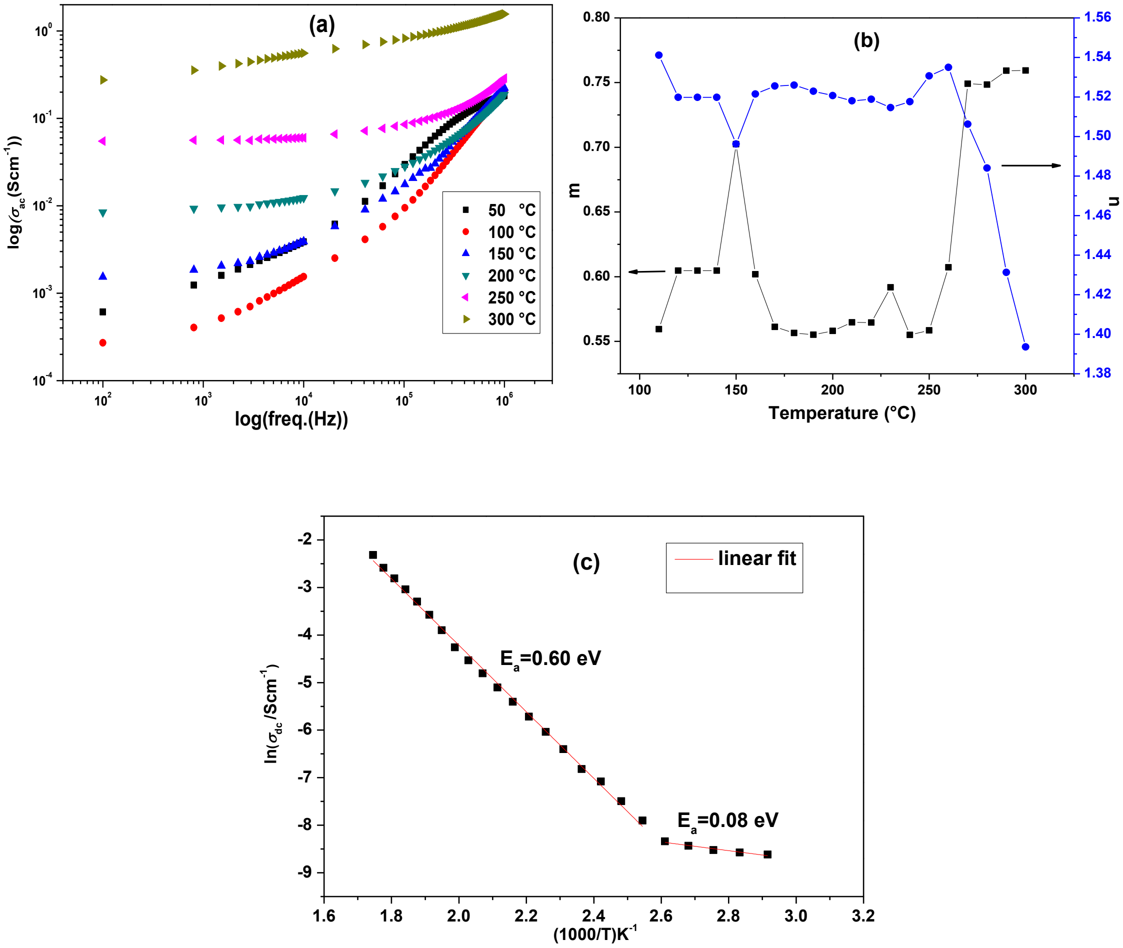

Fig. 8.1: (a) AC conductivity (σ_{ac}) vs. frequency at various temperatures (b) Temperature variation of the extracted parameters, & (c) The variation of dc conductivity with inverse of temperature of the CS BLFN ceramic.

8.2.2 AC and DC Conductivity Study of the CS PBFN Ceramic

Fig. 8.2(a) shows the frequency variation of the σ_{ac} at various temperatures the PBFN ceramics. The dc conductivity increases with the increase in temperature. A high frequency plateau region is observed at low temperature (50°C). With the increase in temperature the conductivity of the grain and the grain boundary increases together and because of that the plateau region does not becomes prominent at high temperatures. The ac conductivity spectrum of the PBFN ceramics obeys Jonscher's double power law. Fig. 8.2(b) shows the temperature variation of the extracted parameters m (0<m<1) and n (1<n<2).

The variation of the dc conductivity with the inverse of absolute temperature of the PBFN ceramics is shown in Fig. 8.2. The dc conductivity of the PBFN ceramics also follows the Arrhenius behavior. The activation energies ~0.68eV (>110 °C) & 0.16 eV (<110 °C) are obtained for the PBFN ceramics.

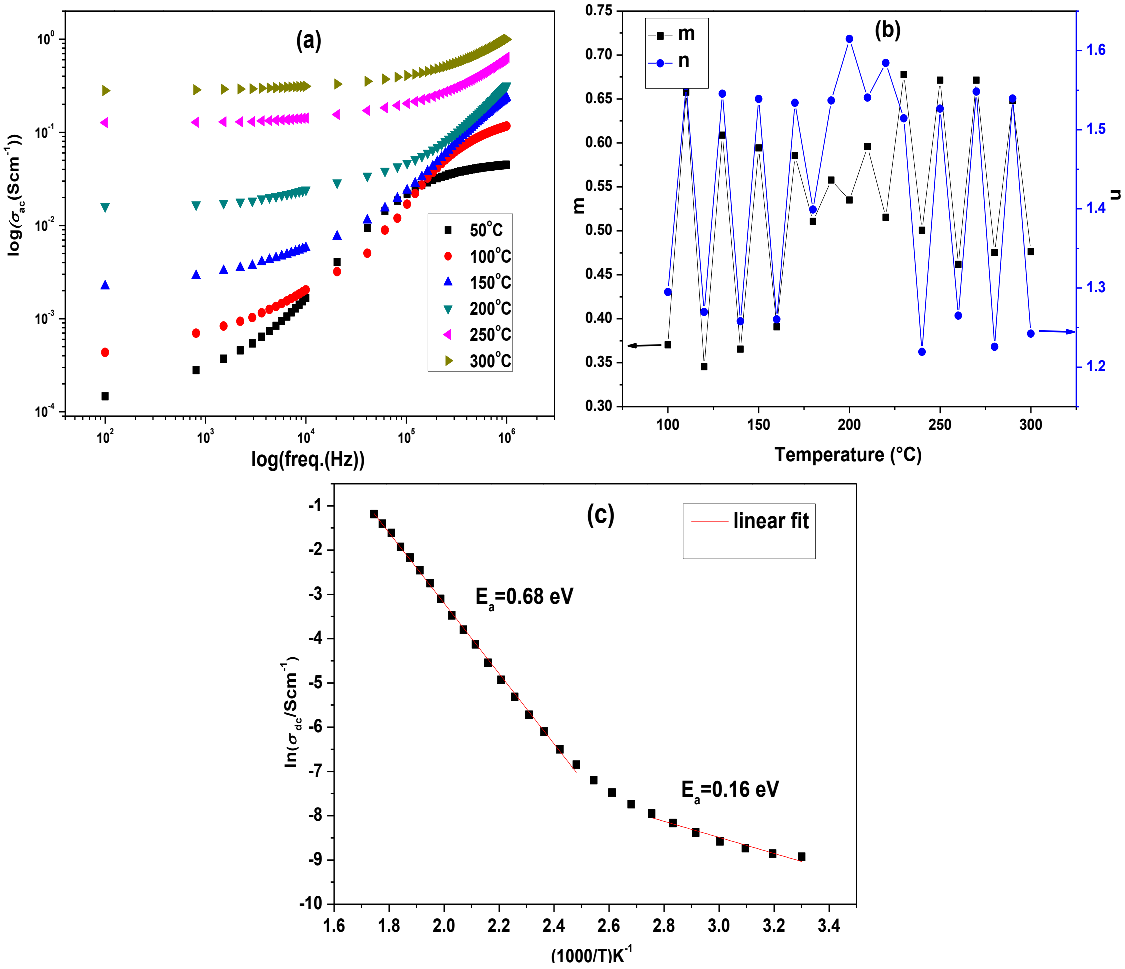

Fig. 8.2: (a) AC conductivity (σ_{ac}) vs. frequency at various temperatures (b) Temperature variation of the extracted parameters, & (c) The variation of dc conductivity with inverse of temperature of the CS PBFN ceramic.

8.2.3 AC and DC Conductivity Study of the CS Cr-BFN Ceramic

Fig. 8.3(a) shows the frequency variation of the ac conductivity at various temperatures of the Cr-BFN ceramics. The ac conductivity spectrum of the Cr-BFN ceramics also obeys the double power law. Fig. 8.3(b) shows the temperature variation of the extracted parameters m (0<m<1) and n (1<n<2). The temperature variation of the d.c. conductivity of Cr-BFN ceramics is shown in Fig. 8.3(c). The dc conductivity variation with temperature the Cr-BFN ceramics also follows the Arrhenius behavior. The activation energies ~0.62 (>120 °C) &0.21 (<120 °C) are found for the Cr-BFN ceramic samples.

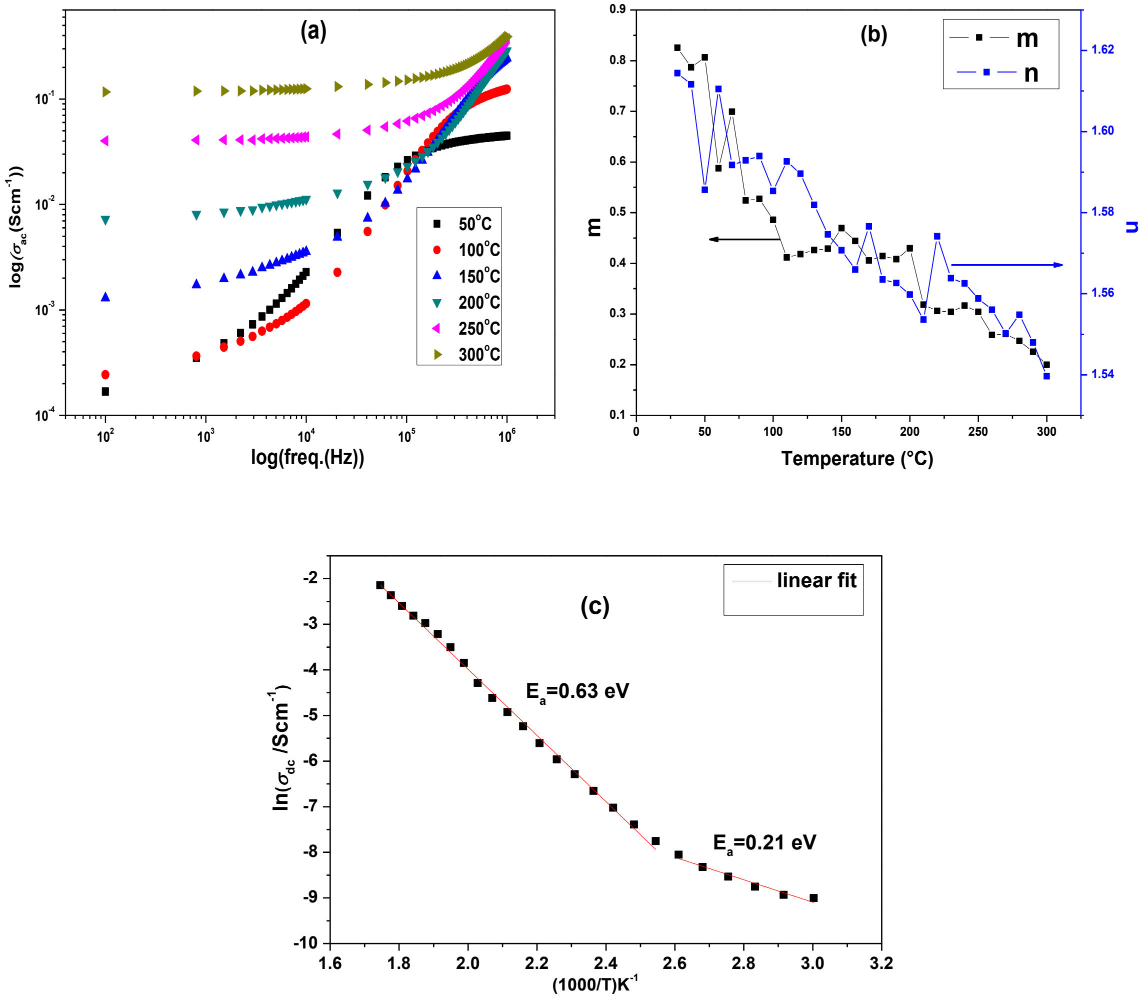

Fig. 8.3: (a) AC conductivity (σ_{ac}) vs. frequency at various temperatures (b) Temperature variation of the extracted parameters, & (c) The variation of dc conductivity with inverse of temperature of the CS Cr-BFN ceramic.

8.2.4 AC and DC Conductivity Study of the CS Mn-BFN Ceramic

The frequency variation of the ac conductivity at various temperatures of the Mn-BFN ceramics is shown in Fig. 8.4(a). Here, we observe two different types of conductivity spectrum in a single plot. One conductivity spectrum at high frequency follows the Jonscher's power law (JPL) and the other conductivity spectrum at low frequency also follows the JPL. Following are the salient observations from the conductivity spectrum of the Mn-BFN ceramics (i) Above 20 kHz (at 50°C), the conductivity spectrum exhibit 2 different regions, one low frequency plateau region (dc conductivity) and the second the high frequency dispersive region, (ii) Below 20 kHz (at 50°C), the conductivity spectrum exhibits only a dispersive region with no low frequency plateau region, (iii) Above 100°C, the high frequency conductivity spectrum becomes diminished whereas a prominent plateau region arises in the low frequency region , (iv) Both the conductivity spectrum obeys JPL.

The variation of the dc conductivity with the inverse of the absolute temperature is shown in Fig. 8.4(c). The dc conductivity variation with temperature of the Mn modified BFN also follows the Arrhenius behavior. Activation energies ~0.89 (>110 °C) &0.32 (<110 °C) eV are observed. The activation energy for the higher frequency conductivity spectrum is lower than that of the lower frequency one. The high value of dc activation energy (0.89) indicates oxygen vacancies responsible for high temperature conduction [7, 8].

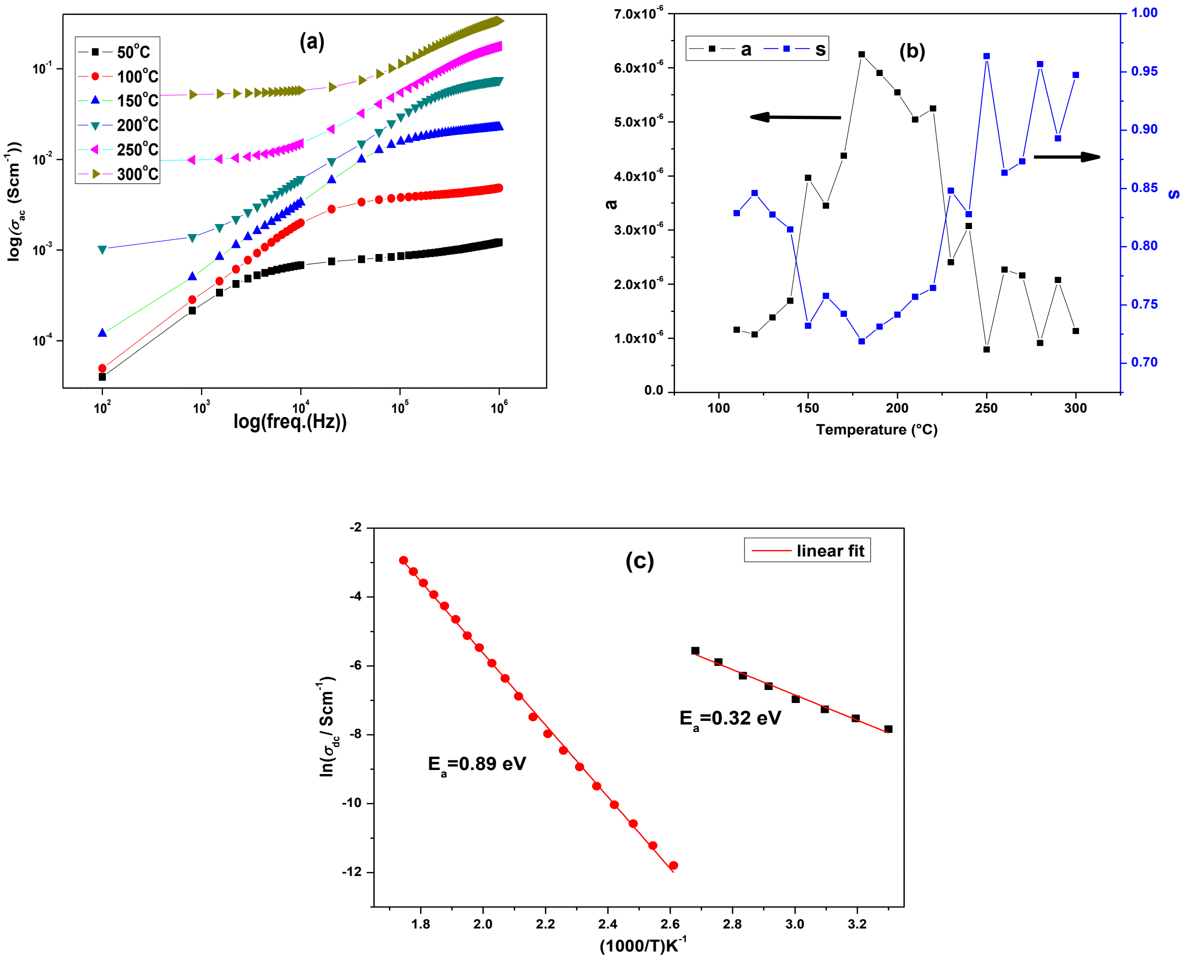

Fig. 8.4: (a) AC conductivity (σ_{ac}) vs. frequency at various temperatures (b) Temperature variation of the extracted parameters, & (c) The variation of dc conductivity with inverse of temperature of the CS Mn-BFN ceramic.

8.2.5 AC and DC Conductivity Study of the MWS BLFN Ceramic

Fig. 8.5 (a) shows the frequency variation of the ac conductivity at various temperatures of the BLFN ceramic samples. The dc conductivity increases with the increase in temperature. The ac conductivity spectrum obeys the Jonscher's double power law. The temperature variation of the extracted parameters m (0<m<1) and n (1<n<2) is shown in Fig 8.5(b). The variation of the dc conductivity with the inverse of the absolute temperature of the BLFN ceramics is shown in Fig. 8.5(c). The dc conductivity variation with temperature follows the Arrhenius behavior. The activation energies ~0.73 (>180 °C) & 0.42 eV (<180 °C) are obtained in the BLFN samples.

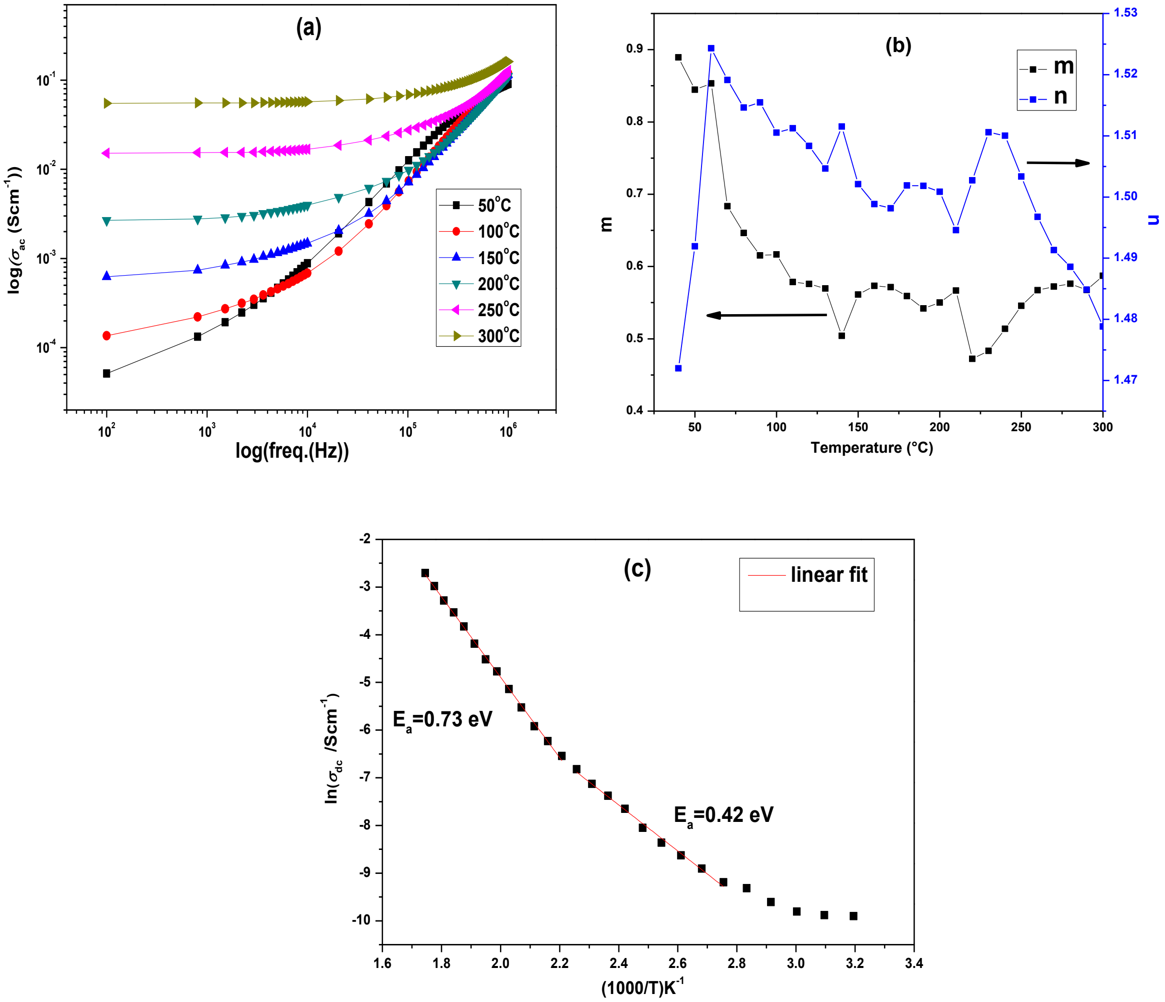

Fig. 8.5: (a) AC conductivity (σ_{ac}) vs. frequency at various temperatures (b) Temperature variation of the extracted parameters, & (c) The variation of dc conductivity with inverse of temperature of the MWS BLFN ceramic.

8.2.6 AC and DC Conductivity Study of the MWS PBFN Ceramics

Fig. 8.6 (a) shows the frequency variation of the ac conductivity at various temperatures of the PBFN ceramic samples. The dc conductivity increases with the increase in temperature. The ac conductivity at different temperatures obeys the double power law. The temperature variation of the extracted parameter m (0<m<1) and n (1<n<2) is shown in Fig 8.6(b).

The d.c. conductivity variation with temperature of the PBFN ceramics also follows the Arrhenius behavior, shown in Fig. 8.6(c). The activation energies ~0.68 (>160 °C) & 0.38 eV (<160 °C) are obtained in the PBFN ceramic samples.

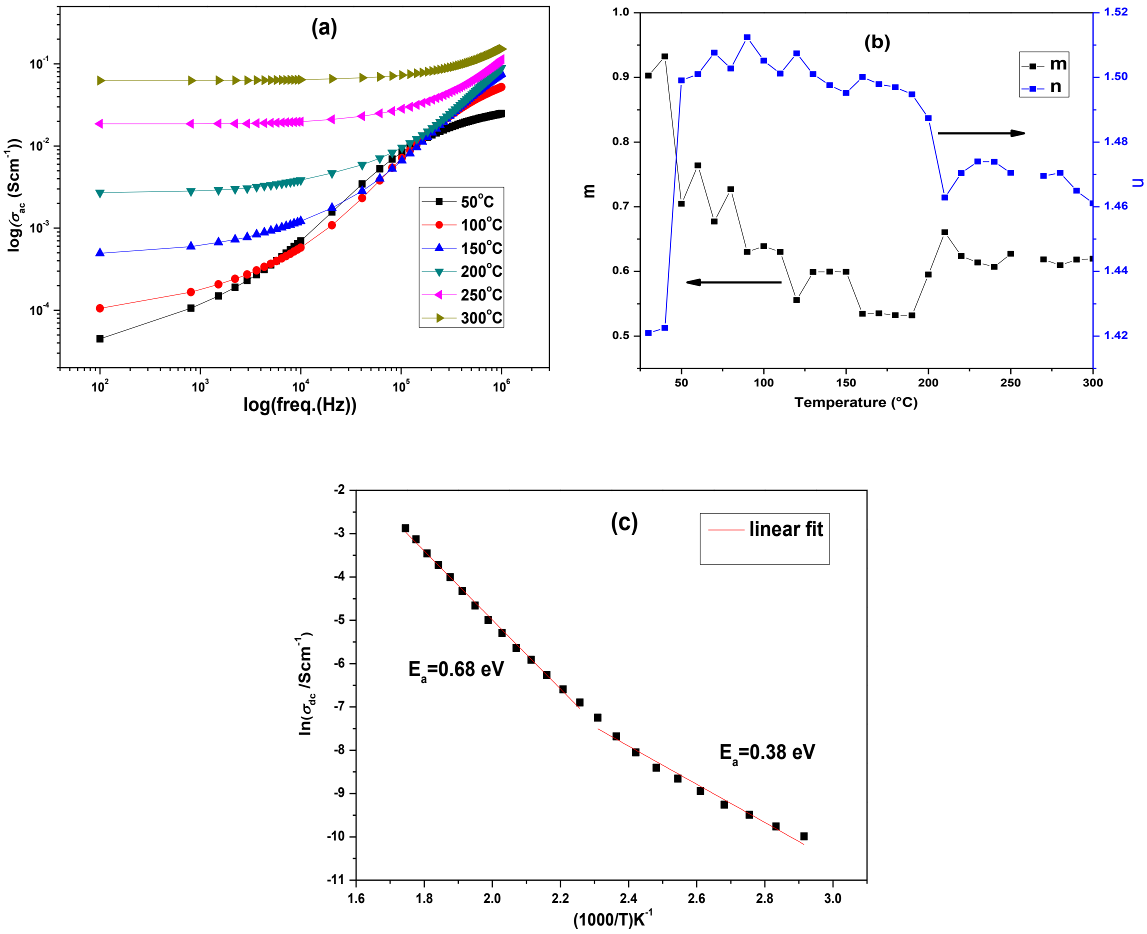

Fig. 8.6: (a) AC conductivity (σ_{ac}) vs. frequency at various temperatures (b) Temperature variation of the extracted parameters, & (c) The variation of dc conductivity with inverse of temperature of the MWS PBFN ceramic.

8.2.7 AC and DC Conductivity Study of the MWS Cr-BFN Ceramic

The frequency dependent ac conductivity at selected temperatures of the Cr-BFN ceramics is shown in Fig 8.7(a). At lower frequencies the conductivity increases with the increase in temperature and at high frequencies all the conductivity curves merged together. The ac conductivity of the Cr-BFN ceramics obeys the double power law behaviour. The temperature variation of the extracted parameters m (0<m<1) and n (1<n<2) is shown in Fig 8.7(b). The dc conductivity values, extracted by using double power law, obey the Arrhenius relation (Fig. 8.7(c)). The activation energies ~0.59 (>100 °C) &0.07 eV (<100)°C are obtained in Cr-BFN ceramics.

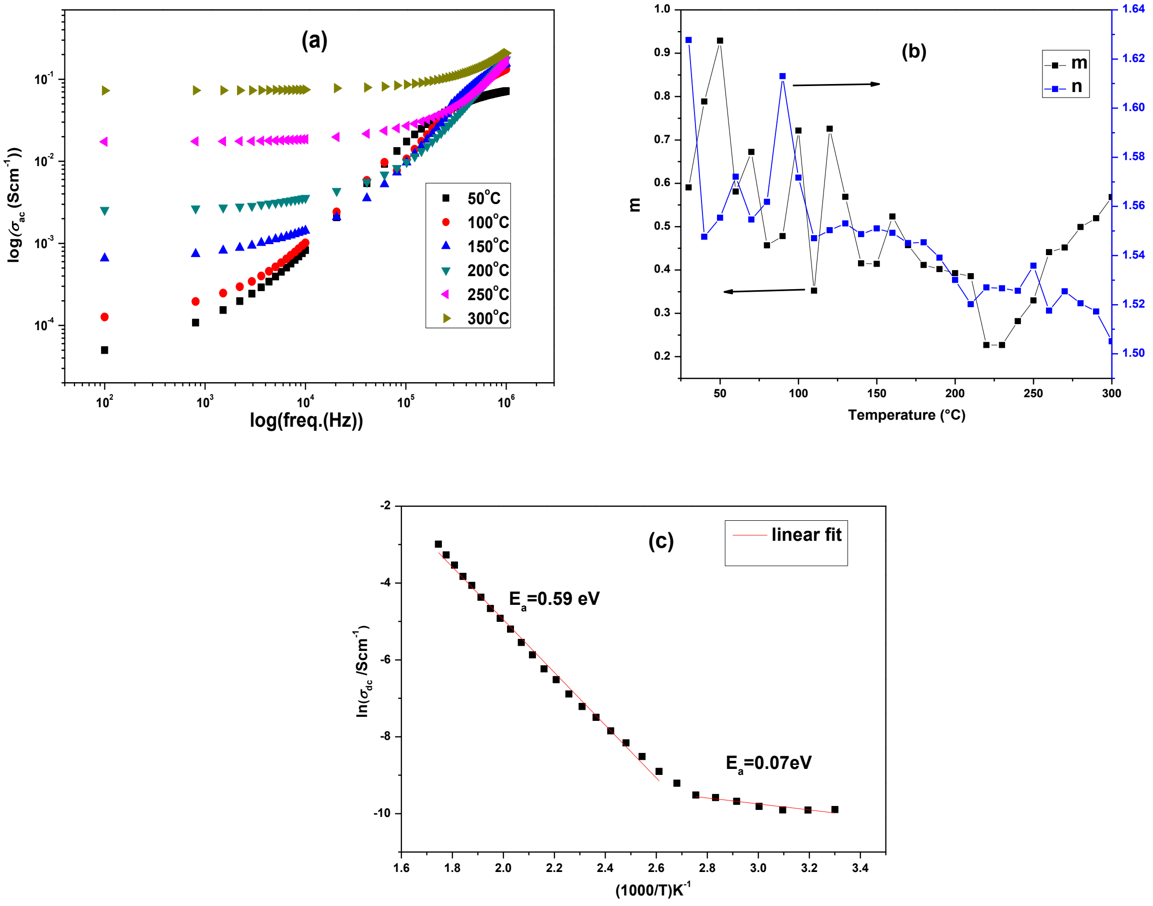

Fig. 8.7: (a) AC conductivity (σ_{ac}) vs. frequency at various temperatures (b) Temperature variation of the extracted parameters, & (c) The variation of dc conductivity with inverse of temperature of the MWS Cr-BFN ceramic.

8.2.8 AC and DC Conductivity Study of the MWS Mn-BFN Ceramic

The frequency variation of the ac conductivity at selected temperatures of the Mn-BFN ceramics is shown in Fig. 8.8(a). This conductivity spectrum has following interesting features:

(i) Below 20 kHz (at 50°C), a frequency dispersive region and above20 kHz a frequency independent region (plateau region).

(ii) Above 100°C, the lower frequency plateau region appears in the spectrum and becomes prominent above 180°C.

(iii) Above 150°C the higher frequency plateau region becomes diminished and the lower frequency plateau region (dc conductivity) becomes prominent.

The higher frequency plateau region is attributed to the resistance of the grains (details given in the impedance spectroscopic part). The ac conductivity of the Mn-BFN ceramics obeys the double power law feature. The extracted parameters, m (0<m<1) and n (1<n<2) variation with temperature is shown in Fig. 8.8(b). The temperature variation of the dc conductivity also follows the Arrhenius relation and shown in Fig. 8.8(c). The activation energies ~0.87 (>180 °C) &0.29 eV (<180 °C) are obtained in the Mn-BFN ceramic samples.

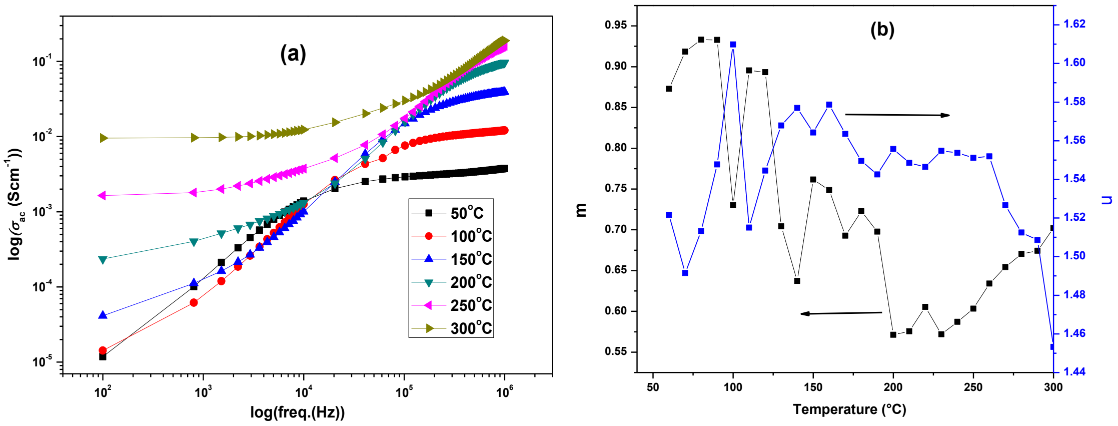

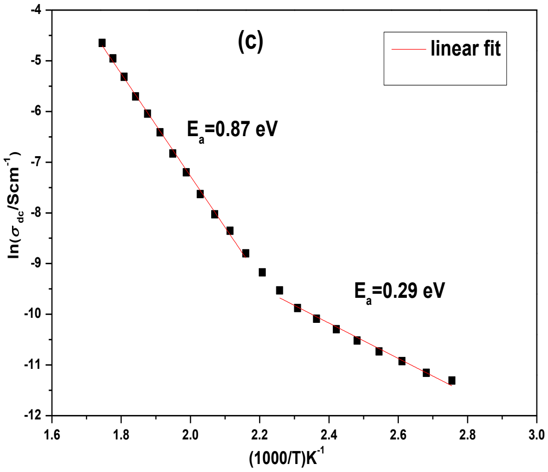

Fig. 8.8: (a) AC conductivity (σ_{ac}) vs. frequency at various temperatures (b) Temperature variation of the extracted parameters, & (c) The variation of dc conductivity with inverse of temperature of the MWS Mn-BFN ceramic.

8.3 Impedance Spectroscopy Study

The complex impedance spectroscopy (CIS) technique helps to separates the grain, grain boundary, and the electrode interface contributions to the electrical properties of a material. The high frequency series resistance is generally attributed to the grain property of the material. The low frequency arc of the impedance spectrum is attributed to the grain boundary. If the centre of the low frequency semicircle arc lies below the real axis then it justifies the presence of a constant phase element (CPE) [9] in fitting the corresponding RC circuit of the material. The CPE admittance is generally represented as: Y(CPE) = $A_0(j\omega)^n = A\omega^n + jB\omega^n$, [10] where, A = A_0Cos(nπ/2) and B = A0Sin(nπ/2). A_0 and n are the frequency independent but temperature dependent parameters, A_0 determines the magnitude of the dispersion and it varies between zero to 1 (0<n<1). The CPE describes an ideal capacitor for n=1 and an ideal resistor for n=0. The presence of CPE in the equivalent circuit represents the departure from Debye like ideality. Inhomogeneous distribution of the grain size and the defects in the grain boundaries can also produce a depressed semicircle in the Nyquist plot.

Appropriate equivalent circuit model can be chosen for fitting the impedance data. Generally, the resistance of the grain, grain boundary and the electrode interface follows the temperature dependence Arrhenius relation, given below as

$$R = R_0 \exp(-E_a / k_B T) \qquad (8.3)$$

8.3.1 Impedance Spectroscopy Study of the CS BLFN Ceramic

The Nyquist plot of the BLFN ceramics at different temperatures is shown in Fig. 8.9(a). This shows the presence of a series resistance followed by a semicircular arc, which indicates that both the grain and grain boundary phenomena are participating in the BLFN ceramic samples. The equivalent circuit, $R_g(R_{gb}CQ)$, is modeled according to the brick layer model. The variation of the resistances of the grain and the grain boundary versus inverse of the temperature is shown in Fig. 8.9(b). The resistance of the grain and the grain boundary follows the temperature dependent Arrhenius relation. Resistance corresponding to the grain and the grain boundary decreases with increase in temperature. The activation energies ~0.23 and 0.60 eV are calculated for the grain and grain boundaries, respectively.

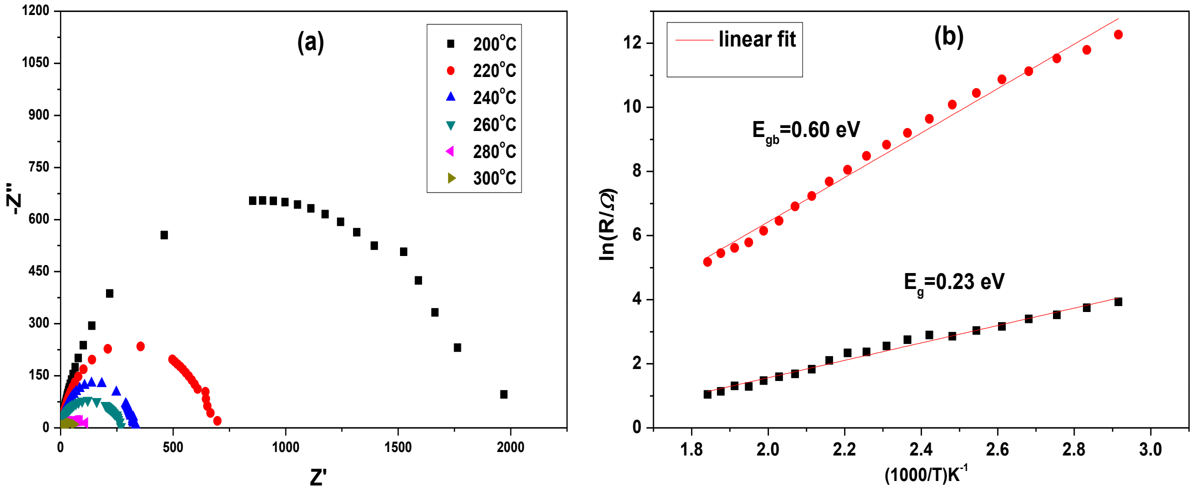

Fig. 8.9: (a) Nyquist plots at different temperature, and (b) Resistance of grain & grain boundary vs. inverse of temperature of the CS BLFN ceramic.

8.3.2 Impedance Spectroscopy Study of the CS PBFN Ceramic

The Nyquist plot of the PBFN ceramic at different temperatures is shown in Fig. 8.10(a). The grain and the grain boundary phenomena, participating in the conduction process, are confirmed by the Nyquist plot. The high frequency end is not terminated at the origin, which confirms the presence of series resistance in the PBFN ceramics. The equivalent circuit, $R_g(R_{gb}Q)$, is modeled for the observed electrical phenomena. The variation of the resistances of the grain and the grain boundary versus inverse of temperature respectively are shown in Fig. 8.10(b). Resistance of the grain and the grain boundary decreases with the increase in temperature and follows the temperature dependent Arrhenius relation. The activation energies ~0.26 and 0.54 eV are obtained for the grain and grain boundaries, respectively.

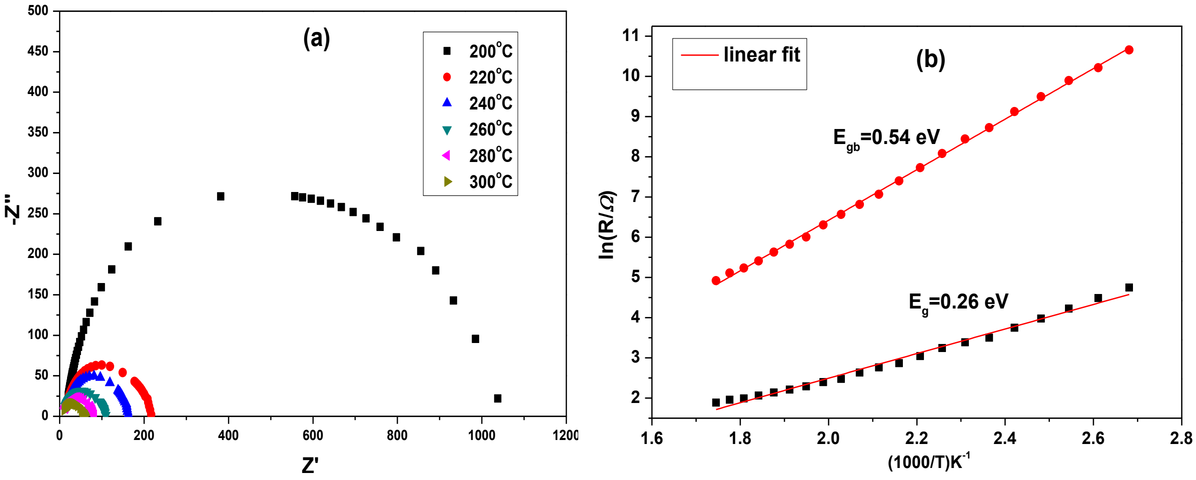

Fig. 8.10: (a) Nyquist plots at different temperature, and (b) Resistance of grain & grain boundary vs. inverse of temperature of the CS PBFN ceramic.

8.3.3 Impedance Spectroscopy Study of the CS Cr-BFN Ceramic

The Nyquist plot of the Cr-BFN ceramics at different temperatures is shown in Fig. 8.11(a). Nature of the Nyquist plot is same as that of the BLFN and PBFN ceramic plots. The equivalent circuit, $R_g(R_{gb}CQ)$, is modeled for the observed electrical inhomogeneity in the material. The area under the semicircular arc decreases with the increase in temperature, which indicates the decrease in resistance and the increase in conductivity of the Cr-BFN ceramics. The temperature variation of the resistance of the grain and the grain boundaries follows the Arrhenius relation (Fig. 8.11(b)). The activation energies for grains and grain boundaries are ~0.27 and 0.63 eV, respectively.

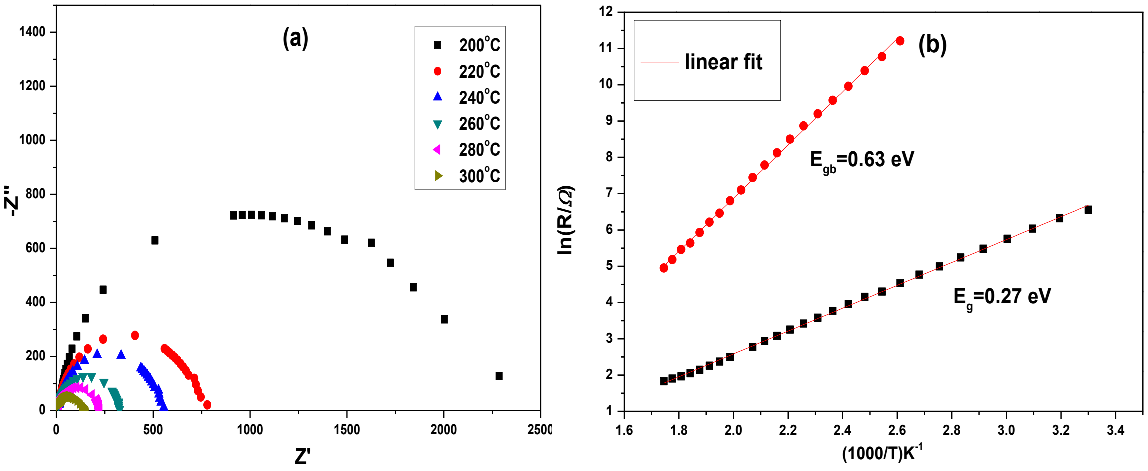

Fig. 8.11: (a) Nyquist plots at different temperature, and (b) Resistance of grain & grain boundary vs. inverse of temperature of the CS Cr-BFN ceramic.

8.3.4 Impedance Spectroscopy Study of the Mn-BFN Ceramic

The Nyquist plot of the Mn-BFN ceramics at different temperatures is shown in Fig. 8.12(a). The equivalent circuit is modeled by observing the ac conductivity data. Impedance data below 150 °C is modeled by using the equivalent circuit (RQ)Q and above it is modeled by using R(Q(R (RC))). The low frequency dispersive part, observed below 150°C, with no plateau region is attributed to the interfacial polarization and Q(CPE) is considered for the circuit whereas, the high frequency conductivity spectrum is relevant to the parallel combination of the resistance R and capacitance C. Above 150°C the conductivity of grain and grain boundary is diffused and the two overlapping semicircular arcs appear in the impedance spectrum. The equivalent circuit, used at higher temperatures, is R_g (Q (R_{gb} (R_{el}C))).

The variation of the resistances of the grain and grain boundary versus inverse of temperature is shown in Fig. 8.12(b). The temperature variation of the resistance of the grain and grain boundary follows the temperature dependent Arrhenius relation. The grain and the grain boundary resistances decrease with the increase in temperature. The activation energies ~0.43 0.84 and 0.94 eV are obtained for the grain, grain boundary and electrode interface effect respectively.

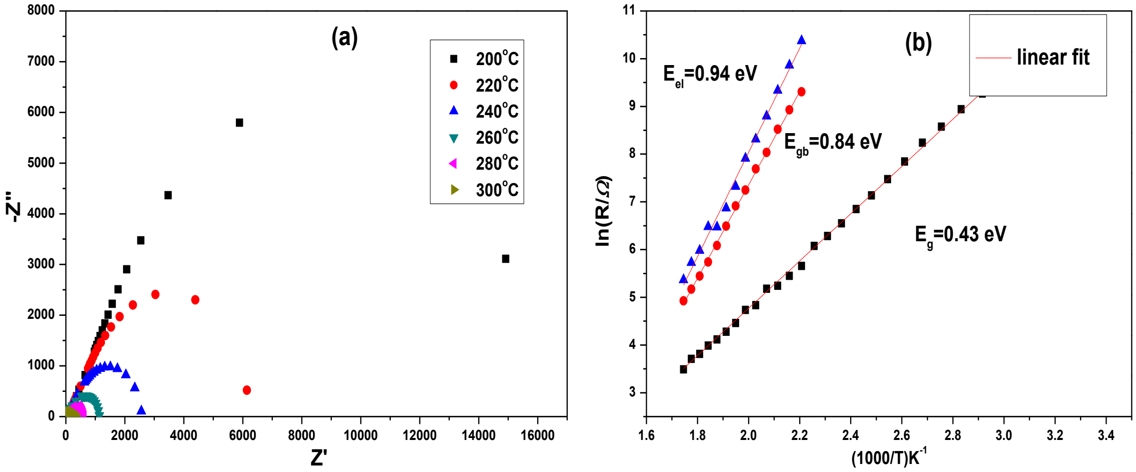

Fig. 8.12: (a) Nyquist plots at different temperature, and (b) Resistance of grain, grain boundary and electrode interfaces vs. inverse of temperature of the CS Mn-BFN ceramic.

8.3.5 Impedance Spectroscopy Study of the MWS BLFN Ceramic

The Nyquist plot at different temperatures of the MWS BLFN ceramics is shown in Fig. 8.13(a). Both, grain and grain boundary effects exist in the BLFN ceramics. The equivalent circuit, $R_g(R_{gb}Q)$, is modeled in order to extract the information about the grain and grain boundary in the conduction process. The variation of the resistances of the grain and grain boundary versus inverse of temperature is shown in Fig. 8.13(b). The resistance variation of both the grain and grain boundary effects follows the temperature dependent Arrhenius relation. Decrease in resistance of both the grain and grain boundary effects with increase in temperature are observed. Activation energies ~0.19 and 0.48 eV are observed for the grain and grain boundary effects, respectively.

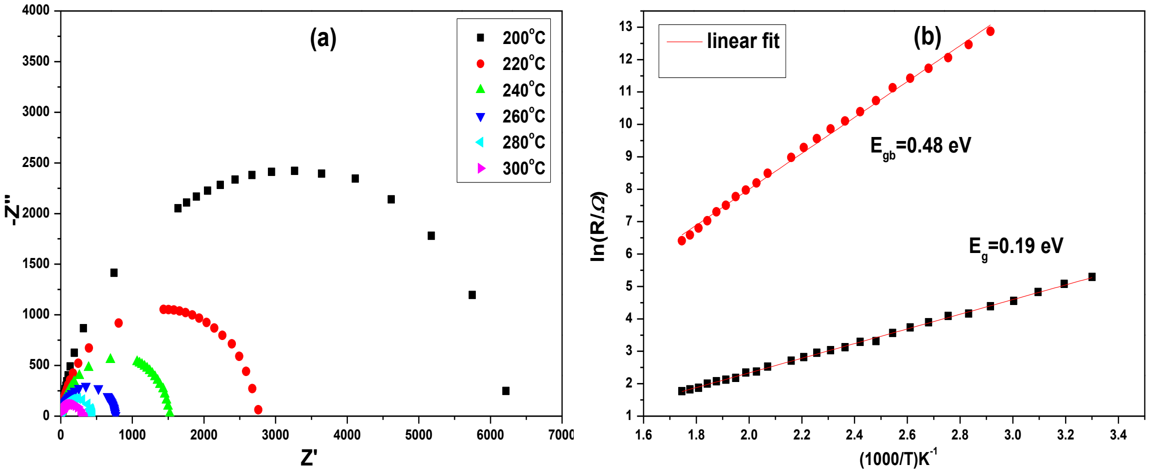

Fig. 8.13: (a) Nyquist plots at different temperature, and (b) Resistance of grain & grain boundary vs. inverse of temperature of the MWS BLFN ceramic.

8.3.6 Impedance Spectroscopy Study of the MWS PBFN Ceramic

The Nyquist plot at different temperatures of the MWS PBFN ceramics is shown in Fig. 8.14(a). The equivalent circuit, $R_g(R_{gb}Q)$, is modeled for the observed electrical phenomena in the PBFN ceramics. The variation of the resistances of the grain and grain boundary effects versus inverse of temperature is shown in Fig. 8.9. The resistances of the grain and grain boundary effects follow the temperature dependent Arrhenius relation (Fig. 8.14(b)). The activation energy ~0.26 and 0.60 eV are obtained for the grain and grain boundary effects, respectively.

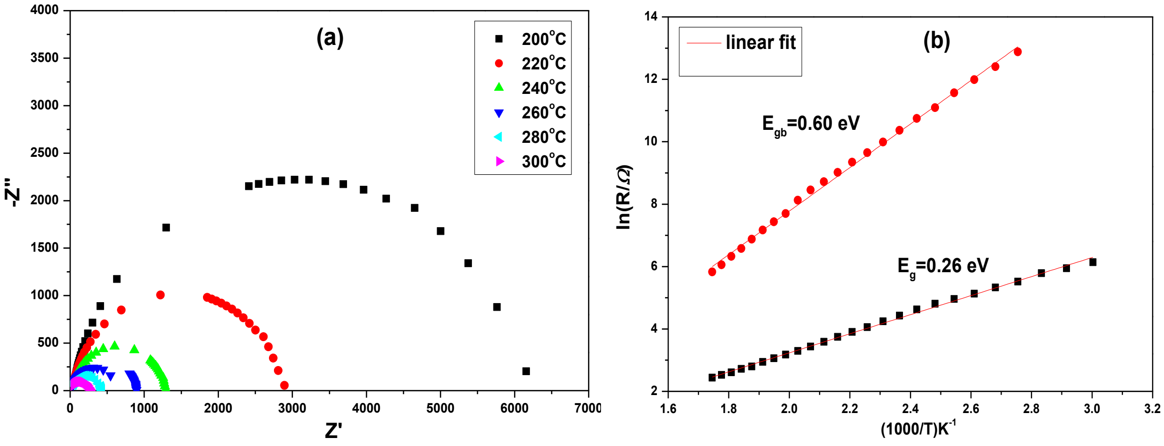

Fig. 8.14: (a) Nyquist plots at different temperature, and (b) Resistance of grain & grain boundary vs. inverse of temperature of the CS PBFN ceramic.

8.3.7 Impedance Spectroscopy Study of the MWS Cr-BFN Ceramic

The Nyquist plot at different temperatures of the MWS Cr-BFN ceramics is shown in Fig. 8.15(a). The observed behavior is similar as that of the MWS BLFN and PBFN ceramics. Both the grain and the grain boundary resistances are calculated by fitting the impedance data using the equivalent circuit, $R_g(R_{gb}Q)$. The temperature dependent resistance variation of the grain and grain boundary effects follows the Arrhenius relation (Fig. 8.15(b)). Activation energies ~0.25 and 0.47 eV are obtained for the grain and grain boundary effects, respectively.

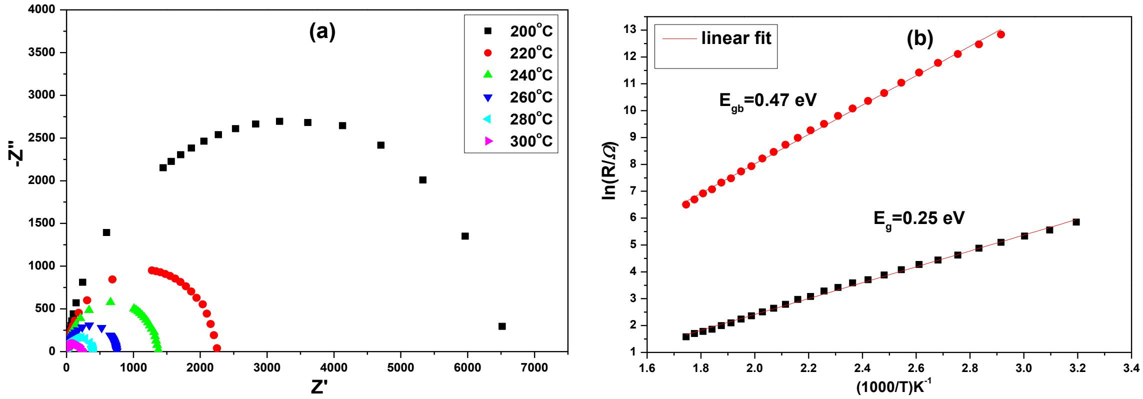

Fig. 8.15: (a) Nyquist plots at different temperature, and (b) Resistance of grain & grain boundary vs. inverse of temperature of the MWS Cr-BFN ceramic.

8.3.8 Impedance Spectroscopy Study of the MWS Mn-BFN Ceramic

The Nyquist plot at different temperatures of the MWS Mn-BFN ceramics is shown in Fig. 8.16(a). The electrical inhomogeneity, present in the Mn-BFN ceramics, is modeled by using the suitable equivalent circuit. The equivalent circuit, $R_g(R_{gb}Q)Q$, is modeled below 100°C and $R_g(R_{gb}Q)$ is modeled above it. The variation of grain and grain boundary resistance vs. inverse of temperature, shown in Fig. 8.16(b), follows the temperature dependent Arrhenius relation. Activation energies ~0.37 and 0.84 eV are obtained for the grain and grain boundary effects, respectively.

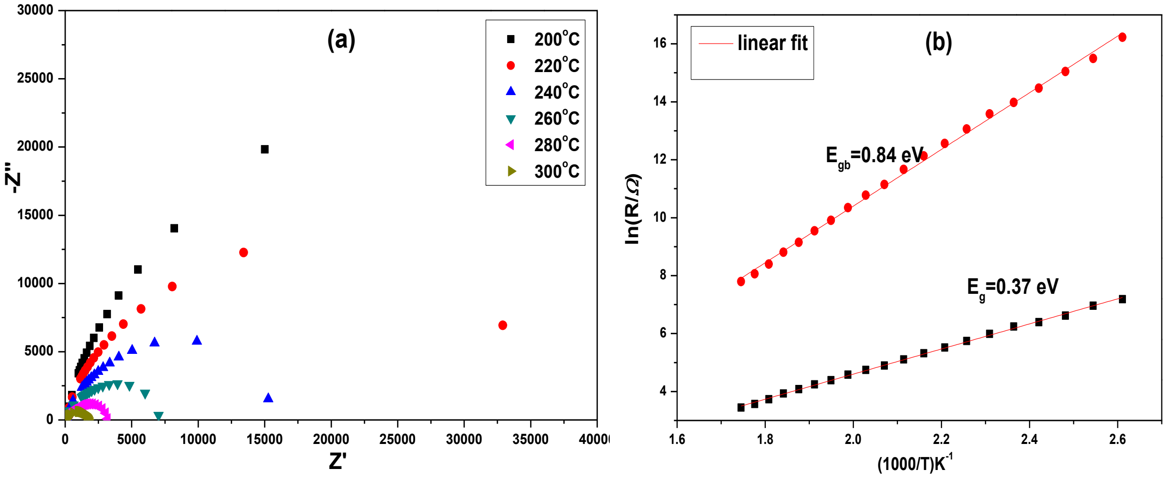

Fig. 8.16: (a) Nyquist plots at different temperature, and (b) Resistance of grain & grain boundary vs. inverse of temperature of the MWS Mn-BFN ceramic.

Table 8.1: DC activation energy; grain, grain boundary activation energy; and model equivalent circuit fitted parameters R_g (Ohm) and R_{gb} (Ohm) of the CS and MWS BFN based ceramics.

Modifications →		**La (x=0.08)**	**Pb (x=0.08)**	**Cr (x=0.5 wt %)**	**Mn (x=0.5 wt %)**
E_a (CS) in eV		0.60 (>120 °C) & 0.08 (<120 °C)	0.68 (>110 °C) & 0.16 (<110 °C)	0.62 (>120 °C) & 0.21 (<120 °C)	0.89 (>110 °C) & 0.32 (<110 °C)
E_a (MWS) in eV		0.73 (>180 °C) & 0.42 (<180 °C)	0.68 (>160 °C) & 0.38 (<160 °C)	0.59 (>100 °C) & 0.07 (<100 °C)	0.87 (>180 °C) & 0.29 (<180 °C)
CS	E_g in eV	0.23	0.26	0.27	0.43
	E_{gb} eV	0.60	0.54	0.63	0.84
MWS	E_g in eV	0.19	0.26	0.25	0.37
	E_{gb} in eV	0.48	0.60	0.47	0.84
CS	R_g (Ω) (RT)	0.87 x10^{2}	3.5 x10^{2}	4.3 x10^{2}	-
	R_{gb} (Ω) (RT)	3.2x10^{4}	6.1 x10^{4}	7.5 x10^{4}	2.6 x10^{4}
MWS	R_g (Ω) (RT)	1.4x10^{2}	4.6 x10^{2}	2.5 x10^{2}	8.4 x10^{2}
	R_{gb} (Ω) (RT)	6.6 x10^{5}	4.4 x10^{5}	6.4 x10^{5}	5.3 x10^{3}

8.4 Discussions on the Conductivity and the Impedance Spectroscopic Results of the CS and MWS BFN Based Ceramics

The ac conductivity and the impedance spectroscopy technique are used to interpret and analyze the frequency variation as well as the temperature variation of the conduction mechanisms of CS and MWS BFN based ceramics. In all the CS and MWS BFN based ceramics the nature of the frequency variation of the conductivity is almost similar. The conductivity spectra of CS Mn-BFN ceramics follow the Jonscher's power law whereas all other ceramics follows the double power law. The value of 's' and 'm' between 0 and1 indicates that the hopping mechanism present in the material is governed by the polaron [6, 11]. The value of 'n' between 1 and 2 indicates that the localized type of hopping mechanism is responsible for the conduction process in the material [6, 12].

The ac conductivity plots are helpful for modeling the equivalent circuit, required for fitting the impedance data of a material. The frequency independent plateau region represents the resistance, used in the equivalent circuit, and the frequency dispersive part, represents the capacitance used in the equivalent circuit. The low frequency dispersive part represents the presence of a CPE in the equivalent circuit.

Both the dc conductivity and the resistance (resistance of grain, grain boundary and electrode interface), obtained from Nyquist plots, follows the temperature dependent Arrhenius relation. The activation energy value <0.1 eV is attributed to the intrinsic conduction in the material due to the creation of a large number of space charges and other carriers [13] and the activation energy >0.5 eV is attributed to the mobility of the defects and the associated charge carriers [7, 8]. The lower grain activation energy in comparison to that of the grain boundary confirms the semiconducting nature of the grain and the insulating nature of grain boundary. The obtained activation energies suggest that oxygen vacancies are contributing to the conduction and relaxation processes in all the CS and MWS BFN based ceramics.

It is difficult to control the loss of oxygen from the processed compound during high temperature sintering, which can make the grains semiconducting. During the cooling process after sintering, the reoxidation may take place along the grain boundaries, which can yield an insulating nature of the grain boundaries. The absorbed oxygen at the grain boundaries are electron traps center, or acceptors, which attract the conducting electrons from the n-type semi conductive grains and can create a depletion layer with built in energy barrier, in the vicinity of grain boundaries. This causes various types of relaxation and conduction processes such as the formation of Schottky type of barrier at the interface [14, 15], Maxwell-Wagner interfacial polarization [16], internal barrier layer capacitor (IBLC) [17, 18] in the ceramics. All the above mentioned processes are suggested for the CS and MWS BFN based ceramics, which indicate the non-intrinsic origin of the high dielectric constant in these ceramics.

In the present study, we have used two different sintering mechanisms, the conventional one and the microwave one. In the CS of the BFN based ceramics, the soaking time is higher (4h) than that of the MWS (45 min). The dc activation energy for all the CS and the MWS BFN based ceramics at higher temperature is nearly same or greater than ~0.60 eV, whereas at lower temperature the values have large variation. From Table 8.1, the low value of the dc activation energy exists below 120°C for the CS whereas, for the MWS BFN based ceramics the dc activation energy exists up to 180°C. This suggests the slow variation of the resistance with temperature of the MWS BFN based samples. The resistance of the grain and grain boundary at room temperature of the CS and MWS BFN based ceramics are given in Table 8.1. The effect of the MWS on the grain and grain boundary effects of the BFN based ceramics needs further study.

8.5 Chapter Summary

AC conductivity and the impedance spectroscopic technique were used to study the electrical phenomena of both the CS and MWS BFN based ceramics. Based on brick layer model, an equivalent circuit model was proposed for the observed electrical response of the CS and MWS BFN based ceramic samples. For all the samples, the grain and the grain boundary resistance decreased with the increase. Oxygen vacancies and related point defects, generated during sintering, were considered for explaining the various conduction and relaxation mechanism, present in the CS and MWS BFN based ceramic. Resistance of the grain and grain boundary of the CS BLFN and PBFN ceramics was higher than that of the same samples sintered in microwave furnace.

References

[1] A.K. Jonscher, Dielectric Relaxation in Solids, Chelsea Dielectrics Press Limited, London 1983.

[2] A.K. Jonscher, The 'universal' dielectric response, Nature 267 (5613) (1977) 673-679.

[3] A.N. Papathanassiou, I. Sakellis, J. Grammatikakis, Universal frequency-dependent ac conductivity of conducting polymer networks, Appl. Phys. Lett. 91 (12) (2007) 122911.

[4] K. Funke, Jump relaxation in solid electrolytes, Prog. Solid State Chem. 22 (2) (1993) 111-195.

[5] A. Mandanici, M. Cutroni, C. Cramer, K. Funke, P. Mustarelli, C. Tomasi, Microwave dielectric spectroscopy and dynamical processes in superionic glasses, in: AIP Conf. Proc., Vol. 513, Aip, 2000, pp. 150-153.

[6] N. Ortega, A. Kumar, P. Bhattacharya, S.B. Majumder, R.S. Katiyar, Impedance spectroscopy of multiferroic $PbZr_xTi_{1-x}O_3$ / $CoFe_2O_4$ layered thin films, Physical review B 77 (1) (2008) 014111.

[7] H.J. Lee, C.W. Ahn, S.H. Kang, S.Y. Lee, I.W. Kim, M.S. Choi, J.S. Lee, B.M. Jin, Conduction mechanism of grain oriented $Bi_{3.15}Nd_{0.85}Ti_3O_{12}$ ceramics fabricated by a hot-forging method, Journal of Electroceramics 17 (2-4) (2006) 165-168.

[8] C. Ang, Z. Yu, Oxygen-vacancy-related low-frequency dielectric relaxation and electrical conduction in Bi : $SrTiO_3$, Phys. Rev. B: Condens. Matter 62 (1) (2000) 228-236.

[9] J. Liu, C.-G. Duan, W.-G. Yin, W.N. Mei, R.W. Smith, J.R. Hardy, Dielectric permittivity and electric modulus in $Bi_2Ti_4O_{11}$, The Journal of Chemical Physics 119 (5) (2003) 2812-2819.

[10] D.K. Pradhan, R.N.P. Choudhary, C. Rinaldi, R.S. Katiyar, Effect of Mn substitution on electrical and magnetic properties of $Bi_{0.9}La_{0.1}FeO_3$, J. Appl. Phys. 106 (2) (2009) 024102.

[11] M. Dult, R.S. Kundu, S. Murugavel, R. Punia, N. Kishore, Conduction mechanism in bismuth silicate glasses containing titanium, Physica B: Condensed Matter 452 (2014) 102-107.

[12] A. Hussain, C.W. Ahn, H.J. Lee, I.W. Kim, J.S. Lee, S.J. Jeong, S.K. Rout, Anisotropic electrical properties of $Bi_{0.5}(Na_{0.75}K_{0.25})_{0.5}TiO_3$ ceramics fabricated by reactive templated grain growth (RTGG), Current Applied Physics 10 (1) (2010) 305-310.

[13] M.M. Kumar, Z.G. Ye, Dielectric and electric properties of donor- and acceptor-doped ferroelectric $SrBi_2Ta_2O_9$, J. Appl. Phys. 90 (2) (2001) 934-941.

[14] Q. Zhang, T. Li, Z. Chen, R. Xue, Y. Wang, The non-ohmic and dielectric behavior evolution of $CaCu_3Ti_4O_{12}$ after heat treatments in oxygen-rich atmosphere, Mater. Sci. Eng., B 177 (2) (2012) 168-172.

[15] G. Deng, P. Muralt, On origin and intrinsic electrical properties of the colossal dielectric constant state in $CaCu_3Ti_4O_{12}$, in: IOP Conf. Ser.: Mater. Sci. Eng., Vol. 8, IOP Publishing, 2010, pp. 012016.

[16] I.P. Raevski, S.A. Prosandeev, A.S. Bogatin, M.A. Malitskaya, L. Jastrabik, High dielectric permittivity in $AFe_{1/2}B_{1/2}O_3$ nonferroelectric perovskite ceramics (A=Ba, Sr, Ca; B=Nb, Ta, Sb), J. Appl. Phys. 93 (7) (2003) 4130-4136.

[17] T.B. Adams, D.C. Sinclair, A.R. West, Giant Barrier Layer Capacitance Effects in $CaCu_3Ti_4O_{12}$ Ceramics, Adv. Mater. (Weinheim, Ger.) 14 (18) (2002) 1321-1323.

[18] A.R. West, T.B. Adams, F.D. Morrison, D.C. Sinclair, Novel high capacitance materials:- $BaTiO_3$:La and $CaCu_3Ti_4O_{12}$, J. Eur. Ceram. Soc. 24 (6) (2004) 1439-1448.

CHAPTER 9

Conclusions and Future Work

9.1 Conclusions

In the present thesis work, BFN based dielectric materials were successfully synthesized by conventional and microwave processing techniques. Here, we have also tried to investigate the intrinsic and extrinsic mechanisms, which contribute to the high value of the dielectric constant of these ceramics. Firstly, the parent BFN ceramics were processed by both the conventional and microwave sintering techniques. The XRD patterns showed that the CS and MWS BFN ceramics retained the single perovskite phase with the cubic structure. The SEM microstructure showed the grain size of MWS BFN ceramics was comparatively larger than that of the CS ones. MWS BFN ceramics, sintered at 1350^{o}C for 30 min, showed better dielectric results compared to the CS BFN ceramics, sintered at 1350^{o}C for 4hr. Maxwell Wagner type interfacial polarization was proposed as the origin of the high dielectric constant in both the CS and MWS BFN ceramics. A non-Debye type relaxation at RT was observed in both the CS and MW sintered BFN ceramics.

Optimum sintering parameters of the BFN based ceramics with La^{3+}, Pb^{2+} substitutions such as $Ba(1-x)La_{2x/3}(FeNb)_{0.5}O_3$ and $Ba_{(1-x)}Pb_x(FeNb)_{0.5}O_3$ with x=0,0.02,0.04,0.06,0.08, were optimized at 1250^{o}C for 4hr in conventional sintering. Whereas, the optimum sintering parameters of the Cr_2O_3 and $MnCO_3$ added BFN ceramics such as $Ba\ (FeNb)_{0.5}O_3$ – x wt% of Cr_2O_3 and $Ba\ (FeNb)_{0.5}O_3$ – x wt% of $MnCO_3$ with x=0, 0.5,1.0,1.5,2.0, were optimized at 1300^{o}C for 4 hr in conventional sintering. Following are major conclusions of the CS modified BFN based ceramics:

- All the La, Pb, Cr and Mn modified BFN systems showed the cubic structure
- All modifications, used in the present study, decreased the sintering temperature in comparison to the parent BFN system.
- Room temperature dielectric studies with frequency revealed the involvement of multiple relaxation mechanisms in the BFN system.
- The high value of ε_r ($\sim10^4$-10^5) at low frequency (100 Hz) indicated the presence of space charge polarization in all the ceramics. The low value of ε_r ($\sim10^2$) at high frequency (1MHz) indicated the presence of intrinsic polarization (i.e. within grain).
- Among the substituted compositions, the 8% La and Pb modified BFN ceramics exhibited the highest room temperature ε_r values ~35845 and ~25999 at 10kHz frequency, respectively.
- Among the added compositions, the 0.5wt% Cr and Mn modified BFN ceramics exhibited highest room temperature ε_r values ~ 38832 and ~ 4245 at 10 kHz frequency, respectively.
- The corresponding experimental densities of the 8% La, Pb substituted and the 0.5wt% Cr, Mn added BFN ceramics showed higher values.
- High temperature coefficient of capacitance in Mn modified BFN suggested its use in the temperature sensor and Bolometer applications.
- From the microstructure studies, the La and Pb modifications in the BFN system indicated their grain growth inhibitor nature.
- Optical band gaps of all the BFN based ceramics showed E_g ~ 1.3eV, which hinted about their semiconducting nature and indicated their importance for optical applications.

- No saturation in the polarization vs. applied voltage loops confirmed the non-ferroelectric nature in all the La, Pb, Cr & Mn modified BFN ceramics.

BFN based ceramics, i.e. 8% La, Pb, substituted and 0.5wt% Cr, Mn added BFN ceramics, showing better dielectric properties were also synthesized by microwave processing technique. Following are major conclusions of the MWS BFN based ceramics:

- It was found that the microwave processing of ceramics greatly reduced the dielectric loss in the systems compared to the corresponding conventional sintered one.
- The ε_r values were nearer to the corresponding CS samples which manifested the benefit of time and energy saving process of the MW processing techniques.
- The polarization vs. voltage loops measurement of all the ceramics confirmed their non ferroelectric nature at RT.
- Both intrinsic (within grain) and extrinsic (near grain boundary or electrode interface) polarization mechanism were proposed for the origin of the high dielectric constant in all ceramics.
- The conductivity of all the ceramics increased with the increase in temperature and the resistances of the grain, grain boundary and the electrode interface decreased with the increase of temperature.
- The activation energy of the grain conductivity was lower compared to that of the grain boundary conductivity, which confirmed the semi conductive nature of the grains.
- Role of oxygen vacancy was considered for the observed conduction mechanism in MWS BFN based ceramics.

9.2 Recommendations for Future Work

In the present study, we have used CS and MWS of the BFN and modified BFN ceramics. In addition to the above work, the following recommendations are made for the expansion of present work.

- ✓ Microstructure of the HDC materials highly influences the dielectric properties. Effect of both the microwave calcination and sintering on the microstructure of the BFN based high dielectric constant ceramics can be studied.
- ✓ Thin film and nano ceramics of the BFN based high dielectric constant ceramics can be prepared.
- ✓ BFN ceramic are good candidate for their application in various electronic devices for its high dielectric constant value. Further reduction of dielectric loss and better densification can be achieved by various other synthesis routes such as combustion, sol-gel techniques etc.
- ✓ Magnetization study can also be done in the BFN based systems to study their multiferroic nature for application in memory devices.

Bio-Data of the Author

Name: Subrat Kumar Kar

D.O.B.: 05-05-1983

Educational Qualification:

Secondary Education: Godibandha High School, Talcher

Intermediate: Talcher College**,** Talcher

B.Sc. (Hons. in Physics): Talcher College, Talcher

M.Sc. in Physics: Ravenshaw University, Cuttack

Ph.D. in Physics: National Institute of Technology, Rourkela

Publications:

1. Structural, morphological and dielectric study of $Ba(FeNb)_{0.5}O_3$ ceramics synthesized by microwave processing technique, **S. K. Kar et al.**, J. Phys. Chem. Solids **74** (2013) 1408-1413

2. Effect of microwave sintering on structural, morphological and dielectric properties of $Ba(FeNb)_{0.5}O_3$ ceramics, **S. K. Kar et al.**, Journal of Electroceramics **31** (2013) 331-337.

3. Permittivity and Modulus Spectroscopic study of $Ba(FeNb)_{0.5}O_3$ Ceramics, **S. K. Kar et al.**, Processing and Application of Ceramics **7** (2013) 181-187.

4. Investigation of relaxation and dc conductivity mechanism in multiferroic $Ba(FeNb)_{0.5}O_3$ ceramics by impedance spectroscopy, **S K Kar et al.**, J. of Solid State Science (**Under review**).

5. High Dielectric Constant and Low Optical Band Gap in La-Modified $Ba(FeNb)_{0.5}O_3$ Ceramics, **S K Kar et al.**, Material Chemistry and Physics (**Under review**).

6. Dielectric, electrical conductivity and optical properties of Cr_2O_3 modified $Ba(FeNb)_{0.5}O_3$ ceramics, **S K Kar et al.**, Ceramic International (**communicated**).

7. Influence of $MnCO_3$ admixture on structural, microstructural, electrical and optical properties of $Ba(FeNb)_{0.5}O_3$ ceramics, **S K Kar et al.**, J. Alloys and Compounds (**Communicated**).

8. Dielectric studies of PbO doped high dielectric constant Ba(FeNb)$_{0.5}$O$_3$ ceramics, **S K Kar et al.**, J of Advanced Dielectrics (**communicated**).

Conference paper:

1. Effect of Sintering Temperature on Dielectric Properties of Ba(FeNb)$_{0.5}$O$_3$ Ceramics NSFD-XVI, Bilaspur, Chhattisgarh, December 2010,

2. "Admittance Spectroscopy Study of Mn-doped Ba(FeNb)$_{0.5}$O$_3$ Ceramics" , CM Days, NIT Rourkela, August 2013.

Permanent Address

Subrat Kumar Kar
S/O: Sashi Bhusan Kar
AT: Luhundi
PO: Radharaman Pur
Talcher, Odisha-759100

*****